STABILITY OF MATERIALS FOR USE IN SPACE-BASED INTERFEROMETRIC MISSIONS

By

ALIX PRESTON

A DISSERTATION PRESENTED TO THE GRADUATE SCHOOL
OF THE UNIVERSITY OF FLORIDA IN PARTIAL FULFILLMENT
OF THE REQUIREMENTS FOR THE DEGREE OF
DOCTOR OF PHILOSOPHY

UNIVERSITY OF FLORIDA

2010

© 2010 Alix Preston

This is dedicated to all who were told they would fail, only to prove them wrong

ACKNOWLEDGMENTS

Much of this work would not have been made possible if it were not for the help of many graduate and undergraduate students, faculty, and staff. I would like to thank Ira Thorpe, Rachel Cruz, Vinzenz Vand, and Josep Sanjuan for their help and thoughtful discussions that were instrumental in understanding the nuances of my research. I would also like to thank Gabriel Boothe, Aaron Spector, Benjamin Balaban, Darsa Donelon, Kendall Ackley, and Scott Rager for their dedication and persistence to getting the job done. A special thanks is due for the physics machine shop, especially Marc Link and Bill Malphurs, who spent many hours on the countless projects I needed. Lastly, I would like to thank my advisor, Dr. Guido Mueller, who put up with me, guided me, and supported me in my research.

TABLE OF CONTENTS

LIST OF TABLES

LIST OF FIGURES

KEY TO ABBREVIATIONS

AOM	Acousto-Optic Modulator
BE	Binding Energy
CFRP	Carbon Fiber Reinforced Polymer
CTE	Coefficient of Thermal Expansion
CVD	Chemical Vapor Deposition
DI	De-ionized
DRS	Disturbance Reduction System
EMRI	Extreme Mass Ratio Inspiral
EOM	Electro-optic Modulator
ESA	European Space Agency
$\mathcal{F}$	Finesse
FFT	Fast Fourier Transform
FSR	Free Spectral Range
FWHM	Full-Width Half-Maximum
GRACE	Gravity Recovery and Climate Experiment
GRS	Gravitational Reference Sensor
GSFC	Goddard Space Flight Center
GW	Gravitational Waves
HPF	High Pass Filter
I.D	Inner Diameter
IMS	Interferometeric Measurement System
ISS	International Space Station
KE	Kinetic Energy
LATOR	Laser Astrometric Test of Relativity
LIGO	Laser Interferometer Ground Observatory
LISA	Laser Interferometer Space Antenna

LPF	Low Pass Filter
MCST	Modified Compression Shear Test
ND	Neural Density
O.D	Outer Diameter
PD	Photodiode
PDH	Pound-Drever-Hall
PZT	Piezo-electric transducer
ROC	Radius of Curvature
S-D	Scratch-Dig
SiC	Silicon Carbide
SIM	Space Interferometry Mission
SMBH	Super-Massive Black Hole
XPS	X-Ray Photoelectron Spectroscopy

KEY TO SYMBOLS

c	speed of light in vacuum
I_D	flux emerging without being scattered
I_0	flux of electrons originating at depth D
σ	Boltzman's constant (1.38065×10^{-23} $m^2kg\ s^{-2}K^{-1}$)
$T_r(f)$	reflected transfer function as a function of laser frequency
$T_t(f)$	transmitted transfer function as a function of laser frequency
Ω	modulation frequency of the electro-optic modulator
ω	laser frequency

Abstract of Dissertation Presented to the Graduate School
of the University of Florida in Partial Fulfillment of the
Requirements for the Degree of Doctor of Philosophy

STABILITY OF MATERIALS FOR USE IN SPACE-BASED INTERFEROMETRIC MISSIONS

By

Alix Preston

August 2010

Chair: Guido Mueller
Major: Physics

Space-based interferometric missions such as SPIRIT, SPECS, TPF, and LISA will take measurements of the universe with unprecedented results. To do this, these missions will require ultra-stable materials and bonding techniques to be used for critical optical components such as optical benches or support structures. As an example, the telescope support structure for the LISA mission must be made of a material that is stable to better than 1 pm/$\sqrt{\text{Hz}}$ at 3 mHz and whose length between the primary and secondary mirrors cannot change by more than 1.2 μm over the lifetime of the mission. Although materials such as silicon carbide (SiC) and carbon fiber reinforced polymers (CFRP) have been suggested for this use, they have not been tested to these strict requirements.

The author is part of a group at the University of Florida that is developing a materials research facility capable of testing the stability and strength of materials and bonding techniques for use in space-based interferometric missions. This work describes the techniques used to test the stability of materials at the femtometer level. Results are presented for SiC, Zerodur, a carbon fiber reinforced polymer, Super Invar, and k-180 piezoelectric material. In addition, several bonding techniques are described along with potential uses for space missions. Specific attention is paid to a promising new jointing method known as hydroxide bonding. The bonding method, bonding mechanism, and shear test strengths are presented for several material combinations. During this work, it was found that hydroxide bonding could be used to bond SiC to SiC with significant

strength in a simple manner and was chosen to bond a prototype telescope support structure for the LISA mission. Initial results and discussion about further improvements to the design are presented.

Finally, investigations were done to determine the differential phase noise in counter-propagating beams through an optical fiber. Results using a polarizing Sagnac interferometer showed a differential phase noise of $\sim 5 \times 10^{-5}$ cycles/$\sqrt{\text{Hz}}$ at 1 Hz. The experimental setup, noise sources, and results are presented.

CHAPTER 1
INTRODUCTION

In an attempt to learn more about why we are here, where we came from, and what the future holds for humankind, countless time and resources have been spent on projects designed to answer these and other questions. Ground-based dark matter and gravitational wave detectors search for signals coming from our universe to learn how it has evolved over time. Giant telescopes map the sky for planets that may be similar to our own. Although ground-based detectors can provide a wide range of information about both the Earth and the universe we live in, noise sources such as seismic activity or atmospheric turbulence make it difficult, or near impossible, to make certain measurements from the ground. For this reason, space-based missions have become increasingly popular in order to make measurements the Earth-bound detectors cannot. Often space-based detectors work complimentary to their ground-based counterparts to provide new and exciting information. While moving detectors into low-Earth orbits and beyond can overcome many challenges faced on the ground, other difficulties such as drag-free orbits or the inability to service components provide new challenges to overcome.

As space-based missions are becoming ever more complex, the sensitivity of necessary measurements has increased as well. This requires the use of ultra-stable materials, oscillators, and lasers that push their achievable limits. Several materials such as silicon carbide (SiC) and Super Invar have been used for critical optical components on several space-based missions, but their dimensional stability has not been studied to determine if they are suitable for the next generation of detectors. Although this work primarily focuses on determining the stability of materials and bonding techniques for their use on the Laser Interferometer Space Antenna (LISA), it can be used as a reference when designing other critical optical components such as optical benches or telescope support structures for future space-based missions

1.1 Space-Based Missions

There are a variety of proposed space-based missions that will study everything ranging from the Earth's climate to gravitational wave sources. Each mission consists of multiple subsystems that work together for a common goal. Discussion of each mission and its components would be unfeasible in this work, so only a select few will be discussed that could potentially benefit form work presented in this dissertation.

1.2 GRACE

The Gravity Recovery and Climate Experiment (GRACE) maps various geophysical processes that produce gravity anomalies [1]. Certain geophysical processes generate gravity anomalies over the surface of the Earth. Measuring these anomalies provides a better understanding of the structure of the Earth. Short-term mass fluctuations such as a variation in the water content of the Earth's crust, global sea level changes, or polar ice sheet balance can be measured with GRACE to determine their impact on the global climate. Data collected from GRACE has provided the scientific community with information that has led to a substantial improvement in our understanding of how the Earth changes over time [2].

GRACE was launched March 17, 2002 and consists of two identical satellites in a near circular orbit ∼500 km above the Earth's surface (see Figure 1-1). The distance between the satellites is ∼220 km along-track and linked by a K-band microwave ranging system. In addition, each satellite carries Global Positioning System (GPS) receivers, attitude sensors, and high precision accelerometers. The satellite orbits decay at ∼30 m/day such that the satellites do not have a fixed repeat pattern which reduces its measurement sensitivity. The satellites are 3-axis stabilized such that the K-band antennas are pointed at each other [1].

In order to produce the necessary precision, several post-processing techniques are used. To reduce the effects caused by the ionosphere, the dual-frequency one-way K-band

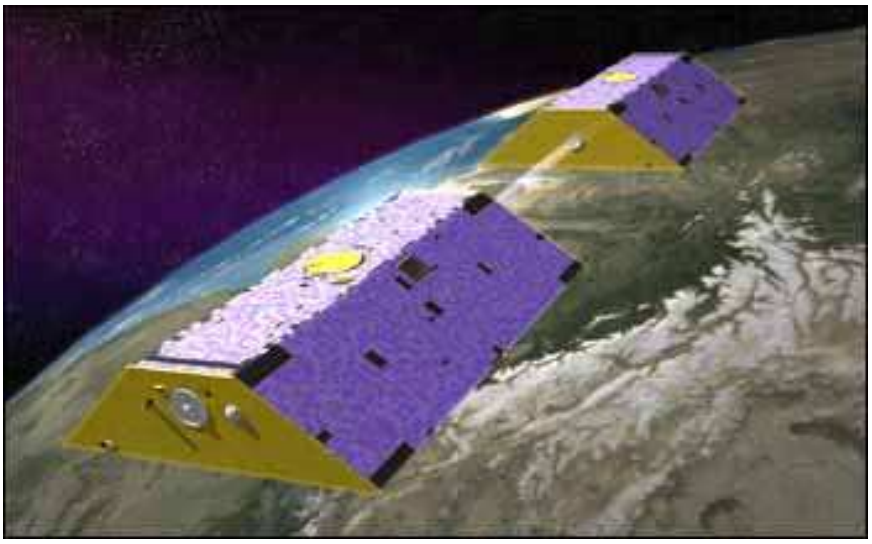

Figure 1-1. Representation of the GRACE satellites in orbit above the Earth. Image courtesy of NASA.

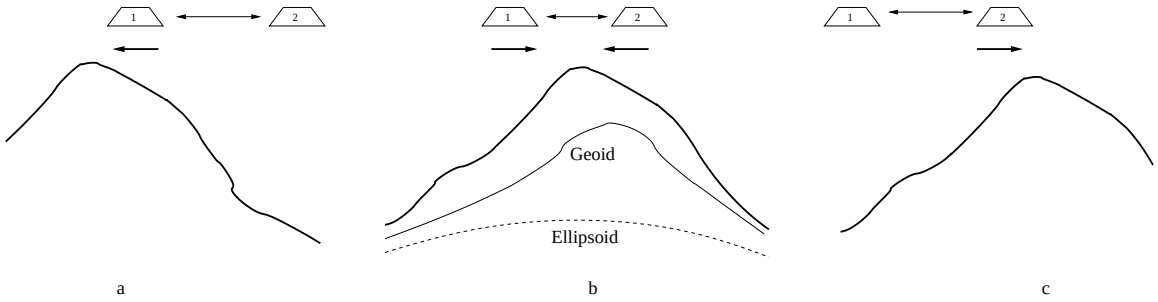

Figure 1-2. Representation of how the GRACE spacecraft move as they pass over a mass anomaly. In (a), spacecraft 1 feels an acceleration due to the anomaly. After spacecraft 1 passes the anomaly, it feels an acceleration in the opposite direction of spacecraft 2 as shown in (b). After spacecraft 2 passes the anomaly, it feels an acceleration in the opposite direction as depicted in (c).

phase measurements transmitted and received by each satellite are combined during ground processing which removes many of the effects caused by oscillator instability.

Data gathered from the precision accelerometers is used to remove non-gravitational forces on the satellites. The GPS receivers allow precision time-tagging of when the data was taken and is used to determine the inter-satellite distance. Precision estimate of the inertial orientation is provided by the attitude sensors. The combination of these measurements along with ancillary data is used to produce a representative gravity field of the Earth.

The data gathered from the GRACE mission has led to a better understanding of variations of mass in the Earth, exchanges between ice sheets and the oceans, ground water storage on land masses, changes due to deep ocean currents, and a detailed map of the Earth's gravity field [3].

1.3 GRACE Follow-On

Although GRACE continues to provide a wealth of information about continental water storage, the Earth's geoid, global sea level changes, fluctuations of the polar ice sheets, and other geophysics processes, a follow-on mission has been proposed that would increase the sensitivity and provide even more information about the Earth's dynamics[4]. These measurements include the time varying ocean bottom pressure, monitoring groundwater and polar ice caps, and measuring the lithosphere thickness. To make these measurements, the proposed follow-on mission would consist of two coplanar spacecraft in circular, polar, orbits at an altitude of 250-600 km. The spacecraft would be small satellites approximately 150-200 kg and would require about 100 W of total power and would have a baseline lifetime of 5 years, with a goal of 10 years. The distance between the spacecraft would be loosely maintained to 50-100 km and measured using laser interferometry. MicroNewton FEEP-type thrusters will be used to provide a drag-free control of the spacecraft in addition to ground track repeating within a few kilometers [4].

For the GRACE follow-on mission to work, the laser interferometry must be capable of precision phase extraction with lasers having a frequency stability of better than 1 part in 10^{16} rms over 1000 seconds. In addition, the spacecraft will need an internal sensor or "accelerometer" capable of measuring non-gravitational accelerations on the spacecraft to better than 1 part in 10^{-13} m/s^2 rms over 1000 seconds. It is important that the inertial sensor be fully integrated with the laser interferometer in order to reduce errors relating the interferometer reference point to the inertial reference point. While there are several designs that could be implemented, a method using freely-falling proof masses on each spacecraft along with heterodyne interferometry containing polarizing optics as a

metrology system appears to be promising [4]. First performance laboratory measurements of a spacecraft-to-spacecraft interferometry design using a metal breadboard have shown a sensitivity of 2.5 nm/$\sqrt{\text{Hz}}$ [4]. Significant improvements in the stability results could be achieved using an optical bench made of a glass-ceramic such as Zerodur and using advanced bonding techniques, such as hydroxide bonding, for the optical components.

1.4 LISA

1.4.1 Introduction

To paraphrase John Wheeler, spacetime tells sources how to move, and moving sources tell spacetime how to ripple. In 1975 Russel Hulse and Joseph Taylor discovered a binary pulsar whose orbit decay over time was in accordance with what general relativity predicts from the emission of gravitational radiation [5]. Recently, the outburst timing of two black holes in the OJ 287 system has provided more indirect evidence that gravitational waves (GW) exist [6], but have yet to be directly detected despite efforts from ground-based gravitational wave detectors such as LIGO and VIRGO. Although ground-based GW detectors have yet to find a signal, the evidence for them is compelling enough to prepare for space-based detectors that will search for complimentary GW sources [7],[8]. One such mission is known as the Laser Interferometer Space Antenna (LISA). LISA is a joint NASA/ESA mission that consists of 3 spacecraft that will form a triangle whose arms are separated by 5×10^9 m. LISA will trail the Earth by 20°, and is inclined to the ecliptic plane by 60°. This orientation will allow LISA to provide angular resolution of sources to about one degree, with sub-degree resolution for many strong sources when averaged over time periods of 6 to 8 months. LISA will detect gravitational radiation from super-massive black hole (SMBH) mergers, galactic binaries, and extreme mass-ratio inspirals (EMRI's) in the 30 μHz to 1 Hz frequency band with a strain sensitivity of $10^{-21}/\sqrt{\text{Hz}}$ at its most sensitive frequency [9]. Since it is thought that the GW sources detectable by LISA play an important role in determining how the

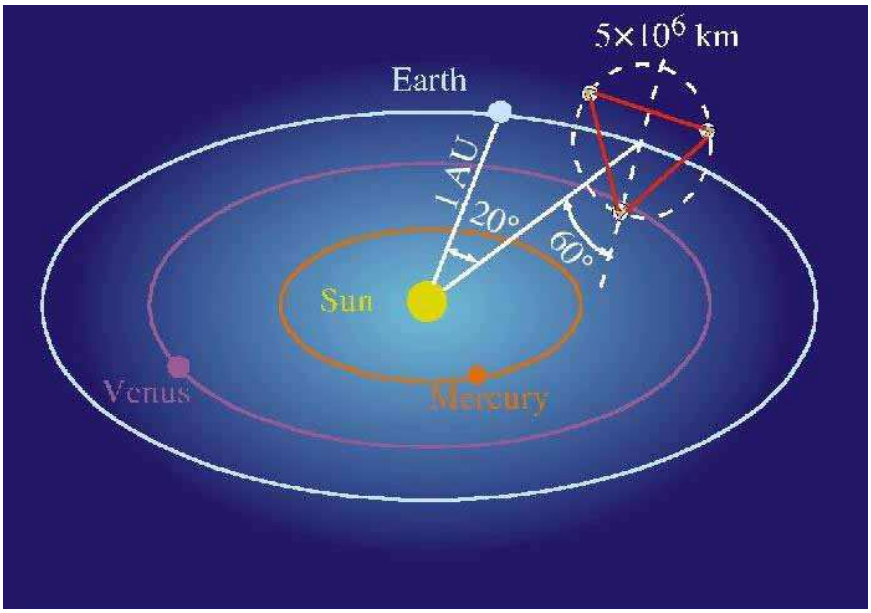

Figure 1-3. Representation of the LISA orbit. Image courtesy of NASA.

early universe formed, LISA will effectively provide us with a glimpse into the past, and subsequently study the structure and evolution of the universe.

1.4.2 Sources

The LISA sensitivity band is expected to be an extremely rich portion of the gravitational wave spectrum. Observing these gravitational waves will provide an insight into the dynamic processes that occur in astrophysics since our view of the universe has been built almost entirely on measurements made using the electromagnetic spectrum. Detection of gravitational wave sources has been a difficult task because the field generated by gravitational radiation, given by $h_{ij} \sim \frac{Gm^{quad}}{rc^2}\frac{v^2}{c^2}$ where m^{quad} is the portion of the source's mass that participates in quadrupolar motions, is so small [10]. For any appreciable signal that has hope of being detected, the source must be extremely massive and compact enough to move at relativistic speeds. Although this does somewhat limit the sources available for detection, there are still plenty of sources that will provide a plethora of information about the universe we live in.

1.4.2.1 Cosmological background sources

Of significant interest to the scientific community are the stochastic sources that are cosmological in origin. Of these sources, the gravitational radiation produced from the first moments of the Big Bang are the most eagerly sought out. Detection of this background radiation would provide insight into how the universe developed much further back in time than measurements of the microwave background can produce since gravitational waves travel undisturbed to us and carry all of their information from the past. Unfortunately these waves will not be detectable by the LISA mission due to their extremely small amplitude. Although this source may be out of reach for LISA, there are other potential cosmological backgrounds that may be within LISA's grasp [10]. For example, when the universe was roughly 1 TeV, the electroweak interaction separated into electromagnetic and weak interactions. Since this separation was not uniform, some regions transitioned before others, producing a background [11],[12]. It has also been suggested through superstring theory that a network of cosmic strings produced in the early universe that have expanded to cosmic size could produce backgrounds detectable by LISA [13]. Although there is an extremely small chance of LISA finding GW background signals, the insight provided into out universe will be tremendous and worth looking for.

1.4.2.2 Binary stars

Within the Milky Way alone it is expected that there are tens of millions of compact binaries that will generate GW's in the LISA band [10]. Most of these are white dwarf binaries which will slowly spiral towards each other as they radiate gravitational waves. These objects are extremely important to the LISA mission because they are guaranteed sources. There are so many of these sources that cannot be distinguished from one another that there is an expected confused background that will be detected in the LISA band. The amplitude of the noise will be of significant importance in determining the distribution of stars within our galaxy [14].

In addition, several binary systems that have already been observed electromagnetically should produce GW's in the LISA band large enough to be distinguished from the background. These sources will provide instant verification of the LISA instrumentation[15].

1.4.2.3 Chirping sources

As objects in a binary system emit gravitational radiation and spiral towards each other, their orbiting periods will decrease and slowly "chirp" upwards. Since the LISA band is at such a low frequency, the required mass for this to happen must be extremely large [10]. The most important chirping sources will consist of systems where both masses are black holes. Black hole binaries with masses ranging from 10^4 to 10^7 solar masses and mass ratios ranging from 1/20 to around 1 will generate gravitational waves directly in the most sensitive spot of the LISA band. The signals will sweep across the LISA band in times ranging from several months to several years. Finding these signals early will be invaluable. With enough warning, telescopes can be positioned to look at that patch of the sky where a gravitational wave is thought to have come from. In this manner both an electromagnetic and gravitational spectrum can be found and provide a more complete understanding to the constituents and interactions of black holes. Even with pessimistic formation rates, at least a few super massive black hole coalescence should be observed over LISA's lifetime, while more optimistic views put this number in the hundreds [16].

1.4.2.4 Extreme mass ratio inspirals (EMRIs)

EMRIs are binary systems in which the smaller member (such as a stellar mass compact object) orbits a much larger object (such as a galactic core black hole). Such systems are created through scattering process in the core of galaxies in which the larger body captures the smaller body into a highly-eccentric strong-field orbit. Current estimates suggest hundreds of these sources could be detected by LISA each year [17]. The manner in which the smaller body spirals into the larger body will tell a great deal of information about the binary's spacetime and essentially map out the gravitational potential of the larger body.

1.4.3 General Measurement Overview

The basic measurement to detect GW sources will be by monitoring the distance between proof masses on adjacent spacecraft. Within each spacecraft are two cubical free-flying proof masses. The spacecraft use capacitive sensing and micro-Newton thrusters to maneuver around the proof masses as to not disturb them. There are three measurement arms between the spacecraft, each of which consist of two links. The links represent a one way travel of the laser from one spacecraft to another. Picometer level changes between the 5×10^9 m proof mass separation will provide the necessary strain sensitivity of $\sim10^{-21}$ [18].

The distance changes between the proof masses will be measured using laser interferometry. Light at a wavelength of 1064 nm will be sent from one spacecraft to a distant spacecraft where it will be interfered with a small amount of light from the local spacecraft. The precision of this measurement relies on measuring the phase of the radio frequency (RF) beatnote as recorded by a digital phasemeter with microcycle accuracy. As a gravitational wave passes through the LISA constellation, the arm lengths will be modulated. The resulting changes in the beatnote will be recorded and sent back to Earth where it will be post-processed. The ability to reach the required strain sensitivity will depend on the arm length, the accuracy to which the relative displacement between the two proof masses can be measured, and the ability to which the proof masses can be shielded from disturbances.

Taking these factors into account, the LISA spacecraft design has been driven by two systems known as the Disturbance Reduction System (DRS) and the Interferometry Measurement System (IMS). The purpose of the DRS is to keep the proof mass as undisturbed as possible, while the purpose of the IMS is to measure the distances between the proof masses using optical interferometry. Both systems work together in a manner to reach the required sensitivity.

1.4.4 The Disturbance Reduction System (DRS)

The DRS consists of a set of local sensors, actuators, and controls that act together to meet the disturbance and pointing requirements [18]. The heart of the DRS is the Gravitational Reference Sensor (GRS) which houses the proof mass. The spacecraft act to shield the proof masses from disturbance forces such as solar winds or cosmic dust. If left unattended, these forces would cause the spacecraft to orient itself in a way that would make measurements impossible. To avoid this, the GRS "senses" where the proof mass is relative to the spacecraft. MicroNewton thrusters provide the actuation needed in order to position and orientate the spacecraft in order to provide drag-free operation as well as provide the necessary pointing of the outgoing laser beams towards the distant spacecraft.

The low frequency end of the LISA band will be limited by the acceleration noise of the proof masses and spacecraft which are directly dependant on the performance of the DRS. The noise allocation for the DRS given as an amplitude spectral density for a single proof mass is given by [18]

$$\sqrt{S_{\Delta a_{DRS}}} \leq 3 \times 10^{-15} \frac{m}{s^2\sqrt{Hz}} \sqrt{1 + \left(\frac{f}{8mHz}\right)^4} \sqrt{1 + \left(\frac{0.1mHz}{f}\right)}. \tag{1–1}$$

To convert Eq. 1–1 into a displacement noise, it is integrated twice. Taking into account that there are four proof masses in each Michelson-type interferometer and that all of the noise is uncorrelated will add a factor of two to the total noise. This results in [18]

$$\sqrt{S_{\Delta x_{DRS}}} = 2\frac{\sqrt{S_{\Delta a_{DRS}}}}{(2\pi f)^2} \leq 6 \times 10^{-15} \frac{m}{\sqrt{Hz}} \frac{1}{(2\pi f)^2} \sqrt{1 + \left(\frac{f}{8mHz}\right)^4} \sqrt{1 + \left(\frac{0.1mHz}{f}\right)}. \tag{1–2}$$

This error budget is made up of subsystems, each with their own noise sub-allocation. Such noise sources include electrostatics, Brownian motion of the residual gas around the proof mass, and thermal effects among others. A detailed acceleration noise budget using all known disturbance effects is given in reference [19].

Significant research has been done to characterize the noise sources to provide a better understanding of how the proof masses will behave on the LISA mission [20]. Much of this work typically involves suspension of the proof mass from a torsion pendulum to model and measure expected noise sources. In addition, the performance of the GRS will be directly tested when it is launched on-board the LISA Pathfinder mission [21].

1.4.5 The Interferometric Measurement System (IMS)

The IMS is the part of the measurement system that measures the distances between proof masses. Since the proof mass orbits vary by about 1% over the course of a year, the interferometer arms are neither equal nor constant. Because of this, the raw data measurements taken on board must be post-processed in order to extract the gravitational wave signals. The measurement performance of the IMS are derived directly from the single link sensitivity [22]. In order to determine this sensitivity, knowledge of the system response to a gravitational wave must be known. This response can be calculated using the sums and differences of the phases measured in each of the six links as they are combined in post-processing with the appropriate delays [18]. From the single link strain sensitivity, the IMS measurement performance can be derived and is given by [18]

$$\sqrt{S_{\Delta x_{IMS}}}(f) \leq 12 \times 10^{-12} \frac{m}{\sqrt{Hz}} \sqrt{1 + \left(\frac{2mHz}{f}\right)^4}. \tag{1–3}$$

Within this total error budget are subsystems with their own noise sub-allocation. For instance, the telescope pathlength stability has an allocation of 1 pm/$\sqrt{\text{Hz}}$, while the optical bench dimensional stability has an allocation of 4.5 pm/$\sqrt{\text{Hz}}$ [18]. All IMS sub-allocations have the same frequency dependance as in Eq. 1–3. Many of the imposed requirements are currently pushing the limits of what is possible and it is imperative that all subsystems and their components be tested in order to determine their stability and limitations.

1.4.5.1 Optical bench

The optical bench consists primarily of three interferometers needed to make the proof mass to proof mass distance measurements. In addition, it also contains other components to perform ancillary functions such as monitoring the outgoing laser power or CCDs to allow establishment of the laser links.

The light-weight baseplate is made of Zerodur and provides the dimensional stability of all other path lengths. Hydroxide bonding is used to mount the fused silica optical components on the polished Zerodur baseplate [23]. The bench will be isostatically mounted to a large interface ring that the GRS is also mounted to.

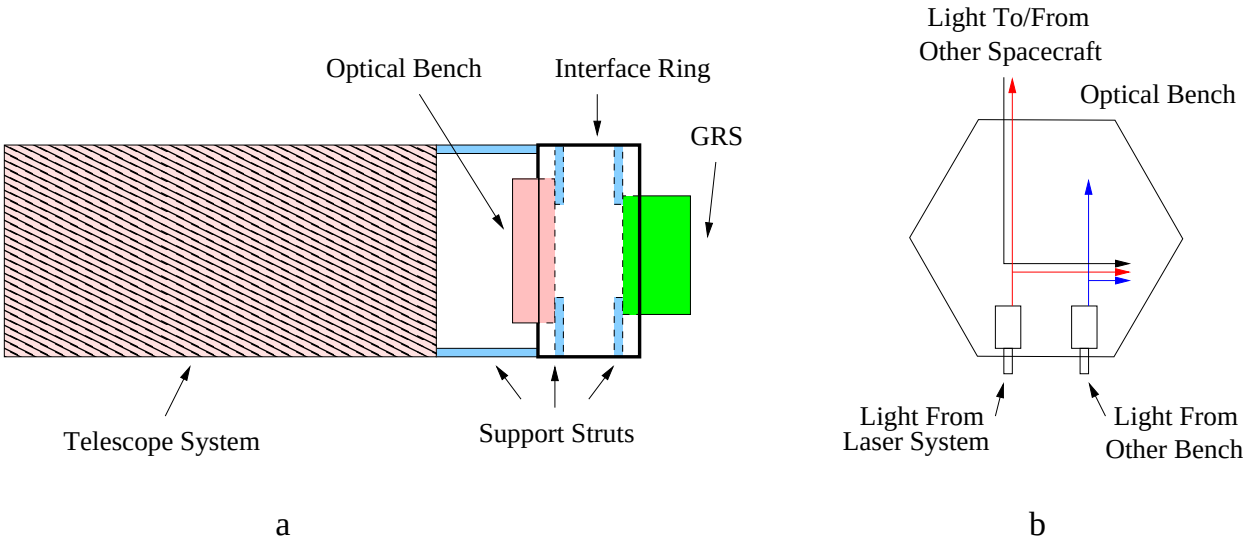

Figure 1-4. Simplified view of the assembly (a) and the optical bench (b).

Light from the laser system is delivered to the optical bench through the use of a fiber optic cable. The majority of this light is then sent to the telescope, with the remainder of the light used as local measurements. The separation of the incoming and outgoing beams from adjacent spacecraft is done through the use of a polarizing beam splitter. In order to make the necessary measurement beatnotes, light from one optical bench needs to be sent to the other, and vice versa. To do this, an optical fiber will be used that contains both beams in counter-propagating directions. The transmitted power entering the telescope

from the optical bench is about 2 W, while the total power received from the adjacent spacecraft is on the order of 200 pW [23].

1.4.5.2 Telescope system

Of particular importance for the telescope is to minimize and control the stray light sources. The most convenient setup to minimize stray light is to use an off-axis two-mirror telescope. Both the primary and secondary would be made of Zerodur and separated by a carbon fiber reinforced polymer (CFRP) spacer. The primary and secondary apertures are ∼400 mm and ∼30 mm, respectively, and are connected through a ∼590 mm CFRP spacer [23]. The telescope design also includes a re-focusing mechanism to correct for the differences in alignment on ground and in flight due to the outgassing of the CFRP spacer.

Another possible configuration would be to use an on-axis design made of SiC. The secondary would be connected to the primary through the use of SiC struts. Although the struts will produce additional stray light in the on-axis design, the effects need to be studied more before a decision on the baseline design can be made since the primary source of stray light will be due to back-reflections from the secondary. Further discussion of this subsystem is presented in Chapter 7.

1.5 LATOR

The Laser Astrometric Test Of Relativity (LATOR) is a proposed mission to measure the non-Euclidean features of a light triangle with sides passing close by the Sun. The goal is to probe General Relativity and other alternate theories of gravity by measuring the deflection of light as it passes close to the Sun [24]. To do this, two spacecraft will be placed in orbit around the Sun in addition to using an interferometer on the International Space Station (ISS). Light from both spacecraft are sent to the other spacecraft and to the ISS. A phase measurement of the interfered light will determine the internal angles of the spacecraft-spacecraft-ISS triangle.

The angle measured by the spacecraft can then be compared to the angle computed using Euclidean geometry. A deviation in this angle will provide a wealth of information

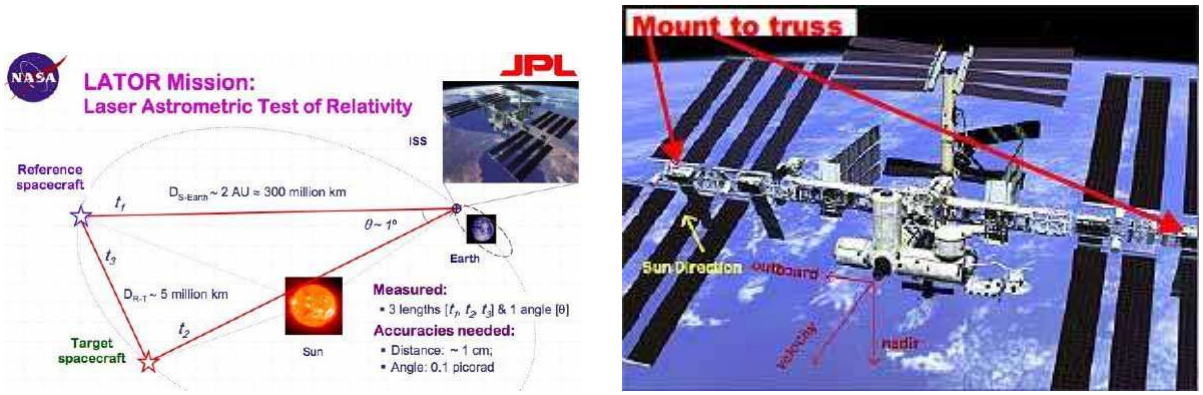

Figure 1-5. Configuration of the LATOR orbits, spacecraft, and interferometer on the ISS. Image courtesy of NASA.

about the second post-Newtonian features of gravity, the mass parameter of the Sun (the spatial metric's "gamma mass"), as well as measuring the solar gravitational field to unprecedented levels [25].

1.5.1 Mission Design

There are numerous subsystems that will all work together in order for the LATOR mission to be successful. Only a select few of these subsystems pertaining to this work will be discussed. For details on these and other subsystems, see references [24], [25].

1.5.2 Spacecraft orbits

To measure the deviation from Euclidean geometry as the light passes through the Sun's gravitational field, the LATOR mission will place two spacecraft in a heliocentric orbit on the opposite side of the ISS. The spacecraft are separated by about 1° when viewed from the ISS [26], and orbit with a 3:2 resonance with the Earth as depicted in Figure 1-5. The 3:2 resonance occurs when the Earth does three revolutions around the Sun, while the spacecraft does exactly two. The exact period of the orbit will vary slightly from a 3:2 orbit by less than one percent depending on the time of launch. The advantage of choosing this orbit are that it imposes no restriction on the time of launch, it will only require small propulsion maneuvers, it provides a very slow change in the Sun-Earth-Probe

angle, and an additional maneuver will allow for a small orbital inclination that will enable measurements at different latitudes.

1.5.3 Optical design

In order to make the necessary angle measurements, the ISS will need to be equipped with three 20 cm diameter telescopes. One telescope is designed with a narrow bandwidth laser line filter in front of it and an InGAs camera at its focal plane that is sensitive to the 1064 nm light that will be used and serves as the acquisition telescope to locate the spacecraft near the Sun.

The second telescope emits the directing beacon to the other spacecraft. A pair of piezo controlled mirrors placed on the focal plane directs the light into and out of the telescope. The collimated light with a power of ∼10 W is injected into the telescope focal plane and properly directed by the piezo mirrors [25].

The third telescope is used for the laser light tracking interferometry and will be used to measure the relative length changes of the spacecraft to an accuracy of less than 10 pm using heterodyne interferometry [24]. Two piezoelectric X-Y-Z stages will be used to move the tips of two single-mode fibers while maintaining focus and beam position on the fibers and other optics. Dithering at a few Hertz will provide the means to make the necessary alignment of the fibers and subsequent tracking of the spacecraft completely automatic.

Both spacecraft are identical and contain a 1 W cavity fiber-amplified laser whose wavelength is 1064 nm and drifts at ∼2 MHz per hour. Most of the power is pointed to the ISS through a 20 cm diameter telescope whose phase is tracked by an interferometer. The remaining power is directed to the other spacecraft through the use of another telescope. In addition to the two transmitting telescopes, each spacecraft is equipped with two receiving telescopes. The telescope that faces the ISS has a laser line filter and knife-edge coronograph to suppress the light from the Sun to 1 part in 10^4 of the light level of the light received from the ISS [25]. The receiving telescope that points towards the spacecraft does not require a filter and coronograph.

In addition to the four telescopes, the spacecraft will also carry a small telescope with a CCD camera that will be used to provide the initial alignment of the spacecraft such that they point at the ISS. Another similar telescope could be installed at right angles to the first to determine the spacecraft attitude using known, bright stars. Star trackers of this design have been used for several years and are readily available.

1.5.4 Interferometry

Interferometry will be used to make the precision angle measurements needed. A simplified schematic of how this can be done is shown in Figures 1-6 and 1-7. In Figure 1-6, two sidereostats are pointed at a target and two fiducials (represented by the corner cubes) determine the end points of the interferometer baseline.

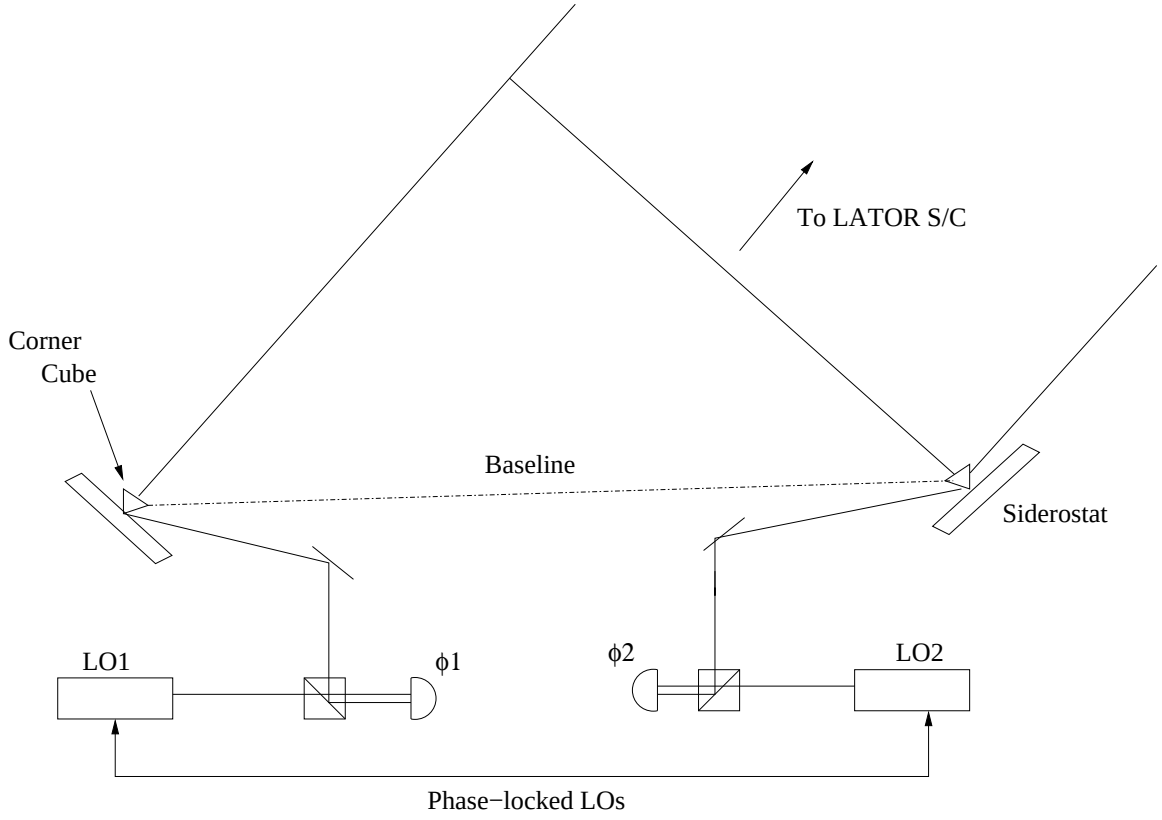

Figure 1-6. Heterodyne interferometry on one spacecraft with phase-locked local oscillator.

Stable local oscillators are interfered with the light from the two arms, and the phase difference is recorded. If the local oscillators were phase locked, then the angles of the

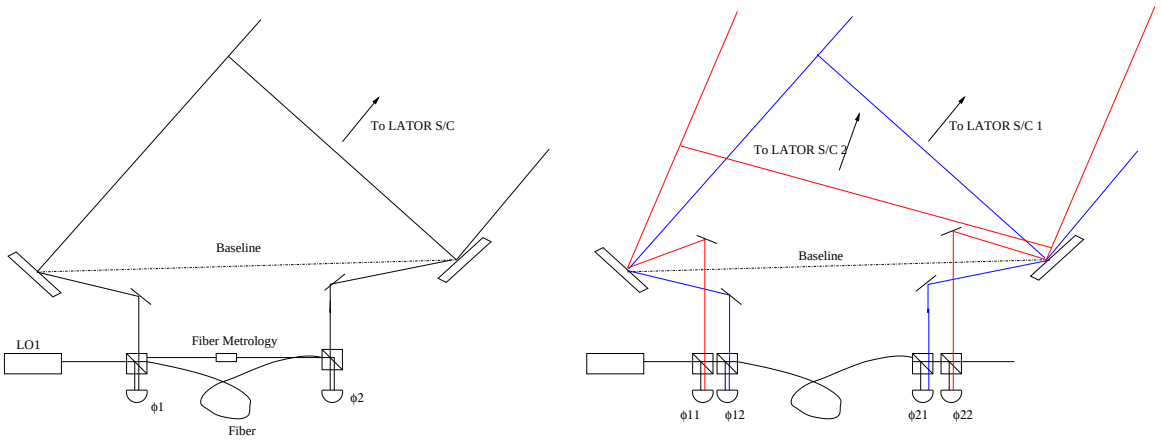

Figure 1-7. Fiber linked heterodyne interferometry and fiber metrology system (left) and fiber linked heterodyne interferometry on two spacecraft (right).

target with respect to the baseline normal is given by [25]

$$\theta = \arcsin\left(\frac{(2\pi n + \phi_1 - \phi_2)\lambda}{2\pi b}\right), \tag{1–4}$$

where λ is the wavelength of the laser, n is an unknown integer arising from the fringe ambiguity, and b is the baseline length [24]. Unfortunately, is extremely difficult to phase lock the two local oscillators of such a long baseline with the precision needed, so another method was proposed that uses a single mode fiber. The signal from the local oscillator can be transmitted to both sidereostats through a single mode fiber. In this configuration, additional metrology is needed in order to monitor the changes in the path length of the fiber as the local oscillator propagates through it as shown in the left side of Figure 1-7. The metrology system measures the distance from one beam splitter to the other and the resulting angle is given by [25]

$$\theta = \arcsin\left(\frac{(2\pi n + \phi_1 - \phi_2 + m_1)\lambda}{2\pi b}\right), \tag{1–5}$$

where m_1 is the phase variations introduced by the fiber. When an additional arm is added to this configuration the phase variations due to the fiber are common to both

arms. The differential angle then becomes [25]

$$\theta = \arcsin\left(\frac{(2\pi(n_1 - n_2) + (m_1 - m_2))\lambda}{2\pi b} + \frac{((\phi 11 - \phi 12) - (\phi 21 - \phi 22))\lambda}{2\pi b}\right). \qquad (1\text{–}6)$$

This is only a general overview of how the angle would be measured between the two spacecraft, and in practice the interferometer will have optical paths that are different lengths and will need to be measured with additional metrology systems.

In order to make the angle measurements, a long baseline will be introduced on the ISS. Optical packages will be integrated on the ISS to the S6 and P6 truss segments which are located at opposite ends of the ISS. Both packages will be separated by ∼100 m and will have a clear line of sight path between the two transceivers during the observational periods in addition to having a clear line of sight to both spacecraft. Location on the ISS is ideal since a limited amount of Sun tracking that is needed to point the telescopes on the ISS to the spacecraft can be done using the α-gimbals on the ISS [25].

Two metrology systems will be used on the ISS to make the angular measurements. The first system measures the optical path difference between the two laser signals while the other system measures the changes in optical path through the fiber. Michelson interferometers will be used in order to make the necessary metrology measurements. Both spacecraft signals will be measured simultaneously using an electro-optic modulator and modulating at a different frequency for each beam. The metrology signals of the fiber will be used in the post processing to determine the angular measurements. The metrology signals sent to the spacecraft from the ISS will be stabilized to better than one part in 10^{10} using a temperature controlled Fabry-Perot etalon that is locked using a Pound-Drever scheme [25].

The current design for LATOR will provide a wealth of knowledge about the limits of general relativity. Moving from a $\lambda = 10$ cm (the current standard) to a $\lambda = 1$ μm wavelength will gain a factor of 10^{10} reduction in the solar plasma optical path fluctuations [25]. Taking advantage of current drag-free technology for use on the

spacecraft will provide ultra-precise orbit determination since the spacecraft will be insensitive to effects from solar wind and radiation pressure. Making use of existing laser and optical technologies will keep costs low. The LATOR mission will also benefit from lasers and optical telecom that have been developed for the Space Interferometry Mission (SIM) [25]. The technology needed for the LATOR mission has already been demonstrated and provides a solid conceptual foundation. The LATOR mission is unique in concept and design, and will lead to robust advancements in the understanding of fundamental physics.

CHAPTER 2
MATERIALS

Satellites for space-based missions are made up of multiple subsystems that all work together to make complex measurements. Often there are strict requirements on subsystems, such as the optical bench or telescope mirrors, that must be met in order for the design sensitivity to be achieved. The choice of materials then becomes an important consideration. In some cases, a material with an extremely low CTE must be chosen in order to reduce thermal effects. Although there are materials available with CTE's on the order of 10^{-8}/K, they may exhibit other mechanical or thermal characteristics which are unwanted, such as a low thermal conductivity, ferromagnetic behavior, are brittle, or have a low Young's modulus. To fully understand a material and its possible applications, the thermal and mechanical properties, along with the production process should be known. For this reason, an introduction to a select, few materials that are either commonly used, or have great potential for space-based interferometric missions are presented. The production process, mechanical and thermal properties, and current or potential applications are discussed.

2.1 Zerodur

Zerodur is a glass ceramic made by SCHOTT whose CTE is extremely low around room temperature. It is characterized by a phase of evenly distributed nano-crystals within a residual glass phase. Zerodur contains about 70-78 weight percent of a crystalline phase with a negative linear thermal expansion. The remaining glass phase consists of a positive linear thermal expansion. Together, these phases act against each other to produce an overall CTE that is very close to zero within a certain temperature range, usually centered around 25°C. General properties of Zerodur are presented in Table 2-1 (it should be noted that these values are for room temperature and are typical for a broad range of Zerodur classes and are not absolute) [27].

Table 2-1. Selected material properties and their values for Zerodur

Property	Value
Density	2.53 g/cm^3
Modulus of Elasticity	13×10^6 psi
Thermal Conductivity	1.43 W/mK
Specific Heat	0.80 cal/g C
Index of Refraction	1.54

2.1.1 Production Process

The production process of Zerodur is outlined in Figures 2-1 and 2-2. The Zerodur is cast into an annealing oven where the temperature is cooled in a controlled manner for several weeks. The outer layers of the material are removed in order to prevent uncontrolled ceramization during the next steps. During the ceramization process, the

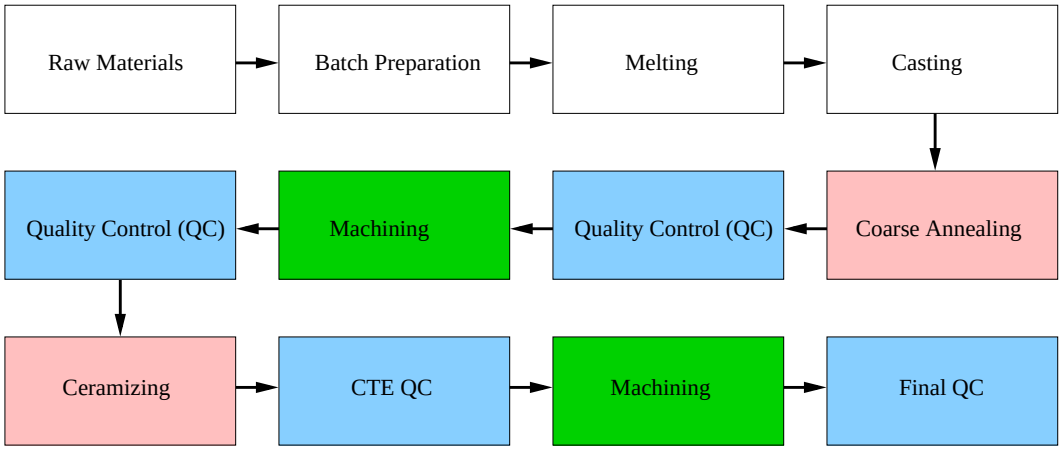

Figure 2-1. Zerodur production process.

material is heated up again to achieve growth of the crystal phase in a controlled manner. The heat treatment process has a critical effect on the CTE homogeneity of the blank and can last several months depending on the Zerodur material needed. Once this step has been completed, the Zerodur can be processed into its final shape. CTE samples are taken directly from the final material to ensure the final CTE value and homogeneity. Depending on the size and shape of the processed parts, the homogeneity of the Zerodur CTE can be kept to less than 0.03×10^{-6}/K per 18 tons of material [28].

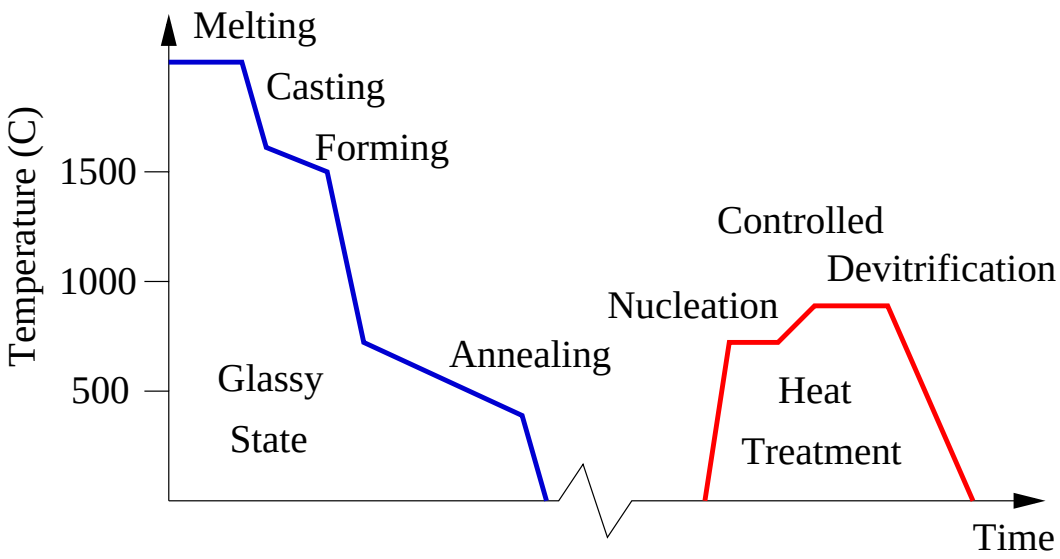

Figure 2-2. Zerodur annealing process.

2.1.2 CTE

Zerodur is optimized for application use from 0-50°C, with a CTE zero crossing that can be tailored within a few degrees around 25°C [28]. The CTE of the Zerodur is derived using the length change measurements from the use of a dilatometer as the material is heated up or cooled down. Depending on the Zerodur class specified, the variation in the mean CTE can be as little as $0.02\times10^{-6}K^{-1}$ for temperatures ranging from 0-50°C. In certain fabrication processes, this variation can be even smaller [28]. The excellent homogeneity and extremely low CTE have made Zerodur an optimal material for many telescope mirrors. Telescope blanks for Keck I and II, Grantecan, and HET were produced using a specifically fabricated Zerodur [28].

Table 2-2. Zerodur class value and corresponding CTE.

Zerodur expansion class	CTE
0	$0\pm 0.02\times10^{-6}K^{-1}$
1	$0\pm 0.05\times10^{-6}K^{-1}$
2	$0\pm 0.10\times10^{-6}K^{-1}$

2.1.3 Thermal Cycling

Zerodur is designed to operate in a temperature range of 0-50°C. Outside this range, the CTE values can change dramatically. In addition, thermal cycling outside its operating temperature can produce a range of effects. For temperatures greater than 700°C, the material properties are irreversibly changed and will be determined by the quenching process. For a temperature cycling in a range between 130-320°C, the total Zerodur length will be changed, in addition to having its CTE zero crossing changed. For most mirror applications, elevated temperatures are encountered when coating the surface. These processes are short in time and have shown to have only negligible effect on the surface figures. Thermal cycles for temperatures between -70 and 40°C show a hysteresis in the CTE and will shift the CTE zero crossing. The only way to reverse the effects of thermal cycling on the Zerodur is to heat the material above 320 C and cool down in the same manner as the original ceramization process [28].

2.1.4 Long Term Stability

Over the course of 10 years, a 400 mm long Zerodur bar was examined at a constant temperature of 20°C at the PTB Braunschweig. During this time, the Zerodur showed a monotone decrease in length, often referred to as aging [28]. The slope of the decrease in length depends on the thermal treatment and the age after the thermal treatment. A slower cooling treatment of the Zerodur will decrease the slope, making the Zerodur appear older. Any thermal treatment will start the aging process anew.

2.1.5 Cryogenic Behavior

The stability of Zerodur at cryogenic temperatures is an important topic due to its use for mirrors in astronomical space-based missions. The CTE of Zerodur has been measured from 10-300°K to show that Zerodur normally expands upon cooling. In addition, the observed mirror shape deviations of a 300 mm diameter mirror under a temperature change from 300 K to 130 K resulted in a figure distortion of less than 0.035 waves RMS over the entire cool down [29].

2.2 Invar

Invar alloys are widely known and used. Their low CTE close to room temperature have made them an attractive metal for use in many precision instruments [30]. Invar alloys are commonly used in clocks, scientific instruments, bimetal strips in thermostats, and many other applications where constant monitoring is necessary. The relative ease in fabricating and machining have also made Invar alloys popular. While there are several Invar alloys available that only vary slightly in elemental composition, only the three most common will be discussed. The production process, chemical compositions, and applications of each alloy are presented.

2.2.1 Invar 36

Invar 36 is an iron-nickel alloy that possesses a CTE roughly one-tenth that of carbon steel at temperatures up to 200°C. This alloy is commonly used for applications where dimensional changes due to temperature fluctuations need to be minimized. This has made Invar 36 an attractive material for use in radio and electronic devices, aircraft controls, and optical and laser systems.

Although the heat treatment process will vary slightly depending on manufacturer, three annealing methods are presented. Each alloy will have its own specific heat treatment, but in general, the process is similar.

Method 1:

1. Heat parts to 830°C and hold at that temperature for one-half hour per inch of thickness.
2. Furnace cool at a rate not to exceed 100°C per hour to 315°C. No additional machining should be done on these parts.
3. Let parts air cool.

Method 2:

1. Rough machine parts.
2. Heat part to 830°C and hold at this temperature for one half hour per inch of thickness.

3. Furnace cool at a rate not to exceed 100°C per hour to 315°C. Air cooling below 315°C is acceptable.

4. Heat parts at 315°C for 1 hour followed by air cooling.

5. Heat parts at 96°C for 48 hours followed by air cooling.

6. Finish machining.

Method 3:

1. Rough machine parts.

2. Heat parts to 830°C and hold at this temperature for one half hour per inch of thickness, then water quench.

3. Semi-finish machining parts.

4. Heat parts for 1 hour at 315°C, followed by air cooling.

5. Heat parts at 96°C for 48 hours followed by air cooling.

6. Finish machining parts.

The variation in heat treatments and elemental purity and concentration from manufacturer to manufacturer can produce alloys that are not as reliably made as other low expansion materials such as Zerodur. This can produce a variation in thermal properties. Although CTE values can vary, typically Invar 36 has a CTE of approximately 1.6×10^{-6}/K [31].

A specific Invar alloy was developed by NASA/JPL for the Cassini spacecraft camera. Dubbed High Purity Invar 36 (HP Invar 36), it has a much improved time varying CTE and dimensional stability [31]. Very pure elements were weighed, mixed, and pressed into a mold and sintered in a controlled atmosphere. Analysis showed this alloy to have a CTE and dimensional stability similar to that of Invar 32-5 [31]. Although this specific alloy is not readily available, it attests to the extent to which the CTE of Invar 36 can be pushed. Reference [31] provide an in depth discussion of the heat treatment and stability of this high purity Invar. It should also be noted that in reference [31], the particular heat

treatment did show some effects on the materials properties, but the differing elemental compositions had a much greater effect on the material properties, specifically the CTE.

All Invar alloys should be handled carefully. Dropping them may disturb the grain structure and cause it to become magnetized to a small extent. The addition of impurities such as sulfur and chromium make Invar 36 easier to machine. This allows for complex structures to be machined, while still keeping its low CTE.

2.2.2 Invar 42

Invar 42 is an alloy whose chemical composition is presented in Table 2-3. The primary use of Invar 42 is for glass-to-metal seals in electronic tubes, automotive and industrial lamps, transformer and capacitor bushings, and other ceramic-to-metal applications. These applications are due to the similar expansion properties of Invar 42 and other glasses, particularly 1075 glass. The heat treatment for Invar 42 is similar that of Invar 36.

2.2.3 Invar 32-5

Invar 32-5, also known as Super Invar, is a magnetic alloy containing iron, nickel, and cobalt. The higher percentage of cobalt in Super Invar provides a lower CTE around room temperature when compared with Invar 36. Typically, Super Invar has a CTE 3-6 times less than that of Invar 36, and is used in many applications including structural supports and optical and laser systems that require precision measurements.

For the lowest thermal expansion and optimum stability, the heat treatment recommended is to initially heat the materials to 840°C for 1 hour and then water quench. This is followed by a stress relieving operation at 315°C for 1 hour, air cool and age at 96°C for 24 hours, then air cool. Due to the high oxidation rate of this alloy above 538°C, it is recommended the parts be heat treated in a protective environment such as a vacuum or inert gas.

Although Super Invar's initial temporal stability is much better than Invar 36, it has been shown that it degrades over time to rates comparable to that of Invar 36. This

process occurred much faster at 60°C than at 27°C and seems to be evidence that the temporal stability of Super Invar is highly temperature dependant [32].

Due to the rarity of literature on the chemical composition as well as the mechanical and thermal characteristics of the Invar family, the following tables are a compiled list of selected properties for Invar 36, 42, and 32-5.

Table 2-3. Compositional values of Invar 36, 42, and 32-5.

Element	36	42	32-5
Carbon	0.15	.05 max	.05
Nickel	36 nominal	41	31.75
Phosphorus	.006	–	–
Iron	balance	balance	balance
Silicon	0.40	0.20	0.09
Manganese	0.60	0.40	0.39
Sulfur	0.004	–	0.01
Chromium	0.25	–	0.03
Cobalt	0.50	–	5.36
Aluminum	–	–	0.07
Copper	–	–	0.08

Table 2-4. Comparison of selected properties for 3 Invar alloys

Property (at room temperature)	Invar 36	Invar 42	Invar 32-5
Density (kg/m^3)	8055	8110	8150
Thermal Conductivity (W/m K)	10.5	10.7	–
CTE ($\times 10^{-6}$/K)	1.3	4.3	0.63
Modulus of Elasticity (MPa)	–	148	144
Tensile Strength (MPa)	–	517	144
Specific Heat (J/kg K)	515	500	–

2.3 Silicon Carbide

Carborundum, more commonly known as silicon carbide (SiC), was first reported in 1810 by Berzelius [33]. In 1890 SiC was accidentally synthesized by Edward G. Acheson while running an experiment to synthesize diamonds. SiC occurs naturally in meteorites, although it is found rarely and often only in small amounts. Acheson was able to produce SiC by passing an electric current through a mixture of sand and petroleum coke at very high temperatures in an electric furnace. Although this process has been modified since its

inception, it is still used to produce certain types of SiC today. It wasn't until the 1960's that SiC could be produced in molded form. Five decades later, SiC is produced at almost one million tonnes per year [33].

Although SiC was discovered 2 centuries ago, not until recently has it become a popular material to replace the use of metals and alloys for structural purposes, especially in extreme environments.

2.3.1 Structure of SiC

There are ∼200 polytypes of SiC, although only a few are common. Each polytype can be visualized as being made up of a single tetrahedranol unit in which each silicon atom is tetrahedrally bonded to 4 carbon atoms. These carbon atoms are then tetrahedrally bonded to 4 silicon atoms. The difference among the polytypes are the varying orientational sequences by which these tetrahedral layers are stacked. Each layer can only be stacked in one of two ways, but the varying sequential combinations of these layers represent different crystal polytypes. These polytypes are then grouped into two specific classifications of SiC known as α-SiC and β-SiC. Although these classifications of SiC differ in crystalline structure, their theoretical densities vary by less than 0.002 g/cm^3. The β-SiC structure forms at lower temperatures than that of the α-SiC structure [33].

2.3.2 Fabrication Process

SiC is produced in a variety of fashions, most of which are proprietary in nature. In addition, the material characteristics can be varied depending on the specific process and materials used. For this reason, only a general outline of the production process of SiC will be presented.

2.3.2.1 Acheson process

The Acheson process uses a mixture of high purity silicon dioxide and petroleum coke to produce α-SiC. Large quantities of this mixture are then covered in a furnace with electrodes on opposing ends and a rod in the center to connect the two. A current of ∼25 kA is then passed through the electrodes causing the material to heat to 2500°C. As the

rod heats up, the mixture heats up form the center outward. This will cause high-purity α-SiC to form close to the rod and lesser purity SiC to form outward. Depending on the process used, some β-SiC is formed closer to the outside. The current is left on for 10-20 hours, resulting in a large chunk of SiC [33]. This chunk is then broken, sorted, crushed, milled, and classified into different sizes and commercial grades of SiC powder. Further processing of the powder can be done in order to produce powders with crystalline sizes on the order of tens of nanometers. The crystalline size plays an important role in the densification process of SiC. The SiC parts made from these powders will have varying properties (specifically porosity) depending on the crystal size used.

2.3.2.2 Sintered SiC

Sintered SiC is produced by using the α-SiC powder formed from the Acheson process. In general, sintered SiC parts are made by mixing α-SiC powder and organic binders such as Boron and Carbon. Carbon is added to remove surface oxygen on the SiC particles, while boron is added to prevent the growth of grains at lower temperatures before reaching the sintering point. Other sintering aids include oxides such as alumina, zirconia, and yttria. The mixed powder is then compacted using cold isostatic pressing. This is done by placing the mixture into a bag and submerging the bag into a fluid. The fluid is then exerted with pressure upwards of 200 MPa, resulting in a "green" solid block. This block is then machined into the desired shape, known as the green shape.

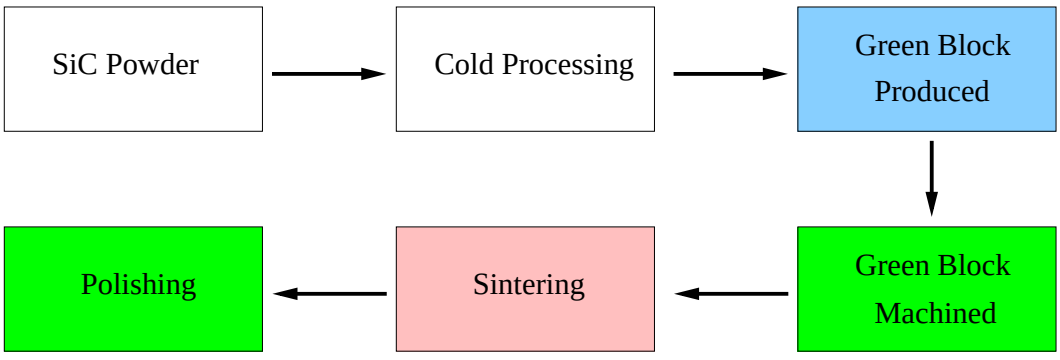

Figure 2-3. Process used to produce sintered SiC.

The green shape is then pressureless sintered. The sintering is done at ∼2100°C in a non-oxidizing environment. This step may last for days or weeks, depending on the thickness of the green shape. In order to reduce the effects of micro-cracks within the material, the sintered shape is cooled at a rate determined by the thickness of the shape. The greater the maximum thickness of the shape, the longer the cool down time will be. This reduces the temperature gradient within the material which may cause micro-cracks to form. During the sintering process, the product typically shrinks ∼17% [33].

The addition of sintering aids can produce impurities within the final SiC product, but much care is taken to remove almost all impurities. High-temperature chlorination can be used to remove a significant amount of impurities, but may cause depletion of silicon in the SiC. Each manufacturer has their own techniques used to keep the level of impurities to a minimum, and in some cases, not even trace amounts can be detected.

2.3.2.3 Reaction-bonded SiC

Reaction-bonded SiC (RBSiC), also called S/SiC or carbon felt SiC in some literature, uses a different process to create SiC products. Instead of using a pressed SiC shape made from SiC powder, RBSiC infuses silica into a carbon pre-form. A β-SiC structure is formed since the infusion process occurs at lower temperatures than α-SiC forms [33].

The process begins by using a graphite that has already been processed and purified. This graphite is then machined into the desired shape, known as the green part. The conversion of the graphite into SiC takes place when they are exposed to silicon-carrying species, typically SiO gas, at high temperatures. Although a gas is typically used, using liquid silicon will also produce similar results. The chemical formula for this step is shown below.

$$\mathrm{SiO} + 2\mathrm{C} \Leftrightarrow \mathrm{SiC} + \mathrm{CO}$$

In order for the green part to convert to SiC properly, it is essential for the graphite to have a reasonable porosity for the SiO to infiltrate the graphite. This reaction is rate-limited by the pore-diffusion resistance and keeping a large SiO concentration

gradient between the SiO gas and SiC/C interface is essential for this to occur [34]. The reaction rate at the SiC/C interface is controlled by surface kinetics which are spontaneous at high temperatures. This means the conversion rate from graphite to SiC is limited by the inward diffusion of SiO and outward diffusion of the CO gas through the SiC shell. For this reason, fabricated parts can only be less than a certain thickness if a complete

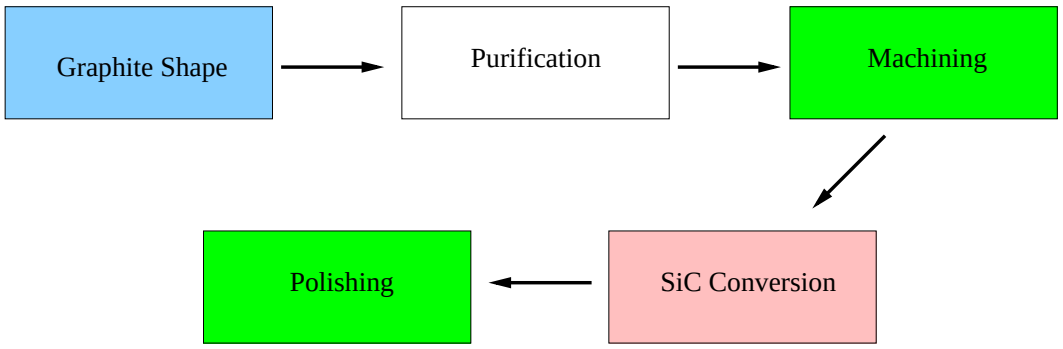

Figure 2-4. Process used to produce reaction-bonded SiC.

infusion is to take place. Using this infiltration process, the resultant part typically shrinks by less than 1% of its original shape.

2.3.2.4 Chemical vapor deposition of SiC

Due to its high reflectance in the visible spectrum, SiC parts are often coated with a dense, thick layer of SiC by use of chemical vapor deposition (CVD). A chemical reaction of compounds consisting of silicon and carbon are heated to a temperature between 1000-1800°C in the presence of hydrogen. The end result is a layer of high purity (typically 99.999% or greater) β-SiC consisting of very fine grains. This process is often used for large mirrors made of SiC. CVD SiC is a very flexible process and can be tailored to meet specific needs such as coating thickness and microstructure [33]. Typically the CVD process produces a SiC with a lower percentage of porosity.

2.3.3 Properties

The variations in the SiC fabrication process from different manufacturers will produce SiC with differing thermal and mechanical properties. These differences tend to be small and the effects due to temperature tend to follow the same trend. For this reason,

typical values will be given for material properties. Specific values from venders will be cited when applicable.

2.3.3.1 Density and porosity

The density of an object is given by the mass per unit volume. This term is general and it will be necessary to specify which density is being used. The crystallographic density is calculated from the chemical composition and interatomic distances given by

$$\rho_c = \frac{4M}{NV}, \tag{2–1}$$

where M is the gram formula weight of the material (M=40.09715 for SiC), N is Avogadros constant (6.0221367×10^{23}/mole), and V the volume of the unit cell.

The theoretical density is the density of a material as if there were no microstructural porosity. Also known as the apparent density, it is given by

$$\rho_a = \frac{m}{V_s}, \tag{2–2}$$

where m is the mass of the material, and V_s is the volume occupied by the solids. Depending on the polytype, the theoretical density lies between 3.166 to 3.249 g/cm^3. These measurements have been verified using X-ray spectroscopy and X-ray diffraction[33].

The bulk density is the measured mass in the total bulk volume of the material. The bulk density is calculated by

$$\rho_b = \frac{m}{V_s + V_p}, \tag{2–3}$$

where V_p is the pore volume.

Often reported with the density, porosity is another important physical property that indicates the amount of free space that is not occupied by solid material. The porosity is detrimental to the strength of the material. The strength is inversely exponentially proportional to the total porosity. Open porosity reduces the oxidation resistance and can present outgassing problems under high vacuum conditions. For RBSiC the open porosity can range from 0.50% to 20%, depending on the grade of SiC and process

used[34]. Typical porosities for sintered SiC are less than 1%, with most having close to zero porosity [35] [36] [37].

Table 2-5. Comparison of density and porosities for selected SiC materials.

Material	Apparent Density	Bulk Density	Total Porosity	Open Porosity
SuperSiC	3.13 g/cm$_3$	2.53 g/cm$_3$	20 %	19 %
SuperSiC-SiC	3.07 g/cm$_3$	3.05 g/cm$_3$	4 %	0.5 %
Hexoloy SA	–	3.10 g/cm$_3$	< 2 %	–
CoorsTek SiC	–	3.10 g/cm$_3$	–	–

2.3.3.2 Oxidation resistance

In general, SiC has excellent oxidation resistance, although this depends largely on the amount of open porosity and particle size. A larger porosity and particle size increases the effective surface area exposed to oxygen which will increase the oxidation rate. SiC is kinetically stable in air up to ∼1000°C. In the 1000-1150°C range, oxidation begins to occur and a thin film of SiO_2 will rapidly form. As the temperature is increased above this range, the SiO_2 layer begins to thicken and densify which results in a slower rate of oxygen being able to penetrate into the SiC. This slows down the oxidation rate. If the temperature is increased above 1650°C, a reaction between the SiO_2 film and the SiC will occur and produce SiO and gaseous CO. The CO gas can cause the SiO_2 layer to rupture, allowing more oxygen to diffuse into the SiC, hence increasing the oxidation rate.

2.3.3.3 Flexural and tensile strength

Defined as a measure of the ultimate strength of a specimen in bending, the flexural strength of a material is an important material property [38]. The flexural strength is most commonly tested using the ASTM C-1161 standard with either a 3- or 4-point test being employed. The equations for the 3- and 4-point bending test are given by

$$\sigma_{3pt} = \frac{3lF}{2bd^2} \tag{2–4}$$

$$\sigma_{4pt} = \frac{3Fa}{bd^2} \tag{2–5}$$

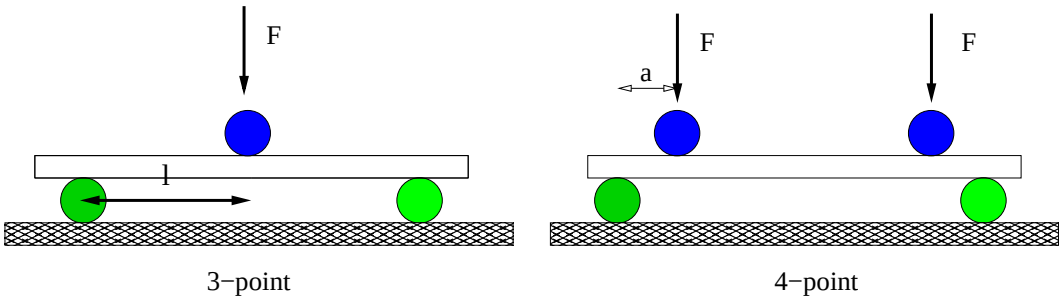

Figure 2-5. Diagram of how 3- and 4-point loading tests are done.

where l is the length of the specimen, F is the total force applied, b is the specimen width, d is the specimen thickness, and a is the distance between supporting beads. If a material is ductile, like most metals and alloys, then the material bends before failure. If a material is brittle, like many ceramics, then there will only be a slight bending of the material before failure.

Defined as the maximum tensile stress sustained by a material when a pulling force is applied along the specimen, the tensile strength determines a material's capability of load bearing in structural applications. The tensile strength is calculated by dividing the maximum load needed to rupture the material divided by the cross-sectional area. When determining the tensile strength of many ceramics, the sample preparation is critical. Micro-cracks in or on the material will propagate rapidly as a load is applied. For this reason, a statistically significant number of tests need to be performed. The most common test method used to determine the tensile strength is the ASTM C-1273 standard method as the elastic modulus can be obtained as well.

Table 2-6. Comparison of flexural and tensile strength for selected SiC materials.

Material	Flexural Strength (MPa)	Tensile Strength (MPa)
SuperSiC	147	129
SuperSiC-SiC	269	138
Hexoloy SA	410	210
CoorsTek SiC	410	307

2.3.3.4 Thermal conductivity and heat capacity

The rate at which heat flows through a material is known as the thermal conductivity (κ). The high thermal conductivity of SiC makes it an appealing material for use in applications where thermal gradients are needed to be kept low. While the thermal conductivity of single crystal SiC has been reported to be as high as 500 W/m K, most commercial grades have a thermal conductivity closer to 50-120 W/mK. Impurities from the production process will also lower the thermal conductivity. In general, as the temperature decreases, the thermal conductivity increases.

For many ceramics, the heat capacity is a strong function of temperature. The heat capacity of a material can be measured through the use of the calorimetry technique, or for high-purity materials it can be taken from published data [39].

Table 2-7. Comparison of thermal conductivity for selected SiC materials.

Material	Thermal Conductivity (at RT in W/mK)
SuperSiC	151
SuperSiC-SiC	218
Hexoloy SA	110
CoorsTek SiC	100

2.4 Carbon Fiber Reinforced Polymers

Carbon fiber reinforced polymers (CFRP), occasionally referred to as "black aluminum," are a group of materials that have a wide range of thermal and mechanical properties. CFRP consist of carbon fiber filaments in a matrix material. The purpose of the matrix is to transfer external loads to the carbon fiber structure. In most cases, the matrix material is a polymer such as an epoxy resin. Since the orientation of the carbon fibers and the specific matrix used will determine the overall mechanical and thermal properties of the CFRP, an almost limitless number of differing CFRP structures can be made. The fabrication process also allows CFRP to be used in many custom applications. In this section, the fabrication process and typical mechanical and thermal properties of CFRP will be discussed.

2.4.1 Fabrication Process

CFRP are composites that consist of two distinctly different components. When combined, the components remain discrete, but function interactively to make a new material whose properties can't be predicted by summing those of the components. Carbon fibers have a tensile strength along the fiber direction many times greater than that of steel, titanium, or aluminum [40]. The matrix transfers the applied load to the high-strength fibers in addition to providing crack and environmental resistance damage to the structure.

The composite part is made from a fiber architecture which is based on a specific "ply." The orientation, thickness, and fiber type of the ply will determine the properties of the composite. The composite properties vary from ply to ply, but it is assumed that each specific ply is homogeneous [40].

Composites are typically made up of several plies with mutually perpendicular planes of symmetry to create a laminate that is symmetrical and balanced. For stronger and lighter parts, a high fiber volume should be used. This is ideal for parts such as aircraft wings, but the price is usually more expensive since the fibers cost more than the resin. A heavier, more chemically resistant part, such as piping at an oil refinery, can be made from plies with a lower fiber-to-resin ratio.

2.4.1.1 Carbon fibers

For high-performance applications such as aircraft wings or support structures in space-based missions, the carbon fibers used are typically made from a variety of materials. These include polyacrylonitrile (PAN), pitch, and (rarely) rayon. Fiber made from these materials are heated and stretched to create a high-strength fiber. The most versatile of these fibers are PAN-based fibers and typically have high strength and stiffness[40]. Pitch fibers are made from petroleum or coal tar pitches and typically have extremely high stiffness and low to negative CTE. Due to these properties, pitch fibers

are often used in applications where thermal contributions need to minimized, such as instrument housings for spacecraft electronics.

Manufacturers produce carbon fibers in tows consisting of thousands of continuous, untwisted filaments that are microns thick. The filament count is designated by a number followed by the letter "K," which designates a multiplication of a thousand. For example, a 10K tow indicates a bundle containing 10,000 continuous filaments. Tow sizes ranging from 1K to 12K are typically used for aerospace applications. For application in the industrial, construction, and automotive industry, filament counts of 48K to 320K are typically used due to the lower processing cost, and faster processing times. The production process for higher filament counts tend to result in a lower tensile strength.

When exposed to metals PAN and pitch fibers experience galvanic corrosion. This can be overcome by using a barrier material or veil ply made of fiberglass or epoxy during the laminate layup in order to prevent direct contact.

In addition to PAN and pitch fibers, other high-performance fibers include aramid (commonly referred to by its trademark name Kevlar) and high-modulus polyethylene. Aramid fibers are composed of aromatic polyamide and provide exceptional impact resistance and tensile strength, making them ideal for applications such as ballistic protection, solid rocket motors, and helicopter blades [40]. Polyethylene fibers are light weight, have excellent chemical resistance, extremely impact resistant, and have a low dielectric constant. Many applications for these fibers are found as the same of the aramid fibers. Quartz, ceramic, basalt, boron, and hybrid fibers are all other options, but not commonly used.

2.4.1.2 Matrix material

Consisting of polymer chains, the resins used to make CFRP parts fall into two broad categories known as thermosets and thermoplastics. Thermosets, such as Eccobond 285 or Duroplast, are the most commonly used matrix material to create CFRP composites. A thermoset permanently cures into a linked network when mixed with a catalyst, is

exposed to heat, or both. Fabricators can control the cure schedule by adding inhibitors and accelerators to achieve the desired CFRP. For applications in the aerospace industry, curing often takes place in a vessel that is heated to elevated temperatures and is under high vacuum. This ensures good consolidation of the laminate to minimize any trapped air or voids from the initial fabrication of the part that would weaken the structure [40]. Under certain circumstances, pressures can be applied to the part to expedite or improve the process.

Unsaturated polyester resins are widely used in commercial, mass-produced applications such as bathware, boats, or car parts due to their ease of handling, relatively low cost, and good balance of mechanical, thermal, electrical, and chemical properties. For high-performance applications, polyester resins are typically not used due to their high shrink rates. Instead, thermosets such as epoxy resins, phenolics, cyanate esters, and polyimides are used.

For high strength, durability, and chemically resistant composites, epoxy resins are typically used. Epoxies come in many forms ranging from liquid, to solid, to semisolid and are typically cured by reacting with amines or anhydrides. Toughening agents such as thermoplastics or rubber compounds can be added to counteract brittleness. This can be useful in aerospace applications that use amine-cured epoxies that require the use of an autoclave at high temperatures that can cause brittleness.

Low cost, flame-resistant, low-smoke products such as aircraft interior panels or rocket nozzle applications are typically made using phenolic resins due to their excellent heat absorbing and low char yield qualities. Although phenolic resins have excellent thermal qualities, their mechanical strengths tend to be lower than when using other high-performance resins.

Polyimides are a more exotic form of resin and have found their way into high-temperature products such as jet engine nacelle components. These resins offer low electrical conductance and high chemical resistance. In some cases, parts made using polyimides

can have service temperatures of 370 C, making them ideal for high-temperature engine parts[40].

Fabricators of CFRP parts buy the fiber form and resin to best suit the needed application. Due to the high volume of CFRP parts now made, specially formulated resin matrixes are reinforced with carbon fibers and partially cured to produce a "prepreg." These prepregs are then frozen and defrosted when they need to be used. The specific prepreg is chosen based on the application needed and can range from golf clubs to airplane and jet engine parts.

2.4.2 Properties

As previously stated, the production process, fiber used, and matrix material used will all determine the mechanical, chemical, electrical, and thermal properties of the CFRP part. Designers can fabricate CFRP materials with a low CTE, good vibration damping, excellent fatigue resistance, good resistance to extreme environmental conditions, or a combination of all of these. For this reason, no specific thermal or mechanical property values will be given. Consultation with a CFRP manufacturer is ideal to determine the specific attributes they can provide. As a general rule of thumb, many thermal and mechanical properties of CFRP are similar to those of SiC.

2.5 Lead Zirconate Titanate

Lead Zirconate Titanate (PZT) is a class of materials whose properties can be tailored to meet specific needs by changing the zirconate-titanate ratio. Piezoelectric ceramics are hard, chemically inert, insensitive to atmospheric influences, and have mechanical properties similar to ceramic insulators. These properties make PZT materials ideal for a wide range of applications. These include spark igniters, solid-state batteries, sonic and ultra sonic generators, pressure and acceleration sensors, and actuators. The application of PZT in this work is limited to its use as an actuator, so only discussion of this use will be given.

2.5.1 The Piezoelectric Effect

Jacque and Pierre Curie first discovered the piezoelectric effect in 1880 [41]. They found that if a mechanical strain was applied to certain crystals, they became electrically polarized. This polarization was proportional to the applied strain. The Curies also discovered that when an electric field was applied to these materials, they would deform. This is known as the inverse piezoelectric effect. This effect is shown to occur in many naturally-occurring crystals including quartz, tourmaline, and sodium potassium tartrate. These materials have been used for many years as electromechanical transducers. If a crystal is to exhibit the piezoelectric effect, its structure should have no center of symmetry. Applying a tensile or compressive stress to such a crystal will change the separation between the positive and negative charge sites in each elementary cell, causing a net polarization at the crystal surface. This effect is linear in a large regime and is direction-dependant such that compressive and tensile stresses will generate voltages of opposite polarity [41]. The piezoelectric effect also occurs in a reciprocal nature. Hence, if a voltage is applied to the crystal, then a mechanical deformation will occur. Applying a voltage of opposite polarity will cause the crystal to deform in the opposite way.

2.5.2 Piezoelectric Materials

PZT are a class of materials that can be considered a mass of tiny crystallites [41]. Above a specific temperature known as the Curie point, these crystallites exhibit simple cubic symmetry such that there are no dipoles present in the material. Below the Curie point, the crystalline structures form a tetragonal symmetry such that an electric dipole is built into the structure (Figure 2-6).

The dipoles are not randomly orientated throughout the material, but rather form regions of local alignment known as Weiss domains. Within the domain all of the dipoles are aligned, giving the domain a net dipole moment and polarization, but no overall polarization is exhibited due to the random orientation of the Weiss domains [41]. The ceramic may be made piezoelectric in any given direction by use of a poling treatment. In

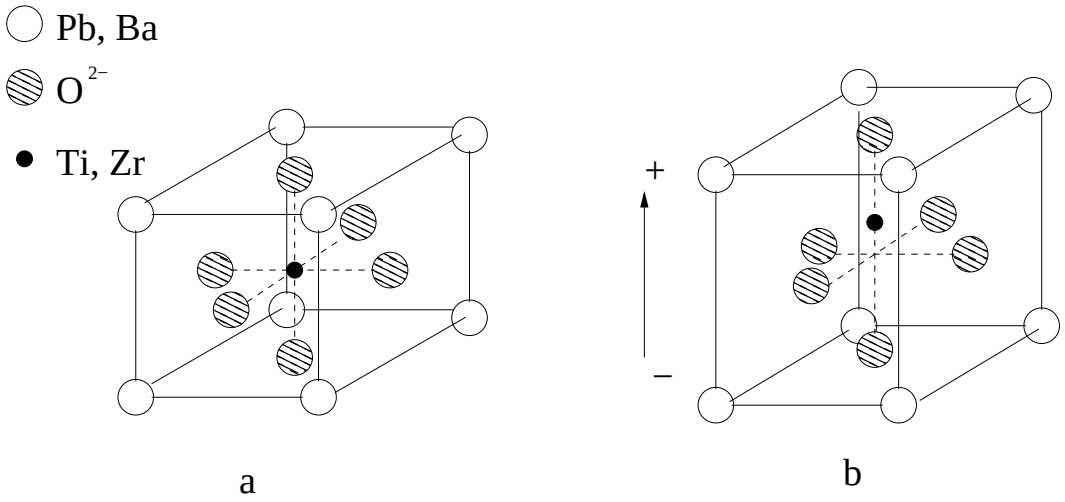

Figure 2-6. a) Cubic lattice above the Curie point b) Tetragonal lattice below the Curie point after the poling process has been applied.

this process a strong electric field is used at a temperature just below the Curie point to orientate the Weiss domains in the direction of the electric field (Figure 2-7).

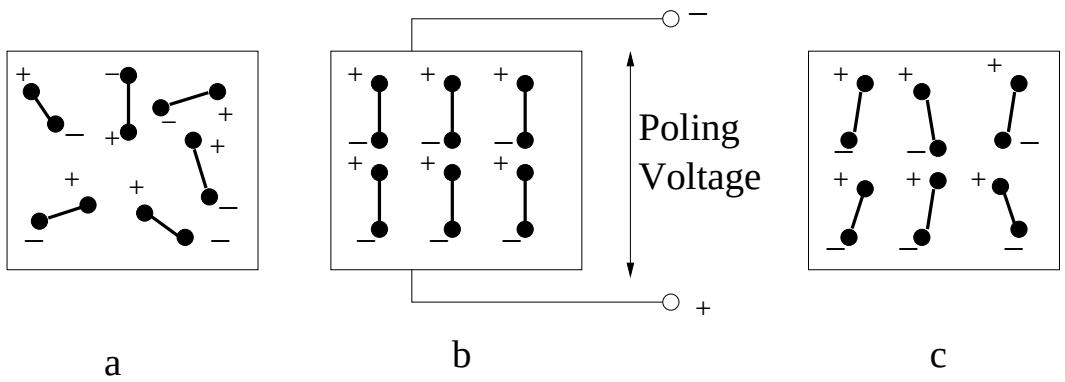

Figure 2-7. Electric dipole moments for the Weiss domains (a) before polarization (b) during polarization and (c) after polarization.

When the electric field is removed, the dipoles remain locked into their new orientation, producing a remanent polarization and permanent deformation. The poling treatment is usually the final step in creating the piezoelectric material.

The poling process will produce a permanent polarization within the material, but these properties can be partially or even totally lost if the material is subjected to certain mechanical, electrical, or thermal conditions [41]. If too large a static electric field or too large a mechanical stress is applied, or if the material is heated to a temperature near its

Curie point, the ceramic may become depolarized. These values vary depending on the type of PZT material.

The basic behavior of a PZT cylinder is shown in Figure 2-8. If a tensile or compressive load is applied to the PZT, the resulting change in dipole moment creates a voltage to appear between the electrodes. Similarly, if a voltage is applied to the electrodes, then the PZT material will stretch or compress depending on the polarity of the voltage.

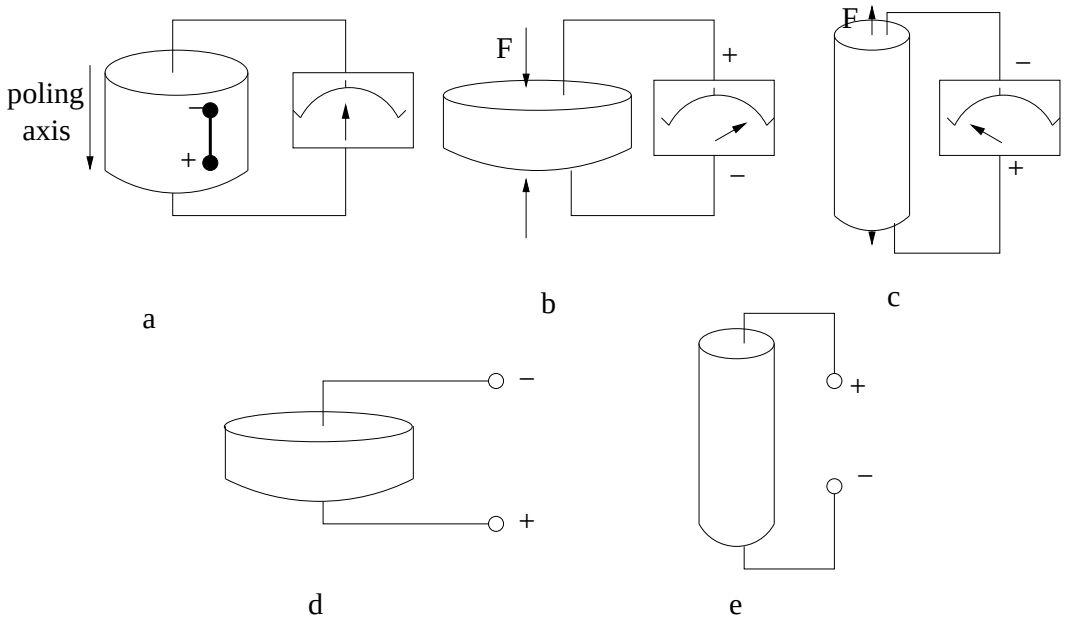

Figure 2-8. The piezoelectric effect of a cylinder for (a) no external action (b) an applied compressive force (c) an applied tensile force (d) an applied voltage (e) an applied voltage of opposite polarity. For clarity only 1 dipole is shown in (a).

The physical constants of PZT materials are given 2 subscripts due to their anisotropic nature. The direction of positive polarization is chosen to coincide with the Z-axis of a rectangular coordinate system [42]. The axes X, Y, and Z are designated by the numbers 1, 2, and 3, respectively, while the shear about these axes are represented by 4, 5, and 6, respectively (Figure 2-9).

For clarity, 3 examples will be given.

1. d_{33} is the induced polarization per unit applied stress in direction 3. Alternatively it is the induced strain per unit electric field in direction 3.

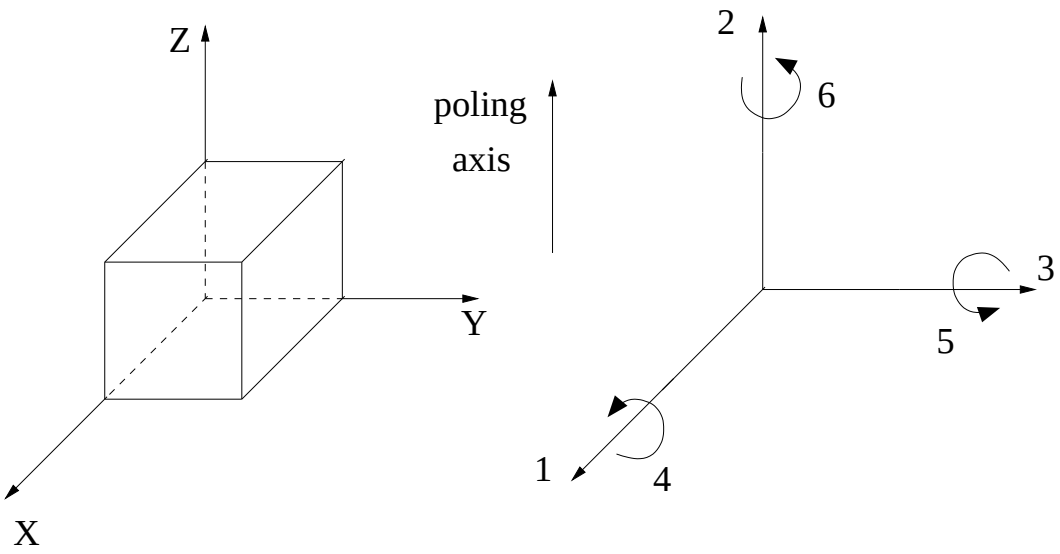

Figure 2-9. Axes designation and directions of deformation. Directions 4, 5, and 6 are the shear about axes 1, 2, and 3, respectively.

2. d_{31} is the induced polarization in direction 3 per unit stress applied in direction 1. Alternatively it is the mechanical strain induced in the material in direction 1 per unit electric field in direction 3.

3. g_{15} is the induced electric field in direction 1 per unit shear stress applied about axis direction 2. Alternatively it is the shear strain induced in the material about axis 2 per unit electric displacement applied in direction 1.

From these numbers the amount of translation and shear can be determined for a certain applied voltage. A few of these values are given in table 2-8 for the k-180 piezoelectric material [43].

Table 2-8. Selected properties and their values for the k-180 piezoelectric material.

PZT Property	Value
Longitudinal Coupling Coefficient (k_{33})	0.68
Piezoelectric Strain Constant (d_{33})	165 pm/V
Piezoelectric Strain Constant (d_{15})	350 pm/V
Piezoelectric Voltage constant (g_{33})	43 mV m/N
Curie Temperature	350 C
Density	7.7×10^{3} kg/m^3
Coefficient of Thermal Expansion	3.6×10^{-6}/C

CHAPTER 3
BONDING TECHNIQUES

When designing critical optical components such as optical benches or telescope support structures for space-based missions, there are two important factors that must be taken into consideration; the material the component is made of, and the bonding technique in which the pieces are put together. As the complexity and sensitivity of space-based missions increases, the jointing technique used needs to be strong in order to survive launch conditions as well as stable in order to not spoil the measurement sensitivity.

While the previous chapter dealt with a variety of materials that are suitable for several different structures, the next two chapters will focus on several bonding techniques that can or have been used to construct optical components.

3.1 Optical Contacting

Optical contacting occurs when two surfaces are polished flat and smooth enough such that the materials bond without the use of a cement. Typically optical contacting is done between two glass materials due to the ease of polishing, but it can be done for other materials, such as SiC and Super Invar, if the surfaces are adequately polished. Once the bond is formed, the bond line effectively disappears and the 2 materials act as one.

Optical contacting has found its way into many areas such as silicon wafer bonding in the electronics field, bonding mirrors to optical benches for use in space-based missions, and bonding optical components for use in lasers. Although optical contacting has been around for several decades and has gained popularity in various industries, literature on the subject is scarce and agreement between theory and experiment vary [44]. It is assumed the primary bonding mechanism is due to the van der Waals interaction at the surface. The force per unit area derived from the van der Waals attraction is given by [44]

$$P(D) = \frac{A}{6\pi D^3}, \tag{3–1}$$

where A is the Hamaker constant and D is the distance between the facing plane surfaces. For most materials, the Hamaker constant is on the order of 10^{-19} J, with fused quartz having a value of A$\approx 0.6\times10^{-19}$ J [44].

There are several optical bonding methods commercially available, but the details of the process are often difficult to ascertain due to their proprietary nature, although many of them require moderate heating of the substrate. For this reason, three optical contacting methods were developed for use at room temperature and have been used on BK7, SiC, and Super Invar.

3.1.1 Method 1

Clean surfaces as described in Appendix B. Place surfaces on top of each other and gently press together. If done properly, a bond will have formed within minutes and strengthens over time. For glass or transparent materials, the quality of the optical bond can usually be gauged by the number of fringes seen. Fewer fringes implies the surfaces are closer together, and hence, will produce a stronger bond. The bond can be non-destructively broken by placing in a sonicator or through thermal stressing.

This method is best used on ultra-polished surfaces. If the surfaces are flat and smooth enough (typically $\lambda/10$ or better), an optical contact will form once the 2 surfaces come in contact and can form appreciable strength with little or no pressure needing to be applied to the materials.

3.1.2 Method 2 (Solution Assisted Optical Contacting)

Clean surfaces as described in Appendix B. Place a small amount of methanol on the surface and place the other surface on top. Gently press together. This method takes approximately 3-4 hours for the methanol to evaporate and for the bond to obtain appreciable strength. Typical amounts of methanol used are 0.50 to 0.75 μL/mm^2.

This method works best when alignment of the two materials is needed. The methanol works as a lubricant that allows the materials to be moved, but still has some initial strength. As the methanol evaporates, the bond strengthens.

3.1.3 Method 3

Clean surfaces as described in Appendix B. Place the surfaces on top of each other and slowly move in a circular motion. After a few seconds, apply a small amount of pressure and keep applying a circular motion. This should cause the two pieces to eventually lock together in one or two places. Repeat if necessary until the two pieces get harder and harder to twist. Once it becomes difficult to move the two pieces, apply pressure. Let the pieces sit for 24 hours for the bond to settle and gain strength.

This method works best for surfaces that are not polished as well, or when the surfaces are dirtier than normal. In many cases if the previous two methods do not work, this method often will succeed, if only to form a partial bond.

These methods have been successfully used on BK7-BK7, SiC-BK7, and Super Invar-BK7 bonds with breaking strengths typically between 0.1-1.0 MPa. Other optical contacting methods exist which have reported breaking strengths ranging from several to tens of megaPascals [45]. Optical contacting was primarily used in this work to attach optical mirrors to substrate to form an optical cavity whose dimensional stability was then tested.

3.2 Anodic Bonding

Of particular interest in the electronic and electrical engineering fields is forming a strong bond between a glass and metal surface. These glass-metal bonds have been extensively used in industrial packaging of microelectromechanical system devices and hermetic feedthroughs. One method of glass-metal sealing, known as anodic bonding, is capable of creating a strong bond without the use of an adhesive paste, or heating the glass to temperatures above its softening point, as is the case with frit bonding.

The basic concept behind anodic bonding is to use the electrostatic attraction between two materials when a voltage is applied across the bond. Since glasses have an extremely high electrical resistivity at room temperature, the parts must be heat to a few hundred degrees before a significant drop in electrical resistivity can be seen. Although the

parts need to be heated, the temperatures used are typically well below the softening point of the glass. The increased electrical conductivity allows a larger current to pass through the materials, resulting in a larger electrostatic attraction between the surfaces [46]. The bond originates at the contact points between the surfaces and spreads out from there. For this reason, flatter and smoother surfaces will produce a bond that will form faster and with greater strength.

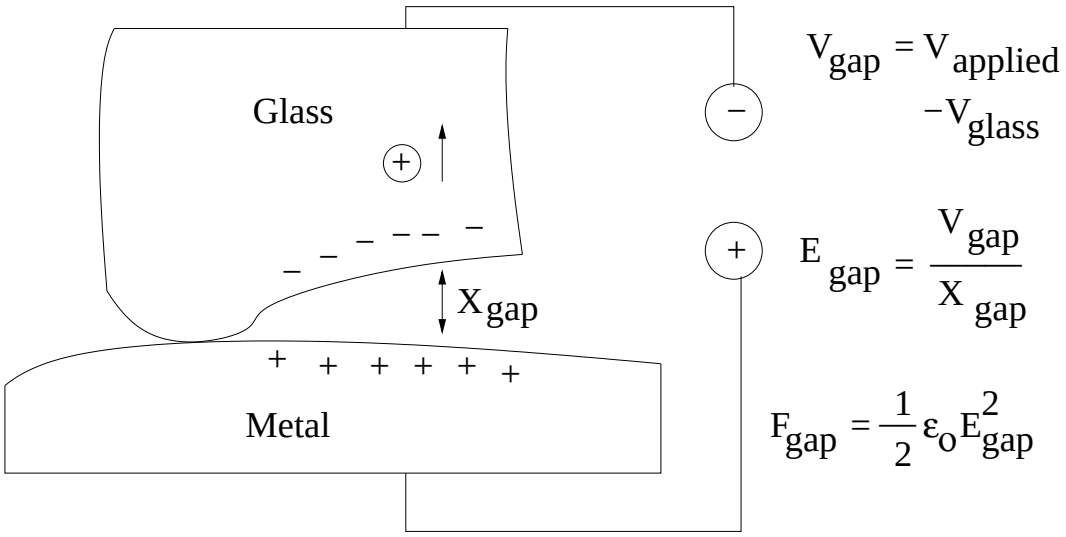

Figure 3-1. Representation of how anodic bonding works.

When one places a well polished surface on top of another, the surfaces usually only contact in a few spots. This can easily be seen when two pieces of well polished glass are placed on top of one another and interference fringes can be seen radiating outward from one or two points. With anodic bonding, these surfaces are brought together by the use of an electrostatic force. The voltage applied across the glass sets generates an electric field within the gap that, in turn, creates an electrostatic force (see Figure 3-1) that pulls the surfaces together. If glass behaved as a perfect insulator, then the voltage needed would be a function of the glass thickness. In addition, bonding would occur irrespective of the voltage polarity used. With most glasses, this is not observed. Glasses with thicknesses ranging from 0.05 to 25.4 mm show no voltage dependence and only bond if the correct polarity is used [46]. This is because at the temperatures used for anodic bonding most

glasses contain mobile positive ions compensated by almost immobile negative ions. This will leave a net negative charge on the bonding surface of the glass. If a positive potential is placed on the glass, then negative ions will build up on the metal surface as well, resulting in a repulsion. If the polarity is switched, then positive ions will be on the metal surface and negative ions will be on the glass surface. This will result in the necessary electrostatic attraction needed to bond. This also explains why the bond forms where the surfaces are in contact and then spreads out. The electrostatic force will be greatest where the gap between the surfaces is the smallest. This occurs where the surfaces are in contact.

When dealing with anodic bonding, there are six process parameters that must be taken into account; temperature, voltage, time of applied voltage and cooling rate, surface finish, CTE, and atmosphere [46].

Most work done with anodic bonding occurs in the 300 to 600°C range, although this can vary depending on the temperature dependence of the electrical resistivity of the glass. Zerodur, for instance, has a resistivity of about 1 MΩ cm at 300°C [46].

Typical working voltages are in the range of 200 to 2000 V. For glasses with a higher resistivity, more voltage should be used to create a larger surface charge at the bonding interface. The upper limit on the voltage is set to inhibit sparking which may damage the parts.

The time required in order for the bonding to occur is typically 1-5 minutes (after the parts have been heated and the applied voltage is turned on). Slow cooling of the parts may be needed for differences in CTE. The slow cooling will work only if the temperature used is high enough that the glass begins to soften. In this case, as the glass cools, it distorts itself such that it absorbs some of the stresses in the bond [47].

For a strong bond to form, it is necessary for the surfaces to be as flat and smooth as possible. This allows fewer and smaller gaps between the surfaces. Typically a surface finish of better than 50 nm rms is used.

As with other glass-metal seals, matching the CTE of the two parts is critical. Due to the heating of the glass and metal components, it is critical for the CTE's of both parts to match as closely as possible over the temperature range in which it is heated. A difference in CTE can cause induced stresses that the bond may not be able to compensate for. If this happens, it may be possible that the bond significantly weakens, or breaks as it is being cooled.

Anodic bonding typically occurs in room air, although other inert gasses could be used as well. For metals that oxide rapidly, it may be useful for bonding to take place in an inert gas as the formation of an oxide may cause the surface profile to change.

Using an aluminum coated piece of ULE, van Elp *et al* [46] were able to anodically bond Zerodur with a tensile strength of 9 MPa. The purpose was to develop a complicated electrostatic clamp for the use in next generation lithography machines.

The investigations into anodic bonding for this work were done to determine potential bonding methods in order to bond low expansion metals, such as Super Invar, to other glasses in order to make an optical cavity to test the dimensional stability of the metal. Using anodic bonding instead of a paste or frit bonding would test only the dimensional stability of the metal, and not that of the metal/bond system. Several investigations into bonding Super Invar to BK7 glass were done, but with extremely poor results. The materials were chosen because of their similar CTE's and that BK7 has a similar chemical composition to that of Zerodur and should allow for a similar current to be passed through it. The Super Invar piece was 50 mm x 50 mm x 6.3 mm and had a mirror finish on it with a global flatness of $\lambda/4$. A variety of BK7 pieces were used ranging in thickness from 6 mm to 1 mm and in diameter from 25.4 mm to 6 mm. The pieces were heated in an oven to 300°C and allowed to soak for at least an hour. A voltage ranging from 200 to 1000 V was applied and left for times between 5 minutes and several hours. After the voltage was applied, the oven was turned off and allowed to cool to room temperature.

This usually took several hours. In each case, a bond did not form. At best, one bond formed that formed that showed a slight resistance to being pulled apart by hand.

The only bond that was able to form with significant strength was between a BK7 disk approximately 6 mm in diameter and 1 mm thick and a piece of aluminum foil. The pieces were heated to 300°C and a voltage of 1000 V was applied for 1 hour. A weight was applied on the aluminum foil in order to keep the surfaces in good contact with each other. The pieces were cooled to room temperature by turning the oven off and allowing the temperatures to equilibrate. Although a bond did form and was difficult to pull apart using a force in a shear direction, it could be peeled off easily.

The lack of results is most likely due to the difference in CTE between the Super Invar and BK7. Although there is a significant difference in the CTE of aluminum and BK7, a bond was most likely able to form because the aluminum foil is thin and able to stretch and contract in order to handle the stresses induced from cooling the pieces. Because of this, anodic bonding was abandoned as a way to bond a low expansion metal to mirrors in order to make an optical cavity.

3.3 Brazing

Brazing is a method that joins two materials through the use of heat and a filler metal in a cost-effective method that produces significant strength and has excellent stress distribution and heat transfer properties. Although brazing is commonly used for metals, its use has begun to expand into other materials as well. In this section, a general outline of the brazing procedure will be discussed. In addition, examples of brazing SiC parts for mirrors and payload structures is presented.

Brazing joins two materials through the use of a filler material. It is performed at a temperature high enough to melt the filler material, but low enough as to not melt the materials being joined. Because of this, brazing is ideal for jointing dissimilar metals. Ferrous and non-ferrous metals can easily be joined by brazing, as well as metals of different melting points. The joints are strong and dependant on the strength of the filler

material. In some cases, the braze-joint will exhibit a tensile strength greater than that of the filler material [48]. Filler materials are chosen such that the tensile strength of the joint is similar to that of the materials being brazed.

Brazing creates a metallurgical bond between the surfaces of the two materials being joined and the filler material. Heat is applied broadly to the jointing materials to raise it to a temperature greater than the melting point of the filler. The filler is then placed in contact with the surfaces and is drawn completely through the joint via capillary action. In contrast, welding uses temperatures higher than the melting point of the two materials and fuses them together with a filler material. Thus, welding temperatures start at the melting points of the materials. This intense heat can cause warping or distortions around the joint, or stresses around the weld area [48]. Often, the extreme temperatures used for welding do not make it suitable for joining thin pieces together, whereas brazing can be done easily.

A good fit of the materials with proper clearance is essential for brazing due to the capillary action needed to pull the filler material through the joint. Typical clearances are 25 to 125 μm. The clearance will also have a significant impact on the strength of the joint[48]. If the clearance is too small, then there will not be enough force to pull the liquified filler through. If the clearance is too large, then the joint strength may be reduced to that of the filler. Highly polished surfaces can also impede the filler flow. A typical "mill finish" will provide a surface roughness allowing for the creating of capillary "paths" for the filler to flow through. In addition, when brazing materials with differing CTEs, the clearance must be adjusted for the elevated temperatures accordingly. For example, consider brazing a brass bushing into a steel sleeve (as shown in Figure 3-2). Brass has a higher CTE than steel and if it is to be the inner part of the assembly, a larger clearance than if both were the same materials should be used. Conversely, if the brass now becomes the outer member and the steel the inner, then less clearance should be used.

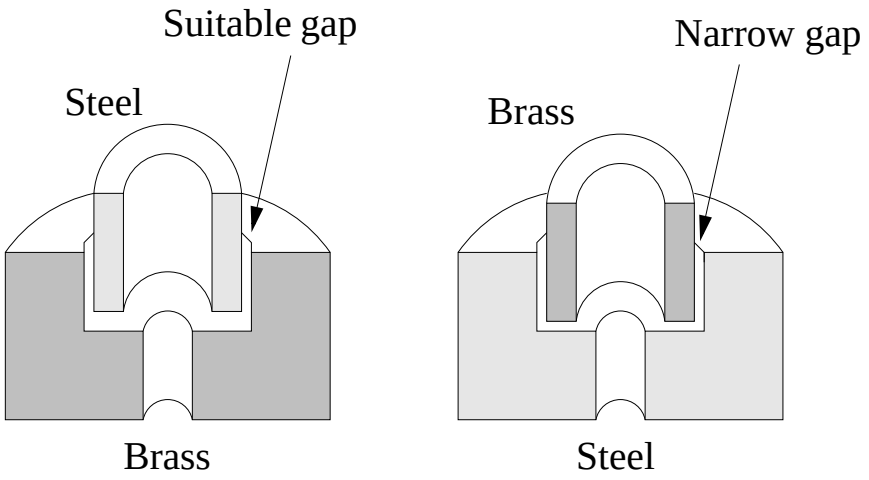

Figure 3-2. Proper spacing for brazing materials of differing CTE.

Of similar importance is the need to clean the surfaces before brazing. Capillary action will work only when the surfaces are clean. For this reason it is essential that all surfaces to be brazed are adequately cleaned.

When heating the materials, it is possible that an oxide layer will form on the surface. This is not ideal for brazing, and may produce a weaker bond since the oxide will prevent the filler from adequately bonding to the surface. For this reason fluxing of the parts should be done. Flux is a chemical compound that is applied to the joint surface before brazing that prevents oxide formation. The flux will dissolve and absorb any oxides that will form during the heating process, allowing the filler to freely flow. Although fluxing the surfaces can be omitted in some cases, even then it can be advantageous to use a small amount of flux as this may improve the wetting action of the filler [48].

When brazing, both materials should be heated as uniformly as possible so they will reach the brazing temperature at the same time. When heating materials of different thicknesses or thermal conductivities, attention should be paid to apply the heat as evenly as possible. For this reason, using an oven is often the best method to braze differing materials. In most cases, observing the color and viscosity of the flux might indicate that the pieces are being heated appropriately. When the assembly has reached the proper temperature, the brazing rod is then placed in contact with the joint area. A portion of

the rod will melt off as it is touched to the surface and the capillary forces will draw it through the joint. Once the assembly has been brazed the excess flux should be removed. Flux residue is corrosive and if not removed can attack the material, possibly weakening the material or joint.

Although typically used for metals, brazing has become an important jointing method for SiC parts as well. It is often difficult, or even impossible, to build some SiC structures in one piece. An example of this is the Herschel Space Telescope primary mirror. With a diameter of 3.5 m, this mirror was far to big to be made in one single piece. To construct this mirror, several smaller sintered segments were brazed together [49]. The filler material was a doped silicon compound with a CTE that closely matched the CTE of the SiC pieces. The brazing process used by Boostec to create Herschel primary produced a very thin, uniform joint. The typical braze thickness is less than 50 μm, and in most cases less than 10 μm. Producing such a thin joint resulted in a joint strength comparable to that of the SiC alone.

In addition to producing the Herschel primary, Boostec also constructed the SiC torus for the GAIA mission using their brazing technique. The torus consisted of 17 individual segments that were brazed into one coherent structure. The final structure is a quasi-octagonal structure that is three meters in diameter and will support the two GAIA telescopes and the focal plane assembly.

3.4 Epoxies

Epoxies are generally considered to be structural adhesives and can form excellent bonds to materials including metals, glass, wood, plastics, rubbers, and masonry products. Epoxies are commonly used to replace other forms of fasteners such as screws and rivets because they can provide a lighter weight structure for lower cost and are easier to assemble. Epoxies are either a one- or two-part system. For most high performance applications, such as in aerospace applications, typical epoxies used are a two-part system. For this reason the focus will be on this area of epoxies, although a leap from two- to

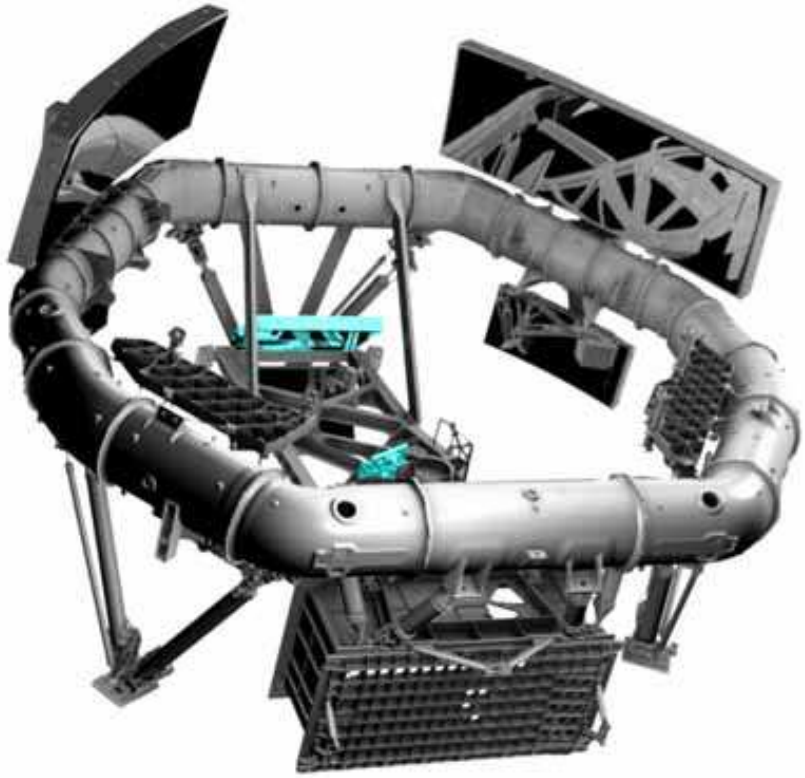

Figure 3-3. Conceptual design of the GAIA SiC torus. Picture courtesy of ESA.

one-part epoxies is easy with suitable knowledge of two-part epoxies. Advantages of two-part epoxies are that they typically have a high peel and shear strength, outstanding chemical resistance, good thermal properties which make them ideal for cryogenic use, low cost, and good adhesion [50]. In addition to being used for bonding, epoxies are often used as coatings because of their excellent chemical and environmental resistance.

A two part epoxy adhesive is a type of thermosetting polymer. As defined by Daly, a thermoset is a material that has the property of undergoing a chemical reaction by the action of heat, catalyst, ultraviolet light, or other means leading to a relatively infusible state [51]. Two-part epoxies consist of a resin and a hardener. Also known as the curing agent, the hardener is required to convert the resin into a plastic-like solid. Once the resin and hardener are thoroughly mixed, the epoxy will begin to set. Often when mixing the components, an extreme amount of heat may be released. For this reason caution

should be taken when mixing large amounts of epoxy. The release of heat may also cause the epoxy to harden faster since elevated temperatures often make the epoxy set faster, while lower temperatures tend to do the opposite. It is often recommended that elevated temperatures are used to set the bond since this typically results in a stronger bond. Working times can range from a few minutes to several hours depending on the specific epoxy, and setting times can range from one to several days. Table 3-1 lists a few epoxies with select properties.

Table 3-1. Comparison of properties for select two-part epoxies.

Product	Application	Work Lifetime (min)	Shear Strength (MPa at 20 C)	Total Mass Loss (%)
100 B/A	Glass-to-metal	5	10.3	5
Mil-Bond	Glass-to-metal	30	–	1
A-12	Glass-to-metal	180	17.2	0.9
Eccobond 285/11	Wide temp. range	240	14.5	0.3
Hysol 1C	Vacuum sealing	30	–	0.8
Epo-Tek 375	Fiber optics	300	15.9	–

Percent total mass loss is a measure of the mass loss after a specified period of time when exposed to elevated temperature. For space-based applications, less than 1% is desirable. Some vendors, such as Master Bond Inc., have special epoxies that are NASA approved for low outgassing and percent total mass loss [52].

Many vendors are capable of taking a specific epoxy and modifying it slightly to produce the desired mechanical, thermal, or chemical properties. For example, small aluminum beads can be added to lower the CTE of an epoxy. Although this may lower the CTE of the epoxy, it may cause the bonding strength to change [50].

There are several ways to adhere surfaces using epoxy. The strength of the bond will be determined not only by the epoxy itself, but by the quality of the surfaces as well. For high strength, all paint, oil, dust, etc.. should be removed. Often, a specific surface roughness is needed for full strength. Although the vendor should be consulted to ensure proper application of the epoxy, a few cleaning methods are suggested below for a few common surfaces as adapted from reference [50]. Steel or aluminum:

1. Wipe the surfaces from all contaminants using a solvent such as acetone or alcohol.

2. Abrade using clean fine grit abrasives (180 grit or finer).

3. Wipe again with solvents to remove any contaminants.

4. Apply a thin coating (typically less than 12 μm) of epoxy and cure according to specific epoxy. Slightly elevated temperatures tend to produce a stronger bond.

Plastics/rubber:

1. Wipe with isopropanol. Using acetone may damage the plastic or rubber.

2. Proceed as with steps 2-4 above.

Glass:

1. Clean using acetone, or solvent wipe. Allow time for surfaces to completely dry.

2. Apply a thin coating (typically less than 12 μm) of epoxy and cure according to specific epoxy. Slightly elevated temperatures tend to produce a stronger bond.

To break the epoxy bond, mechanical, chemical, or thermal means may be employed, although this may cause damage or destruction of the pieces. These methods include using a pick, screwdriver, razor blade, heating the bond, or soaking in strong solvents such as MEK.

CHAPTER 4
HYDROXIDE-CATALYSIS BONDING

Chapter 3 describes a few select bonding techniques that have been used in a variety of applications. Unfortunately, these techniques suffer from drawbacks which may not make them ideal for some space-based interferometric missions. For example, optical contacting works well over a large temperature range when small areas with similar CTE's are used. Although optical contacting can be done between materials with differing CTE's, changing the temperature at which the materials were bonded will induce stresses the bond may not be able to handle. Brazing essentially makes the bonded components as one, but the elevated temperatures needed may cause the material properties to change, or may effect possible coatings applied to the material (as with a telescope for example). A chemical bonding technique, colloquially known as hydroxide bonding, provides strong bonds, is capable of using smaller surface areas that do not need to meet the high polishing tolerances of optical contacting, and can be used for precision alignment needed for optical benches [53]. This chapter will detail the hydroxide bonding mechanism and present strength results for several materials that have been bonded using the hydroxide bonding technique.

4.1 Introduction

Hydroxide-catalyzed bonding was originally developed at Stanford University by Gwo to adhere optical components for the Gravity Probe B mission [54]. The characteristics of hydroxide bonding make it ideal for optical benches due to the high bond strength while still allowing for precision alignment. As described by Gwo, the hydroxide bonding process is capable of forming bonds as long as a silicate-like network can be created between the surfaces. The most obvious of materials for use of hydroxide bonding is Zerodur. Extensive measurements have been made involving the mechanical and thermal properties of hydroxide bonded Zerodur, specifically for the LISA mission [53]. Over the past few

years, this method has been expanded significantly and the list of materials suitable for use with hydroxide bonding has grown.

4.2 Bonding Mechanisms

The hydroxide bonding mechanism takes place in 3 steps:

1. Hydration and etching: In this step, a hydroxide solution (typically NaOH or KOH) is added to one of the surfaces where the free OH^- ions act to liberate silicate ions.
2. Polymerization: The silicate ions dissociate and form siloxane chains.
3. Dehydration and bonding: As the water evaporates, the siloxane chains intertwine and bond the 2 surfaces together.

Although the overall process for hydroxide bonding is the same, it varies slightly depending on the materials and bonding solution used. In the case of glass-glass bonds, the hydration and etching step is easily done since silica materials easily liberate silicate ions in the presence of OH^-. For metals, there are no silicate ions for the siloxane chains to attach to, so the second step must occur in a different manner [53]. In the case of SiC, which contains silicon but is extremely chemical resistant, the manner in which the siloxane chains attach to the SiC surface must be different than that of glass-glass bonds. In the following subsections a more complete analysis of the hydroxide bonding mechanism will be discussed for the cases of glass-glass, glass-metal, metal-metal, and SiC-SiC bonds.

4.2.1 Glass to Glass

For glass-glass hydroxide bonding to take place, a small amount of an alkaline solution such as sodium hydroxide or sodium silicate is placed on one surface and the other silica material is placed in contact. The OH^- in the bonding solution etches the silica surface and liberates silicate ions. This process can be described by

$$SiO_2 + OH^- + 2H_2O \rightarrow Si(OH)_5^-. \tag{4–1}$$

As the etching takes place, the number of OH^- ions are reduced and the pH of the bonding solution decreases. Once the pH is below 11, the silicate ions dissociate to form

$Si(OH)_5^-$ as described by

$$Si(OH)_5^- \rightarrow Si(OH)_4 + OH^-. \tag{4–2}$$

The $Si(OH)_4$ molecules then combine to form siloxane chains and water as described by

$$2Si(OH)_4 \rightarrow (OH)_3SiOSi(OH)_3 + H_2O. \tag{4–3}$$

The siloxane chains start to form as the water evaporates and provide the overall rigidity of the bond [54]. As the dehydration continues, a 3D network of siloxane chains form and eventually join the two surfaces together.

4.2.2 Glass to Metals and Metal to Metal

For other oxide materials which cannot form a silicate-like network on the surface, an existing network can be introduced into the hydroxide solution for the surface to bond to. This is typically done by using a sodium silicate solution with 14% NaOH and 27% SiO2 as the bonding solution. This solution is readily available from companies such as Sigma Aldrich. The SiO_2 in the solution forms the necessary network for the surfaces to attach to. It is critical for the materials to be easily oxidized, as the oxygen will provide the link for the siloxane chains to bond to. This makes many metals such as aluminum, copper, and silver possible to bond to silicate materials using the hydroxide bonding technique. It is a simple step in logic that the silicate material could also be replaced with another readily oxidized material to form a hydroxide bond between two non-silica containing materials. This has been achieved with materials such as copper and aluminum [54].

4.2.3 SiC to SiC

Although SiC is a material which largely consists of silicon, its extreme chemical resistance to oxidation and alkaline solutions should not allow SiC to bond using the hydroxide bonding technique. It has been shown in reference [55] that hydroxide bonding can take place with limited results by growing an SiO_2 layer on the SiC surface by heating the SiC to temperatures in excess of 1000°C. The oxidized SiC layer allows the siloxane chains to bond the two surfaces in the same manner that glass-glass bonding occurs.

Although promising results were obtained using this method, the oxidation of the SiC makes it unattractive for use in space-based missions, as this would ruin any optical coating that may be necessary for components such as mirrors on the optical bench. For this reason other methods to make SiC-SiC bonds using the hydroxide bonding method were investigated. As it turns out, the oxidation step is not necessary and bonding with significant strengths can be done by simply using a sodium silicate solution. The reason as to why this should happen was at first perplexing, since there should be no oxide layer on the SiC surface to bond to, and virtually no silicate ions should be liberated from the alkaline solution.

In order to determine the bonding mechanism between SiC and SiC, the chemical compositions of the surfaces were analyzed both before and after bonding. This was easily done as the SiC-SiC bond almost always broke at the bond line. To determine the surface composition of the silicon carbide surfaces during SiC-SiC bonding, an X-Ray Photoelectron Spectroscopy (XPS) system was used. The XPS system is based on the photoelectric effect and is the least destructive of all the electron or ion spectroscopy techniques. The XPS is routinely used in industry and research when elemental or chemical state analysis of a surface needs to be done. For a solid, XPS probes approximately 5-500 $\mathring{A}$ deep, depending on the material, the energy of the x-rays and emitted photoelectrons, and the angle with respect to the surface of the measurement.

4.2.3.1 X-ray photoelectron spectroscopy

The XPS works on the basis of the photoelectric effect. Photons of energy $h\nu$ (typically 1486.6 eV in most commercial systems) produced from an x-ray source saturate the surface. The photo-ionization process begins with the photon absorption which then causes an electron emission. This electron then either travels from the surface or through the material into the vacuum where it is detected by a spectrometer and its energy is measured. Using the principles of conservation of energy, we find that the binding energy

of the electron to first order is simply

$$KE = h\nu - BE \tag{4–4}$$

where KE is the kinetic energy of the photoelectron, $h\nu$ is the energy of the x-ray, and BE is the binding energy of the particular atom concerned. Thus, element identification can be done by analyzing the photoelectron energy distribution. The measured spectrum will exhibit photoelectron signals attributed to core-level (O1s, C1s, Fe2p, etc...), valence level (Fe3s, Fe3p, etc), and Auger emission. Auger emission occurs from the filling of the core-level vacancy by an electron in an outer layer state. As this electron relaxes, energy is emitted. If the energy is absorbed by another electron, this electron will be ejected from the material and detected on the spectrometer. The Auger peaks are much broader than the photoelectron peaks due to the multiple paths the electron may escape from within the orbital.

The tightly bound core-level electrons of an atom have energies that are nearly independent of the chemical species in which the atom is bound because they are not involved in the bonding process. Thus, a compound will have core-level energies that are similar to the elemental energy values. For example, in nickel carbide, the C1s BE is within a few eV of its value for elemental carbon. In addition, the Ni2p BE is within a few eV of its natural value for Ni metal. Identifying the core-level BE's of certain elements will provide signatures of the elements in the compound. Although cross section values are needed to determine relative atomic concentrations, when comparing relative intensities of the same atomic core-level to get compositional data, the cross section values do not need to be taken into account. Thus the relative abundances can be taken directly from the relative peak heights. For example, figure 4-1 shows the sample constituents as well as their relative abundances. These numbers are calculated using the cross sections of the elements and their relative peak intensities. Figure 4-5 on the other hand only represents

the C1s orbital and the relative concentrations can be directly taken from the area under the peaks. In this case, peak 1 and peak 2 are of similar abundances.

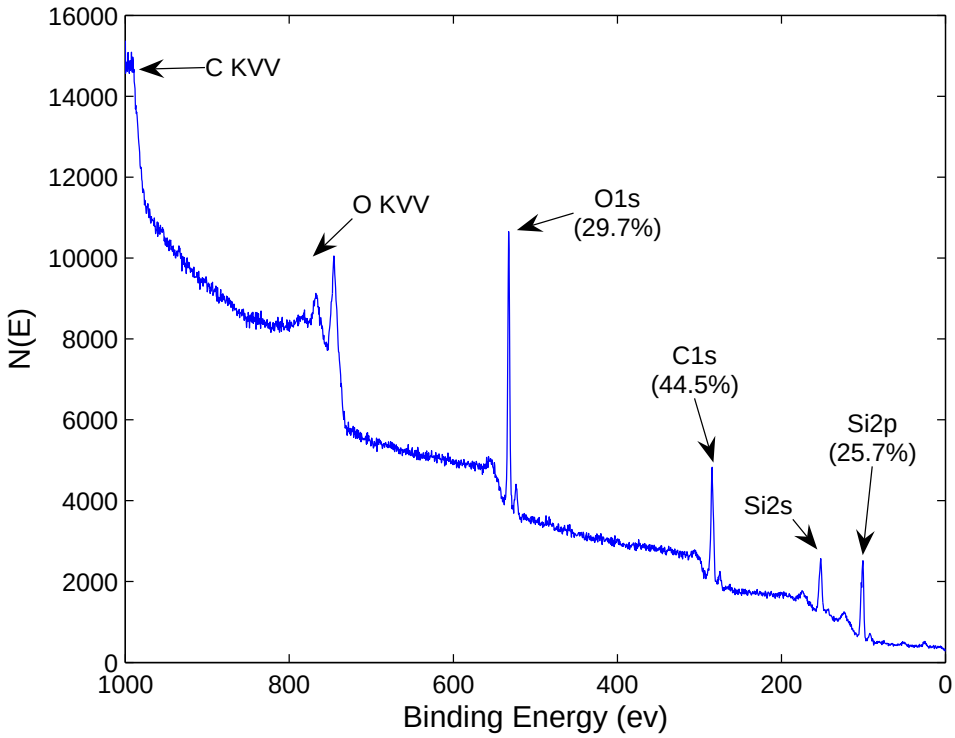

Figure 4-1. Spectrum of an unbonded CoorsTek SiC sample. The peaks from left to right are the Auger carbon peak, Auger oxygen peak, oxygen 1s peak, carbon 1s peak, and the silicon 2s and 2p peaks.

The x-ray source of the XPS will produce photoelectrons to the depth that it penetrates the sample. Photoelectrons that are ejected from the top layers of the sample will be detected with minimal scattering and show up as peaks. The electrons that are released deeper within the sample will interact with the sample and multiple scattering will take place, reducing their chances to make it to the detector. These electrons show up at lower KE and mostly end up in the background after the XPS peaks (Figure 4-2).

Thus, peaks come primarily from the surface photoelectrons, while the background is a result of the scattered electrons within the material. The intensity of the flux of

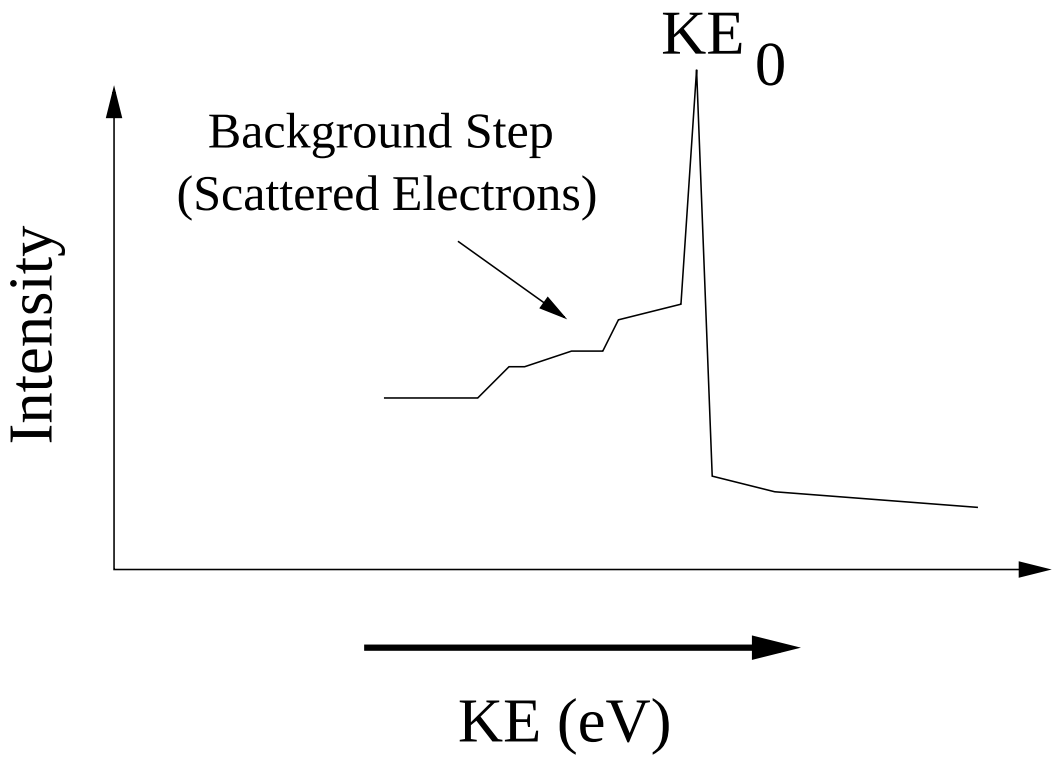

Figure 4-2. Kinetic energy distribution obtained due to the inelastic scattering of electrons. The peak corresponds to the photoelectrons emitted near the surface, while the signal at lower kinetic energies results from the scattering of the electrons deeper within the sample surface.

electrons as a function of depth and electron angle emission is given by

$$I_D = I_0^{\frac{-D}{\lambda sin(\theta)}} \tag{4–5}$$

where I_0 is the flux of electrons originating at depth D, I_D is the flux emerging without being scattered, D/sinθ is the distance traveled through the solid at that angle, θ is the angle of electron emission, and λ is the inelastic mean free path. The value of λ depends on the KE of the electron and the material through which it travels. It also determines what the surface sensitive of the measurement is. The values of λ can be found in standard tables from books [56]. To detect the surface composition, the grazing emission angle, θ, can be lowered, while detecting deeper layers requires a larger angle.

4.2.3.2 SiC-SiC bonding mechanism

The individual SiC pieces were first cleaned and then analyzed using the XPS. The SiC pieces were bonded and then broken. The broken SiC samples were cleaned and analyzed again. Cleaning the SiC pieces after they were broken removed almost all of the sodium that was in the bonding solution. This was verified using the XPS and finding either no sodium peak, or a very small peak which was typically less than a few percent of the total chemical composition.

Samples of Hexoloy SA from Saint Gobain, POCO Super SiC from POCO graphite, and UltraSiC from CoorsTek were analyzed in the XPS. An integrated background was subtracted from the raw data and Gauss-Laguerre peaks were fitted using AugerScan software. Once the energy of the peaks were found, they were matched to the NIST online database to determine the chemical composition. Although some of the peaks did not match up exactly with the NIST database, all peaks were within 0.10-0.15 eV of the database, with the next suitable candidate being significantly further away. From this information a bonding mechanism was formulated consisting of the following steps:

1. The hydroxide ions in the sodium silicate solution break the SiO bonds on the SiC surface. The SiO is present on the surface possibly due to either the polishing process or from oxidation during the manufacturing process.

2. The broken SiO bonds then attach to the SiO_2 in the sodium silicate solution.

3. As the water in the solution evaporates, the aqueous SiO_2 forms a solid layer that binds the two SiC surfaces together.

The end result is that two pieces of SiC are bonded together by a layer of SiO_2 [57]. This can be seen from the surface composition of the SiC before and after bonding. Figure 4-3 shows the O1s orbital energies both before and after bonding. Before bonding, only the SiO peak is present. After bonding, an SiO/SiO_2 peak is present [57]. This would indicate that a bond between the SiO and SiO_2 has occurred. Due to the different number of detected counts before and after bonding, the figures show the normalized data. While this will not show the relative abundance of compounds both before and after bonding,

it shows the relative abundance of the chemical compounds at the time the sample was tested. Analyzing the $Si2p_3$ orbital, we find that only SiC and SiO are present before bonding, but after bonding an SiO_2 peak is found (Figure 4-4). In a similar manner, analyzing the C1s orbital, we find that only SiC and graphite are found before bonding, but an additional SiO_2 + SiC peak is present after bonding (Figure 4-5). This supports the bonding process presented above.

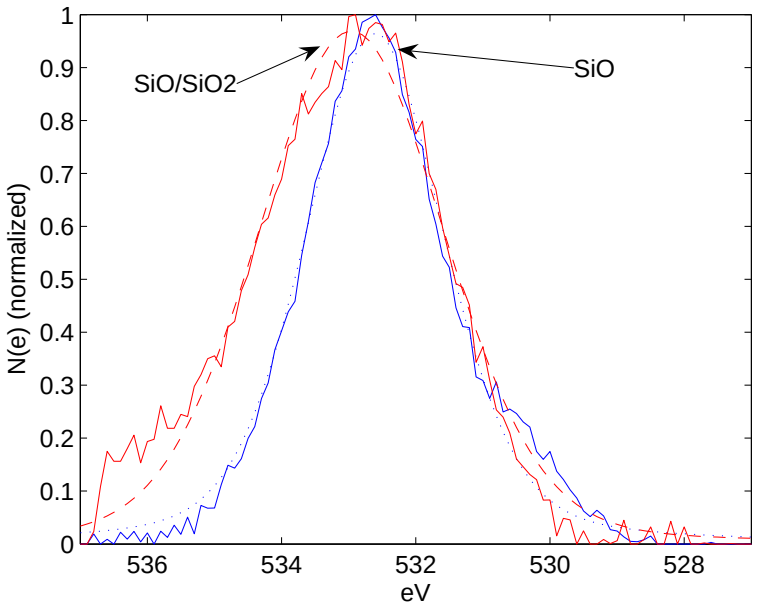

Figure 4-3. O1s orbital both before (blue curve) and after (red curve) bonding. The dashed and dotted lines represent the peak fit values while the solid lines are the raw data taken from the XPS. The unbonded peak is at 532.61 eV and the bonded peak is at 532.96 ev.

Using the XPS to probe deeper into the samples, it was found that as the depth increased, the effects of the SiO_2 diminished, and the chemical compositions became identical. This mechanism also explains the poor bonding results when an NaOH solution is used. Since SiC is extremely resistant to both acids and bases as well as being an extremely poor oxidizer at room temperature, there is no intermediate material that is either produced or present during bonding when an NaOH solution is used.

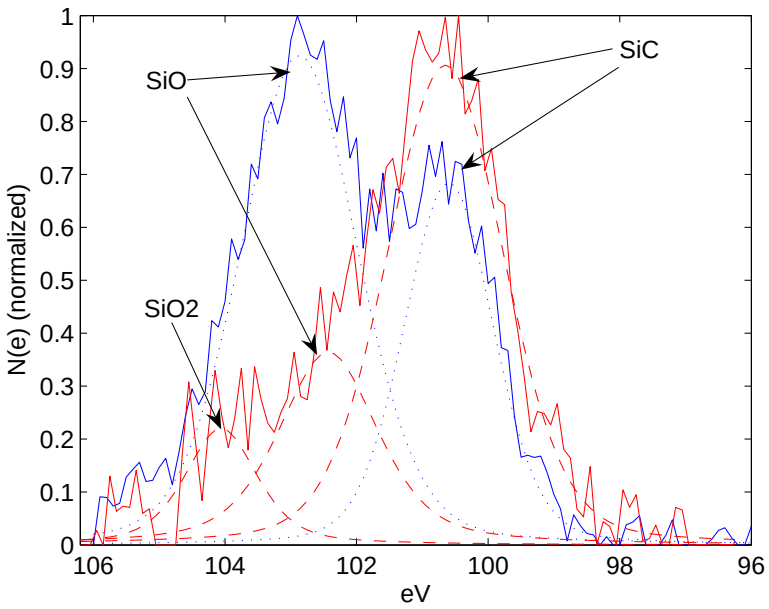

Figure 4-4. $Si2p_3$ orbital both before (blue curve) and after (red curve) bonding. The dashed and dotted lines represent the peak fit values while the solid lines are the raw data taken from the XPS. The unbonded peaks are at 102.87 eV and 100.60 eV. The bonded peaks are at 100.42 eV, 103.82 eV, and 102.21 eV.

4.3 Bonding Method

In order to get the best bond, it is important to keep the surfaces as clean as possible. In addition, the smoother and flatter a surface, the more likely a strong bond will form. Although there are many different methods to clean the surfaces, and many surfaces capable of bonding, below describes the bonding method used for the hydroxide bonding process.

1. Preparation of the surfaces: The surfaces were cleaned as described in Appendix B.

2. Application of solution: After the surfaces have been cleaned and sonicated, they are then taken out of the sonic bath and cleaned again with an optical wipe and methanol. This step helps to remove any particulate that may still be on the surfaces as well as removing the surface of any DI water left from the sonic bath.

3. Jointing of the 2 surfaces: After the surfaces have been cleaned, one piece is placed on a leveling table and the solution is then applied. The other piece is then placed on top. A leveling table is used to avoid any slipping of the bonding pieces after the bonding solution has been used. A small weight (typically a few to several ounces) can then be placed on top of the pieces, but this is usually only needed for surfaces

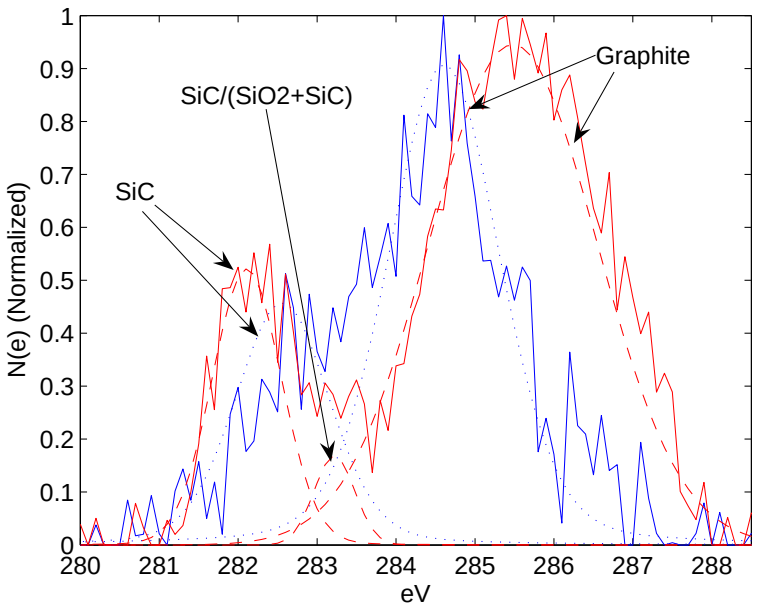

Figure 4-5. C1s orbital both before (blue curve) and after (red curve) bonding. The dashed and dotted lines represent the peak fit values while the solid lines are the raw data taken from the XPS. The unbonded peaks are at 282.79 eV, and 285.12 eV. The bonded peaks are at 285.48 eV, 283.22 eV, and 282.11 eV.

that are not very flat. If a weight is not ideal, then pressure can be administered by pressing down on the top piece. The pieces are then not disturbed for at least 18 hours.

While all preparation and bonding was done in a clean room, any clean area, such as a vented hood, will suffice. A clean room reduces the chance of particulates contaminating the surface which may lower the bonding strength.

4.4 Strength Measurements

For all materials tested, the mode of failure with the least amount of applied force will be parallel to the bond area. By testing the shear strength of the hydroxide bonded materials, a lower bound on the breaking strength can be determined. To test the breaking strength, two different apparatuses were used. The first consisted of a lever arm with a 3 mm diameter stainless steel wire on one end, and a spring-based force meter with a maximum force indicator (a spring scale from Cabela's) on the other as shown in Figure 4-6. The lever arm is approximately 39 cm long and has a 5:1 torque advantage.

The bonded pieces were held in place by a slot machined in a solid piece of aluminum that was held in place using a clamp that was mounted to a table.

The wire was then wrapped around the bonded piece and a downward force was applied on the other until the test piece broke. The applied force was measured by reading the maximum force indicator from the spring scale. It should be noted that similar to experiments in reference [53], by placing the wire a few millimeters from the bond, a slight torque or peeling effect was created on the bonding area perpendicular to the direction of the shear stress. After extensive testing using this apparatus, promising results were obtained. However, the variation of the measured bond strength was higher than expected, so a more precise method of measuring breaking strengths was used. This method uses a modified compression shear test (MCST) as described in reference [58] (Figure 4-6). A linear actuator with an 8 mm/s travel speed was used to apply the force while a LabVIEW program sampled the amplified output of an MLP series load cell from Transducer Techniques at 1 kHz. Sampling at this rate showed a clearly defined peak and produced an error in the applied force measurements of less than ± 1.5 lbs. In every instance, the range of the measurements was greater than the error produced from the measuring device. To compare the lever arm apparatus and MCST, eight BK7-BK7 bonds were made using 0.50 μL of solution and then half were broken in each device. For each apparatus, the range of breaking strengths were similar, but the average using the MCST was higher. This is most likely due a slight cutting in the glass from the wire used in the lever arm apparatus as the force is being applied, which causes the glass to break at lower strengths. In our results both the data obtained using the lever arm apparatus and MCST are used.

4.4.1 BK7-BK7 Bonding

If hydroxide bonding is to be used on space-based interferometric missions, the bond must be able to withstand the significant accelerations endured during launch. A typical optical component on an optical bench with a bond area of 100 mm^2, an approximate

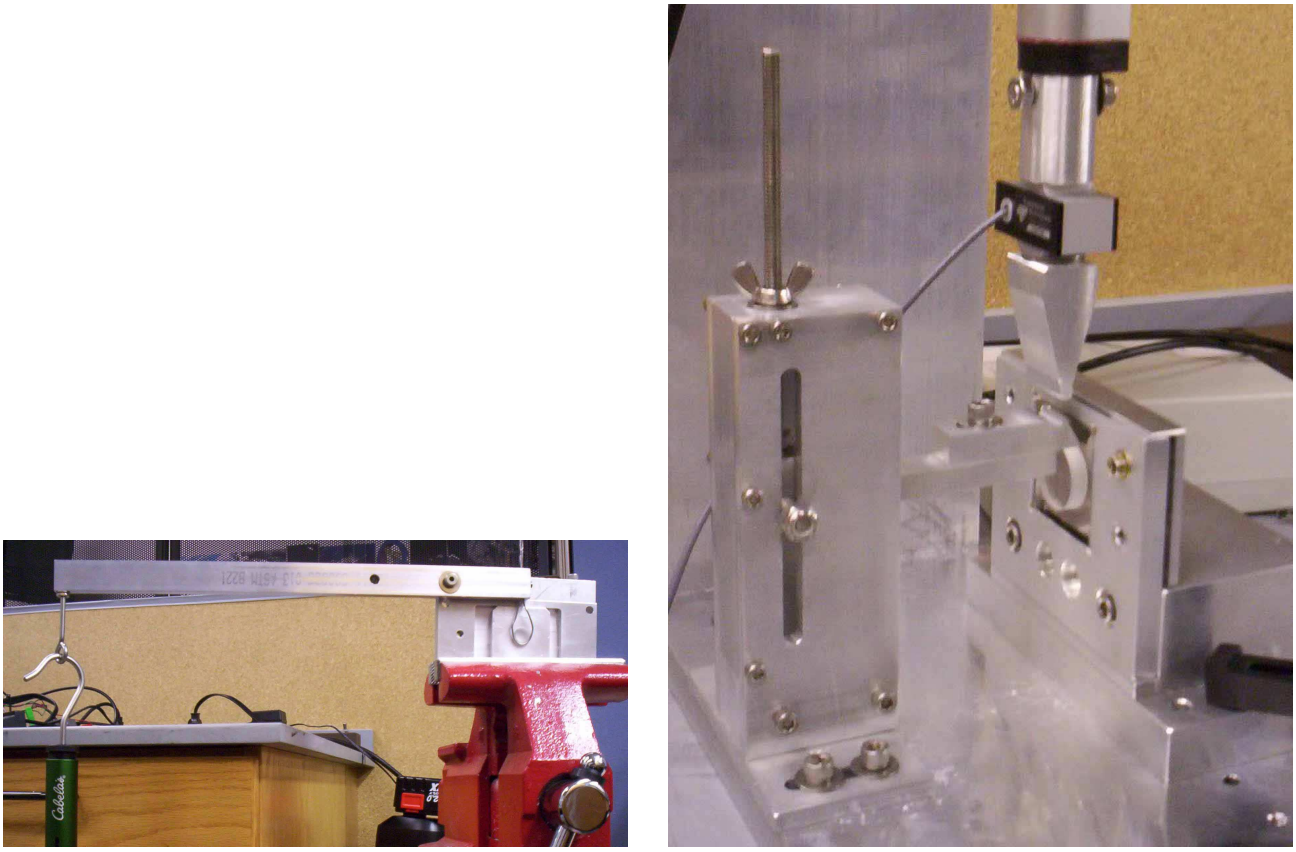

Figure 4-6. Lever arm apparatus used to initially test the hydroxide bonded shear strengths (left) and MCST apparatus used for later tests (right).

mass 10 mg, and subject to 35g accelerations during launch conditions results in a requirement that the bonds be able to withstand on the order of tens of kiloPascals. Results from the University of Glasgow have shown hydroxide bonds to be significantly stronger than what is required [53], although more research is needed to better understand the process and its limitations. In this section I elaborate on existing hydroxide bonding results to gain a more complete understanding of this process.

While Zerodur or ULE are usually used for optical components in space-based interferometric missions, BK7 glass has a similar molecular structure and composition to these materials and bonds in the same manner with similar breaking strengths [45]. Consequently, BK7 provides us with a cost-effective alternative to Zerodur or ULE to

test the hydroxide bonds. The BK7 glass rods (CTE of 7 to 8×10^{-6}/C) are 12.7 mm in diameter and 10 mm thick. One side was polished to a $\lambda/8$ global flatness with a 20-10 scratch-dig finish, while the other side had a ground polish. This allowed the testing of bonds with both rough and smooth surfaces.

The dehydration of the water molecules in the hydroxide solution plays an important role in the hydroxide bonding process. As the water evaporates or moves into the bulk of the material, the siloxane chains form a 3D network and join the two surfaces. If it takes appreciable amount of time for the bonds to reach their maximum strength, then the bonds must be left to cure for this time before their breaking strength should be measured. In addition, if the dehydration process occurs over an extended period of time, then this may cause the bonded pieces to shift slightly and may cause problems when used for precision alignment for uses such as optical benches. To determine the effects of dehydration time on the shear strength, multiple samples were prepared using 0.40 μL/cm^2 of a volumetric 1:4 sodium silicate to deionized water solution between two BK7 pieces using the unpolished side. Each sample had 1.27 cm^2 of bonding area and stayed in the clean room approximately 18 hours. The shear strength of one bonded piece was then tested using the lever arm apparatus. The other pieces were kept in an oven at 50°C until broken in the same manner. Two bonded pieces were also left in the clean room for 11 days to determine if the elevated temperature within the oven had any effect on the bonding strength (see Figure 4-7). The temperature the oven was set at was based on previously bonded samples that had been heated to various temperatures to determine what temperature range the hydroxide bonds could survive [59]. Most either failed or weakened significantly above 100°C. Using an oven temperature of 50°C will expedite the dehydration process, but shouldn't cause the bond to weaken or fail.

It appears the dehydration time has no appreciable effect on the breaking strength when using a sodium silicate solution and the bond reaches significant strength after approximately 18 hours [59]. After breaking the pieces that were left in the clean room

for 11 days, it was found that they had a similar breaking strength to the pieces left in the oven for the same amount of time. It should be noted that when breaking the bonded glass pieces with the lever arm apparatus, the failure was almost always a few millimeters above the bond where the wire on the apparatus applied the force on the glass, and not at the glass to glass interface.

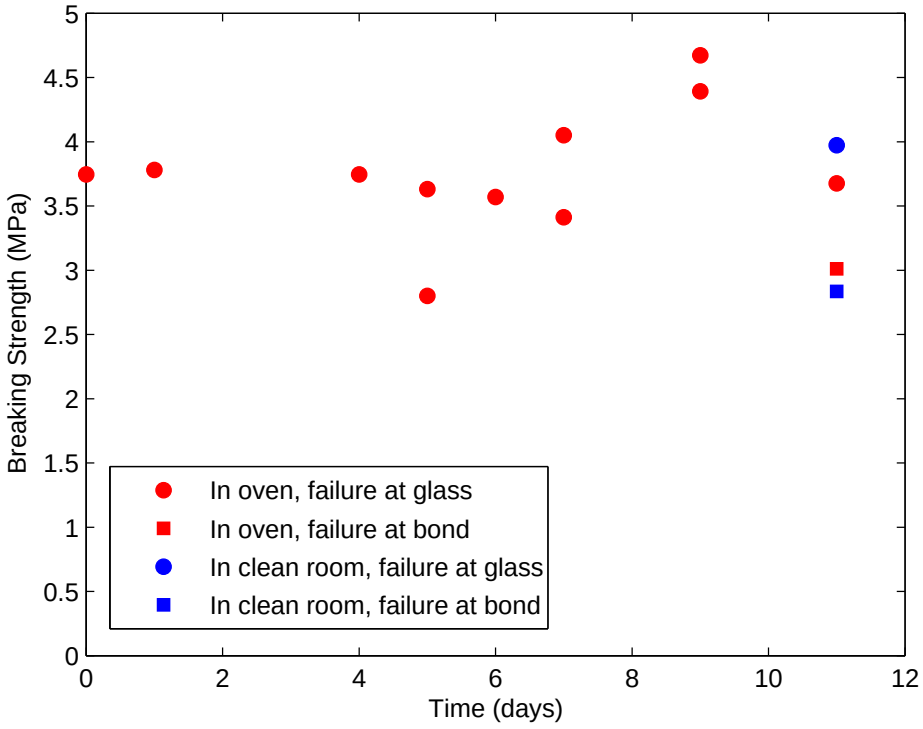

Figure 4-7. Breaking strengths of BK7-BK7 bonds after being kept in an oven at 330 K. The zero on the x-axis represents the time after the samples were in the clean room for approximately 18 hours. All data points were taken using the lever arm apparatus.

It was suggested in reference [53] that the water in the hydroxide solution may be weakening the glass material, causing the fracture to occur in the glass and not along the bond interface. Through extensive testing of multiple samples, it is believed that this effect is most likely caused by the small surface area of the wire that makes contact with the glass, which in turn, creates a much higher localized pressure at the wire-glass interface, and not over the bond area. This results in the wire cutting or scoring the glass,

which then creates a small crack. As more force is applied, the micro-crack propagates through the BK7, causing the glass to break at the glass-wire interface.

To test this, multiple samples that had been broken at the glass-glass interface after having their shear strength tested had their bulk shear strength tested using the MCST. The values of these data points were compared to the bulk shear strengths of glass pieces broken using the MCST that had not been bonded. Both bonded and unbonded samples had similar shear strengths. From the similar breaking strength values, it is assumed that the water in the hydroxide solution does not weaken the glass in an appreciable manner, if at all [59].

The primary advantage the MCST has over the lever arm apparatus is that the MCST applies the force evenly over the glass rod, which reduces localized forces and scratching. Comparing the breaking strengths of the bonded BK7-BK7 samples using the MCST and the lever arm, it was found that the MCST breaking strengths were higher than those using the lever arm. In addition, it was also found that all pieces tested using the MCST broke at the bond, and did not break the glass. This supports the assumption that the reason the glass pieces were breaking at the glass-wire interface when using the lever arm device is because of a cutting effect produced when using the wire, and not due to a weakening of the glass from the water used in the bonding solution.

It was shown in reference [53] that the molarity of the hydroxide solution was varied, a maximum breaking strength was found. This value was different each alkali metal used. Another parameter that could effect the bonding strength is the amount of solution used per square centimeter. Using a volumetric 1:4 sodium silicate to deionized water solution and varying the amounts of solution used from 0.20 μL to 1.25 μL while keeping the bond area constant and using the polished surfaces of the glass rods, multiple samples were made and kept in a clean room at least 18 hours before being tested. The data consisted of three bonded pieces using 0.20 μL of solution, seven pieces using 0.50 μL, four pieces using 0.75 μL, five pieces using 1.00 μL, and two pieces using 1.25 μL.

The majority of the data fell close to each other within approximately 35% of their mean, but in one case the deviation was as high as 90% [59]. In this case, it was a single data point that was well above the average. From the data it was found that there was no significant correlation between the shear strength of the bonds and the amount of solution used. It should be noted that as the amount of solution used was increased, more solution would spill out of the sides. Unfortunately there was no way of determining how much fluid was spilling out. The average of the 21 samples was 3.2 MPa with a range of 1.7 to 7.6 MPa. Comparing the average breaking strength of the hydroxide bonds to those obtained in reference [45] by optically contacting similar materials, the average breaking strength of the hydroxide bonds is approximately 2.5 times greater using the hydroxide bonding technique when compared to optical contacting. In addition, the greatest breaking strength found in reference [45] was comparable to the lowest breaking strength when hydroxide bonding is used.

4.4.2 SiC-BK7 Bonding

While glass to glass bonding for multiple glass materials has been studied for both optical contacting and hydroxide bonding, only limited experimental results are available for SiC bonds using hydroxide bonding [60] [61]. To determine the shear strength for SiC-BK7 hydroxide bonds, a volumetric 1:4 dilution of sodium silicate to DI water was used. The amount of solution was varied while keeping the bonding area constant and using the polished side of the glass rods. The SiC tiles are made of Hexoloy SA (CTE of 4×10^{-6}/C) are 50.8mm on each side and 6.4mm thick with a $\lambda/8$ global flatness and 60-40 scratch-dig on both large sides. The SiC tiles were cleaned using cerium oxide and sodium bicarbonate as described in Appendix B. Although the surfaces were cleaned using cerium oxide, similar results should be obtained using only a sonic bath to clean the SiC. The data consisted of three glass rods bonded using 0.12, 0.35, 0.60, 0.75, 1.00, and 1.20 μL of solution, five rods at 0.25 μL, and four rods at 0.50 μL of solution. The typical deviation from the average for each amount of solution used was below 50%. As

with the BK7-BK7 bonds, there appears to be no significant correlation between the amount of solution used and the breaking strength of the bonds. The average of the 27 data points is 3.0 MPa with a range of 1.0 to 5.0 MPa [62]. For a comparison between the breaking strength of SiC-BK7 hydroxide bonds and SiC-BK7 optically contacted bonds, the breaking strength of one optically contacted SiC-BK7 bond was broken and found to have a breaking strength of a little under 1 MPa. More data is need to draw a conclusion on the comparison between optically contacted and hydroxide bonds between SiC and BK7. It should be noted that optically contacting SiC to BK7 is difficult to do with much success.

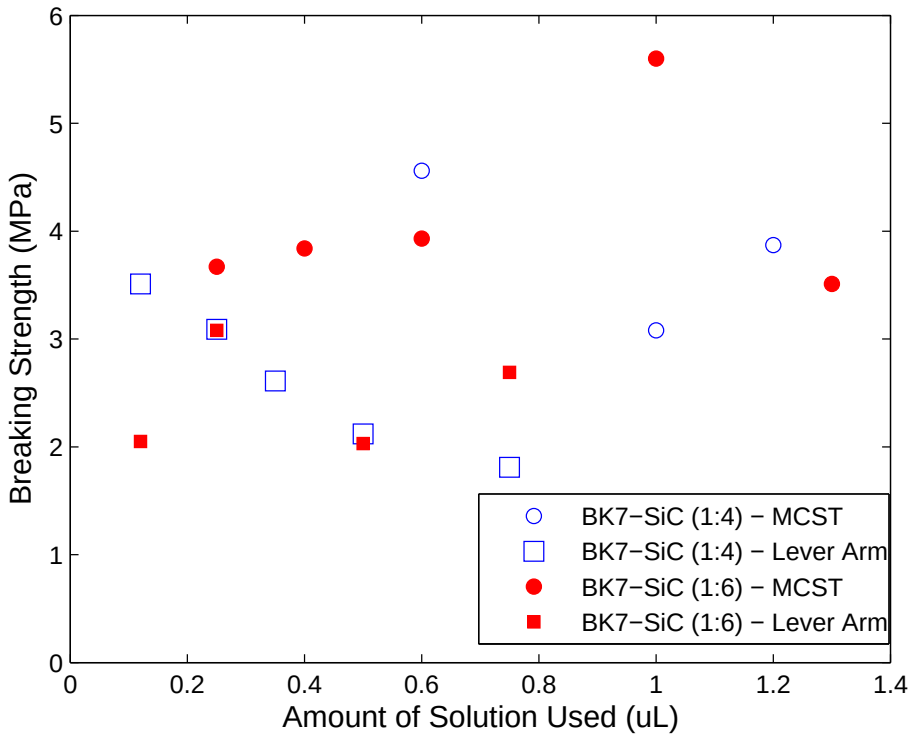

Figure 4-8. Averages of the data obtained using the lever arm and modified compression shear test (MCST) devices for both a 1:4 and 1:6 dilution factor.

4.4.2.1 Dilution factor

It may be possible that the shear strength is effected by the concentration of the solution used. Using a dilution factor of 1:4 may produce a stronger bond than a 1:6

dilution factor since the 1:4 solution will have a greater bond thickness and may allow the siloxane chains to bond to the SiC surface more readily. To test this, multiple samples were prepared and bonded in the same manner as above, although a 1:6 sodium silicate solution was used instead of a 1:4 solution (Figure 4-8). Two glass rods each bonded using 0.12, 0.40, 0.60, and 1.30 μL of solution, six rods using 0.25 μL, and three rods at 0.50, 0.75, and 1.00 μL. The variability in the measurements stayed consistent as with what was obtained above and no significant correlation between the amount of solution used and the shear strength could be observed [59]. The average of the 23 data points is 3.4 MPa, with a range of 1.0 to 6.3 MPa.

4.4.2.2 Surface profile

The surface profile of the bonding surface plays an important role in determining what solution should be used. If the surface is too rough, then a bond cannot form. A sodium silicate solution can be used as a filler/intermediary to fill the gaps and allow the siloxane chains to bond. The data taken above used the polished surface of the glass. Using the rough surface may produce different breaking strengths since there is a greater probability the bond will not completely form and gaps will be created within the bond[53]. To test this, three glass rods were bonded using the rough side of the glass with 0.25 μL of 1:4 sodium silicate solution, two rods at 0.40, 0.75, and 1.00 μL, and six rods were bonded using 0.50 μL of solution. The variation was again comparable to previous measurements with an overall mean of 3.0 MPa and a range of 1.1 to 7.3 MPa. This is comparable to what was achieved when using the polished side of the BK7 [59]. The fact that a ground finish will suffice to bond these materials and still produce a substantial bond has a significant cost-reducing effect. It is often expensive to polish glass or SiC flat and smooth enough to obtain a strong optical contact, especially as the surface area increases. Using hydroxide bonding allows the faces of the pieces to be bonded to have significantly less demanding polishing tolerances, which, in turn, reduces the cost of the materials.

4.4.3 Super Invar-BK7

Bonding glass to metals with appreciable strength in a non-destructive manner can be a difficult process. While anodic bonding or frit bonding can be used for some glass-metal bonds, it often requires the metal to be very thin, or that the pieces be heated to several hundreds of degrees Celsius [63] [64] [65], or the glass and metal have close CTE's. This makes it virtually impossible to bond bulk materials with differing CTE's in a non-destructive manner. Using the hydroxide bonding technique allows metals ranging from aluminum to copper [66] [67] to Super Invar to be bonded to glass while retaining their thermal and mechanical characteristics. To test the shear strength of the Super Invar BK7 hydroxide bond, two bonds using 0.20, 0.40, 0.60, 0.80, and 1.00 μL of 1:4 sodium silicate solution were made using the polished side of the glass rods. The Super Invar tiles (CTE of 0.7×10^{-6}/C) are 38.1mm on each side and 6.4mm thick and polished to a $\lambda/4$ global flatness and 60-40 scratch-dig on both large sides. The Super Invar tiles were cleaned using cerium oxide as described in Appendix B. All bonds were tested using the MCST and no significant correlation between the amount of solution used and the shear strength could be obtained. The average of the measurements is 5.8 MPa with a range of 2.3 to 8.1 MPa.

In addition to these test, anecdotal experiments were done to determine what thermal stresses the Super Invar-BK7 bonds could endure. In one instance, a BK7 glass window 25 mm in diameter and 6 mm thick was bonded to a Super Invar tile and then heated to 100°C at 0.70°C/min, left for 1 hour, and then quenched in ice water. Although the glass window broke, pieces of the glass were still bonded to the Super Invar. In another case, a 12 mm diameter plano-convex lens was bonded to another Super Invar tile and heated in the same manner. After being quenched in ice water, no visible degradation of either the bond or the materials could be detected. This remarkable property needs to be studied in greater detail since it may be possible the siloxane chains in the hydroxide bond may be reducing the thermally induced stresses of the materials.

4.4.4 SiC-SiC

A variety of tests were performed to characterize the strength and durability of the SiC to SiC bonds on three types of SiC. The three SiC materials tested were Hexoloy SA, POCO SuperSiC, and CoorsTek UltraSiC. To determine the shear strength of the SiC-SiC hydroxide bonds, the MCST was used on all tests.

4.4.4.1 Hexoloy SA

A 50.8 mm x 50.8 mm x 6.4 mm tile of Hexoloy SA was obtained from Saint-Gobain Ceramics. It was polished to a $\lambda/8$ global flatness with a mirror quality surface finish. A section 9mm x 6mm was cut from this tile and both polished faces were bonded using 1.0 μL of 1:4 sodium silicate solution. The resulting bonded piece was left to cure for several weeks. It was then cooled to approximately liquid nitrogen temperatures. Although the bond strength was not tested while it was cooled, the bond could not be broken trying to pry it apart using hand strength. From previous testing experience, this results in a breaking strength that is greater than approximately 100 kPa [68]. The SiC was then allowed to return to room temperature and the bond strength was tested and found to be 6 MPa.

Another section of the same tile 10 mm x 10 mm was cut and the flat faces were bonded using 1.0 μL of 1:4 sodium silicate solution. The bonded piece was then left to cure for 10 days and was cut with a diamond tile saw rotating at 3600 rpm. The cut was made approximately 3mm from the outside and took roughly 45 minutes to perform. No degradation of the bond could be seen and the resulting cut SiC could not be pried apart using hand strength. Although the bond retained significant strength after cutting, it may be possible that prolonged exposure to water or other cutting fluids may cause the bond to fail. The bonded pieces were then dipped in liquid nitrogen for several seconds and then taken out for a few seconds. This was done multiple times. The bond could not be broken using hand strength after this process.

4.4.4.2 POCO SuperSiC

Although it was claimed in reference [55] that the surfaces need a peak-to-valley flatness of ≤60 nm, it was found that it is possible to bond with surfaces as rough as 24 μm over a 2 mm length. An unpolished disc 3 mm thick and 50.8 mm in diameter of SuperSiC was obtained from POCO Graphite. The surface roughness was found to be as large as 24 μm over 2 mm (figure 4-9). A 10mm x 10mm section was cut from this piece and bonded using 3.0μL of solution. The resulting shear strength was found to be 2.45 MPa [68].

4.4.4.3 CoorsTek UltraSiC

Two 50.8 mm x 50.8 mm x 7.6 mm and six 10 mm x 10 mm x 7.6 mm SiC samples were obtained from CoorsTek. They were polished at the CoorsTek facilities and the larger tiles were found to have a flatness between 0.95 μm and 0.99 μm, both with a surface finish of 0.05 μm Ra. The smaller SiC pieces were found to have a flatness ranging from 0.07 μm to 0.30 μm with a surface finish ranging from 0.03 μm Ra to 0.09 μm Ra.

The smaller SiC pieces were bonded to the larger SiC tiles using differing amounts of sodium silicate solution and the shear strengths were measured. Two pieces were bonded using 1.00 μL of solution and had breaking strengths of 7.12 MPa and 4.00 MPa. Two pieces were bonded using 0.50 μL of solution and had breaking strengths of 5.78 MPa and

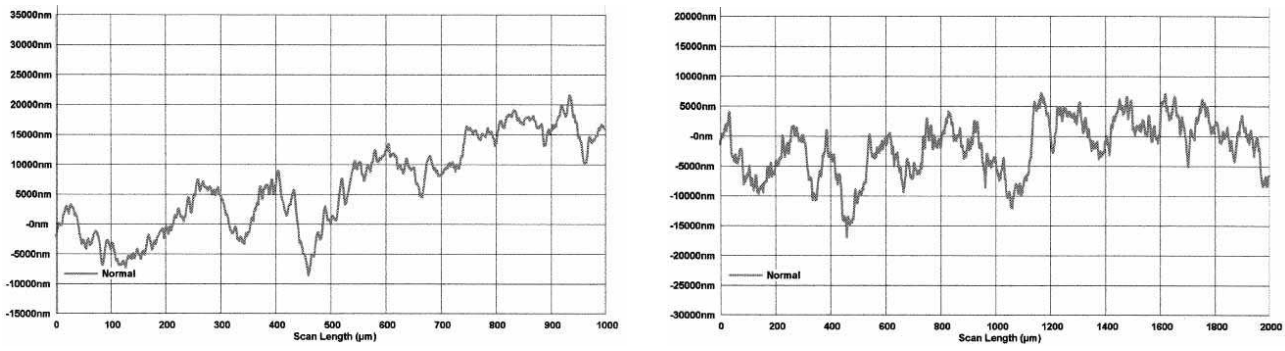

Figure 4-9. Surface profiles of areas on the POCO SuperSiC using a Tencor surface profiler. Image courtesy of Petar Arsenovic at Goddard Space Flight Center.

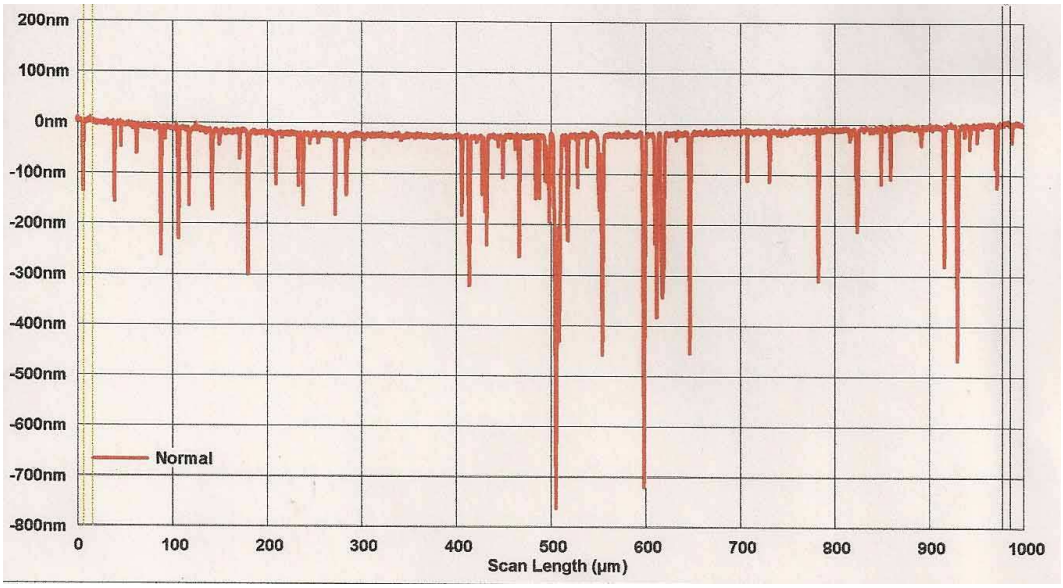

Figure 4-10. Surface profile of one of the large CoorsTek SiC tile using a Tencor surface profiler. Image courtesy of Petar Arsenovic at Goddard Space Flight Center.

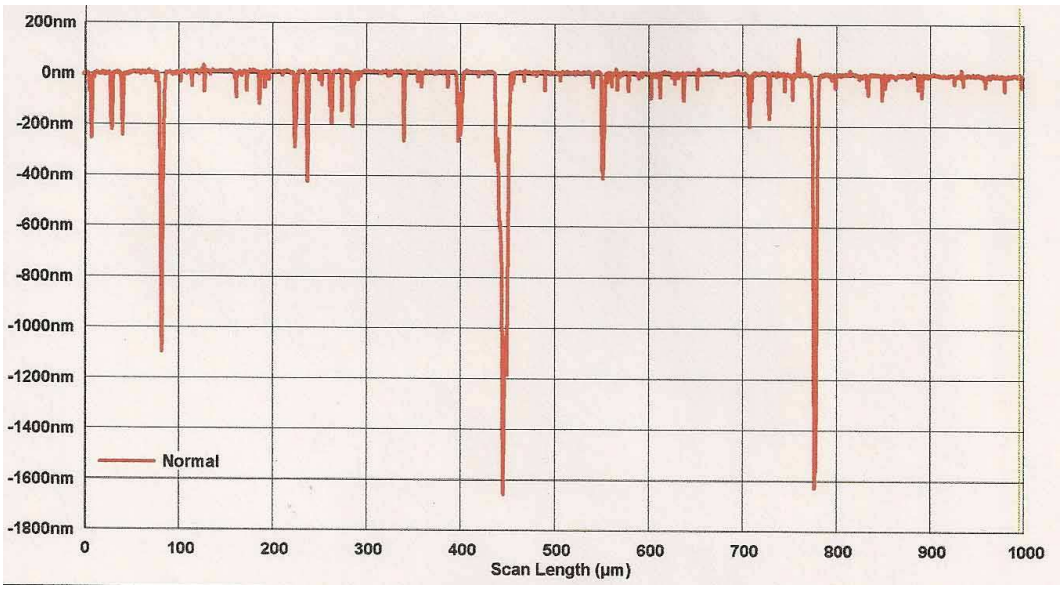

Figure 4-11. Surface profile of one of the small SiC pieces using a Tencor surface profiler. The large spike around 750 μm is most likely a speck of dirt. Image courtesy of Petar Arsenovic at Goddard Space Flight Center.

3.25 MPa. One piece was bonded using 0.25 μL of solution and had a breaking strength of 2.22 MPa [68].

It was previously shown that by using this testing method of the shear strengths, the typical variance in breaking strengths was approximately 35%. The variation in our

measured breaking strengths could be from either a lack of samples, or from a possible roll-off of surface curvature in some of the samples due to the polishing process. Although the surface finishes and flatness were all measured to be similar, the sampled areas were only taken at random places and only in local areas. Hence, although the local areas tested all had similar profiles, the overall profile (taken over the entire surface) was not measured. In some cases, a noticeable rolling off of the edges could be seen by visual inspection. When a roll off in surface profile could be noticed, the breaking strength of the bond was significantly less than those when no roll off could be noticed, holding all other bonding factors constant.

Another piece of SiC was bonded using 1.50 μL of solution. The bonded pieces were cured overnight and then cooled to 77 K in a 2-step process. In the first step, the SiC was placed on an aluminum block that sat in a small reservoir. The reservoir was filled with liquid nitrogen which slowly cooled the aluminum block. As the temperature of the aluminum block was lowered, the temperature of the bonded SiC piece fell as well. Once the boiling rate of the liquid nitrogen appeared to be constant, the bonded SiC piece was taken off the aluminum block and dipped a few times into the liquid nitrogen for a few seconds. The bond showed no noticeable signs of degradation. Although the SiC piece was not tested for its shear strength after it warmed back to room temperature, it could still not be broken using hand strength, and is assumed to have similar breaking strength to the pieces tested above.

In addition to cooling the bonded pieces, the sample that was cooled was also heated to determine the effects of heating on the bond. The sample was heated in an oven from room temperature to 80°C at 5°C/min and allowed to soak at 80°C for 1 hour. After this was done, the bond could not be broken using hand strength. The bond was then heated to 100°C at 5°C/min and allowed to soak at 100°C for 30 minutes. The bond could not be broken using hand strength. The sample was then further heated to 130°C at 5°C/min and allowed to soak for 30 minutes. The bond was then broken using a significant amount

of strength. Although this bond was not broken using the MCST, based on previous bonding experience, the bond strength at 100°C is at least 100 kPa.

4.5 Other Bonding Results

In addition to these breaking strength measurements, hydroxide bonding was attempted between other materials, although the shear strength of these bonds were not tested. Successful bonding occurred between copper-copper, aluminum-aluminum, and a silver coated PZT material and BK7. In many cases, the surfaces of these materials were not polished and in the case of the aluminum-aluminum bond, the surface polish was done by a mill in the machine shop. Although the breaking strengths were not tested, they could not be broken using hand strength, implying a shear strength of greater than 100 kPa. In addition, a bond between a strip of nichrome and aluminum was attempted, but the bond failed. This supports the theory that metals that are oxidized easily are capable of hydroxide bonding, since nichrome has an extreme resistance to oxidation. This also supports the theory that the oxide plays a critical role in the bonding process, and not the material itself as nichrome has a composition with elements in it that are present in other materials that have successfully bonded.

CHAPTER 5
RELATIVE STABILITY MEASUREMENTS

Continuous-wave (cw) lasers have played a major role in advancing precision measurements in many fields. Frequently, the linewidth of such lasers is not adequate for many applications without active stabilization of the laser frequency. For example, some atomic clocks require extremely stable laser sources to probe sub-Hertz linewidths available in laser cooled samples [69]. Interferometric gravitational wave detectors, such as LIGO and LISA, require laser systems with extremely low frequency and amplitude noise. Through the use of an optical cavity and feedback control system, the stability of the cavity can be transferred to the laser which can then be measured against another stable laser source. In this chapter a versatile feedback control known as Pound-Drever-Hall (PDH) frequency stabilization will be discussed for its application to measure the stability of select materials on the femtometer level. A brief discussion of optical resonators is presented as well as how the optical cavities were made in order to test the dimensional stability of several materials. Lastly, the relative dimensional stability of Zerodur, Super Invar, SiC, CFRP, and a tunable PZT-actuated cavity are presented.

5.1 Optical Cavities

The core concepts needed to make measurements at the femtometer level revolve around knowledge of both optical resonators and PDH frequency stabilization. In this section, a few select concepts of optical cavities is presented. Referring to Figure 5-1, the laser fields of an optical cavity are described by

$$\begin{aligned} E_1 &= it_1 E_{in} + r_1 E_2 \\ E_2 &= r_2 E_1 e^{i2L(2\pi f)/c} \\ E_t &= it_2 E_1 e^{iL(2\pi f)/c} \\ E_r &= it_1 E_2 + r_1 E_{in} \end{aligned} \tag{5–1}$$

where f is the laser frequency, L is the length of the cavity, c is the speed of light, and r_i and t_i are the reflection and transmission coefficients of mirror i. The transmitted and

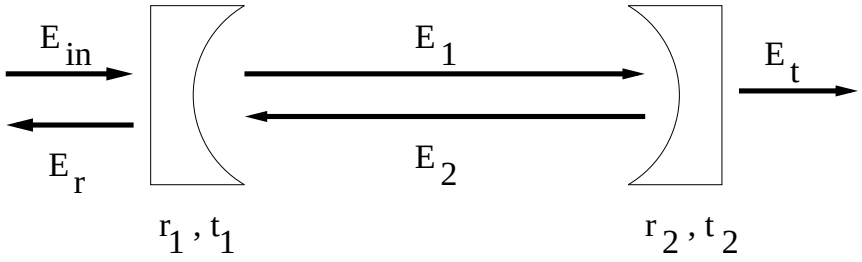

Figure 5-1. Electric fields inside and outside of an optical cavity.

reflected transfer functions, $T_t(f)$ and $T_r(f)$, can be found by solving Eq. 5–1 in terms of E_t/E_{in} and E_r/E_{in}, respectively. Doing this results in

$$\begin{aligned} T_t(f) &= \frac{-t_1 t_2 e^{2\pi i f L/c}}{1 - r_1 r_2 e^{2i(2\pi f)L/c}} \\ T_r(f) &= \frac{r_1 - r_2(r_1^2 + t_1^2)e^{2i(2\pi f)L/c}}{1 - r_1 r_2 e^{2i(2\pi f)L/c}}. \end{aligned} \tag{5–2}$$

For a lossless cavity ($r_1^2 + t_1^2 = 1$) the transfer function of the reflected field simplifies to

$$T_r(f) = \frac{r_1 - r_2 e^{2i(2\pi f)L/c}}{1 - r_1 r_2 e^{2i(2\pi f)L/c}}. \tag{5–3}$$

Eq. 5–3 will present resonant behavior when $T_r(f)$ is a minimum and occurs when

$$\frac{2(2\pi f)L}{c} = 2\pi n, n \epsilon \mathbb{N}. \tag{5–4}$$

This equation can also be written as

$$f_n = n\frac{c}{2L}. \tag{5–5}$$

The frequency difference between neighboring resonant modes is constant and is known as the free spectral range (FSR). It is given by

$$FSR = f_{n+1} - f_n = c\frac{n+1}{2L} - c\frac{n}{2L} = \frac{c}{2L}. \tag{5–6}$$

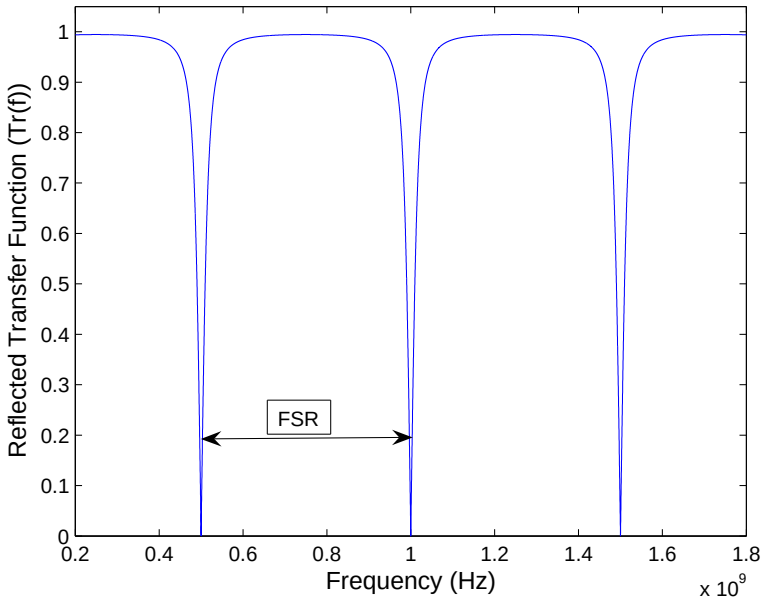

Figure 5-2. Plot of the reflected transfer function for a lossless cavity 30 cm long with both mirrors having reflectivities of r=0.90. The FSR is 500 MHz.

In addition to the FSR, another important parameter of optical cavities is the finesse, $\mathcal{F}$. The finesse is defined as the ratio of the FSR to the linewidth. This can also be represented in terms of the reflectivities or transmissivities by

$$\mathcal{F} = \frac{\text{FSR}}{\text{linewidth}} = \frac{\pi\sqrt{r_1 r_2}}{1 - r_1 r_2} \approx \frac{\pi}{t_1 + t_2}. \tag{5–7}$$

The mirrors used for the optical cavities were made from fused silica and were quoted by the vendor (AT Films) as having transmissivities near 360 ppm.

5.1.1 Stability of Optical Resonators

Light within the cavity will bounce back and forth between the mirrors and experience a periodic focusing action. Depending on the radius of curvature of the two mirrors, the periodic focusing can be classified as either stable or unstable [70]. A cavity with spherical mirrors is an example of a periodic focusing that can result in either stable or unstable behavior. Using what are known as the g parameters, the stability of

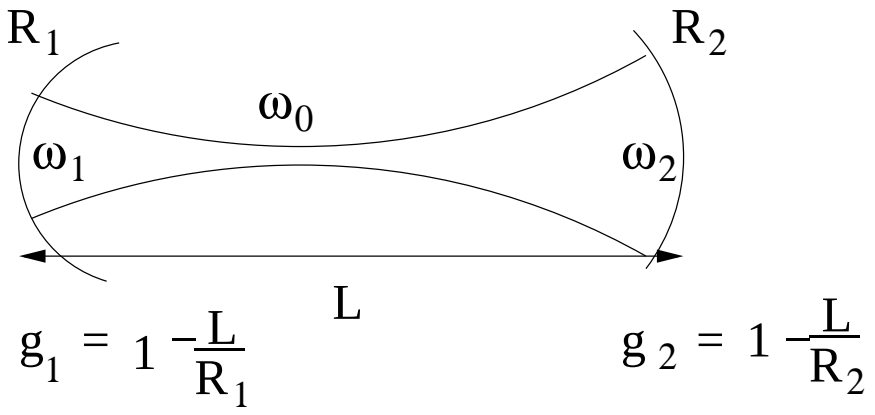

Figure 5-3. The resonator g parameters.

the resonator can be determined. Each mirror is given a g-value defined by

$$g_i = 1 - \frac{L}{R_i}, \tag{5–8}$$

where L is the length of the cavity, and R_i is the radius of curvature of the ith mirror (i=1 is the front mirror and i=2 is the back mirror). For a cavity to be a stable resonator, the condition

$$0 \leq g_1 g_2 \leq 1 \tag{5–9}$$

must be met. The waist spot size, ω_0, of the resonator can then be written in terms of the g parameters, namely

$$\omega_0^2 = \frac{L\lambda}{\pi}\sqrt{\frac{g_1 g_2(1-g_1 g_2)}{(g_1+g_2-2g_1 g_2)^2}}. \tag{5–10}$$

The spot sizes at the ends of the resonator are given by

$$\begin{aligned} \omega_1^2 &= \frac{L\lambda}{\pi}\sqrt{\frac{g_2}{g_1(1-g_1 g_2)}}, \\ \omega_2^2 &= \frac{L\lambda}{\pi}\sqrt{\frac{g_1}{g_2(1-g_1 g_2)}}. \end{aligned} \tag{5–11}$$

In the case when the front mirror is flat (as is the case with all cavities presented in this work), then g_1=1 and Eqs. 5–11 reduces to

$$\begin{aligned} \omega_0^2 &= \omega_1^2 = \frac{L\lambda}{\pi}\sqrt{\frac{g_2}{(1-g_2)}}, \\ \omega_2^2 &= \frac{L\lambda}{\pi}\sqrt{\frac{1}{g_2(1-g_2)}}. \end{aligned} \tag{5–12}$$

Knowing only the length of the cavity and the radius of curvature of the two mirrors will determine the resonant mode of the cavity. From this data the laser beam can be mode-matched using lenses to fit the mode of the cavity.

5.1.2 Misalignment Analysis

In addition to specifying the RMS polishing tolerances of the spacer ends, the parallelism needs to be specified as well. The mirrors have a high reflectivity (HR) coating for the center 5 mm. If the displacement of the optical axis is too large, then the beam may be misaligned so much that the beam does not hit the coated area on the mirror. This would produce a cavity with a lower finesse in addition to producing additional noise. For this reason, parallelism tolerances need to be specified as well. Using Figure 5-4 as

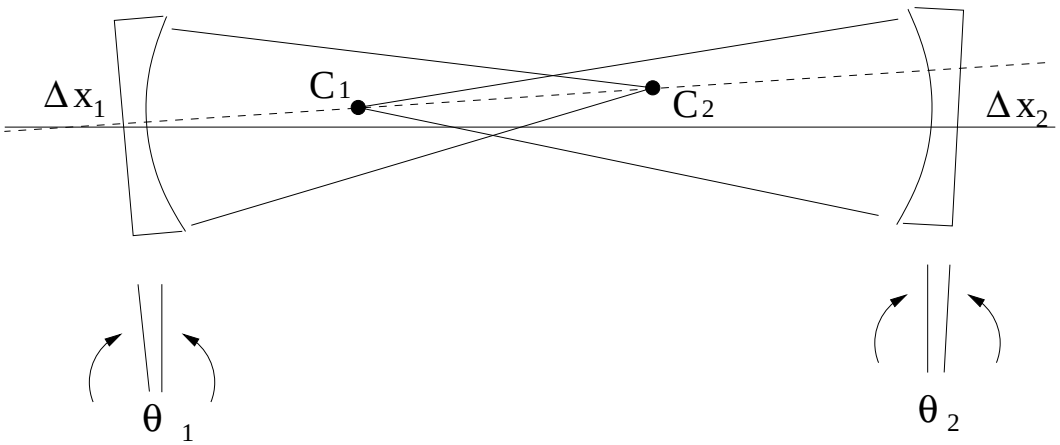

Figure 5-4. Geometry for analyzing the misalignment of a cavity.

a guide, where L is the length of the cavity, Θ_1 and Θ_2 are the small angular rotations of the two end mirrors, Δx_1 and Δx_2 are the small sideways translations of the new optical axis at the point where it intercepts the end mirrors, and C_1 and C_2 are the centers of

curvature of the two end mirrors, the parallelism tolerance can be found. Based on the HR coated area of the mirrors and a typical spot size of 300 μm, the displacement should be kept to within 1 mm. From Figure 5-4 and some geometry [71], it can be found that the misalignments are given by

$$\Delta x_1 = \frac{g_2}{1 - g_1 g_2} \times L\theta_1 + \frac{1}{1 - g_1 g_2} \times L\theta_2 \tag{5–13}$$

$$\Delta x_2 = \frac{1}{1 - g_1 g_2} \times L\theta_1 + \frac{g_1}{1 - g_1 g_2} \times L\theta_2. \tag{5–14}$$

The front face can be assumed to be the reference, so θ_1 can be assumed as zero. This holds as long as the center hole is large enough for the beam to easily pass through and the perpendicularity of the front face to the spacer is reasonable. In this case, Eq. 5–14 reduces to

$$\Delta x_2 = \frac{g_1}{1 - g_1 g_2} \times L\theta_2. \tag{5–15}$$

Since all the front mirrors are flat for the cavities produced in this work, $g_1 = 1$, and Eq. 5–15 then reduces to $\Delta x_2 = \frac{L}{1-g_2}\theta_2$. Most of the cavities in this work are approximately 25 cm long with a flat front mirror, and a back mirror with a radius of curvature of 1 m. For these parameters, the typical parallelism needs to be better than ~3 mrad. This tolerance is not hard to obtain as most polishing companies can easily achieve a parallelism of better than 1 mrad.

5.1.3 Cavity Construction

5.1.3.1 Zerodur cavities

Three Zerodur cavities were made to test their relative stability. Two consisted of optically contacted mirrors, and one with hydroxide bonded mirrors. The two cavities with optically contacted mirrors were constructed as part of another group members dissertation work [72]. The third cavity with hydroxide bonded mirrors was constructed by the author. Table 5-1 specifies the length of the Zerodur spacer, the radius of curvature for the mirrors used, the FSR, linewidth, and finesse of all 3 cavities. The biggest difference

Table 5-1. Parameters of the three Zerodur cavities constructed by either optically contacting or hydroxide bonding the mirrors.

Cavity	L	R_1	R_2	FSR	linewidth	Finesse
Z_1	260 mm	∞	0.5 m	576 MHz	50 kHz	11,500
Z_2	225 mm	∞	2.0 m	647 MHz	140 kHz	4,600
Z_3	210 mm	∞	1.0 m	715 MHz	60 kHz	11,700

between the three cavities is that Z_2 has a much higher linewidth than the other two cavities. This is most likely from the mirrors that were used to make the cavities. Both Z_1 and Z_3 were made using mirrors that had been made at Wave Precision and then coated at AT Films. The mirrors on Z_2 were older mirrors from a different vendor that had possible contaminations of the coatings. The specifics of the construction of Z_1 and Z_2 can be found in reference [72].

To construct Z_3, the Zerodur spacer was first cleaned as described in Appendix B. It was allowed to dry overnight in order to make sure the surfaces were completely dry. The curved mirror was then cleaned in the same manner. After it was cleaned, it was allowed to dry for approximately five minutes. During this time, the surface of the Zerodur spacer was cleaned using a cleanroom wipe that had been wetted with methanol. Both surfaces to be bonded were then inspected for any contaminates on their surfaces. The Zerodur spacer was then placed such that the surface to be bonded was facing straight up. 1.90 μL of hydroxide solution that had been diluted by a factor of 1:128 KOH:H_2O was then pippetted on the Zerodur surface and the mirror was then placed on top. The mirror was then aligned by eye to be in the approximate center. The bond was left to cure for two days. To bond the flat mirror, it was cleaned in the same manner as the curved mirror. The Zerodur spacer was flipped around and the surface to be bonded was cleaned with a cleanroom wipe wetted with methanol. The same solution and amount was used to bond the flat mirror as the curved mirror. A small amount of the hydroxide solution leaked into the center but did not spread enough such that it would be in the path of the beam as it passed through the cavity.

5.1.3.2 Super Invar cavity

There are several manufacturers of Super Invar in the United States. The specific manufacturer of the material used to create the Super Invar cavity is unknown as the material was already in possession before work on constructing the cavity began. The Super Invar bar is 178 mm x 44.5 mm x 44.5 mm. The smaller area surfaces were polished by Surface Finishes Co., Inc with a surface flatness of $\lambda/4$, 60-40 S-D finish or better, and both ends parallel to better than 0.127 mm.

To make the Super Invar cavity, a similar method was used when constructing the Zerodur cavity. The Super Invar spacer was cleaned as described in Appendix B. It was then allowed to dry overnight. The curved mirror was cleaned in the same manner as the Zerodur mirrors were. 1.70 μL of a sodium silicate solution that had been diluted by a factor of 1:4 volumetrically with DI water was used. The bond cured for two days. The flat mirror was then cleaned in the same manner and bonded using the same amount of solution using the solution from the previous bonding.

The cavity parameters for the Super Invar cavity are given in table 5-2. Although

Table 5-2. Parameters of the Super Invar cavity with hydroxide bonded mirrors.

L	R_1	R_2	FSR	linewidth	Finesse
178 mm	∞	1.0 m	843 MHz	167 kHz	5030

the measurement for the linewidth of the Super Invar cavity was done in air, measurements of the linewidth for Z_3 were done both in air and in vacuum and were within 10% of each other. Similar values should hold for the Super Invar measurements.

5.1.3.3 SiC cavity

Hexoloy SA SiC made at Saint Gobain was used to make the SiC cavity. The specific type of SiC was chosen because of its excellent mechanical strength and low CTE. SiC is a possible material for the telescope support structure on the LISA mission. For this reason, a spacer design similar to what might be expected on the LISA mission was made, though scaled down in length by a factor of approximately 3. The SiC spacer is shown

in Figure 5-5. It consists of three struts that represent the struts that would hold the secondary in place. The overall structure of the SiC spacer is that of a tube 250 mm in length and 28.6 mm in diameter with a 12.7 mm hole through the center. The struts are 6.35 mm thick and spaced 120° apart. The ends were polished at Surface Finishes Co.,

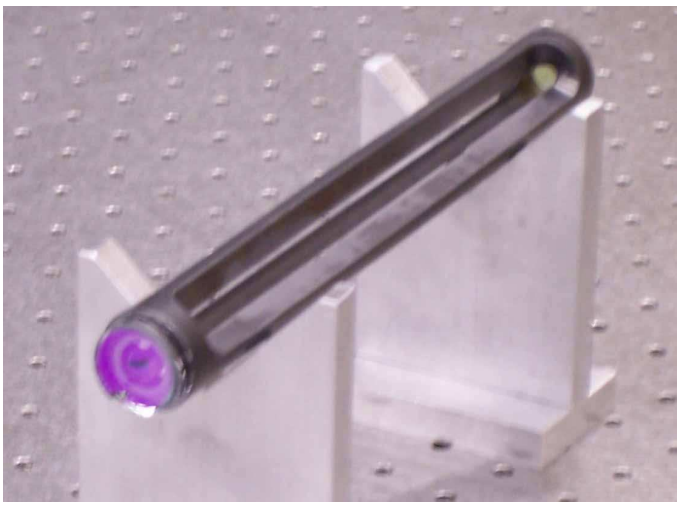

Figure 5-5. Completed SiC cavity made of Hexoloy SA.

Inc with a surface flatness of $\lambda/8$, mirror finish, and end parallelism to better than 0.05 mm. Due to the extreme hardness of SiC, polishing to these specifications can be difficult. In particular, the flatness can be hard to achieve. Although the polishing was still kept within the stated specifications, a small dips could be seen on the polished ends and made optical contacting difficult (Figure 5-6). The SiC spacer and mirrors were cleaned in the same manner as the previous two cavities. In addition to being cleaned using a sonic bath, the SiC spacer was cleaned thoroughly using cleanroom wipes wetted with methanol because of the extremely dirty nature of the struts due to the fabrication process. After this was done, the spacer was sonicated again. The polished faces of the spacer were significantly cleaner and did not need the extra cleaning using the methanol. Both mirrors were optically contacted using a combination of methods 2 and 3 as presented in Chapter 3.1. A small amount of methanol was put on the surface and the mirror was then placed on top. The mirror was then rotated in a circular fashion until the mirror stuck. The

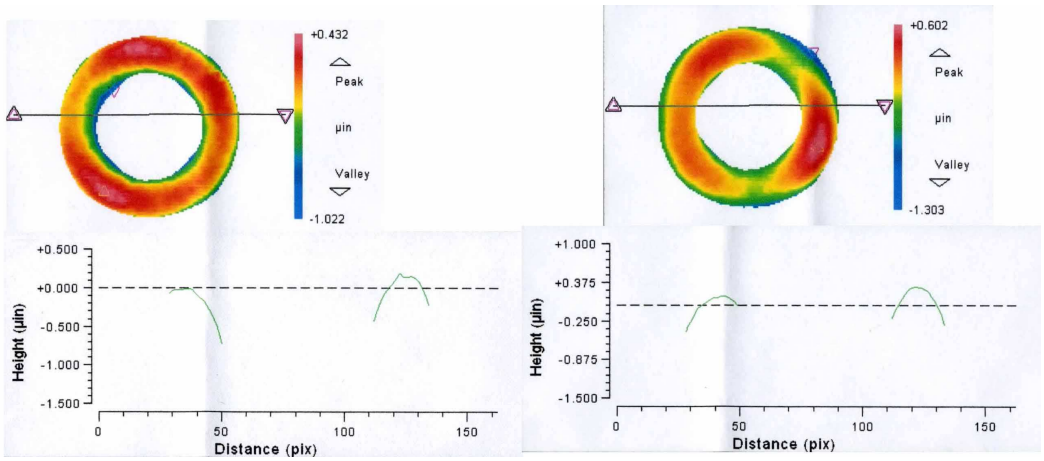

Figure 5-6. WYKO images of the polished ends of the SiC spacer. Images produced by Surface Finishes Co., Inc.

mirror was then pushed and rotated until it was close to centered on the spacer. The cavity was left for two days to allow all of the methanol to evaporate. The linewidth was then measured in air and found to be 97 kHz.

Table 5-3. Parameters of the SiC cavity with optically contacted mirrors.

L	R_1	R_2	FSR	linewidth	Finesse
250 mm	∞	1.0 m	600 MHz	97 kHz	6200

5.1.3.4 CFRP cavity

A CFRP spacer was made at the University of Birmingham in the United Kingdom by the Center for Space and Gravity Research group. This group has experience in making CFRP structures for space-based missions. They have had their CFRP parts flown on several missions including Solar-B [73]. The spacer consisted of a thin outer shell that was used to provide additional support to an inner tube whose thickness is larger than the outer shell. Struts connected the outer shell to the inner tube (see Figure 5-8). The outer shell has a diameter of ~200 mm and is a few millimeters thick. The inner tube has an outer diameter of ~45 mm and an inner diameter of ~30mm. The length of both the tube and shell are 230 mm. The struts connecting the shell and tube are a few millimeters thick and span the length of the spacer. The process flow used to create the CFRP cavity is shown in Figure 5-7.

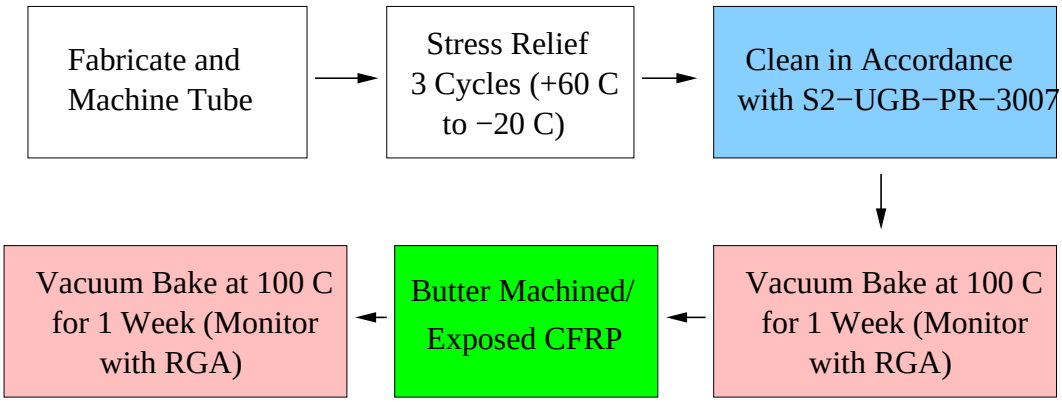

Figure 5-7. Fabrication flowchart of the CFRP spacer at the University of Birmingham.

In addition to providing the CFRP spacer, the University of Birmingham group also sent Zerodur tubes that had been polished on one face. One flat mirror and one mirror with ROC of 1 m were optically contacted to the Zerodur tubes. These Zerodur/mirror plugs were then epoxied into the center of the CFRP tube. To do this, an alignment jig was made such that the plugs could be slid in and out of the tube while still keeping the alignment. A laser was then aligned through the cavity such that the cavity had an 80% visibility. The plugs were taken out and epoxied using eccobond 285 epoxy that was mixed with catalyst 9 and a small amount of acetone to make the mixture less viscous. Eccobond 285 was recommended by colleagues at the University of Birmingham since it is the epoxy used to create the CFRP structure. The amounts of epoxy, catalyst 9, and acetone used were 100 g, 3.5 g, and 2.0 g, respectively. The contents were mixed thoroughly using a glass rod in a glass beaker for approximately 5 minutes. After about 15 minutes the paste becomes less viscous. After 30 minutes the epoxy had a consistency that could be spread onto the plugs and then inserted.

The CFRP spacer had been left in atmosphere approximately 4 months while working on the alignment jig and the alignment process. During this time, it is speculated that the CFRP spacer should have absorbed a small amount of water vapor from the surroundings. For this reason, the CFRP spacer was baked in an oven at 100 C for 7 days to get rid of any absorbed water. After this was done, the plugs were epoxied into the CFRP spacer.

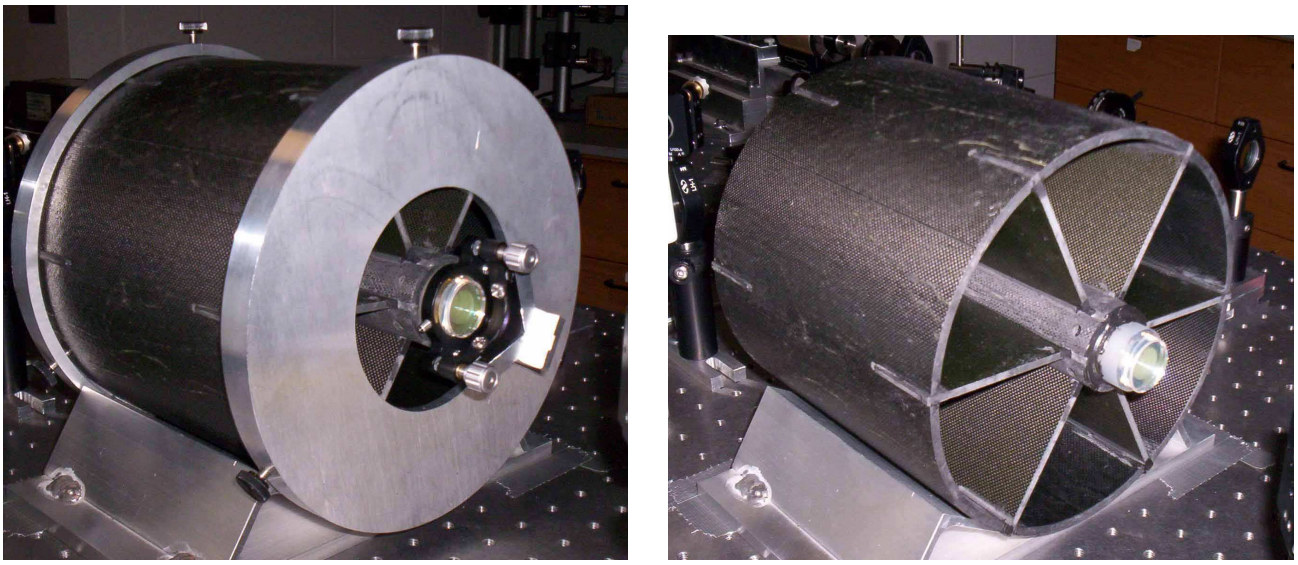

Figure 5-8. CFRP spacer, Zerodur/mirror plugs, and the alignment jig (left). Finished CFRP cavity after epoxying the plugs (right).

The curved mirror was first epoxied into place using the alignment jig and allowed to cure for 2 days. The flat mirror was then epoxied and the laser was aligned such that the cavity had a visibility close to 80%. The cavity was then left for 1 week and when the visibility was checked again, it was close to 40%. The laser was then realigned and a visibility of 80% was achieved again. The change in visibility is most likely from the epoxy settling and causing the mirrors to move slightly.

The CFRP cavity was then left in atmosphere another 3 months. It could not be moved into vacuum due to another ongoing experiment. The Finesse and linewidth of the cavity was measured to be 2900 and 224 kHz, respectively, in air. After the CFRP was moved into high vacuum and allowed to stay there for approximately 5 months, the Finesse and linewidth were measured to be 4060 and 160 kHz, respectively. The error in both measurements was ~10%. The cause of the change in linewidth and Finesse is unknown.

Table 5-4. Parameters for the CFRP cavity.

L	R_1	R_2	FSR	linewidth	Finesse
230 mm	∞	1.0 m	650 MHz	225 kHz	2900

5.1.3.5 PZT-actuated cavity

In order to suppress the 12 orders of laser frequency fluctuations necessary for gravitational wave detection on the LISA mission, a combination of pre-stabilization, arm-locking, and time-delay interferometry (TDI) will be used. Pre-stabilization consists of locking a free-running laser to an optical cavity to transfer the stability of the cavity to the laser. The next step, known as arm-locking, will stabilize the laser frequency using the LISA arms as a reference. The last step, TDI, is a post-processing technique that will simulate an equal arm interferometer.

To use arm-locking, it will become necessary for the pre-stabilized laser to be tuned to follow the changing LISA arms. This requires a continuous tuning of the pre-stabilized lasers over 20 MHz. There are several methods available for this including sideband locking and phase locked lasers [74]. Another possible method is to use a tunable cavity. By changing the length of a cavity, the resonant frequency of the cavity will change as well. This can be done by bonding a PZT actuator to a stable spacer material and applying a voltage to the PZT. To make this cavity, a PZT ring made of k-180 material from Piezo Technologies was used as the actuator. The specific PZT material was chosen due to its low CTE and high d_{33} coefficient. The PZT ring has a 41 mm O.D, 12.7 mm I.D, is 3.2 mm thick, and the wide faces are covered with a silver coating. The capacitance of the PZT is 1.3 nF and was found using a multimeter. The spacer material was chosen as Zerodur for its high stability and has a 25.4 mm O.D, 6.4 mm I.D, and is approximately 51 mm long. The Zerodur spacer was polished by Mindrum Precision to a $\lambda/10$ global surface flatness, 40/20 S-D, and $\leq$12.7 μm parallelism. The silver coated faces allow hydroxide bonding to take place between both the Zerodur spacer and the mirror (see Figure 5-9).

To construct the cavity, the Zerodur spacer was cleaned as described in Appendix B. It then dried overnight. The PZT was cleaned in the same manner as the Zerodur. A cleanroom wipe wetted with methanol was used to wipe the surface of the Zerodur to

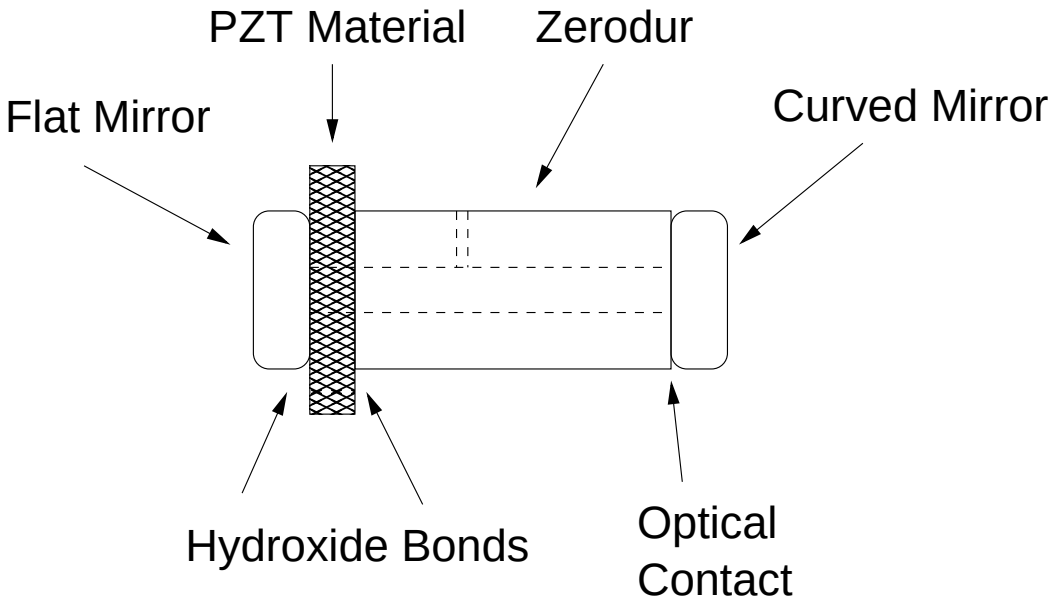

Figure 5-9. Representation of the PZT-actuated cavity. Note the lengths are not to scale.

be bonded. 1.75 μL of a sodium silicate solution (Sigma Aldrich) that had been diluted volumetrically with deionized water by a ratio of 1:4 was applied to the Zerodur tube and the PZT material was placed on top and allowed to cure overnight. The next day a flat mirror was cleaned in the same manner and bonded using 1.75 μL of the same sodium silicate solution. The bond cured for 2 days. A mirror with a ROC of 1.0 m was then cleaned and optically contacted to the Zerodur spacer using 0.75 μL of methanol. Kapton coated wires were soldered to the PZT using a silver solder.

The Finesse and linewidth were measured in air and found to be 6900 and 400 kHz, respectively.

Table 5-5. Parameters for the PZT cavity.

L	R_1	R_2	FSR	linewidth	Finesse
54 mm	∞	1.0 m	2780 MHz	400 kHz	6900

5.2 Pound-Drever-Hall Laser Frequency Stabilization

The PDH technique is both powerful and simple. The idea is that a laser's frequency noise can be measured with a Fabry-Perot cavity, and this measurement is fed back to the laser to suppress frequency fluctuations. In this manner, the stability of the cavity can

be transferred to the laser. The basis for PDH is a form of nulled lock-in detection that decouples the frequency measurement from the laser's intensity [75]. A similar technique used extensively in atomic physics is known as frequency-modulation (FM) spectroscopy and is discussed in further detail in Chapter 6. The foundations of both are similar and by understanding one, the other is often easy to understand.

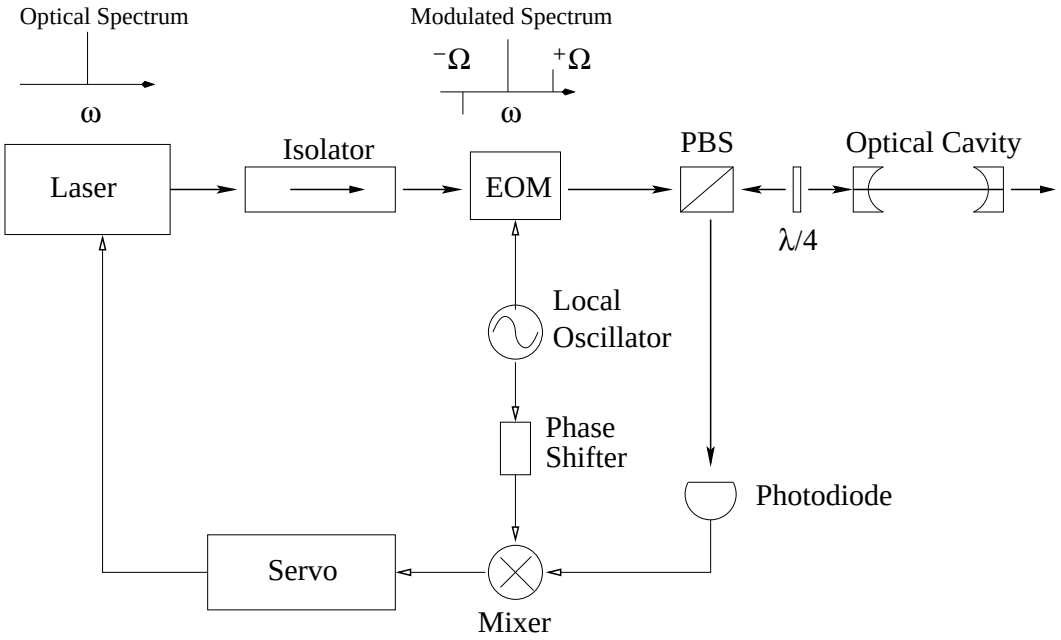

Figure 5-10. Diagram of the PDH locking technique.

5.2.1 Conceptual Model

The basic layout of a PDH stabilization system is shown in Figure 5-10. The laser beam is passed through a Faraday isolator to reduce back-reflections from coupling into the laser. The beam then passes through an electro-optic modulator (EOM) which modulates the carrier by frequency Ω to produce sidebands on both sides of the carrier. The beam then passes through a polarizing beam splitter and $\lambda/4$ waveplate. These components act as an optical diode for the reflected light from the cavity. If the sidebands of the beam are well outside the cavity resonance, then they will be reflected from the cavity input mirror with no significant phase shift. When the laser carrier matches the cavity resonance, the reflected light from the cavity at the carrier frequency will be in

phase with the incident light. The reflected carrier and sidebands produce two heterodyne beats at the frequency of phase modulation (Ω) and are detected by the photodiode. If the carrier is on resonance, then the two beats will be 180° out of phase with respect to each other. Hence, the beats will cancel each other and there will be no photodiode signal at the frequency of modulation.

When the laser is slightly off resonance, the reflected light carrier will experience a phase shift. The sign of the phase shift is determined from the deviation off resonance. For example, if the carrier frequency is higher than resonance and produces a positive phase shift, then a frequency lower than the resonance will produce a negative phase shift. In this case, the heterodyne beats will no longer cancel since they are not 180° out of phase. Figure 5-10 shows how the amplitude of the beat is extracted from the photodiode signal. The photodiode signal is mixed with the local oscillator that drives the EOM to produce an error signal. The phase shifter (typically differing lengths of coaxial cable) is used to ensure the mixer inputs have the correct phase. The mixed signal can then be fed into control electronics that produce signals that are fed back to the laser.

5.2.2 Quantitative Model

To provide a more complete understanding of how the error signal is produced for the PDH technique, a brief mathematical derivation is described. The electric field of the laser beam as is comes out of the laser can be described as $\mathrm{E}_{laser} = \mathrm{E}_0 \mathrm{e}^{i\omega t}$. After the laser has passed through the EOM which is driven at frequency Ω, the electric field then becomes $\mathrm{E}_{afterEOM} = \mathrm{E}_0 \mathrm{e}^{i(\omega t + msin(\Omega t))}$, where m is the modulation depth or modulation index of the EOM. Expanding $\mathrm{E}_{afterEOM}$ in terms of Bessel functions results in

$$\begin{aligned} E_{afterEOM} &\simeq e^{i\omega t}(J_0(m) + 2iJ_1(m)\sin(\Omega t)) \\ &= E_0(J_0(m)e^{i\omega t} + J_1(m)e^{i(\omega+\Omega)t} - J_1(m)e^{i(\omega-\Omega)t}). \end{aligned} \tag{5–16}$$

From Eq. 5–16 it becomes apparent that the EOM adds two sidebands in frequency space, each one located $\Omega/2\pi$ Hz away from the carrier frequency as shown in Figure 5-10. The

powers in the carrier and first-order sidebands then become

$$P_c = J_0^2(m)P_0$$
$$P_s = J_1^2(m)P_0,$$

where $P_0 = |E_0|^2$ is the total power in the beam before the EOM. When the modulation depth is small, almost all of the power is in the carrier and first-order sidebands.

After the laser has passed through the EOM, it passes through the polarizing beam splitter and $\lambda/4$ waveplate. The beam is then incident on the cavity and either reflected or transmitted through the cavity. The reflected beam passes through the $\lambda/4$ waveplate and beamsplitter again and is reflected onto the photodiode. Since the reflected beam is used for actuating the laser, the reflected field will be considered, and the transmitted signal will be ignored. Using the transfer function in reflection as defined by Eq. 5–3, where $\omega = 2\pi f$, the reflected electric field is

$$E_{ref} = E_0(T_r(\omega)J_0(m)e^{i\omega t} + T_r(\omega+\Omega)J_1(m)e^{i(\omega+\Omega)t} - T_r(\omega-\Omega)J_1(m)e^{i(\omega-\Omega)t}). \quad (5\text{–}17)$$

Since power is measured by a photodiode and not the electric field, $P_{ref} = |E_{ref}|^2$ is the signal of interest. After some algebra, this can be expressed as

$$\begin{aligned} P_{ref} &= P_c \mid T_r(\omega) \mid^2 + P_s \left(\mid T_r(\omega+\Omega) \mid^2 + \mid T_r(\omega-\Omega) \mid^2 \right) \\ &\quad + 2\sqrt{P_c P_s}(\mathrm{Re}[T_r(\omega)T_r^*(\omega+\Omega) - T_r^*(\omega)T_r(\omega-\Omega)]\cos(\Omega t) \\ &\quad + Im[T_r(\omega)T_r^*(\omega+\Omega) - T_r^*(\omega)T_r(\omega-\Omega)]\sin(\Omega t)) + (2\Omega\text{terms}). \end{aligned} \quad (5\text{–}18)$$

Eq. 5–18 represents three waves of different frequencies being mixed together. The 2Ω terms represent the interference produced from mixing the two sidebands with each other. There may also be some contribution from higher order terms that were neglected when Eq. 5–16 was expanded in terms of Bessel functions. These may make a significant contribution to the 2Ω terms, but are not considered here [75]. When using a photodiode to measure Eq. 5–18, all terms will show up. Near resonance, the first two terms in Eq.

5–18 are negligible since most of the power in the carrier will be transmitted through the cavity, and the power in the sidebands is typically small. This leaves only the sine and cosine terms.

Mixing the photodiode signal with the driving signal from the EOM isolates the sine term. Thus, the error signal becomes

$$\epsilon = 2\sqrt{P_c P_s}\mathrm{Im}[T_r(\omega)T_r^*(\omega+\Omega) - T_r^*(\omega)T_r(\omega-\Omega)].$$

Since the laser frequency must be near a cavity resonance in order to lock, we are only interested in the error signal near this frequency. In this case, the transfer function of the reflected field for the sidebands will be nearly one. This results in an error signal near resonance of the form

$$\epsilon_{res} = 2\sqrt{P_c P_s}\mathrm{Im}[T_r^*(\omega) - T_r(\omega)] = -4\sqrt{P_c P_s}\mathrm{Im}[T_r(\omega)].$$

Linearizing $\mathrm{T}_r(\omega)$ for small ω and to first order yields

$$T_r(\delta\omega) = \frac{r_1 - r_2}{1 - r_1 r_2} + \frac{2ir_2(r_1^2 - 1)}{(1 - r_1 r_2)^2}\frac{\delta\omega L}{c}.$$

Substituting, and letting $\mathrm{r}_1 = \mathrm{r}_2 = \mathrm{r}$ (since all mirrors used have the same coatings), the error signal now becomes

$$\epsilon_{res} = -4\sqrt{P_c P_s}\left(\frac{2r(r^2-1)}{(1-r^2)^2}\frac{\delta\omega L}{c}\right) = 8\sqrt{P_c P_s}\frac{r}{T}\frac{\delta\omega L}{c}.$$

Making use of the fact that

$$\mathcal{F} \approx \frac{\pi r}{T} = \frac{c/2L}{\Delta f},$$

where Δf is the linewidth of the cavity, and using ω=2πf, the error signal close to resonance becomes

$$\epsilon_{res} = 8\sqrt{P_c P_s}\frac{\delta f}{\Delta f}. \tag{5–19}$$

From this, it is easy to see that the error signal is linear around resonance. Figure 5-11 shows two error signals for the same cavity length and EOM modulation frequencies,

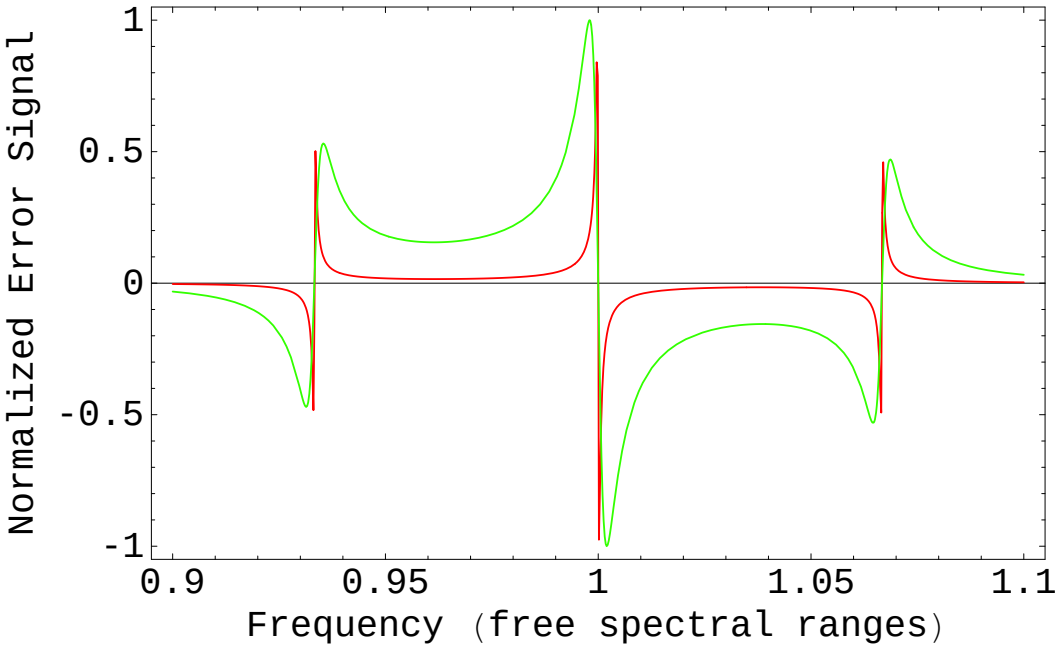

Figure 5-11. Two error signals produced from cavities of different finesse. The green curve is for a cavity of length 200 mm and finesse 500. The red curve is for a cavity of the same length but finesse of 5000. Both have EOM modulation frequencies of 50 MHz.

but different Finesse. Three error signals can be seen. The center error signal is produced from the carrier interfering with the sidebands while the signals on either side corresponds to the error signals produced from the sidebands. Figure 5-12 shows a closer view of the carrier beatnote from Figure 5-11. The narrower curve corresponds to the cavity with a higher Finesse as is expected from Eq. 5–19.

5.3 Relative Stability Measurements

The PDH frequency locking scheme is a powerful tool that can be used for a variety of applications. Of importance to many space-based interferometric mission will be the dimensional stability of select materials for their implementation in critical optical components. This section presents how the relative dimensional stability of select materials was found in addition to providing results for these materials.

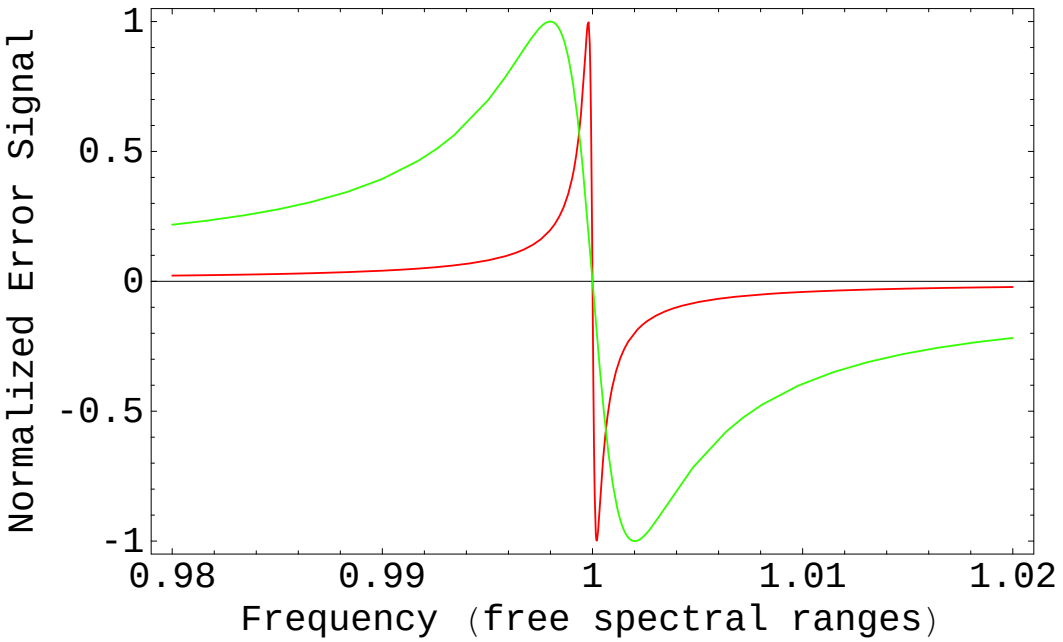

Figure 5-12. Error signals for only the carrier frequency from Figure 5-11. The green curve is for a cavity with a lower finesse.

5.3.1 Electro-Optical Setup

To test the relative dimensional stability between certain materials, the PDH locking scheme is used to lock the frequency of one laser to one of the cavities described above. The experimental setup consists of two vacuum tanks which house the cavities (as shown in Figure 5-13). Tank 1 uses five cylindrical layers of gold-coated stainless steel shells which are separated by Macor spacers to provide passive thermal isolation for two cavities that are placed in the middle. Tank 2 uses five layers of aluminized PET (basically a thick Mylar) separated by Macor spacers to provide passive thermal isolation to one cavity that is placed in the center of the thermal shields (see Appendix A for a complete analysis of the aluminized PET thermal shields). In this manner, the dimensional stability can be tested under common and uncommon thermal conditions.

Laser 1 is locked to Cavity 1 and Laser 2 is locked to Cavity 2 using the PDH stabilization method. Pick-offs from each laser are then superimposed on each other to produce a beatnote. The beatnote is sent into a photodiode where the frequency is read by

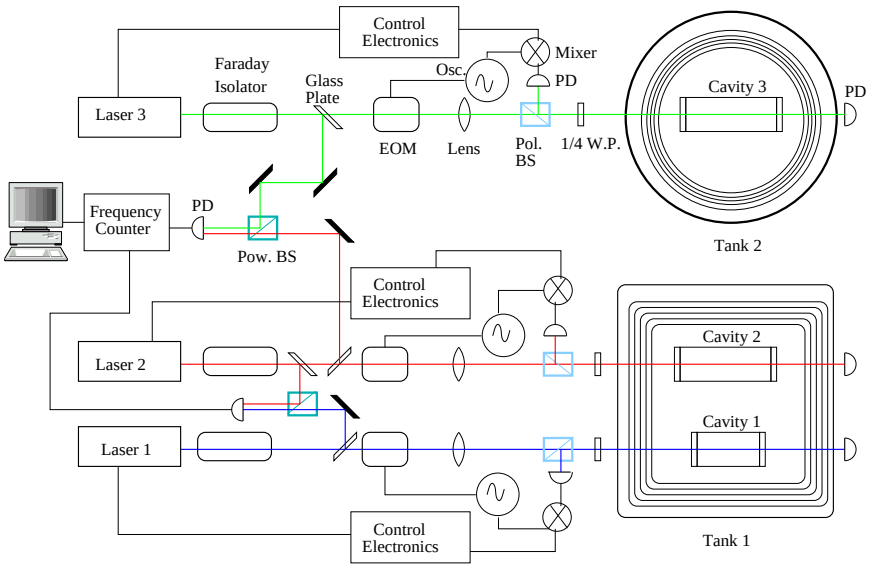

Figure 5-13. Electro-optical setup used to test the dimensional stability of select materials.

a frequency counter. Using the relationship

$$\frac{\delta\nu}{\nu} = \frac{\delta l}{l}$$

where $\delta\nu$ is the linear spectral density of the measured beatnote, ν is the laser frequency, δl is the linear spectral density of the length of the cavity, and l is the length of the cavity, the relative noise spectrum of the cavity can be found.

Laser 3 is locked to Cavity 3 in Tank 2 using the PDH method. A pick-off from this laser is superimposed on the pick-off from Laser 2 to determine the relative stability between Cavity 2 and Cavity 3.

5.3.2 Zerodur-Zerodur

As previously stated, Zerodur is an ultra-stable material with a low CTE around room temperature. This makes it an ideal material for use in laser frequency stabilization since the stability of the cavity is transferred to the laser by using the PDH locking technique. Narrow linewidth lasers are critically important for space-based interferometric missions since the frequency noise of the laser will couple into the measurement sensitivity. The more stable the frequency of a laser, the more sensitive a measurement can be made.

For this reason the frequency stability of Zerodur with optically contacted and hydroxide bonded mirrors was studied.

5.3.2.1 Optically contacted mirrors

To test the relative frequency stability of two Zerodur cavities with optically contacted mirrors, the cavities described above were both placed in Tank 1 and Laser 1 and Laser 2 were locked to Cavity 1 and Cavity 2, respectively, using the PDH locking technique as depicted in Figure 5-13. The beatnote between the lasers was continuously monitored for 28 days using a frequency counter sampled every 20 seconds. The resultant beatnote is shown in Figure 5-14. In addition to this measurement,

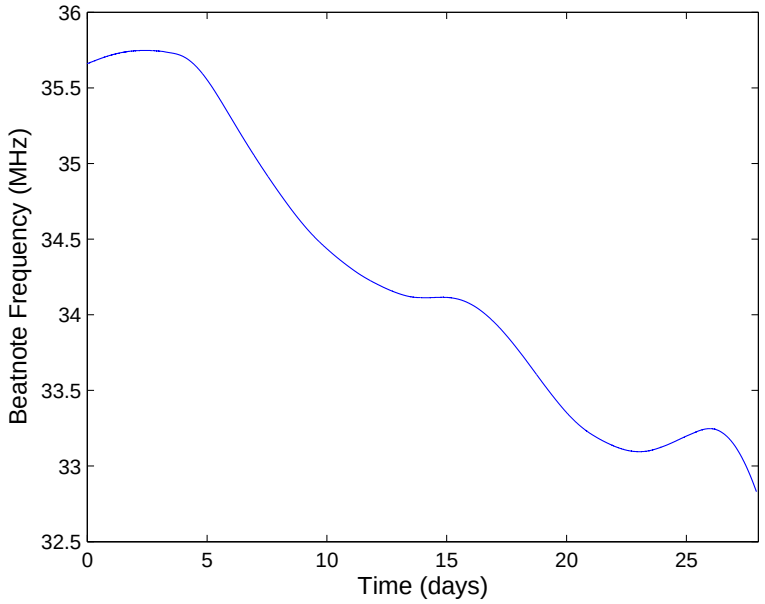

Figure 5-14. Time series of the beatnote taken over 28 days.

frequency measurements were taken using a phase-meter sampling at 98 kHz and 15 Hz. To determine the frequency stability, the frequency time series is broken into smaller pieces. These pieces have a linear regression fit to the data sets that is subtracted. A fourier transform is done on the residuals and the resultant linear spectral density (LSD) in frequency-space is given. For a discussion on the process that was used, see Appendix C. The resultant LSD for the frequency counter and phase meter measurements is shown

in Figure 5-15. Although measurements less than 10 Hz/$\sqrt{\text{Hz}}$ at 1 Hz have been reported for this experimental setup [72], typical results are between 20-100 Hz/$\sqrt{\text{Hz}}$. For the

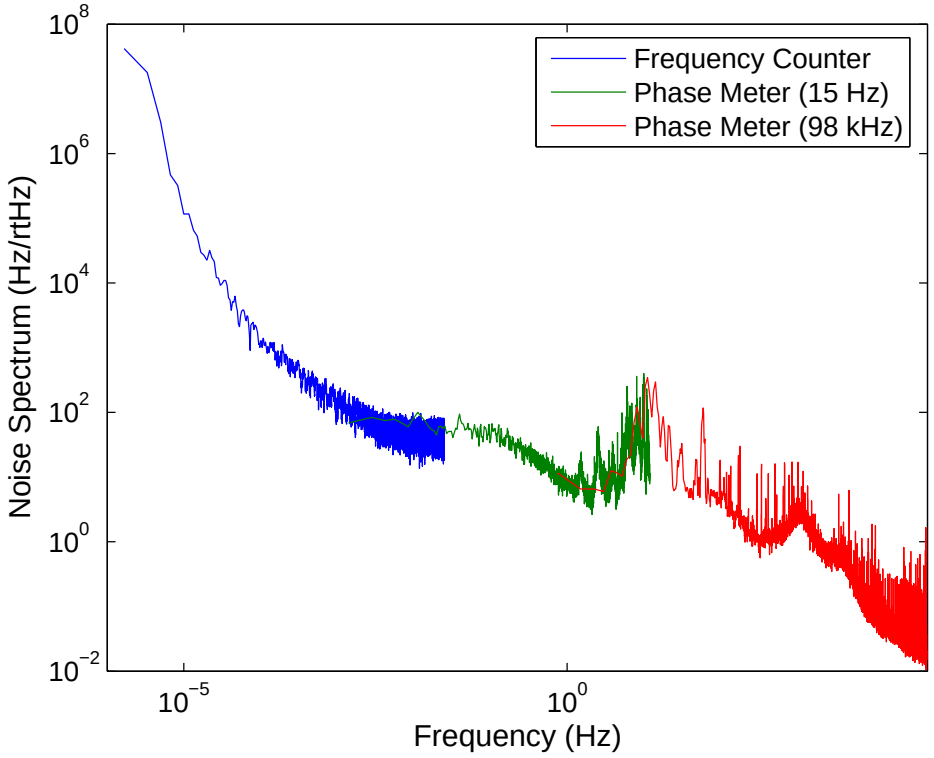

Figure 5-15. Noise spectrum of the Zerodur cavities with optically contacted mirrors. Measurements were taken using the frequency counter, phase meter sampling at 15 Hz and 98 kHz.

LISA mission, the prestabilization step could be done by locking the Nd:YAG lasers to cavities made of Zerodur. The required stability for this step is [76]

$$\nu(f) = \frac{282Hz}{\sqrt{Hz}}\sqrt{1+(3mHz/f)^4}. \tag{5–20}$$

The relative stability of the Zerodur cavities is shown in Figure 5-16 along with the LISA pre-stabilization requirement. The results in Figure 5-16 were taken from a data run that lasted for 7 days and was sampled at 1 Hz. From Figure 5-16, it can be seen that the Zerodur cavities easily meet the LISA pre-stabilization requirement in the entire frequency band.

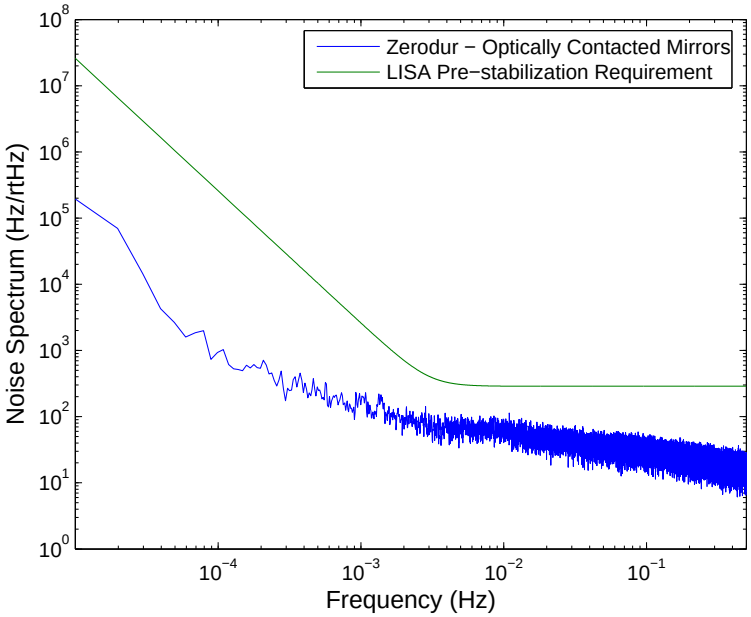

Figure 5-16. Noise spectrum of the Zerodur cavities with optically contacted mirrors and the LISA pre-stabilization requirement. The results are from a time series taken over seven days and sampled at 1 Hz.

There are several noise sources within the LISA band that may be affecting the achieved sensitivity. Among them are the temperature fluctuations of the cavity due to changes in the lab temperature, the RFAM due to the EOM, and the heating of the mirrors due to the laser power stored within the cavity. Noise from the feedback controllers is also a potential source, although measurements of these noise sources are typically an order of magnitude or more below the measured noise. An additional noise source due to acceleration from the optical table is also significant, although it is found outside the LISA band and is typically averaged out by the frequency counter when sampled at a low enough frequency. The peak between approximately 8-60 Hz shown in Figure 5-15 is most likely due to this acceleration noise [77].

Models have shown that frequency noise below $\sim$1 mHz tend to be dominated by temperature changes in the lab propagating through the thermal shields into the cavity which cause an expansion and contraction of the cavity. The five layers of gold-coated stainless steel thermal shields provide an excellent low pass filter for temperature

fluctuations, but at low enough frequency, the thermal shields will not provide any suppression. To test this, the temperature of the outside of Tank 1 was simultaneously monitored while the 28 day beatnote was taken as shown in Figure 5-17. The temperature was monitored using an OM-PLTT temperature logger from Omega Engineering, Inc. and provides a temperature resolution of 0.10 F using a thermocouple probe. From the figure, it is clear that as the temperature of the tank increased, a notable decrease in the beatnote could be observed. The ∼3.5 MHz beatnote change over the 28 days is almost the largest change in beatnote frequency observed. The beatnote between the two Zerodur cavities has changed by less than 5 MHz over 3 years. This is most likely due to seasonal temperature changes in the lab and electronic offset effects in the feedback controls.

The large temperature swing over a relatively short time (typically these temperature changes occur over six months, not one) means the temperature of the lab was not in a steady state. Although it is obvious from Figure 5-17 there is a temperature dependance on the beatnote, by high pass filtering the data a more steady state transient can be seen. Both the beatnote and temperature data were high pass filtered using a 2-pole Butterworth filter whose 3 dB frequency was set at 5×10^{-6} Hz. The resulting high pass filtered (HPF) data is shown in Figure 5-17. Again, it is clear there is a definitive correlation between the changing temperature of the tank and the change in beatnote frequency. Although the cavities are in the same thermal environment, this shows there is some non-common temperature effects due to the changing temperature in the lab. This may be due to the different lengths and orientation of the cavities.

5.3.2.2 Hydroxide bonded mirrors

The hydroxide bonding technique has shown to be a versatile way to joint a variety of materials with significant strength. Although there are many bonding techniques that produce similar, or even greater, bonding strengths, they most likely do not provide the precision alignment needed for critical optical components such as optical benches. This, determining the amount of noise the bonds produce will be critical as interferometric

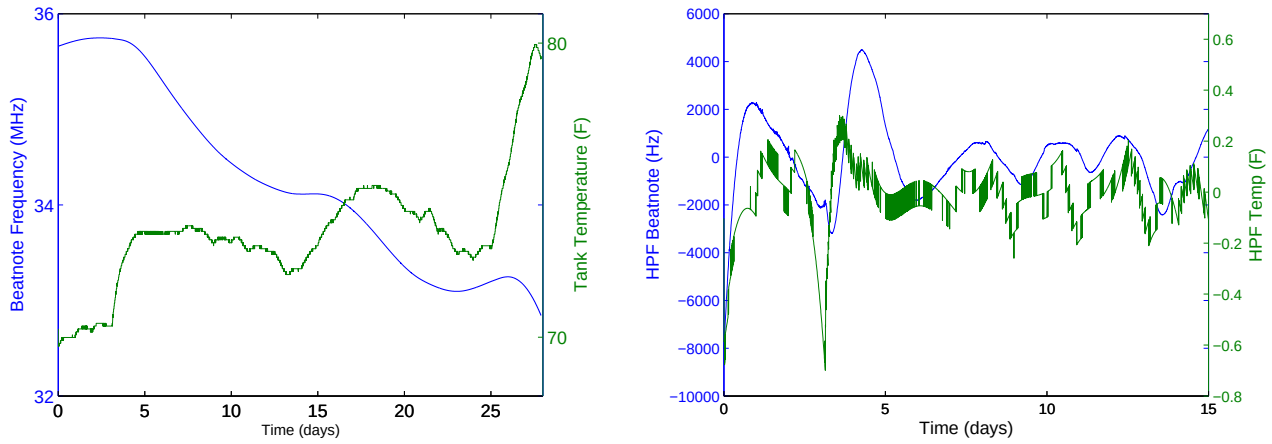

Figure 5-17. Plots of the Zerodur beatnote and tank temperature (left) and plots of the beatnote and temperature data after being high pass filtered (right).

missions keep pushing measurement limits. The frequency stability of the hydroxide bonding technique was tested by hydroxide bonding mirrors to a Zerodur spacer as described in Sect. 5.1.3.1. This cavity replaced Z_2. The resultant noise spectrum is shown in figure 5-18 [78].

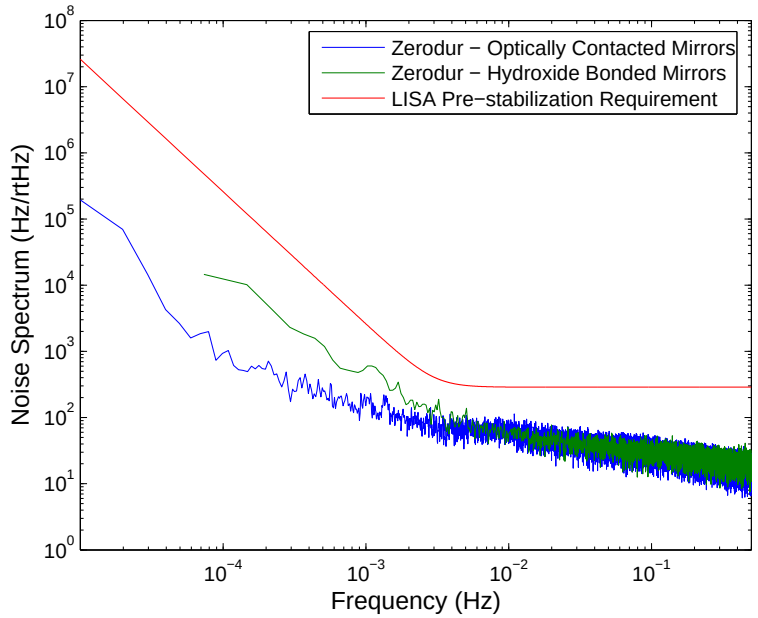

Figure 5-18. Comparison of the noise spectrums of the Zerodur cavities with optically contacted and hydroxide bonded mirrors.

The noise spectrum shown in Figure 5-18 compares the noise spectrum from the cavities with optically contacted mirrors and that when one of the cavities has hydroxide bonded mirrors. Above approximately 3 mHz, the noise spectrum is the same. Below this frequency the noise spectrum is slightly higher. This may be due to different temperature fluctuations within the lab when the measurements were taken, or it could be noise attributed to the hydroxide bonds. Unfortunately, these noise sources were not studied at the time the measurements had been taken. Despite this, it appears that the hydroxide bonding process adds little or no additional noise and, more importantly, the noise spectrum is still below the LISA pre-stabilization requirement.

5.3.3 Zerodur-SiC

SiC has become an ever increasingly popular material for use in space-based interferometric missions due to its high strength, low CTE, non-magnetic nature, and its ability to be made in complex shapes [62]. In addition, using the hydroxide bonding technique on SiC open up new possibilities for its use ranging from telescope support structures to optical benches. To test the stability of Hexoloy SA, a cavity was constructed as described in Sect. 5.1.3.3 and locked to Laser 1 in Tank 1. A time series of the beatnote between Laser 1 and Laser 2 taken over a long weekend is shown in Figure 5-19 (left). The temperature stability in the lab is typically much better over weekends, so there is a lack of an oscillatory nature in the beatnote as is commonly seen. For longer time periods, or when the beatnote is taken during the week, the beatnote would oscillate with an amplitude between 80 and 120 MHz over several days as shown in Figure 5-19 (right).

The resultant noise spectrum for the beatnote shown on the left side of Figure 5-19 is shown in Figure 5-20 and meets both the LISA telescope and pre-stabilization requirements. The spike in noise around 0.20 Hz is most likely from having too much gain in the temperature feedback controller to the laser and is not present in other measurements. The noise above ∼0.01 Hz is similar to that of the Zerodur cavities [79].

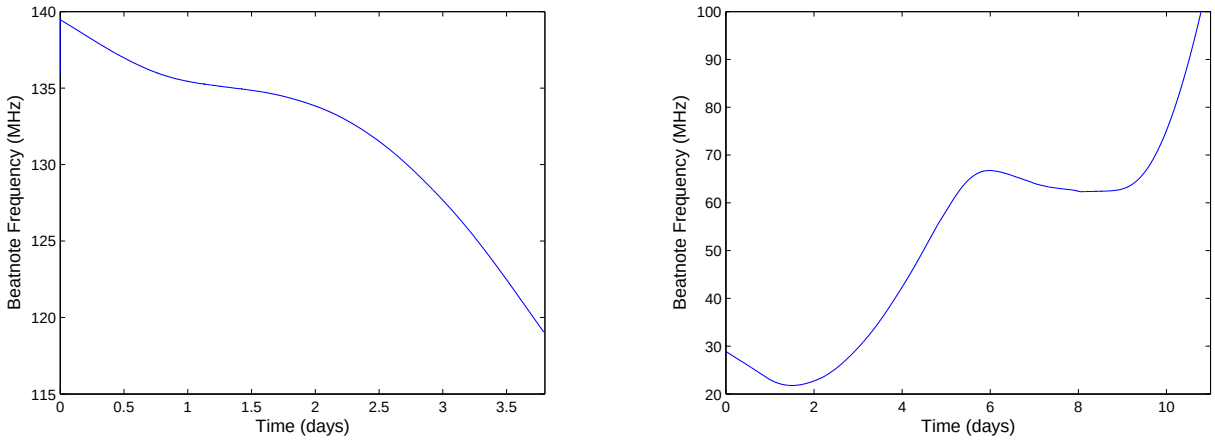

Figure 5-19. Plots of the SiC beatnote taken over a long weekend (left) and plots of the beatnote taken over 11 days(right).

This suggests a limitation of the measurement system is being reached. Although the mirrors were optically contacted to the SiC spacer, it is assumed that hydroxide bonding the mirrors should not produce any additional noise that would be detectable.

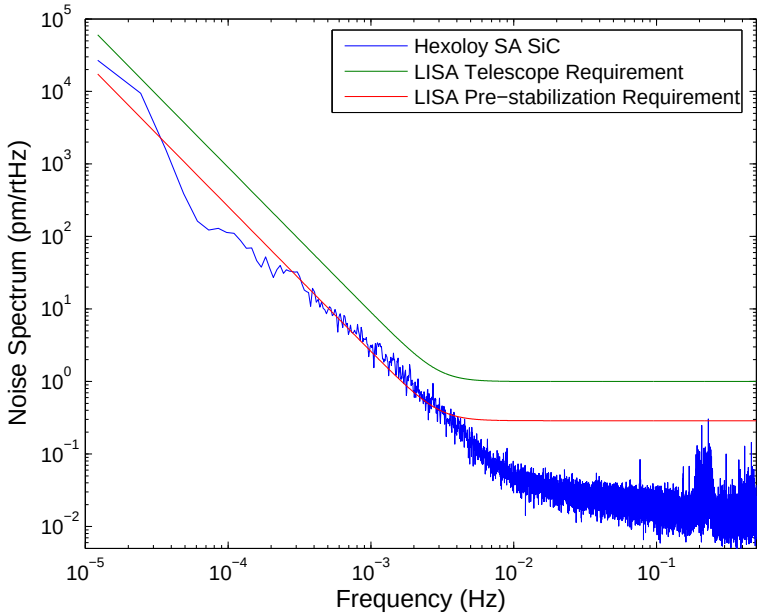

Figure 5-20. Noise spectrum of the Hexoloy SA SiC cavity with optically contacted mirrors along with the LISA pre-stabilization and telescope requirements.

The CTE of the SiC is around two orders of magnitude larger than of Zerodur. Because of this, the beatnote measurement between SiC and Zerodur will be much more sensitive to temperature fluctuations than the Zerodur−Zerodur measurements. If the limiting noise source is assumed to be from temperature fluctuations in the lab that propagate into length changes in the SiC cavity, then the temperature stability of Tank 1 can be found. The inferred temperature stability is shown in Figure 5-21. At 1 mHz, the temperature stability is $\sim 3\ \mu\mathrm{K}/\sqrt{\mathrm{Hz}}$ which is close to what is expected on the LISA mission.

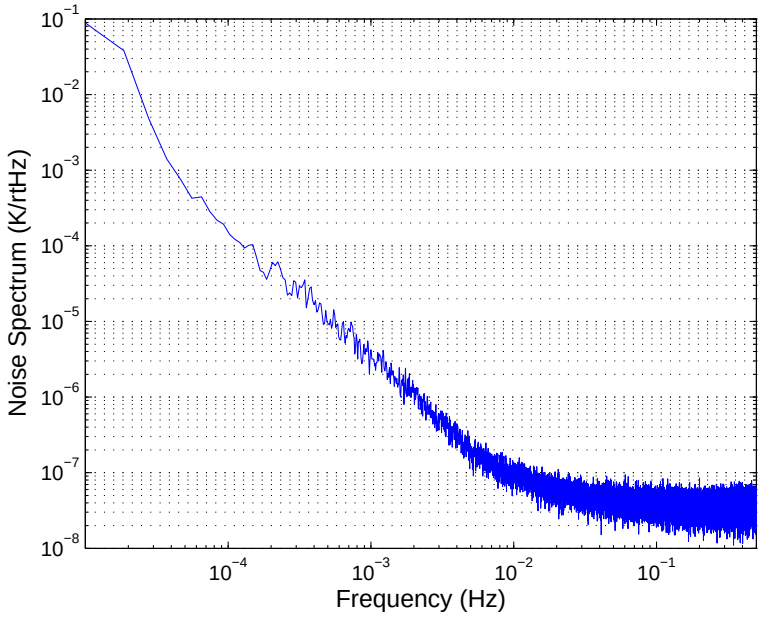

Figure 5-21. Inferred temperature stability at the center of Tank 1.

The surprising result is that the SiC cavity performed so well at high frequencies and had noise levels the same as the Zerodur cavities. Temperature stabilization of the cavity could bring down the low frequency noise, while using less input power would lower the noise in the 10^{-3} to 10^{-2} frequency band (as will be discussed in the CFRP cavity section). Thus, it would appear that SiC would be a viable candidate for the LISA telescope support structure.

5.3.4 Zerodur-Super Invar

Super Invar is a high stability, machinable metal that has been used on previous space missions [65]. Its high strength, low CTE, and ease of machining make it ideal for support structures such as the narrow angle camera on the Cassini spacecraft. Although the dimensional stability of Super Invar has been measured, it has not been measured at the fm/$\sqrt{\text{Hz}}$ level. In addition, this test will provide additional information about the stability of the hydroxide bonding technique when a sodium silicate solution is used.

To test the dimensional stability of Super Invar, a cavity was constructed as described in Sect. 5.1.3.2 and placed in Tank 2. Laser 3 was locked to the cavity and the beatnote between Laser 2 and Laser 3 was monitored. A 28 day measurement was made at the same time the Zerodur measurement in Sect. 5.3.2.1 was made. The temperature of the tank was measured at the same time using another OM-PLTT temperature logger. The resultant beatnote and corresponding tank temperatures are shown in Figure 5-22 (left). The corresponding dimensional stability is shown in Figure 5-23. Not only does the Super Invar meet the LISA telescope requirements, but it meets the pre-stabilization requirement as well, and is similar to what was found with the SiC cavity. Above ∼10 mHz, the noise level is almost identical to that obtained from the Zerodur cavities. This would also imply that an experimental noise floor for our system is being met.

The resulting noise spectrum at high frequencies of the Zerodur-Super Invar measurement again shows that there is no detectable addition of noise from using the hydroxide bonding technique. Two separate solutions which produced two different bond thicknesses both showed no additional noise.

From Figure 5-22, it is apparent that as the temperature of the tank changes, so does the beatnote frequency. To further test this, both the beatnote and temperature data sets were high pass filtered as described in Sect. 5.3.2.1 to look at a more steady state of the data. The results are shown in Figure 5-22 (right). It is evident the beatnote is influenced

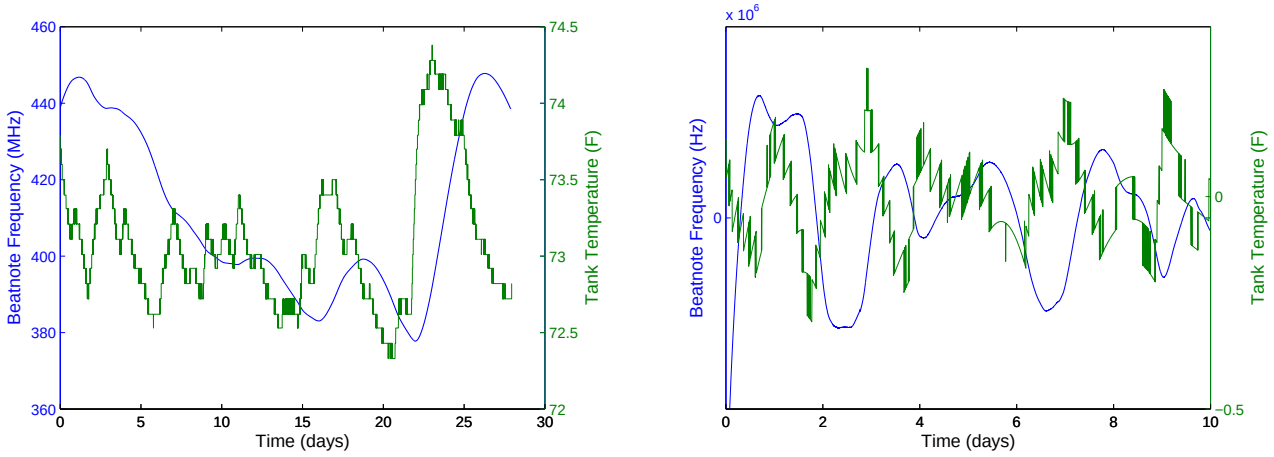

Figure 5-22. Plots of the Super Invar beatnote and tank temperature (left) and plots of the beatnote and temperature data after being high pass filtered (right).

by the tank temperature and the beatnote change lags the tank temperature change by approximately one day.

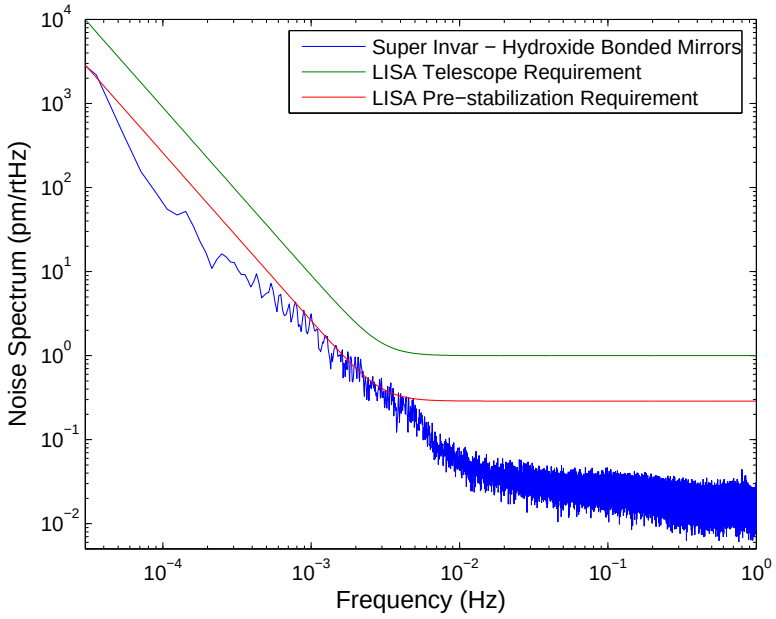

Figure 5-23. Noise spectrum of the Super Invar cavity with hydroxide bonded mirrors along with the LISA telescope and pre-stabilization requirement.

Knowing the temperature stability inside Tank 2 will be critical in order to determine temperature effects on the material. The gold-coated stainless steel thermal shields in

Tank 1 provide excellent suppression of temperature fluctuations due to the low emissivity and high mass. A cost-effective alternative to these thermal shields was designed and built using an aluminized PET material that is separated by Macor spacer (see Appendix A for a full description). If it is assumed that the limiting noise source at low frequencies is from temperature fluctuations in the lab that couple into length changes of the cavity, then an upper limit on the temperature stability of Tank 2 can be found. Although this assumption will be valid at lower frequencies, at higher frequencies only an upper bound can be determined since it is assumed the temperature effects are significantly lower than other noise sources such as electronic or acceleration noise. The estimated temperature stability of the inside of Tank 2 is shown in Figure 5-24.

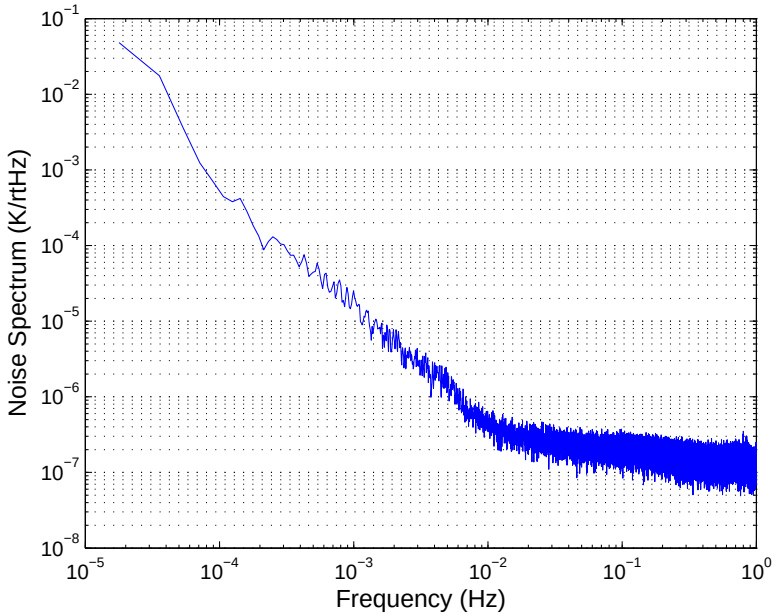

Figure 5-24. Inferred temperature stability inside Tank 2.

It should be noted that to make this calculation, the CTE of the Super Invar cavity needs to be known. Unfortunately the CTE of the Super Invar is not known since it was bought by a previous group member and records of where it was purchased can not be found. After searching several sources, a range of CTE values was found. Although the

stated values for the CTE of Super Invar can vary from 0.2×10^{-6}/K to 2.0×10^{-6}/K, a typical value of 0.7×10^{-6}/K is used.

An estimation of the CTE of the Super Invar cavity can be done using the outside tank temperature and the beatnote time series. To estimate the CTE of the Super Invar cavity, measurements of both the tank temperature and beatnote were simultaneously taken for spans of several days. Since the thermal shields will have little attenuation of the temperature changes in the tank at low frequencies, if the tank temperature is constantly changing in the same direction over a long period of time, then the beatnote will be continuously changing in a similar manner. By cutting off the first and last 1-2 days of data, and looking at the change in beatnote compared to the change in tank temperature, the CTE of the Super Invar can be found. Once the change in beatnote frequency per degree is found, the CTE can be found via

$$CTE_{ppm} = \frac{\Delta\nu}{\Delta T}\frac{\lambda}{FSR}\frac{1}{2L}, \tag{5–21}$$

where $\Delta\nu$ is the change in beatnote frequency, ΔT is the corresponding change in tank temperature, λ is the wavelength of the laser, FSR is the free spectral range of the cavity, and L is the length of the cavity. Doing this, the CTE of the Super Invar is found to be approximately 0.2-0.3 ppm, which is within the CTE values previously stated. This is, in fact, a lower bound on the CTE, since it is expected that there is some attenuation at frequencies of 10^{-5} Hz as shown in Figure A-4 and would produce a larger CTE value. For this reason, a CTE value of 0.7×10^{-6}/K is an appropriate approximation to the CTE of the Super Invar cavity.

For the inferred temperature stability inside Tank 2, a CTE of 0.7×10^{-6}/K was assumed. Comparing the thermal stability of Tank 1 and Tank 2, Tank 2 appears to have approximately an order of magnitude worse temperature noise at low frequencies. Although the temperature stability of Tank 2 is worse than that of Tank 1, the difference

in cost is substantial, and making a few changes to the thermal shield design could result in a significantly better temperature stability while still keeping the cost low.

5.3.5 Zerodur-PZT Cavity

Several methods can be used to tune the frequency of a pre-stabilized laser by tens or hundreds of megaHertz. These include using an acousto-optic modulator, offset sideband locking, and offset phase-locking, among others. Probably the most straightforward method is to integrate a PZT into the cavity. By applying a voltage to the PZT, the length of the cavity will change, hence changing the resonant frequency of the cavity. This has a particular interest for use in the AURIGA and LISA gravitational wave detectors. In the case of AURIGA, a PZT cavity has been tested and shown promising results, despite its more complicated design than the PZT cavity presented above [80]. For LISA, a PZT cavity could be implemented for use in arm-locking. To utilize arm-locking, it will become necessary for the pre-stabilized laser to be tuned to follow the changing distances of the LISA arms. This requires a continuous tuning of the pre-stabilized lasers over 20 MHz. Due to the length stability necessary for LISA, the PZT cavity must be extremely stable as well.

To test the stability of the PZT-actuated cavity, it was placed in Tank 2 and Laser 3 was locked to it. The stability of the two Zerodur cavities with optically contacted mirrors were put in Tank 1 and the relative stability between the two were measured while the PZT cavity measurements were taken. The stability of the two Zerodur cavities were found to be similar to what was measured above and typically showed a noise spectrum of 20 to 50 Hz/$\sqrt{\text{Hz}}$ at 1 Hz.

To determine the tuning coefficient of the PZT, the PZT cavity was locked and an 8 V peak-to-peak triangle wave at 0.10 Hz was applied to the PZT. The measured tuning coefficient was found to be $\sim$1.5 MHz/V [81]. The current estimates for the necessary tuning frequency for arm-locking is 20 MHz and is based on the variations in the LISA arms. Due to the drifts of the cavity itself, which are on the order of Hz/s, a

tuning capability of 100 MHz would provide enough margin to ensure that the locking stretches are not interrupted by a saturated high voltage amplifier. The required voltage for this tuning would only be 70 V. It is also important to note that LISA will not take data continuously and that the science runs will be interrupted for short periods due to maintenance such as rotations of the high gain antennas.

Commercially available amplifiers rarely specify their performance in the LISA band. For this reason, a low cost (less than $100), low noise alternative to a commercially produced amplifier was built. The design shown in Figure 5-25 is almost identical to the design in reference [82], except for a 60 mHz low-pass filter that is placed on the output of the amplifier, and the 1000 V source is provided by a commercial high-voltage DC source. The input voltage is provided by a 12 V voltage reference and voltage divider in which one of the resistors is a potentiometer. The input voltage can be tuned through the potentiometer.

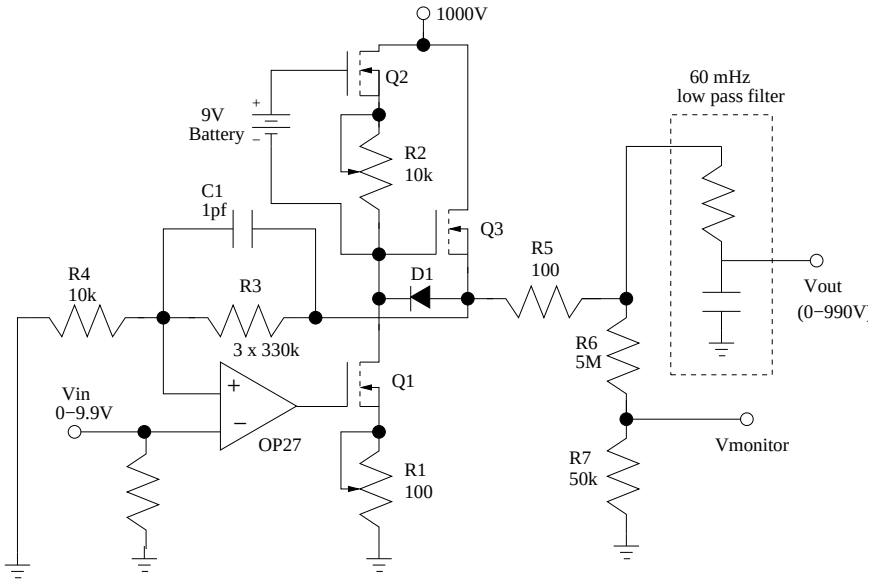

Figure 5-25. Voltage amplifier used to provide the applied voltage to the PZT on the PZT cavity.

When the amplifier needs to charge the piezo, the charge rate is fixed at the value of the current source, which is determined by Q2 and R2. Since the Q2-R2 value also determines the quiescent current of the amplifier, the quiescent current must be low

(around 1 mA) in order to not overheat the device when it is working at 1 kV. For a 10 nF piezo, the slew rate is 0.1 V/μs for a 1 mA quiescent current. The up and down slew rates can be trimmed using R2 and R1, respectively.

When the amplifier needs to discharge the piezo, the output of the op amp goes up and Q1 acts as a sink whose current is limited by the set value of R1. The diode provides a path for the discharge current through Q1.

The gain is set at 100 through the R3 and R4 resistors. Both R3 and C1 must support a 1 kV drop and are rated such that the operating voltage and wattage can support this. R5 is used to isolate the capacitive load in addition to improving the stability. Resistors R6 and R7 act as a voltage divider to monitor the output voltage.

The beatnote between Laser 2 and Laser 3 was measured using a phasemeter sampling at 98 kHz and 15 Hz, as well as using a frequency counter when no voltage was applied to the PZT. The noise spectrum is shown in Figure 5-26. The two peaks in the 10 Hz regime are most likely due to the seismic noise and the different damping mechanisms of the two vacuum tanks. The peak around 20 kHz is most likely from the resonant frequency of the PZT [83]. The beatnote frequency was also measured using a frequency counter for several days. The resultant noise spectrums for 0 V and 200 V applied to the PZT are shown in Figure 5-27. A typical noise spectrum for applied voltages up to 200 V shows that the PZT cavity meets or exceeds the LISA pre-stabilization requirement in all but a small frequency band. For applied voltages ranging from 0-100 V, the noise spectrums showed similar levels. For applied voltages between approximately 100-200 V, the noise increased slightly. Above 200 V, the noise increased as the applied voltage increased. The visibility of the cavity and peak-to-trough voltage of the error signal were found to be similar up to 300 V. A decrease of less than 10% was found for an applied voltage of 450 V. This might be due to the shearing effects of the PZT.

A typical beatnote between the laser locked to the Zerodur cavity and the laser locked to the PZT cavity will drift at 50-350 Hz/s and is assumed to be from the changing

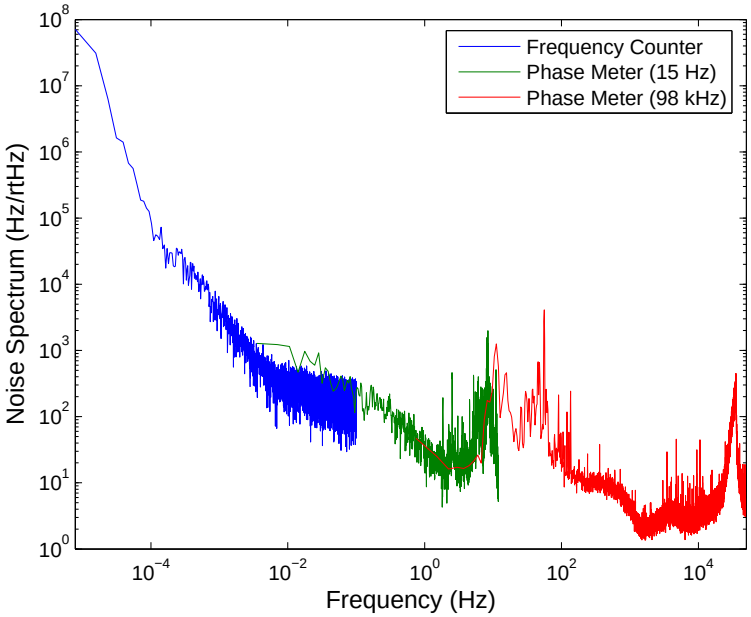

Figure 5-26. Noise spectrum of the PZT cavity with no applied voltage. Measurements were taken using the frequency counter, phase meter sampling at 15 Hz and 98 kHz. The spike around 20 kHz is most likely the resonance of the PZT ring.

temperature within the lab that cause the cavity to expand or contract [81]. When a voltage was applied, changed, or removed from the PZT, a temporal change in the beatnote drift could be observed. The amount of time for the beatnote to return to normal increased as the voltage increased. For example, when 10 V was applied to the PZT, the initial drift of the beatnote increased to approximately 2000 Hz/s. After about 30 minutes, the drift in the beatnote returned to 100-400 Hz/s. When 200 V was applied, the initial drift increased to approximately 18000 Hz/s, and the time for the beatnote to return to normal increased to several hours (Figure 5-28). Monitoring the voltage output of the voltage amplifier showed the change in beatnote frequency could not be attributed to any drift in the voltage amplifier. The slope of the beatnote decays exponentially when a voltage was changed on the PZT, and is believed to be attributed to the relaxation phenomenon of the charged domains slowly returning to their final state in the PZT material [84]. This could be seen since the beatnote would change in one direction as the

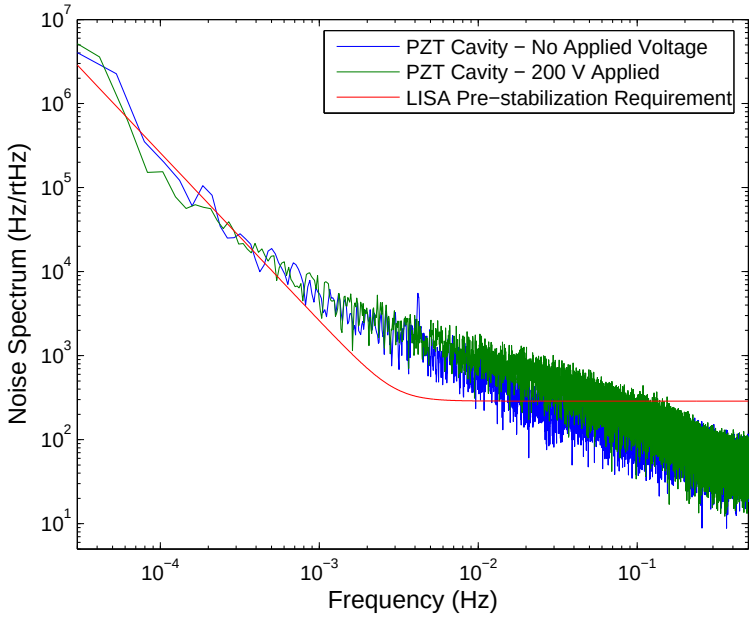

Figure 5-27. Noise spectrum of the PZT cavity with 0 V, and 200 V applied to the PZT along with the LISA pre-stabilization requirement.

voltage was applied, and then change in the other direction after applying the voltage. This implies that the relaxation process occurs in the opposite direction of when a voltage is applied.

Arm-locking uses the stability of the LISA arms to further suppress the frequency noise of a pre-stabilized laser. An error signal can be generated from a pre-stabilized laser and its transponder signal from the far spacecraft. This error signal is then fed into an arm-locking controller (ALC) which serves as a tuning mechanism for the frequency of the laser [74].

It has already been experimentally verified that by using an ALC the frequency noise of a pre-stabilized laser can be further suppressed and that the experimental results are in close agreement to what is theoretically expected [74].

To test this, the beat signal between the Laser 2 and Laser 3 was measured with a phasemeter. The signal was delayed by 0.98 s and Doppler shifted using a delay unit. The delayed and Doppler shifted signal is then mixed with the prompt signal to form the arm

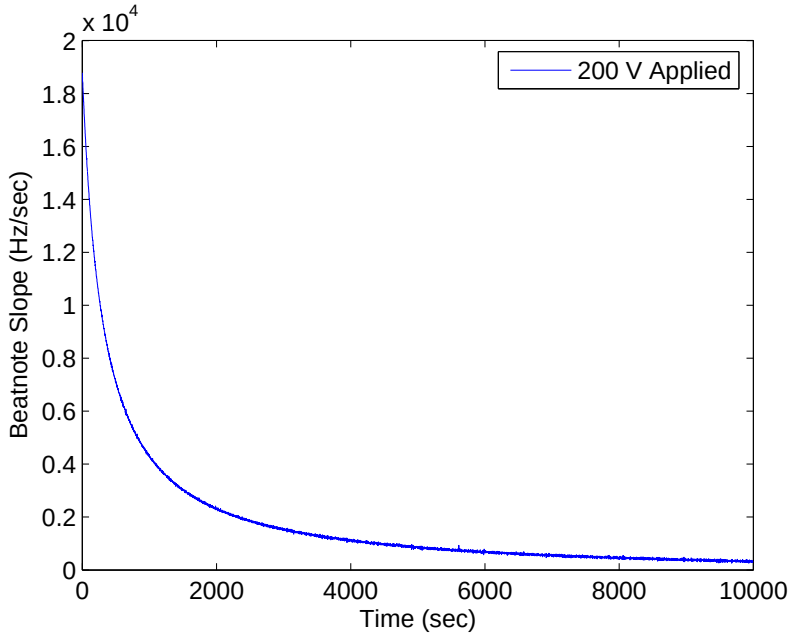

Figure 5-28. The slope of the beatnote over time with 200 V applied to the PZT. The time series was taken approximately 10 minutes after the voltage was applied to the PZT.

locking error signal upconverted by the Doppler shift similar to the upconverted signal in LISA. A second phasemeter is used to demodulate the Doppler-shifted signal with the Doppler frequency. Any differential laser frequency fluctuations will change the phasemeter output. This signal is appropriately filtered, amplified, and applied to the PZT to change the length of the PZT cavity and stabilize the beat frequency of the lasers to the delay line. Note that Laser 2 is only providing a reference to be able to electronically delay the phase noise of the main laser.

The frequency noise of the beat signal is shown in Figure 5-31. The frequency noise between 10^{-4} and 10^{-2} Hz is 4 to 6 orders below the requirements and then rolls up with $\sim f^2$ up to 0.5 Hz. The peaks at multiples of the inverse delay time are caused by the fact that the arm locking sensor is insensitive at these frequencies [81]. Using this method, the cavity can be stabilized from noise levels that are just at the LISA pre-stabilization requirement, to levels that are several orders of magnitude below the requirement. Using

this method alone can suppress seven of the twelve orders of magnitude in frequency suppression from a free running-laser needed for the LISA mission.

The main difference in this setup when compared to what will be experienced on LISA, is that there is a 0.98 s delay instead of the 32 s delay that the light will experience between the LISA spacecraft. However, LISA will use a linear combination of the signals from both arms. This linear combination is insensitive to laser frequency noise at multiples of the inverse of the light travel time difference. These nulls in the response function are at or above 1 Hz for most of the time of the mission, which is equal to the response we have in our system.

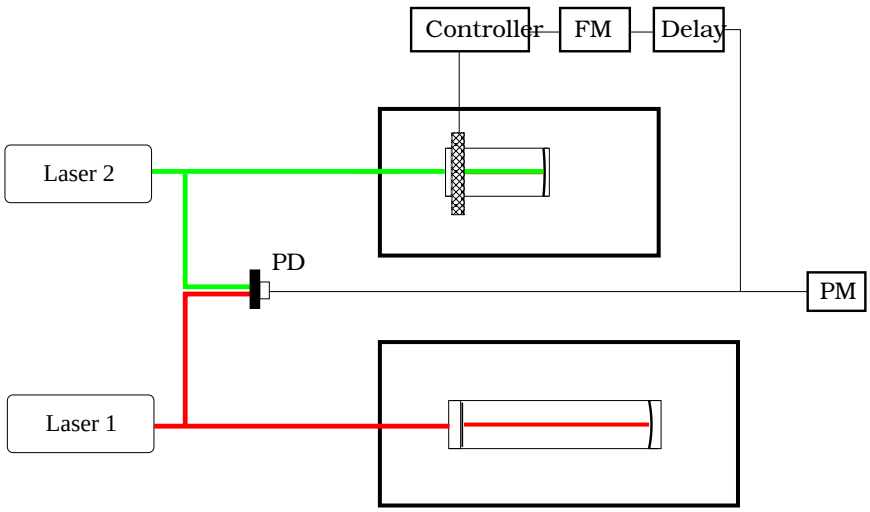

Figure 5-29. Arm-locking setup used to arm-lock the PZT cavity to a Zerodur cavity. The feedback controls used to initially lock the lasers to the cavities are not shown. PD: photodiode, PM: phasemeter, FM: frequency meter

Although the noise spectrum of the PZT cavity almost meets the LISA requirements in most of LISA band, sudden jumps in the time series of the beatnote do occur. Depending on the size and frequency of these data glitches, they are often not seen in the noise spectrum due to the averaging of the time series before the FFT is performed. These glitches may cause problems in keeping the laser properly locked if arm-locking is to be used. A sudden jump in frequency may have a large enough slope such that the ALC controller is not able to track the beatnote, subsequently causing the laser to lose lock.

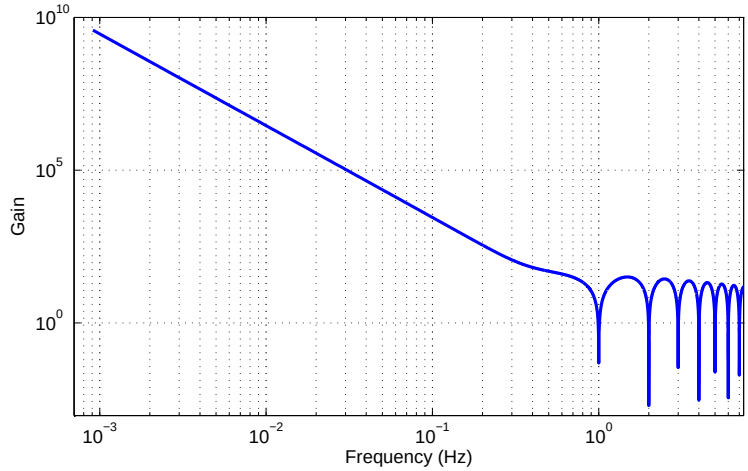

Figure 5-30. Modeled open-loop transfer function of the arm-locking controller used to suppress the laser noise.

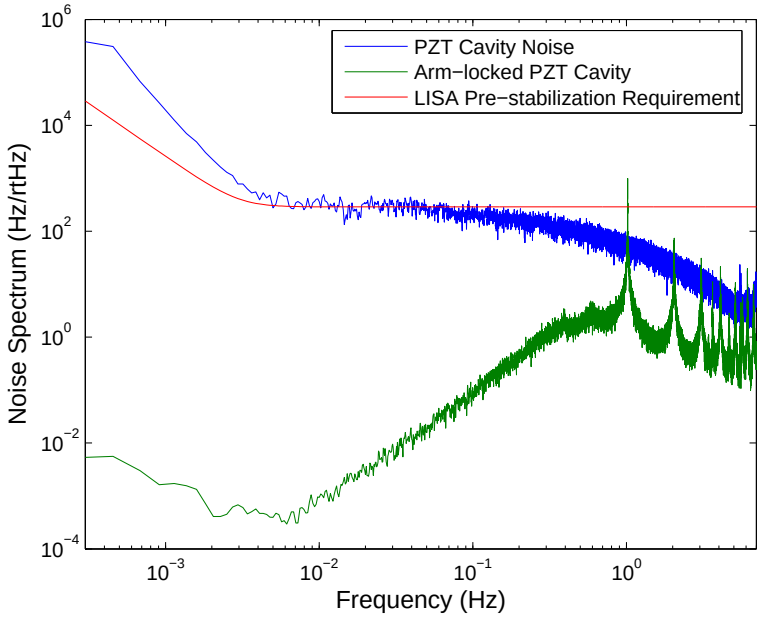

Figure 5-31. Noise spectrum of the PZT cavity without an applied voltage, the noise spectrum of the PZT cavity using arm-locking, and the LISA pre-stabilization requirement.

The amplitude, frequency, and cause of the glitches are important factors to consider when designing the ALC as well as determining their propagational effects within the LISA signals.

There are 2 distinct types of data glitches that occur within the data. The first is the step-glitch (Figure 5-32, top) and is characterized by a sudden jump in frequency that does not return to the normal beatnote frequency. The second type of glitch is the spike-glitch (Figure 5-32, bottom) and is characterized by a jump in frequency that returns to the normal beatnote frequency.

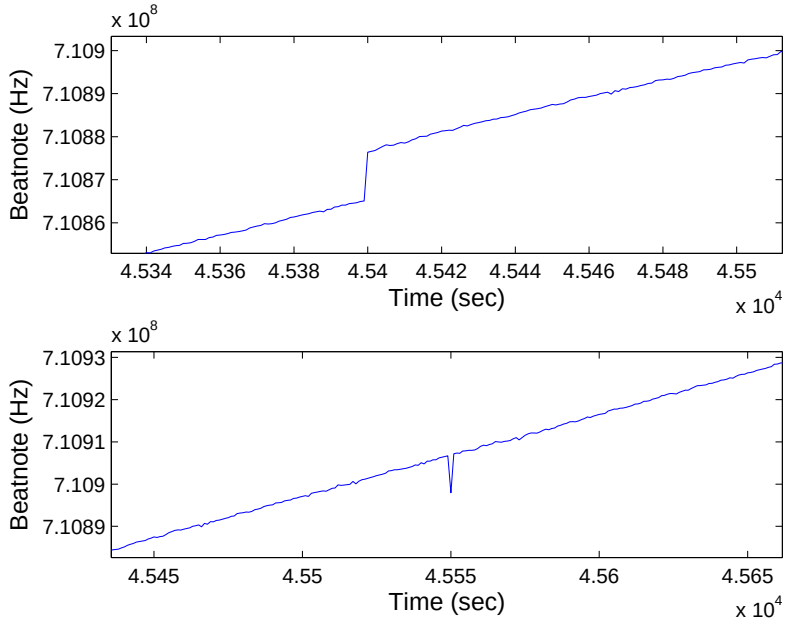

Figure 5-32. Example of a step glitch (top) and spike glitch (bottom).

Three different causes for the step-glitches were investigated. Sudden changes in the alignment of the laser beam caused by human activity in the lab is always an issue but can usually be accounted for. Electronic disturbances such as sudden changes in an offset voltage within the laser feedback system produces step-glitches. In addition, internal relaxation processes within the Zerodur or PZT material cannot be ruled out as a cause for step-glitches. However, once the feedback system was optimized, step glitches occurred

on average only every 3.8 days. Their amplitude ranges from 3000 to 6000 Hz with an average of 3900 Hz [81].

The overwhelming majority of the glitches that occur are spike-glitches. The detection rate of spike-glitches can depend on the sampling rate. Only spike-glitches where the average frequency variation during a sample time is large compared to the normal rms noise can be detected. Consequently, shorter spikes require a larger amplitude to be detectable. However, when we increased the sampling rate from 1 Hz to 8 Hz, the rate stayed essentially the same. In contrast to this, when the sampling rate was reduced to 0.1 Hz, most of the spike-glitches disappear into the rms noise. The only identifiable source for these spike-glitches was the PZT voltage. At 50 V, the spike-glitch rate was about once every 3-4 hours. A typical amplitude of 1000 Hz at a 1 Hz sampling rate was typically measured, while the amplitude rarely exceeded 4000 Hz when sampled at 8 Hz. The scaling indicates that the amplitude is probably not low pass filtered by the sampling rate.

Although spike-glitches were shown to increase as the applied voltage increased, they were not able to be completely suppressed with no voltage applied to the PZT. Both the beatnote and the voltage applied to the fast actuator of the laser were simultaneously measured and showed that spikes in the beatnote often showed a spike in the laser actuator voltage as well. These spike-glitches are most likely caused by electronic noise in the laser feedback controllers and/or human activity in the lab [81].

To test the mechanical feasibility of using the constructed PZT cavity on the LISA mission, a "shake test" was done at GSFC. To measure the vibrational signature of the PZT cavity and determine if the cavity would survive expected launch conditions, two accelerometers were used. One sensor was cemented to the PZT to sense motion along the cavity axis only. The other sensor detects motion in all three axes and was cemented to the top of the mounting clamp that holds the cavity. Two rounds of testing were done for a total of six tests. One round of testing consisted of vibrating the PZT cavity transverse

to its optical axis using a 0.25 g sine sweep for frequencies of 20-2000 Hz, a 0.14 g^2/Hz amplitude with random frequency vibrations, and a 0.25 g sine sweep for frequencies of 20-2000 Hz after the random vibrational test was done. These tests were then repeated for a vibrational direction axial to the optical axis. The cavity showed no appreciable change based on the vibration signature, and would be expected to survive launch conditions. Further tests will need to be done to determine if the vibration testing caused the stability of the cavity to decrease, but it is expected that the stability should be similar to what was originally found.

5.3.6 Zerodur-CFRP

SiC and CFRP have become widely used in many applications due to their high mechanical strength and low CTE. CFRP has been used in support structures for space based missions, and is under consideration for use as an off-axis secondary mirror support for the LISA mission [23]. To the authors knowledge, there is no information on the stability of CFRP materials, although it is claimed by manufacturers of space-qualified CFRP that the outgassing is well understood and can be accounted for through the use of optics to adjust the beam as the strut outgasses. To test both the dimensional stability and outgassing properties of CFRP, the CFRP cavity described above was placed in Tank 2 and Laser 3 was locked to the cavity. A time series between Laser 2 and Laser 3 taken over 4 days is shown in Figure 5-33 [68]. Typical beatnote fluctuations range from 250-600 MHz, but have been measured to be over 1 GHz. For this reason it is difficult to get data runs that last several weeks because the beatnote will drift out of range of either the photodiode or the frequency counter.

Typical drifts in the beatnote frequency are a few kiloHertz per second. When the CFRP cavity was initially placed in the vacuum tank, the tank was pumped down using a roughing pump for approximately one day. The turbo pump was then turned on and left on for several weeks before the ion pumps were turned on. The first measurements of the CFRP beatnote were taken approximately one day after the turbo pump were turned on

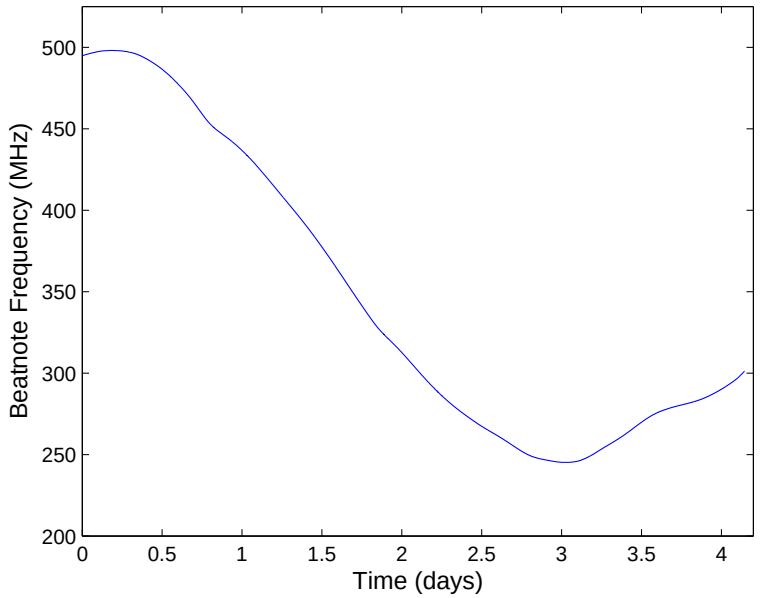

Figure 5-33. Beatnote of the CFRP cavity in Tank 2 taken over 4 days.

and showed a drift in the beatnote of ∼12 kHz/s. The next day, the drift was observed to be ∼ 6 kHz/s, and the following day it was observed to be ∼3 kHz/s [68]. It then continued to drift at this rate for several days. It is assumed this drift is most likely due to the outgassing of the CFRP cavity.

Although the CTE of the CFRP cavity is not known, it is assumed to be larger than that of the Super Invar cavity since the beatnote oscillations are significantly higher than those of the Super Invar cavity. Comparison of the tank temperature fluctuations when the Super Invar cavity was measured and when the CFRP cavity was measured show to be within a factor of two. This can not explain the order of magnitude larger frequency fluctuation of the CFRP beatnote and it is assumed the large swing is due to a larger CTE than that of the Super Invar cavity. Based on this, it is expected that the CTE of the CFRP should be about an order of magnitude larger than that of the Super Invar cavity.

To estimate the CTE of the CFRP cavity, the same process was done to find the CTE of the Super Invar cavity. Using Eq. 5–21 the resultant CTE was found to be 1-3 ppm. As expected, this CTE is about an order of magnitude higher than that of the Super Invar.

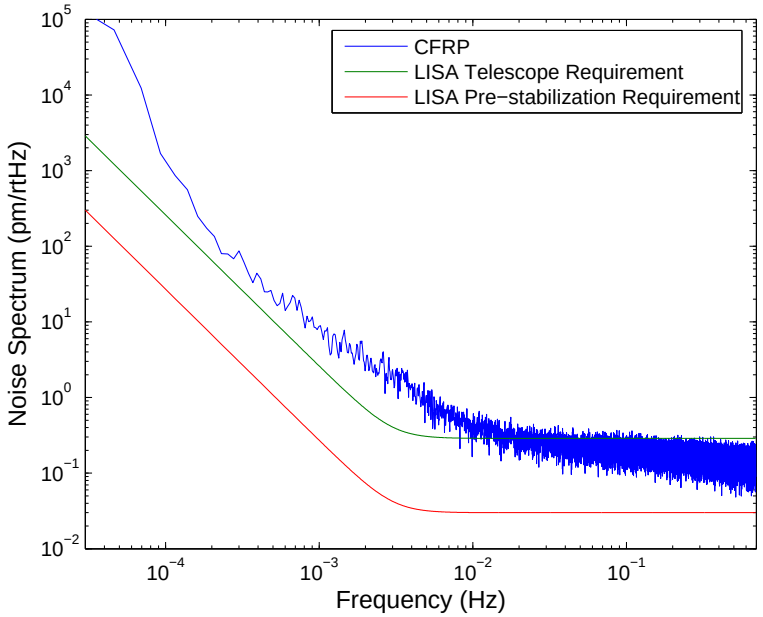

Figure 5-34. Stability of the CFRP cavity along with the LISA telescope and pre-stabilization requirements.

Although the CFRP cavity meets the LISA telescope requirement at higher frequencies, the causes of the high noise at lower frequencies is of interest in order to determine what processes are responsible. It is known from the previous cavities that the low frequency noise is due to the high CTE of the CFRP material. The frequency these temperature effects typically occur at are below $\sim 1 \times 10^{-3}$ Hz. The additional noise between 10^{-3} and 10^{-2} Hz was of interest and it was speculated that the mirror coatings could be the cause.

The high reflectivities of the cavity mirrors will cause the light to bounce back and forth within the cavity, causing a power build-up. This will cause a local heating of the mirrors and mirror coatings that will translate into a length expansion. The effect of the incident power on the noise spectrum can be tested by changing the input power of the

laser. To change the incident power, a neutral density (ND) filter was placed before the polarizing beam splitter. The ND filter was then aligned such that the visibility of the cavity was not changed compared to when there was no ND filter. The laser was then maximized on the photodiode used to produce the PDH error signal. Without any ND filter the DC voltage was 3.7 V and the incident power was about 3 mW. One ND filter caused the PD voltage to drop to 1.8 V, and another ND caused the PD voltage to drop to 0.18 V. These voltages correspond to 1.6 mW and 150 μW, respectively. A time series at each of the photodiode voltages were taken over three days and the resulting noise spectrums are shown in figure 5-35. It is clear that by decreasing the incident power, the noise spectrum decreases in the 10^{-4} to 10^{-2} frequency range. With a low enough incident power, the CFRP cavity noise spectrum will meet the LISA telescope requirement.

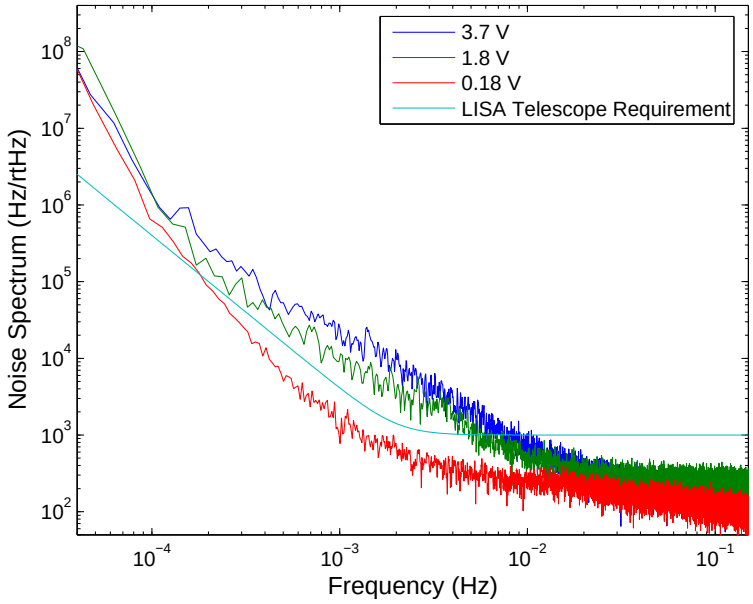

Figure 5-35. Dimensional stability of the CFRP cavity for differing incident intensities along with the LISA telescope requirement.

From the noise spectrum alone, it would appear that CFRP would be a viable option for use on the LISA mission. Unfortunately, the outgassing properties and absolute length stability still need to be studied in order to determine if they meet the LISA requirements.

In addition, the shape of the CFRP cavity is not indicative of what would be designed for the LISA spacecraft. The outer shell around the CFRP cavity was designed such that when the CFRP outgassed, the bending of the structure would be kept to a minimum. This supporting ring would not be viable for the LISA telescope support and a more realistic design needs to be made and tested before a final decision on material should be chosen for the LISA telescope support structure.

CHAPTER 6
ABSOLUTE STABILITY MEASUREMENTS

In some cases, it will be necessary to know the absolute stability of a material in addition to its relative stability. An example of this is the telescope support structure for the LISA mission. The material chosen must have a relative stability of better than 1 pm/$\sqrt{\text{Hz}}$ above 3 mHz in addition to expanding or contracting by less than 1.2 μm over the lifetime of the mission in order to prevent de-focusing of the laser. Although results for the relative stability of materials were presented in Chapter 5, the experimental setup used is not adequate to determine the absolute stability of a material over month time scales or longer due to the large frequency dependence on laboratory temperature and the densification of the optical cavities. The strong temperature dependence can be reduced using heaters and feedback controllers, but the densification of the material used for the optical cavity is not very well known. Changing the frequency reference from an optical cavity to an atomic transition will provide a much more suitable frequency reference over long periods of time. For this reason, two methods known as frequency-modulated spectroscopy (FMS) and modulation transfer spectroscopy have been used to determine the absolute dimensional stability of a material.

6.1 Saturation Spectroscopy

Figure 6-1 shows a laser beam transmitted through both a gas cell containing an absorbing molecular vapor and a laser transmitted through a Fabry-Perot cavity. The transmitted intensity for the optical cavity will peak around resonance, while the transmitted light for the gas cell will dip around the molecule's transition. Deriving an error signal to lock a laser to the resonant frequency of an optical cavity has already been presented and is similar to using a molecular transition [85]. In the case of a molecular transition, the linewidth of the transition is significantly larger than that of a high Finesse optical cavity.

To understand the concepts of saturation spectroscopy, consider the situation where the laser is being modulated, with the frequency of the modulation being fairly low and the amplitude of that modulation is small. If the laser frequency is in the vicinity of an absorption line, then the frequency modulation causes the absorption to modulate synchronously which causes the laser frequency modulation to map onto the laser's transmitted frequency [85]. Another way of stating this is that the frequency modulation on the laser converts to an amplitude modulation by the absorption.

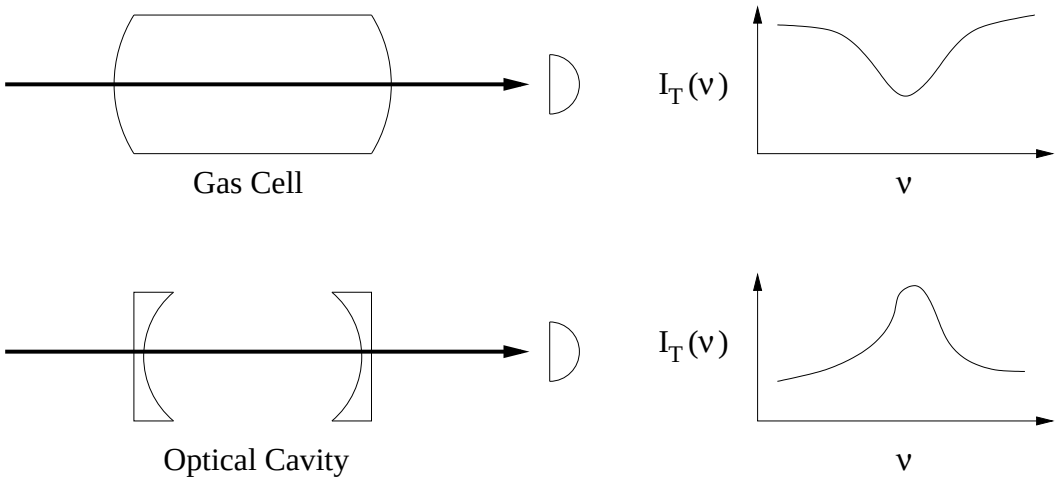

Figure 6-1. Intensity as a function of frequency for both an optical cavity and gas cell.

Near the frequency of maximum absorption, the conversion from frequency modulation to amplitude modulation will be small, and goes to zero at the transition line's center. After it passes through the line's center, the amplitude conversion increases, but the phase relationship has now reversed. If the laser's frequency is well outside the absorption line, the amplitude modulation goes to zero due to the lack of absorption [85]. The phenomenon is know as frequency modulation spectroscopy and is extremely useful in locking a laser to the frequency of an absorption line of a gaseous substance [85].

When the beam passes through the gas cell, the laser frequency does not have to be in exact resonance with the transition to experience an absorption of light. This is due to the Doppler effect. The Doppler broadening of the transition line occurs because the atoms or molecules are in motion [85]. If an atom or molecule is moving such that it has a velocity

component that is parallel to the direction of the beam, then the resonant frequency of the Doppler shifted atom or molecule will be [85]

$$\nu = \nu_0(1 + \frac{v_{||}}{c}), \tag{6–1}$$

where ν is the resonant frequency of the moving molecule, ν_0 is the resonant frequency of the molecule with no velocity, c is the speed of light, and $v_{||}$ is the parallel component of the moving particle with respect to the laser beam. It is clear from Eq. 6–1 that as the gas is heated up, the Doppler frequency will be larger, resulting in a broader transition line [85].

Let's now consider a weak beam passing through a gas cell that is incident on a photodiode and a strong beam propagating in the opposite direction as the weak beam such that the two beams nearly overlap. It will be shown that this results in significantly narrowing the widths of the absorption lines. As the weak beam passes through the gas cell, it will experience a Doppler broadening of the transition line. The strong beam will experience a Doppler shift, although in the opposite direction, and so both beams interact with a completely different group of atoms as long as the laser frequency is far enough off resonance. If the laser frequency is near ν_0, then both beams are now competing for the same atoms. The strong beam will quickly deplete the number of atoms with $v_{||} = 0$, leaving very few atoms to interact with the weak beam [85]. This causes the weak beam to pass through the cell with little loss in intensity, resulting in a spike in intensity at resonance on the photodetector. This effect can be seen in Figure 6-6 and can be used to generate an error signal that the laser can lock to. In this manner, an absolute frequency reference can be established.

6.2 Experimental Setup

The only known absorbers near 1064 nm are $^{133}Cs_2$, CO_2, C_2H_2, and C_2HD [86] [87]. Of these absorbers, only molecular cesium ($^{133}Cs_2$) can be investigated by standard sub-Doppler techniques. The other absorbers have low cross-sections and require

saturation powers that are very high. Because of this, special techniques, such as using a high-finesse cavity, have been developed to study their sub-Doppler spectra [86]. Many difficulties associated with laser locking to molecular cesium can be circumvented by using second-harmonic generation and locking to sub-Doppler lines of molecular iodine ($^{122}I_2$) as discussed in Chapter 7.

The majority of the development of frequency standards at 1064 nm has been done using Cs_2 [88]. Cesium spectroscopy in the 0.90 to 1.14 μm regime occur in the $A^1\Sigma_\mu^+ \leftarrow X^1\Sigma_g^+$ band and have been reported by Orlov and Ustyugov [86]. It has also been shown by Mak *et al.* that laser frequency stabilization is possible using sub-Doppler lines of a cesium cell which was heated to 220°C and achieved a stability of 6×10^{-11} at a measurement time of one second [89]. Investigations into the sub-Doppler spectroscopy of molecular cesium were done in addition to using two different laser locking methods known as modulation transfer spectroscopy and frequency modulation spectroscopy to provide a frequency reference for use in determining the absolute stability of a material.

6.2.1 Laser Stabilization Using Modulation Transfer Spectroscopy

Using modulation transfer spectroscopy allows the sub-Doppler spectrum of molecular cesium to be studied in great detail. The experimental setup used for cesium spectroscopy is shown in Figure 6-2. The laser passes through a Faraday isolator, half-wave plate, and polarizing beam splitter. By rotating the half-wave plate, the power in the pump and probe beams can be easily changed. The probe beam then passes through the oven and cesium cell. A detailed drawing of the oven and cesium cell are shown in Figure 6-3.

The cesium cell is 150 mm long, 19 mm in diameter, and has Brewster windows at each end to prevent back-reflections from interfering with the incident beam. The cesium cell is held in place by two circular copper supports at each end of the cell. These supports are then held in place by stainless steel rods. The support structure is able to slide in and out of a thin copper tube 200 mm long and 50 mm in diameter. The copper tube is wrapped in a heating mesh whose power is controlled by a temperature controller (model

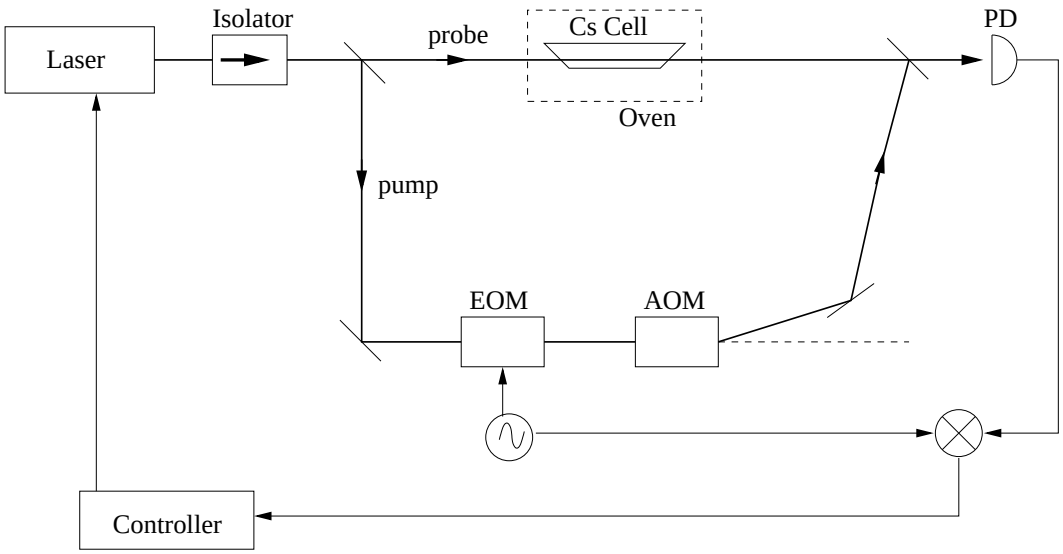

Figure 6-2. Experimental setup used for modulation transfer spectroscopy.

BriskONE from BH Thermal Corporation). A K-type thermocouple is attached to the end of the glass tube using high temperature adhesive tape and is fed into the controller to regulate the temperature. The heating mesh is wrapped with a high temperature insulator, and this is then surrounded by additional insulation. The tube and insulation are enclosed in a high temperature glass with a high transmission at 1064 nm. The temperature stability of the cesium cell is better than 0.10°C over 10 s as measured by the thermocouple and temperature controller.

After the probe beam passes through the cesium cell it passes through a 50/50 power beam splitter and is incident on a high-bandwidth photodetector. Simply using the probe beam in this setup will allow spectroscopy of molecular cesium to be done, although results with a low signal-to-noise ratio were typically achieved. This is due to the fact that cesium is a poor absorber at 1064 nm, so temperatures in excess of 220°C are needed in order to see significant absorption which also causes additional noise. Typical cesium lines at 240°C are shown in Figures 6-4 and 6-5. To determine the wavenumber of the dips, a pick-off from the laser was sent into a wavemeter and the location of the dips were matched to line numbers in references [90] and [89].

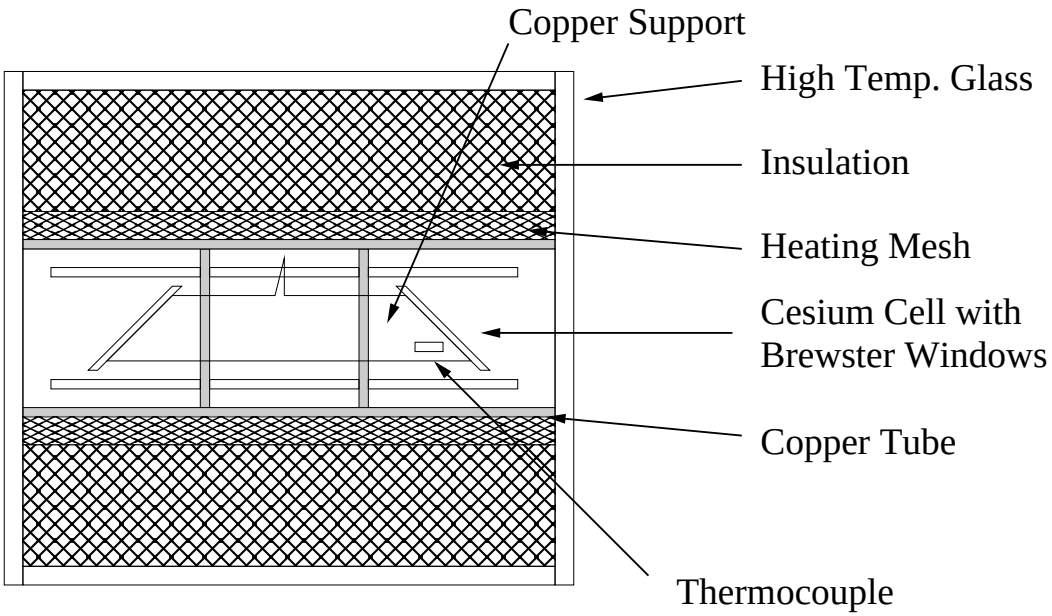

Figure 6-3. Diagram of the oven used to heat the cesium cell.

The pump beam was phase modulated at 12 MHz using an EOM and then shifted in frequency by ∼20 MHz using an acousto-optic modulator (AOM) to prevent interference between the probe and scattered pump beams. The pump beam had a diameter of ∼2.0 mm with a power of 5 mW and the probe beam a diameter of ∼1.3 mm and power of 1 mW as they passed through the cesium cell. A four-wave mixing interaction of the pump and one of its side sidebands and the probe beam induce two new fields in the direction of the probe beam at frequencies of $\omega \pm \Omega$, where ω is the probe carrier frequency and Ω is the modulation frequency of the EOM [90]. In this manner, modulation transfer spectroscopy has no Doppler-induced baseline offsets, since the four-wave mixing is not influenced by the Doppler background [90]. For this reason additional modulation, such as using a chopper, is not needed to remove the Doppler background.

A sub-Doppler error signal was obtained in a similar manner as that of the PDH signal described in section 5.2 by mixing the photodetector signal with the EOM modulation frequency. Due to the low signal to noise ratio produced from the lack of high absorbing cesium lines, a significant amount of signal conditioning had to be done

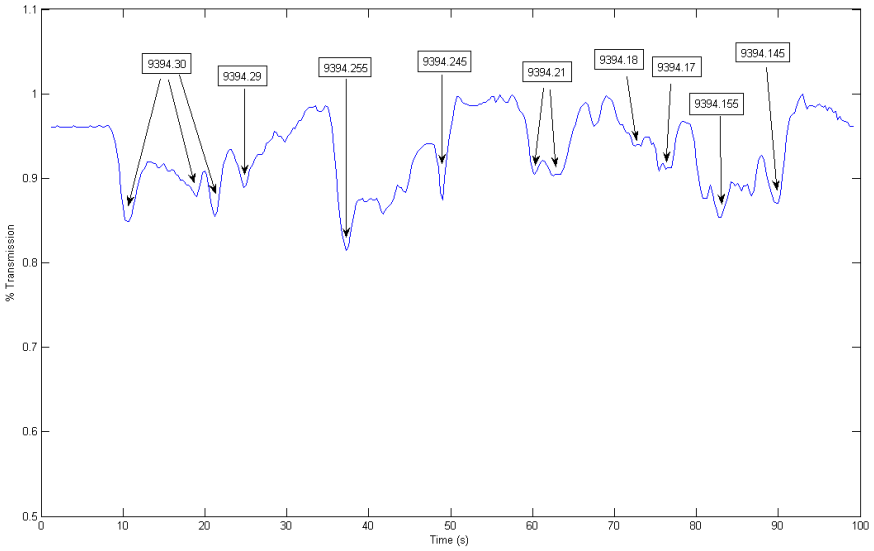

Figure 6-4. Intensity profile as the laser frequency is scanned over multiple absorption lines.

to produce a suitable error signal. The AC signal from the photodiode was amplified by approximately two orders of magnitude before it was mixed with the function generator used to power the EOM. After the photodiode and oscillator signal were mixed, the error signal was filtered using a 30 Hz low pass filter and amplified again, typically by a factor of ten to fifty depending on the cesium line used.

Molecular cesium is a poor absorber at 1064 nm at room temperature and requires significant heating before noticeable absorption occurs. To determine the temperature dependence on the absorption percentage, the cesium cell was heated to 200°C, 220°C, and 250°C while scanning over the same line. The results are shown in Figure 6-6 and clearly show that as the temperature increases, the absorption percentage increases as well. In addition to determining the absorption percentage, the linewidths of the transitions can be determined as well. It was found that most transitions had FWHM linewidths of 300 to 500 MHz.

From figure 6-6 it would seem that to obtain the best error signal, temperatures in excess of 250°C should be used to increase the absorbtion. Unfortunately at these

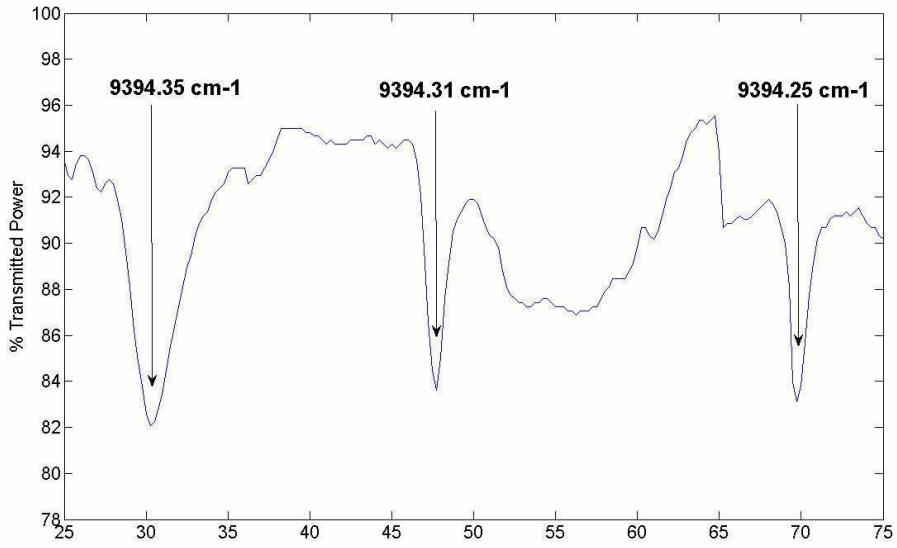

Figure 6-5. Detailed intensity profile of three absorption lines.

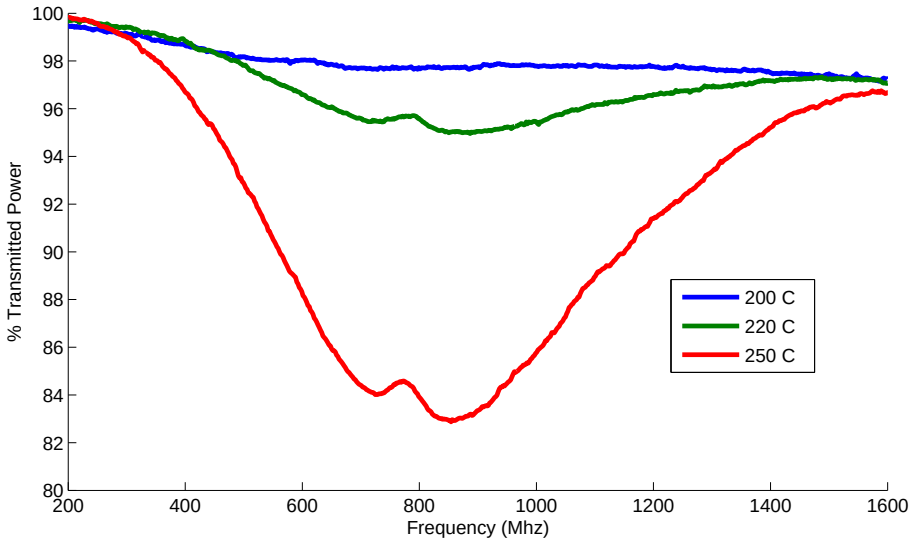

Figure 6-6. Temperature dependance on absorption of molecular cesium.

temperatures, the cesium reacts violently with the glass cell and will often degrade the cell to a point where micro-cracks are induced in the cell and air enters and reacts with the molecular cesium and becomes useless [90]. Even if the cesium cells were kept at temperatures less than 240°C, they would often have lifetimes less than eight months.

In addition to the accelerated degradation of the cesium cells at high temperatures, significantly higher beam powers are needed to overcome the increased Doppler effects. Typically above 250°C, the signal to noise ratio of the error signal did not improve. For these reasons, the cesium cell was typically operated at 235°C in order to obtain a good error signal in addition to lengthening the lifetime of the cesium cell.

Using the modulation transfer spectroscopy technique and scanning over a wide range of frequencies will produce a set of error signals. In addition to providing a set of suitable locking points, the error signals also provide information about the spectroscopy of cesium. A larger peak-to-peak voltage implies the line is a better absorber. Using the error signals also makes it easier to see where the cesium lines are. This is easily seen by comparing Figures 6-4 and 6-7. The dips in Figure 6-4 are often hard to spot without having a reference to match them up to. Alternatively, the lines are easily

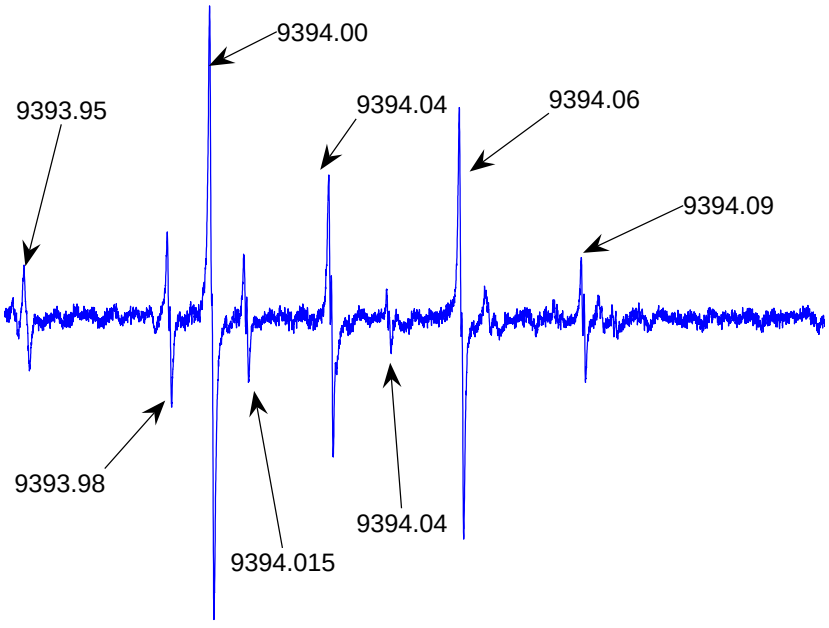

Figure 6-7. Error signals produced for a range of cesium lines.

determined from Figure 6-7. In this manner the cesium spectra can be obtained with

high precision. The knowledge of the cesium spectra and strength of the error signal is important when measuring the absolute stability of a material. While cavities have set frequency shifts defined by their FSR, there is no pattern that can be used for locking to cesium. This becomes difficult as many cesium lines are gigaHertz apart and most commercial photodectectors have a range of less than a few gigaHertz. By knowing the cesium spectra, a suitable line can be chosen and locked to in order to make the necessary measurement to determine the absolute stability.

6.2.2 Laser Stabilization Using Frequency Modulation Spectroscopy

Although modulation transfer spectroscopy is ideal for cesium spectroscopy, and presents a good signal-to-noise ratio, it was found in reference [90] that better results were obtained using FM spectroscopy. For this reason, both modulation transfer and FM spectroscopy methods were studied for laser locking.

The experimental setup used for FM spectroscopy is shown in Figure 6-8 and is similar to that of modulation transfer spectroscopy. In the case of FM spectroscopy, the pump is phase modulated and a chopper is used to extract the signal from the Doppler background. The modulated probe beam is detected on the photodiode and is mixed with the signal generater that is fed into the EOM. This signal is then fed into a lock-in amplifier whose reference is provided by the chopper source. Most of the amplification and low pass filtering was done by the lock-in amplifier and only a small amount of signal conditioning was needed to produce an error signal with similar peak-to-peak and noise levels as those obtained using modulation transfer spectroscopy. A range of chopper frequencies were studied and it was found that using chopper frequencies on the order of hundreds to a few thousands Hertz produced better error signals than using slower frequencies.

6.3 Results

A pick-off from the cesium stabilized laser is beat with a pick-off from Laser 2 in Figure 5-13. In this manner, the absolute stability of the material Laser 2 is locked to

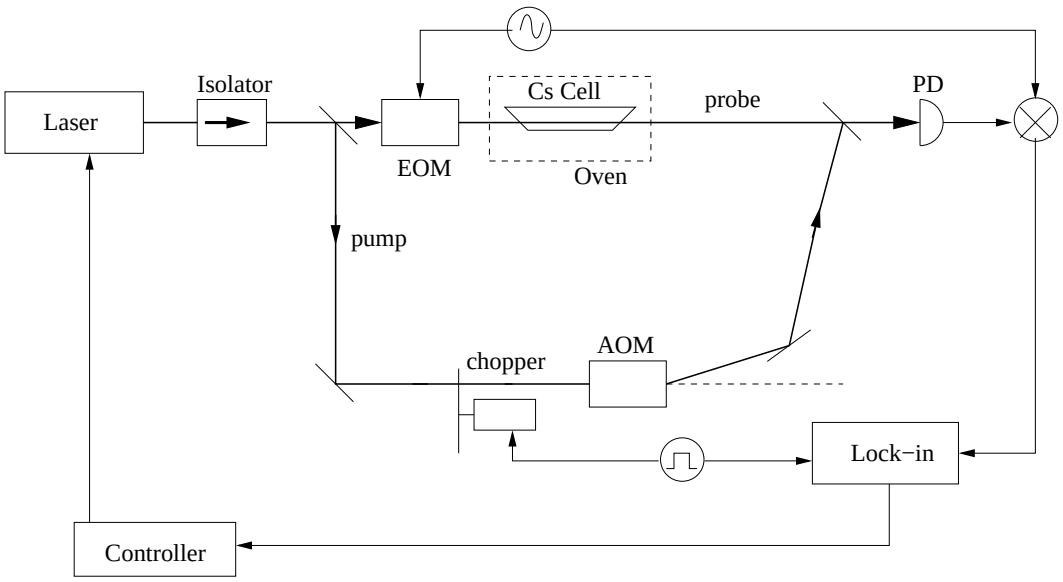

Figure 6-8. Experimental setup used for frequency modulated spectroscopy.

can be determined. In this case, the material chosen was a Zerodur cavity with optically contacted mirrors.

Although it was reported in reference [90] that better results were achieved when FM spectroscopy was used, the opposite was found to be true for my setup. The results for using modulation transfer spectroscopy, FM spectroscopy, and a free-running laser are shown in Figure 6-9. For almost all frequencies, using modulation transfer spectroscopy was better than using a free-running laser, but locking a laser using FM spectroscopy was worse than using a free-running laser. The cause of the excessive noise using FM spectroscopy is unknown and several noise sources were investigated for both experimental setups. The most plausible noise sources in both setups are RFAM noise produced from the EOM, noise produced from the AOM, noise produced from a changing chopper frequency, and temperature changes in the cesium cell.

6.3.1 RFAM Noise

Misalignment of the EOM will cause residual amplitude modulation on the photodiode that ultimately shows up as noise in the beatnote. This can easily be seen if the output of the photodiode is monitored by a spectrum analyzer around the frequency the EOM

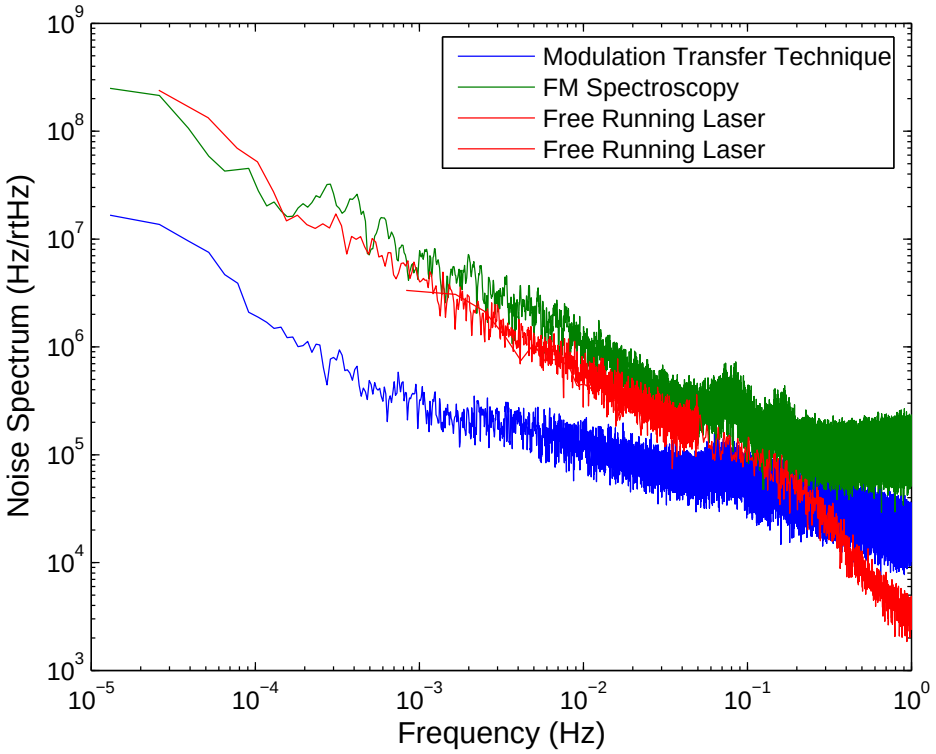

Figure 6-9. Stability results of the modulation transfer and frequency modulated spectroscopy techniques compared to a free-running laser.

is modulated at. As the beam alignment is changed, the peak amplitude changes as well. A change in the input polarization of the beam will also cause the residual amplitude modulation (RAM) to change. In addition, if the alignment and polarization are left constant, the RAM will change over time due to the length change of the EOM crystal which is caused by temperature fluctuations of the crystal. All of these sources will cause a changing RAM which is then detected on the photodiode.

To determine if the RFAM produced from the EOM was a limiting noise source, the incident beam was misaligned such that the RFAM detected on a spectrum analyzer was ten times more than normal. The noise spectrums between the aligned and misaligned beams were then compared and showed no difference.

6.3.2 AOM Noise

In addition to RFAM noise produced from the EOM, it is possible the instability of the AOM could be causing a source of noise. If the shifted frequency changes over time, this will cause a misalignment into the cesium cell, which will cause the counter-propagating beams to overlap less, which causes the lamb dip to decrease. It is also possible that by changing the AOM frequency, spurious interference between the pump and probe beam can occur. The net effect if that by changing the AOM frequency, the beatnote frequency will change as well.

To test the effects of a changing AOM frequency, the laser was locked and the beatnote was monitored as the AOM frequency was changed. This effect was noticeable but small, and it was concluded that this was not a significant enough noise source to be causing the low frequency drift in the beatnote.

6.3.3 Changing Chopper Frequency

The optical chopper has a rotating blade that periodically blocks the laser beam passing through it. When a chopper is used on the pump it will periodically affect the absorption of the probe beam only when the frequency is near a resonance. Consequently, only then will the chopping of the pump beam result in a modulation of the probe beam. By measuring the probe beam with a photodiode and sending it and the chopper signal into a lock-in amplifier, an error signal can be generated.

To test the effects of changing the chopper frequency, the laser was locked and the beatnote was monitored as the chopper frequency was changed. The effect was negligible and it was concluded that this was an extremely small contribution to the noise.

6.3.4 Cesium Cell Temperature Changes

The high frequency noise in Figure 6-9 is assumed to be from noise produced from atom-molecule collisions in the cesium cell. This is because the atomic pressure is almost three orders of magnitude higher than the molecular pressure at 220°C [90]. Thus, operating at lower temperatures would be ideal, but this becomes difficult since the

signal-to-noise ratio decreases dramatically as the cell temperature is decreased. While there are methods that would allow the signal-to-noise ratio to significantly improve at lower temperatures [90], they are not discussed here.

Although the high frequency noise is assumed to be from operating the cesium cell at elevated temperatures, it was found that the low frequency noise could not be attributed to drifts in the temperature of the cesium cell. Figure 7 in reference [90] shows how the beatnote frequency changes as the temperature of the cell is increased. Similar trends were obtained from my experimental setup, with a change in frequency per degree Celsius found to be 250 kHz/°C. The assumed temperature stability of the cesium cell is ±0.10°C which was determined by monitoring the feedback controller used for temperature stabilization. From these two numbers, it was determined that the low-frequency noise could not be attributed to the drifts in the cesium cell temperature. In addition, if the low frequency noise was due to the changing cell temperature, the beatnote should show an oscillatory nature that would arise from the cell heating and cooling. This effect was not seen.

After an analysis of the potential noise sources, it was postulated that the low frequency noise seen in the noise spectrum was due to the expansion and contraction of the Zerodur cavity, and not from an inherent noise source in the system. To test this, the cesium-Laser 2 (or cesium-Zerodur) beatnote was recorded at the same time the Laser 1-Laser 2 (or Zerodur-Zerodur) beatnote was recorded and the results are shown in Figure 6-10. The kink in the Zerodur-Zerodur beatnote is due to one of the lasers coming unlocked during the run. The kinks in the cesium-Zerodur beatnote is unknown, but were commonly present in many data runs. It is possible the kink in data is from the control electronics locking onto a different point due to the high level of noise in the error signal. Despite the kinks in both data sets, it is evident that both beatnotes are drifting in the same direction. A comparison of other, shorter, data runs shows that the cesium-Zerodur beatnote consistently drifted ∼1 MHz for every 10 kHz the Zerodur-Zerodur beatnote

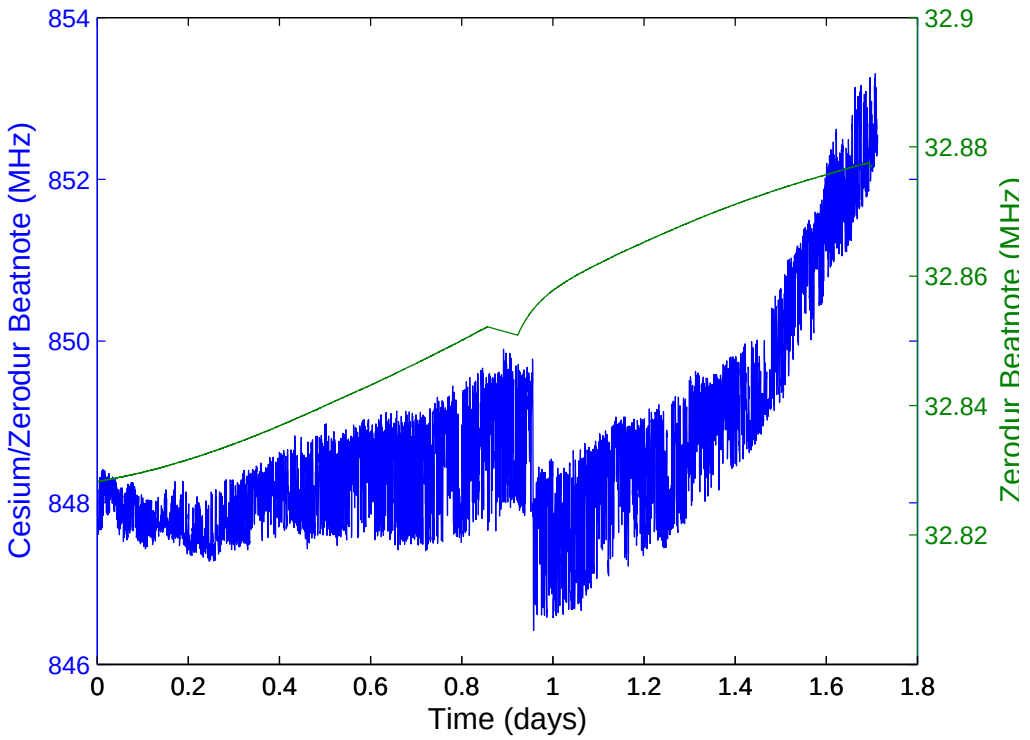

Figure 6-10. Beatnotes of both the cesium-Zerodur and Zerodur-Zerodur locked systems.

drifted. The exact cause of this is unknown, but it may possibly be from temperature drifts in the cavity, or laser intensity drifts over time.

CHAPTER 7
LISA TELESCOPE PROTOTYPE DESIGN

In order for the LISA mission to achieve its goal of detecting low frequency gravitational waves, the distances between proof masses on adjacent spacecraft must be measured to picometer precision. To do this, three distances must be measured; The distance from proof mass to optical bench on one spacecraft, the distance from the optical bench on one spacecraft to the optical bench on the other spacecraft, and the distance from the proof mass to the optical bench on the other spacecraft. In order to make these measurements, the light on adjacent spacecraft must be sent to each other. This will be done via a two-mirror reflecting telescope. The light on the optical bench will be focused and sent to a secondary mirror where it will be magnified and reflected to the primary mirror. The end result will be a highly collimated beam that will be sent to the optical bench on the other spacecraft. Through the use of the same telescope mechanism mounted on the second spacecraft, the light will be refocused and used on the second optical bench. In this manner the necessary measurements can be taken to determine the distance between proof masses on opposing spacecraft. Far-field wavefront distortions caused by misalignment of the mirrors, a change in mirror separation, clipping from the secondary support structure, or errors in pointing the telescope will decrease the sensitivity of the length measurements needed. In some cases, such as the de-focusing of the mirrors or beam pointing, if the effect is large enough, then the measurements may not be able to be taken, and the link will essentially be lost. This makes the telescope and its support structure critical optical components for the LISA mission. Despite the importance of the telescope to the LISA mission, a design for either an on- or off-axis telescope had yet to be designed, fabricated, and tested. Through collaboration with several group members at the Goddard Space Flight Center (GSFC) and the University of Florida, an on-axis telescope was designed, fabricated, and currently is in the process of determining its feasibility for the LISA mission.

7.1 Introduction

The choice of telescope design for the LISA mission is restricted to only reflecting telescopes since the size of the spacecraft ultimately constrains the length of the optical bench plus telescope (in general reflectors are physically shorter than the corresponding refractor of the same aperture). While there are many reflecting telescopes available, the Cassegrain type is ideal due to its long focal length but short physical length. In addition, either an on- or off-axis design can be employed as shown in Figure 7-1. The

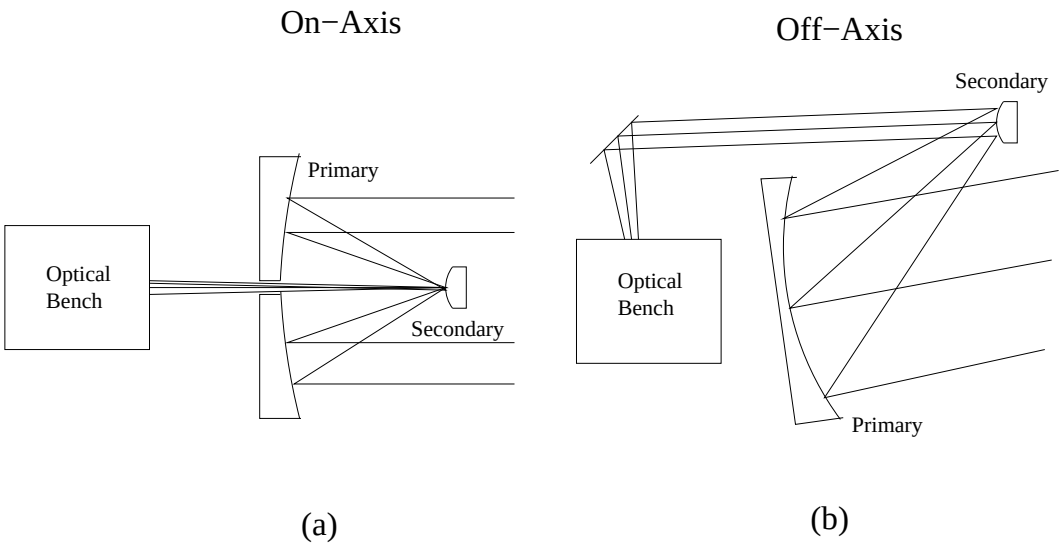

Figure 7-1. Representation of (a) an on-axis Cassegrain telescope and (b) an off-axis Cassegrain telescope.

choice of material used for the secondary support structure will have direct influence on the overall telescope design. The in-band length requirement of 1 pm/$\sqrt{\text{Hz}}$ above 3 mHz and the expected temperature stability of $\sim 10^{-6}$ K/$\sqrt{\text{Hz}}$ at 3 mHz at the telescope require the material chosen to have a CTE of $\sim 10^{-6}$/K [18]. Currently, the two most appealing materials for the task are SiC and CFRP due to their high strength, extreme stiffness, and low CTE. Both materials can be implemented in both on- and off-axis designs, but CFRP is typically favored more for the off-axis design, and SiC is favored more for the on-axis design. The current baseline for the LISA mission is an off-axis design using CFRP for an f/1 telescope [23]. Although the viability of both on- and off-axis designs using both

CFRP and SiC has been done using computer models, more concrete evidence is needed before a final design can be chosen. For this reason, a telescope support structure was designed and built in order to gain more insight into what is needed in order to meet the LISA telescope requirements.

7.2 Telescope Design

The shot noise limited phase error between the received and transmitted beams at a far spacecraft is a significant noise source in the displacement sensitivity of LISA [91]. The magnitude of this noise will depend on several factors including the intensity of the detected laser light, the beam width at the output of the telescope, and how well the beam is focused. The quality of the telescope will directly effect these factors and must be taken into account.

As an example, take into account the defocusing of the telescope. The distance between the primary and secondary mirrors is a critical component of the telescope design. If the distance between the primary and secondary change by too much, then the f/1 telescope may defocus the laser by too much. The following is an brief analysis that describes the requirement on the primary-secondary distance change.

The telescope design calls for a flat wavefront of the outgoing beam of size ω immediately after the primary. If the wavefront is not flat and has a sagitta of size h, the beam appears to have come from a focus with a radius given by [91]

$$\omega_0^2 = \frac{\omega^2}{1 + (\frac{2\pi h}{\lambda})^2}. \tag{7–1}$$

An analysis has shown that a sagitta of $h = \lambda/2\pi$ will decrease the apparent beam radius by $\sqrt{2}$ which will increase the divergence angle by a factor of $\sqrt{2}$ and the received power at the far spacecraft by a factor of two [91]. The f/1 design of the telescope results in a strongly diverging beam. At the primary, the beam is already in the far field regime and the radius of curvature is equal to the distance from the apparent focus, which is behind

the secondary. For a perfect adjustment, the primary will add a negative sagitta of

$$h = -\frac{\omega^2}{2R} \tag{7–2}$$

which flattens the wavefront [91].

If we assume that we move the primary by δz, then this will cause a change in the radius of curvature of the wavefront by the same amount which introduces a mismatch to the primary and the resulting sagitta after reflection at the primary becomes [91]

$$h = -\frac{\omega^2}{2R}\frac{\delta z}{R}. \tag{7–3}$$

For the current design, estimates of h $\leq \lambda/20$, R = 0.6 m, and ω = 17.8 cm are appropriate[91]. A value of ω = 17.8 cm is the Gauss beam radius which optimizes the intensity at the far spacecraft for a 40 cm aperture Gaussian beam. Substituting these numbers into Eq. 7–3 results in an allowable length change of

$$\delta z \leq 1.2\mu m. \tag{7–4}$$

This means that in order for the telescope to meet the wavefront distortion requirement of $\lambda/20$, the distance between the primary and secondary mirrors cannot change by more than 1.2 μm over the lifetime of the mission. Other noise sources, such as the tilt of the received wavefront, beam divergence, and pointing stability, will play a critical role in the achieved sensitivity of LISA [92].

Taking these potential noise sources into account and current material fabrication limitations, a design for the telescope was chosen as shown in Figure 7-2. It consists of a 400 mm diameter primary, a 135 mm diameter secondary, and four 5 mm $\times$ 30 mm struts that connect and separate the primary and the secondary by 600 mm. SiC was chosen to make the entire structure due to its high stiffness, low CTE, and high thermal conductivity. The high stiffness and thermal conductivity will reduce temperature gradients in the telescope which will reduce the effects of tilting and pointing errors, while

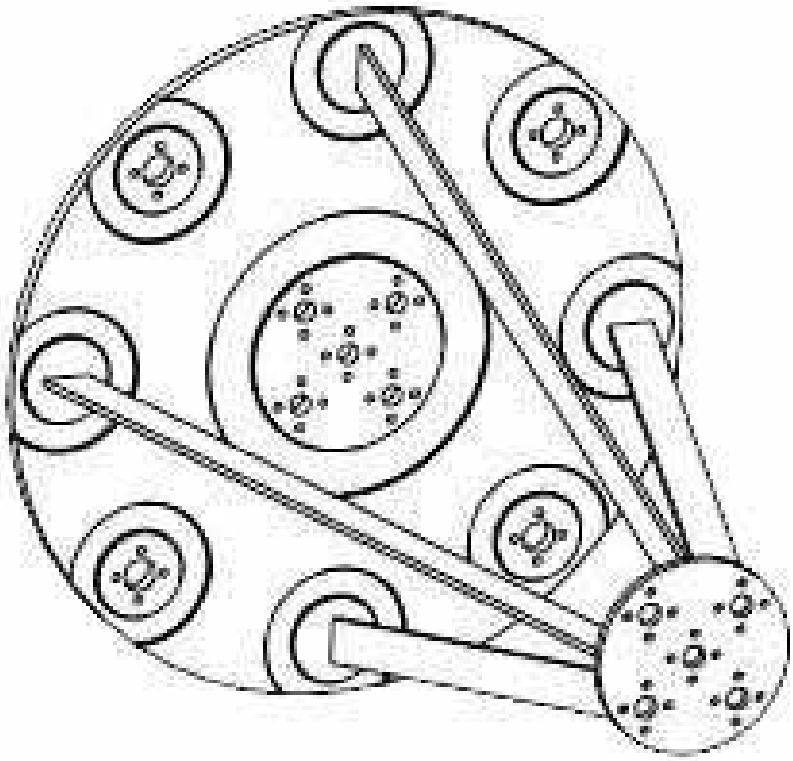

Figure 7-2. Isometric view of the telescope design. Figure courtesy of Joseph Generie at Goddard Space Flight Center.

the low CTE will keep the in-band noise below the required 1 pm/$\sqrt{\text{Hz}}$. In addition, results for the relative dimensional stability of SiC were already known during the design process, while those of the CFRP cavity were yet to be studied. Although it is claimed that there are manufacturers that can make CFRP with a low CTE, high thermal conductivity, high stiffness, and are able to describe the outgassing and shrinking process, SiC was chosen primarily due to the familiarity of the material. SiC also has the advantage that numerous bonding techniques, specifically hydroxide bonding, can be used to joint parts together with high precision.

Although a three strut design seems like a more logical choice than four struts from a mechanical point of view since a four strut system will be an over-constrained system,

the decision to use four struts was made due to the main quadrant photodiode that is used downstream in the incoming beam optical path. This photodiode not only detects the interference signal between the received and reference beams, but also acts as a wavefront sensor by comparing the relative phase of the signal in the four quadrants. Using four struts will produce four equal shadows that will be imparted on each photodiode quadrant. By aligning the photodiode such that the shadows are 45° off the photodiode axis, then the effect of the shadows produced by the struts is equal in each quadrant. Although it may be possible to align three struts such that the shadows seen on the photodiode doesn't interfere with the wavefront sensing, further analysis is needed. The cross section of the struts was chosen such that the shadow produced on the quadrant photodiode was minimized while still providing enough area such that multiple bonding techniques could be used.

Finally, the holes in the primary and secondary were designed to allow a large flexibility in measurements. The use of either a Fabry-Perot cavity or Michelson interferometer can easily be implemented or changed depending on the specific measurement that needs to be made. The outer holes are ideal for Michelson interferometers that will measure the induced tilt of the telescope as it cools down, while the center holes are ideal for using a Fabry-Perot cavity to determine the in-band noise.

Once the telescope design had been finalized, the next task was to determine what temperatures would be expected on the telescope. The current design for an on-axis telescope has the secondary effectively seeing open space temperatures, while the primary experiences the heat generated from the optical bench. A finite element analysis of the LISA spacecraft was done at the Goddard Space Flight Institute and it was found that the expected operating temperature of the telescope was -71°C and that there was an axial gradient of about 1.5°C and negligible radial gradient. The low temperature gradient is due to the high thermal conductivity of the SiC. This is ideal since the uniform temperature will decrease the tilting effects of the telescope. In order to meet

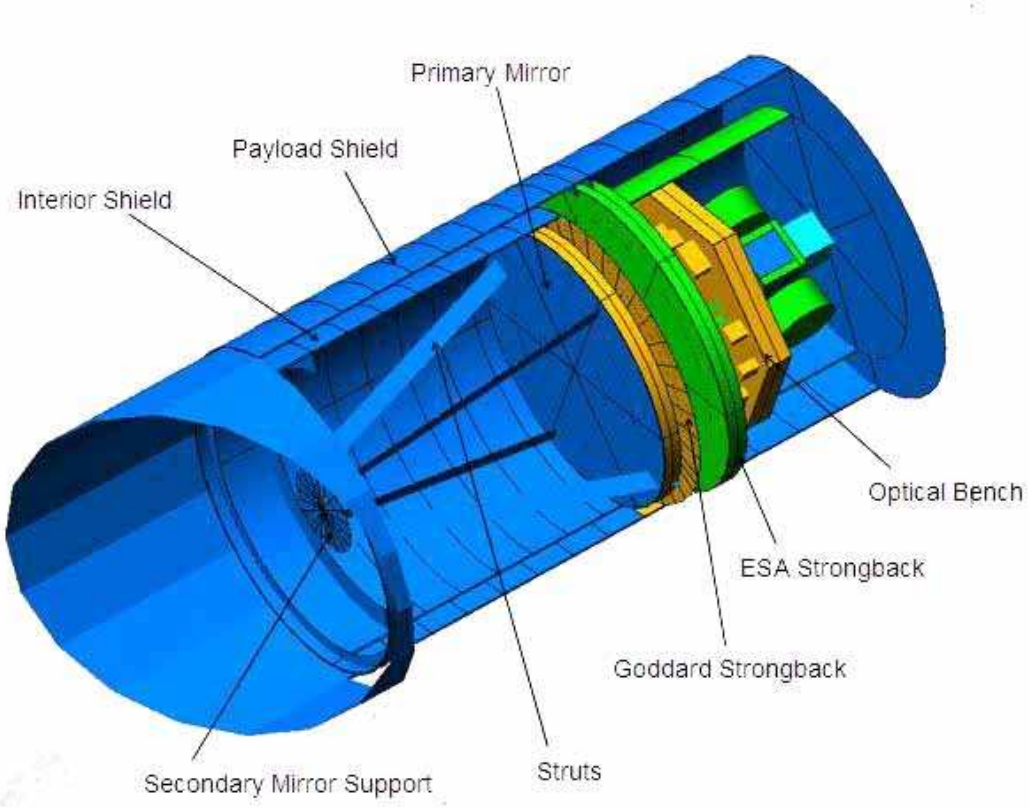

Figure 7-3. Payload assembly for one of the optical benches, on-axis telescope, and thermal shield for one "tube" of the LISA spacecraft. Each spacecraft will consist of two tubes. Figure courtesy of NASA.

the parallelism tolerances needed in the design of the telescope support structure, a high-stability, strong bonding technique needed to be chosen that also provided precision alignment. The hydroxide bonding technique was chosen due to its flexibility and ease of use, strong bond strength, and it ability to survive thermal cycling from room temperature to liquid nitrogen temperature.

7.3 Telescope Fabrication

A significant portion of the telescope design process occurred while discussing options with several SiC vendors. Each vendor has their own brand of SiC and their properties and design tolerances vary depending on the vendor and type of SiC. Eventually, it was decided that CoorsTek would supply the SiC parts. This was decided primarily due to the fact that they could supply the parts as needed in addition to meeting the polishing

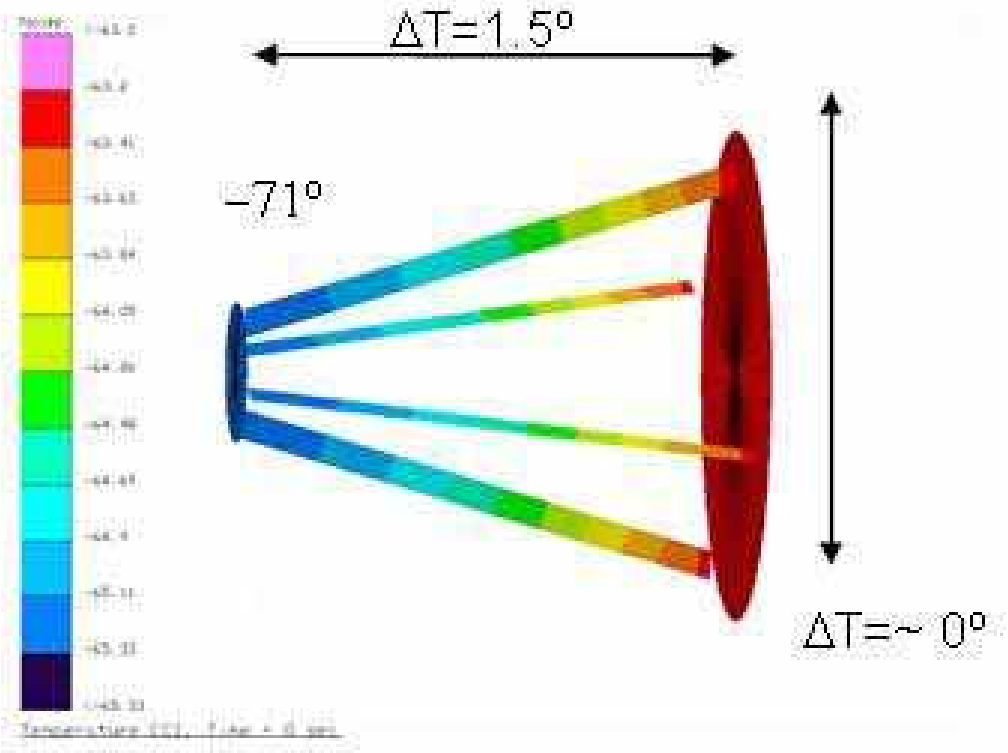

Figure 7-4. Expected operating temperatures on the LISA telescope. Figure courtesy of Angelique Davis at Goddard Space Flight Center,

tolerances required. Brazing and using an epoxy were considered as options to assemble the telescope, but were eventually discarded. Brazing and sintering would require elevated temperatures and could ruin any optical coatings that would be on the final telescope design, and so it was considered an unrealistic option. Using epoxy was discarded as an option due to the extreme difficulty in getting the right bond thickness in order to keep the parallelism requirement between the primary and secondary mirrors. It was decided that hydroxide bonding would be used because it allowed for precision bonding, has significant bonding strength, and could survive thermal cycling beyond the operating temperatures of the telescope. The use of hydroxide bonding also required that significant dimensional tolerances be placed on the telescope parts since large gaps cannot be filled using a sodium silicate solution.

The most stringent polishing specifications require that the struts all be to within 2 μm in length of each other and that the global flatness on the strut ends be to better than 2 μm. This was in order to avoid a gap large enough such that hydroxide bonding would not be able to bridge [68]. Estimates of an upper limit on the gap size hydroxide bonding could fill were placed as 8 μm and were based on data from the University of Glasgow. An analysis by the group members at GSFC showed that if the following polishing tolerances were met, then there would be gaps small enough that the hydroxide bonding process would be able to bridge:

Primary disk tolerance:

1. Flatness on four strut mount pads - 1 μm
2. Flatness on four small mirror mount pads, and center mirror mount surface - 5 μm
3. Flatness on primary disc backside - 0.5 mm
4. Surface finish on four strut mount pads, four mirror mount pads, and center mirror mount surface - 0.1 μm

Secondary disk tolerances:

1. Flatness on bottom side - 2 micron
2. Surface finish on bottom side - 0.1 μm

Strut tolerances:

1. Flatness on bottom surface - 1 μm
2. Parallelism between top surface and bottom surface - 2 μm
3. Perpendicularity between bottom surface and side surfaces and angularity- 1mm (This means the top of the strut could be 1 mm out of tolerance on all four sides at top of strut. The 1 mm tolerance is peak-to-valley)
4. Surface Finish on top and bottom ends - 0.1 μm
5. Variation in length between all four struts - 2 μm

The other polishing requirements (specifically the 0.1 μm requirement) were such that the surfaces would be flat enough for a strong bond to form when using the hydroxide bonding technique.

The primary, secondary, and struts were all fabricated and polished at the CoorsTek facility and shipped to GSFC where the tolerances were checked. It was found that the requirements had been met. An alignment jig was designed at GSFC and built by an outside company (Figure 7-5). The alignment jig held the struts in place and allowed them to slide up and down in a reproducible manner. In three of the four cases the alignment jig allowed the struts to be lifted and then placed back on the primary with no change in the surface contact between the strut and primary. In the other case, a small weight

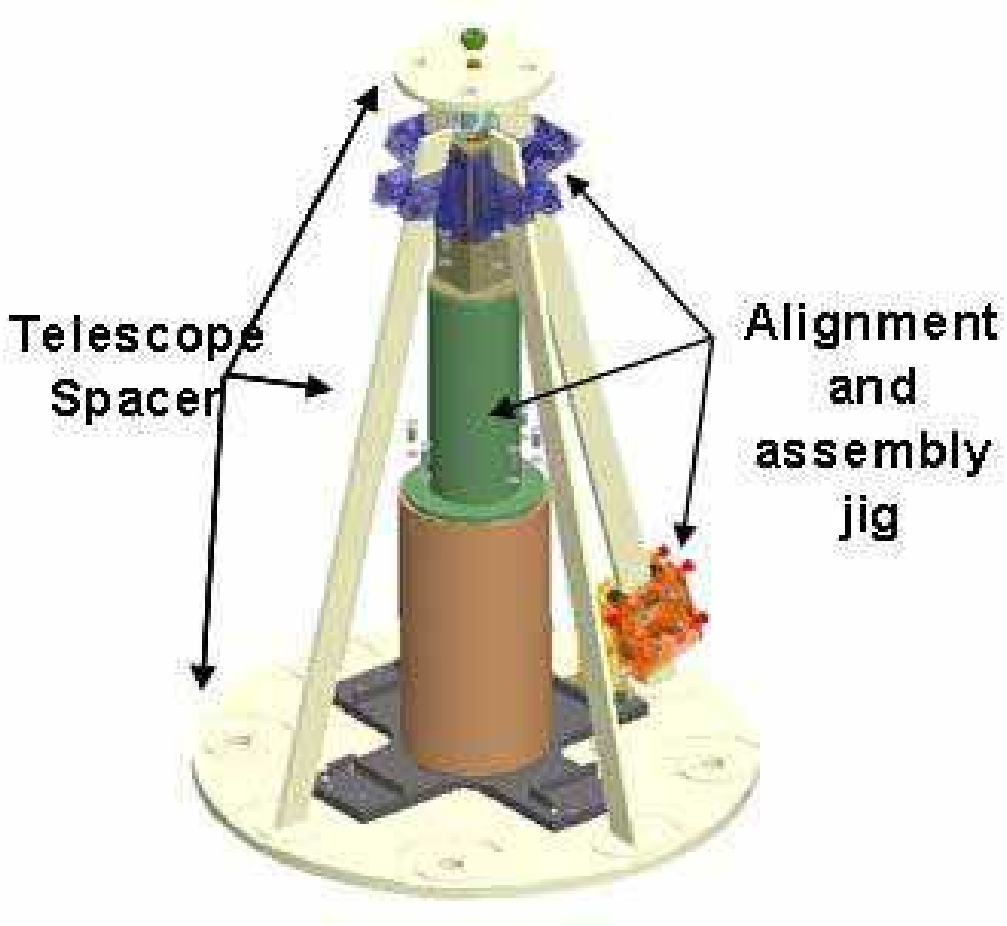

Figure 7-5. Diagram of how the telescope parts fit using the alignment jig. For clarity, not all of the strut clamps are shown. Courtesy of Jeff Livas at Goddard Space Flight Center.

(approximately 2.5 kg) was needed in order to keep the strut in suitable contact with the primary. This small weight was needed to counteract a spurious restoring force that would push the strut upwards. This sometimes resulted in small gaps unless a weight was placed on top of the secondary. All four struts were placed such that they were flush with the primary and the secondary was then placed on the struts. After doing this, a noticeable gap could be seen and the alignment of the struts were modified to produce the best suitable contact for hydroxide bonding.

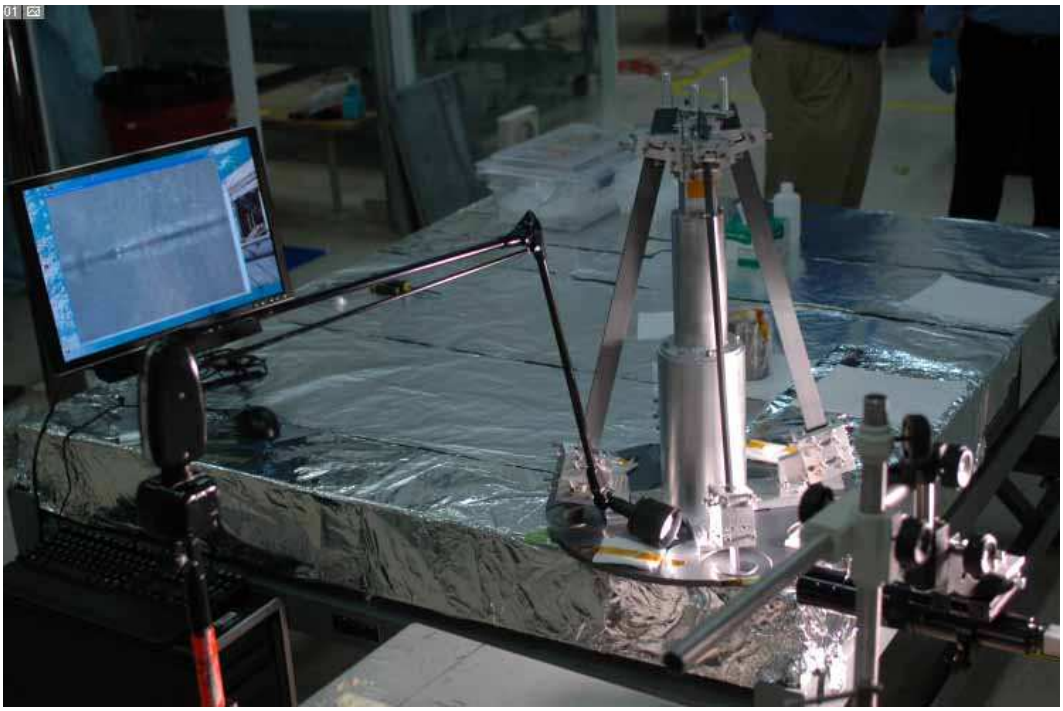

Figure 7-6. Picture of workstation to determine the gap sizes between the struts and either primary or secondary mirrors.

To produce this alignment, a weight of approximately 5 kg needed to be placed on top of the secondary to make sure the struts stayed flush with the primary and secondary as much as possible. From previous bonding experience, the additional weight should not cause a weakening of the bond. In fact, several SiC-BK7 bonds have been produced with significant strength by applying a downward force on the BK7 rod when bonding. All SiC pieces were cleaned thoroughly before bonding. The struts had been cleaned using methanol and the struts ends were sonicated in DI water for 30 minutes before being

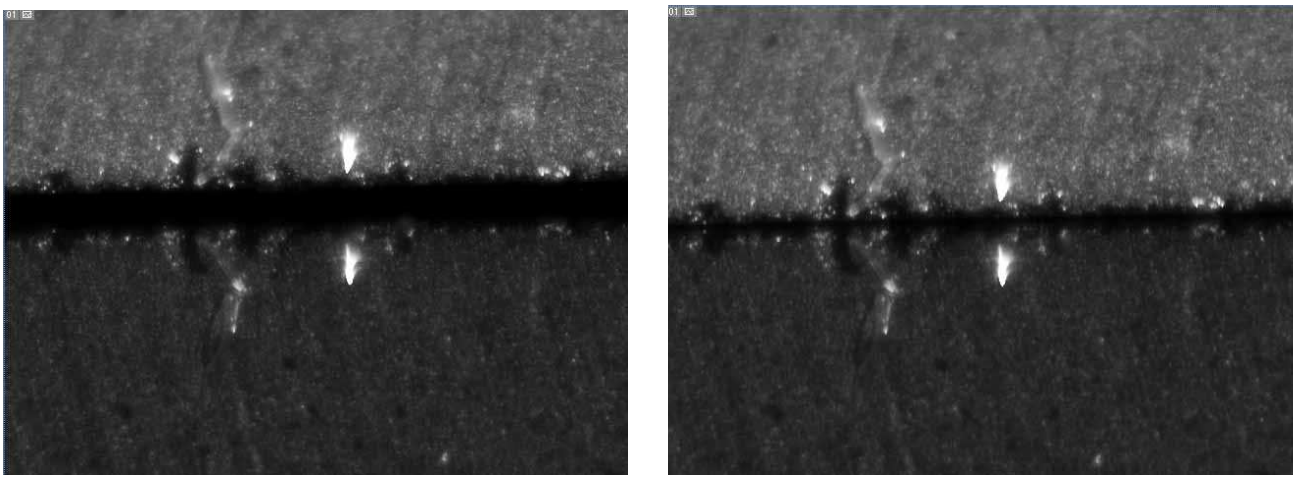

Figure 7-7. Gap size when not a strut is not properly aligned (left) and gap size when a strut is aligned properly (right). In some cases a downward force was needed in order for the gap to close. Gaps shown on the left side of the figure were typically 10 to 20 μm.

cleaned with methanol and clean room wipes. The primary and secondary were too big to be placed in the sonicator, so they were cleaned using methanol and clean room wipes. The bonding was done in a clean room that had been used a few weeks before to assemble the Lunar Reconnaissance Orbiter (LRO).

In order to bond the telescope pieces together, all four struts were lifted and approximately 3.0 μL of sodium silicate solution that had been diluted volumetrically by a 1:4 ratio was placed under the strut one at a time. After the solution had been applied the strut was then lowered and kept in place by the alignment jig. Once all four struts were lowered onto the primary, the same sodium silicate solution was applied to the top of the struts and the secondary was placed on top along with the weight. The bonds cured overnight in the clean room and were analyzed using the same method described for the alignment of the struts. Analysis of the bonds showed that all gaps had been filled by the sodium silicate solution, and in some cases a gap of $\sim$5 μm was seen to be filled.

The telescope was then transported by car from GSFC to the University of Florida where it was kept in a low-traffic, low-dirt room. It stayed in this room while preparation

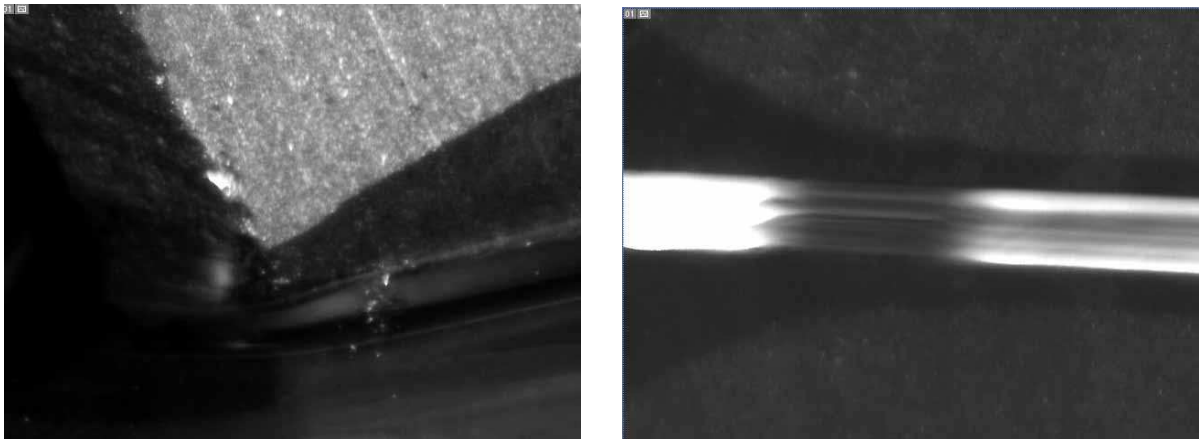

Figure 7-8. Picture of the sodium silicate solution filling in gaps between contact points of the struts.

were made to test the telescope. It was kept in this room for several weeks with no visible degradation to the structure. Within a month, it was noticed that one of the struts had come loose and was leaning against the opposite strut but was fully intact. The most plausible explanation was that it had been bumped by workers that had been in the room although no concrete evidence could be found to support this. There was also no evidence that would suggest the bond broke due to any other reason. The bonds were visually inspected and it was decided that the telescope should be cooled to -70°C to see if the damaged structure would survive the thermal cycling. A Michelson interferometer was set up in the center of the telescope to monitor the distance between the primary and secondary to determine if the bonds failed as the telescope is cooled. Both the vacuum chamber and Michelson interferometer are described in detail in section 7.4 and 7.6, respectively. Temperature sensors on the primary and secondary indicate they were cooled to -70°C and -60°C respectively before being brought back up to room temperature. A visual analysis of the telescope showed that it was still in-tact, but collapsed after applying a small amount of force to the secondary in the direction perpendicular the optical axis. One of the struts fell onto the mounting structure for the Michelson interferometer and

broke. The other two struts and secondary were caught before any damage could be done to them.

To gain an insight as to why the structure collapsed, the hydroxide bonds were investigated. It was determined that the alignment jig constrained the struts well in the in the radial plane, but not it a torsional motion, and because of this the telescope experienced a twisting motion as it was bonded (Figure 7-9). This was verified by a visual inspection of the bonds using a low-power microscope camera. Using the camera, it

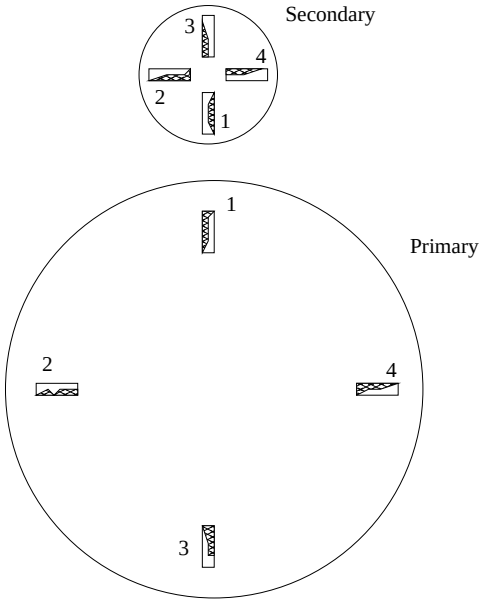

Figure 7-9. Representation of how the struts bonded to the primary and secondary at a tilt. The view of the secondary is as if one was looking up at the secondary from the primary. The view of the primary is as if one was looking at it from the secondary. The shaded areas are where the hydroxide bonds are thicker.

was clear the bond was thicker on one side of the struts than it was on the other. When looking at the primary and secondary, the thicker part of the bond was seen on opposite sides.

After a visual inspection of the bonds it was thought that another reason the telescope collapsed could have been to the bond not fully forming over the bonding surface. To test this, a piece of the strut that had broken was cut and analyzed using an XPS. One piece was cut where it looked like the bonding occurred, and one piece

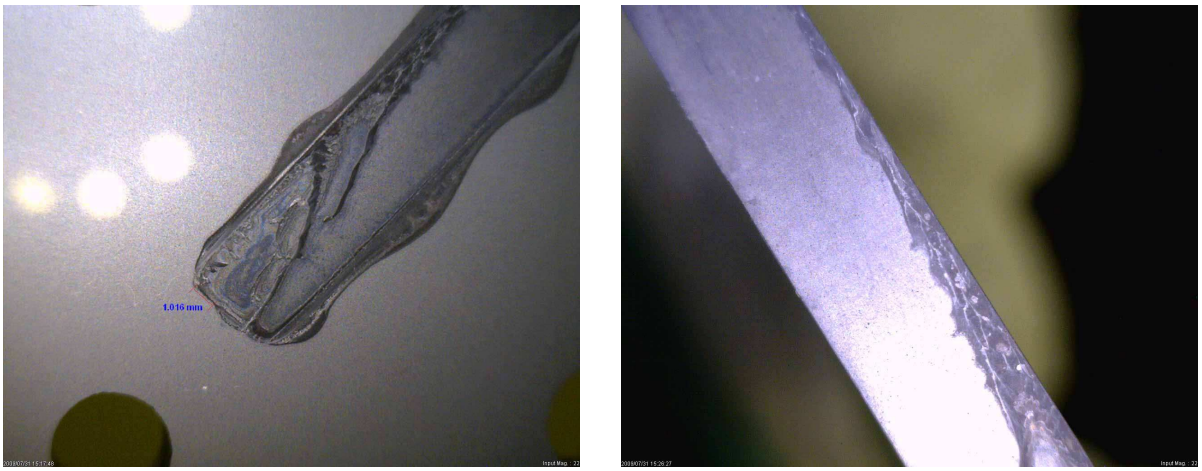

Figure 7-10. Picture of the secondary where the strut had bonded to it (left) and a picture of part of a strut that had been bonded (right). The bonds appear to be much thicker on one side, which leads to evidence that the structure twisted during bonding.

was cut where it appeared little or no bonding occurred. If no bonding took place, then there should be little or no SiO_2 peaks in the spectrum. Analysis of the XPS data proved inconclusive evidence for this theory. While the sample that appeared to bond showed a higher relative abundance of SiO_2 than that of the piece that appeared not to bond, the piece that appeared not to bond showed a spectrum similar to that of previously pieces that had bonded. The most likely theory for this is that the bond thickness of the sample that appeared not to bond is very thin, and so appears to not have bonded since the bonding agent is glass. In the sample that appeared to have bonded, the bond is most likely significantly thicker and is easier to see. Thus, it would appear that the majority of the surface did bond, but the strut bonded at a tilt which produced a thicker bond on one side of the strut than it did on the other [68].

After the analysis of the bonds were done, it was decided that the telescope parts would be repolished and rebonded. The primary and secondary were sent back to be repolished at the CoorsTek facility. When the original telescope pieces were made, copies were made by CoorsTek in case something happens to the original. Since one of the struts

was broken, it was decided that the back-up struts would be used and polished instead of the original struts. In order to prevent tilting of the struts on the next assembly, the alignment jig was redesigned to prevent motion in that direction. In addition, an aluminum mock-up of the telescope was fabricated to not only test out the alignment jig modifications, but to also determine how feasible hydroxide bonding will be for the telescope.

Since no conclusive evidence could be found as to why one of the struts came loose, a combination of hydroxide bonding and "sister-block" bonding will be used. The idea behind sister-block bonding is that a small rectangular piece of SiC (roughly 3 mm $\times$ 4 mm $\times$ 20 mm) will be epoxied to both sides of the strut where the strut meets the primary and secondary. Using the sister-block bonding will provide extra strength in addition to the hydroxide bonds. After extensive research was done into different types of epoxies, it was decided that EP21TCHT-1 from Master Bond would be used for the sister-block bonding. This choice was primarily due to the fast cure time at room temperature, low outgassing, low CTE, high strength, and ability to be used at cryogenic temperatures. As discussed in Chapter 3, for an epoxy to form appreciable strength, a rough surface and elevated temperatures are usually required to form the best bond. To assemble the telescope neither of these conditions would be ideal. The surface recommended would be too rough to keep the required parallelism of the telescope, and heating the telescope too much may cause the hydroxide bonds to fail. To determine what bond strength would be obtained using the sister-block bonding, a strut was bonded to a tile with the same polish as the telescope using the sister blocks and epoxy (Figure 7-11). The strut used for this test was cut using a tile saw from the strut that had broken after thermally cycling the telescope. The use of the tile saw made the strut such that it didn't sit flush with the tile, and a small gap could be seen.

The sister blocks were bonded and allowed to cure for two days at room temperature. The shear strength of the sister-block bonding was tested using the MCST and found

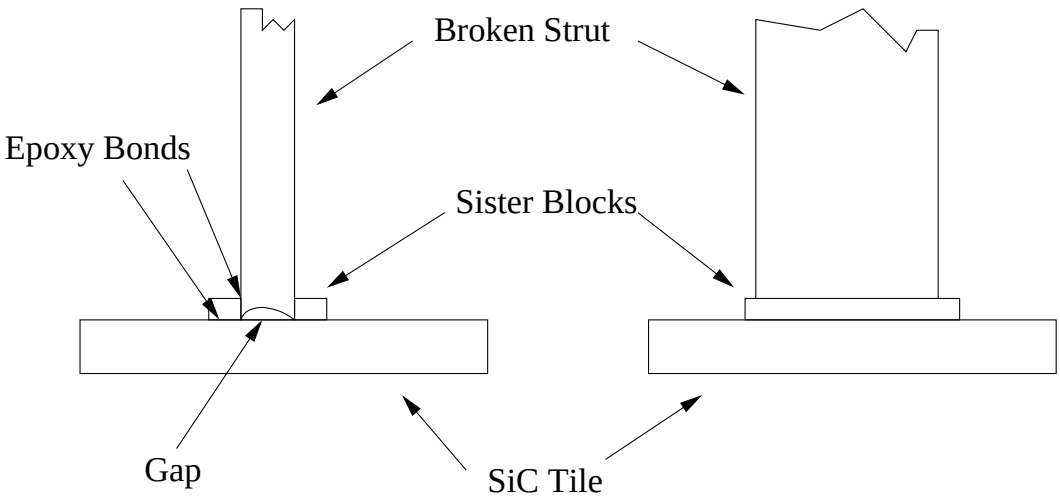

Figure 7-11. Diagram of how the sister blocks were used to bond the strut and tile.

to be 8 MPa. This is half of what is quoted by Master Bond and is most likely due to the smoother surface finish and lack of using an elevated temperature to cure the epoxy. Although the EP21TCHT-1 epoxy is capable of curing at room temperature, it is recommended that an elevated temperature be used to form the strongest bond. It is most likely these two factors that contributed to the lower shear strength. Despite the lower than expected shear strength, the sister-block bonding proved to be a method that produced significant strength (larger than using hydroxide bonding) and would be feasible for use when assembling the telescope again [68]. With this result, it was decided that hydroxide bonding will be used to allow for the precision alignment needed to keep the primary and secondary within parallelism tolerances, and the sister-block bonding will be used to provide additional strength to the telescope structure.

7.4 Vacuum Tank Design

After the expected operating temperature of the telescope was known, the next major task was to design a vacuum chamber that was capable of housing the telescope and all of the optics needed to make the necessary measurements while keeping the telescope at the correct temperature (-70°C) with the expected temperature stability. A vacuum chamber 1.4 m in diameter and 1.8 m high with several ports was already in

possession, but not being used at the time. The expected temperature of the telescope made it difficult to design thermal shields and a cooling mechanism. Although solid carbon dioxide has a temperature close to what is needed, the heat flow from the outside would require frequent refilling, and the source would have to be close to the telescope, which was nearly unfeasible. The next logical substance for cooling the telescope then became liquid nitrogen. Placing a reservoir beneath the telescope was considered, but ultimately ruled out due to the potential vibrational noise from filling the reservoir and having the liquid nitrogen evaporate that would couple into the sensitivity measurements. Using a lumped thermal model, a passive thermal shielding design with a liquid nitrogen reservoir close to the top of the tank was decided on. The initial design did not get to the desired temperature, but a few changes were made and the right temperature was met (Figure 7-12). To impede the flow of heat from the tank base to the telescope, a series of stainless steel tubes and plates were used. The plates are 1.2 m in diameter, 3.1 mm thick and the bottom face is covered in a layer of aluminized PET. The tubes are 25.4 mm long, 25.4 mm in diameter, and have a wall thickness of 1 mm. Ten tubes are placed on the tank base followed by a stainless steel plate. This layering is then repeated. Four aluminum rods 38 mm in diameter and 1 m long are screwed into the top stainless steel plate and a support structure that holds the reservoir in place. The top of the reservoir is equipped with a flange that allows a filling tube to be removed so the tank lid can be placed over the entire structure. In this manner, the reservoir and thermal shielding are enclosed in vacuum, but filling the reservoir can be done outside the tank. Four Macor rods 50.8 mm in diameter and 25.4 mm long are used to support an aluminum baseplate. This baseplate has holes drilled and tapped in a 25.4 mm square grid to allow optics to be placed on it. The aluminum baseplate is connected to the liquid nitrogen reservoir through the use of four copper rods 25.4 mm in diameter and 38 cm long. In addition, two layers of aluminized PET that are directly connected to the liquid nitrogen reservoir are used to shield the telescope from thermal radiation. The first layer surrounds the reservoir

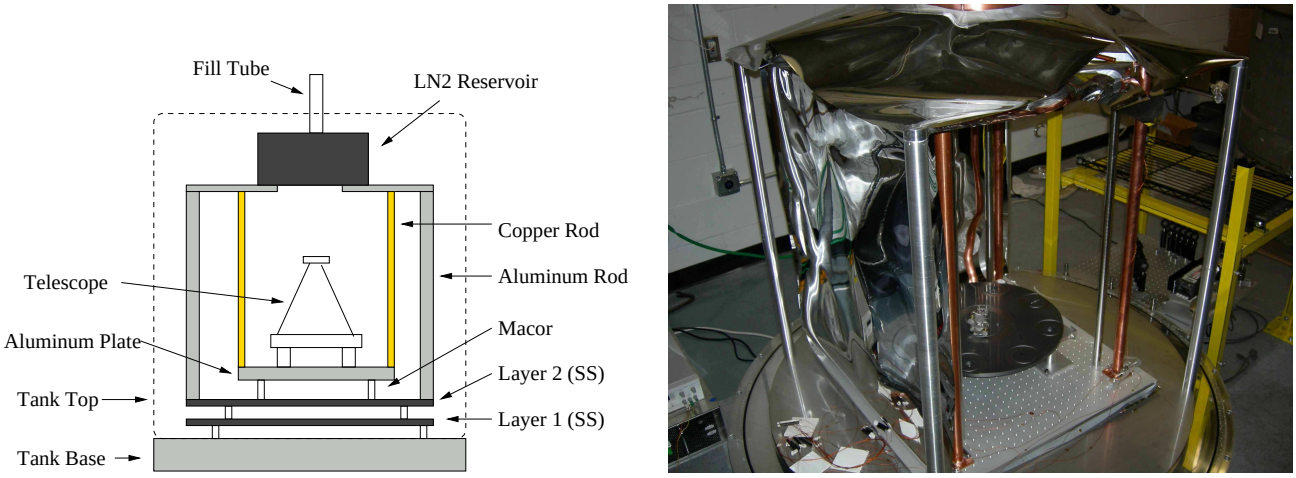

Figure 7-12. Representation of the system used to cool the telescope (left) and a picture of the finished system (right). Not shown on the left figure are the two layers of aluminized PET. The aluminized PET shields are partially shown in the figure on the right along with the SiC primary after the structure collapsed.

and second stainless steel plate. The second layer surrounds the telescope and aluminum baseplate. Cooling an aluminum mock-up of the telescope using this configuration produces a temperature of approximately -95°C on the primary. To raise the temperature to the necessary -70°C, a feedback controller using heaters and temperature sensors are used to produce the desired temperature. In this manner the temperature of the telescope can be changed over a wide range of temperatures. Although the computers models showed the nominal operating temperature of the LISA telescope was -70°C, this number varied depending on the model used, material properties, and were based on estimates of heat generated from the optical bench. Testing over a wide temperature range will give a greater insight into how well the telescope design will work on the LISA mission. Using the combination of thermal shields, temperature sensors, and heaters, a temperature range of -90 to -50°C can be obtained with a temperature stability of better than 100 $\mu K/\sqrt{Hz}$ above 1 mHz. The temperature measurement is limited by the sensitivity of the temperature sensors and the actual temperature stability of the telescope is expected to be better above 1 mHz. In addition, the secondary faces one of the thermal shields that is in

direct contact with the liquid nitrogen reservoir. In this manner, the secondary is seeing an environment that is similar to what would be expected on the the LISA spacecraft and the gradient across the optical axis of the telescope should form naturally.

7.5 Experimental Setup

The most significant aspects of the telescope are the in-band noise, the absolute length stability (or de-focusing), and the tilt between the primary and secondary. To test the in-band noise, a Fabry-Perot cavity will be made using mirrors placed on the primary and secondary. Initially a low Finesse ($\sim$600) cavity will be used to get a general characterization of the telescope and the optical setup. The lower Finesse cavity will allow a better tracking of how the optical system changes due to the temperature change. Although the noise levels are expected to be higher using the low Finesse cavity, once an understanding of how the optical system works, a higher Finesse cavity can be made using mirrors with a higher reflectance. Using the same method as described in Chapter 5, by beating a laser locked to a cavity on the telescope and a laser locked to a Zerodur cavity, the relative in-band noise can be found (Figure 7-13). By varying the temperature of the telescope, the in-band noise can be characterized as a function of temperature.

To test the absolute length stability of the telescope, a laser locked to a molecular iodine transition will be used. Iodine will be used instead of cesium due to the difficulties associated with operating the cesium cell in an oven. The process is similar to that described in Chapter 6, although an iodine cell and frequency doubling crystal are used instead of an oven and cesium cell. The frequency doubling crystal is needed in order to convert the 1064 nm light into 532 nm light since iodine has strong absorption lines at 532 nm. The details of the experimental setup will not be discussed due to the similarity of the cesium locking experiment presented in Chapter 6. By locking a laser to a molecular transition of iodine and beating it with a laser locked to a cavity on the telescope, the absolute stability of the telescope can be measured. This work is currently underway by other members of the group

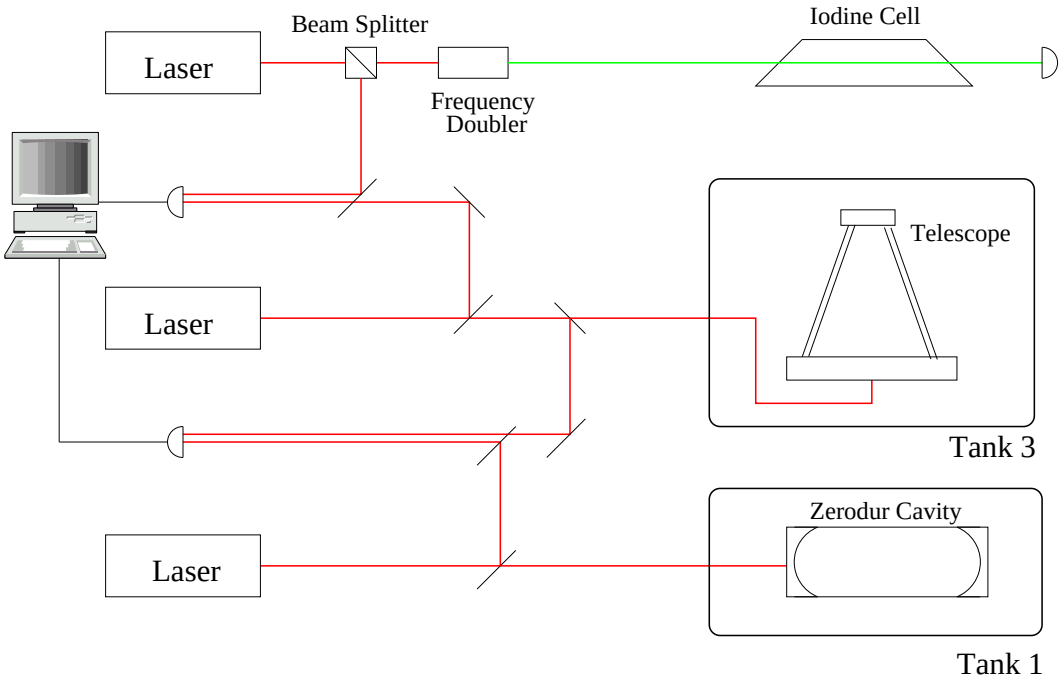

Figure 7-13. Representation of how the in-band and absolute length noise for the telescope will be found.

Although it would be ideal to determine the absolute stability of the telescope at -70°C, it may be more feasible to determine the absolute stability at room temperature. Determining the absolute stability at higher temperatures should provide an upper limit on the compactification of the material since dislocations are less likely to propagate through a material at lower temperatures, and are thought to be the leading cause of the shrinking of a material. Once the compactification has been characterized at higher temperatures, the temperature of the telescope could then be lowered for several weeks to determine the effects of lower temperatures on the densification process.

The telescope was designed such that the tilt between the primary and secondary could be measured in several ways. One way would be to use Fabry-Perot cavities placed around the central cavity used to measure the in-band noise. Locking a laser to each of the cavities and monitoring the beatnotes between them would provide a precise way to determine the induced tilt in the telescope, but would require the addition of four extra lasers. A more feasible way would be to set up Michelson interferometers around the

central cavity and monitor the outputs over time. Placing a power beamsplitter with a highly-reflective coating on one face of the beam splitter and positioning it on the primary and securing a mirror to the secondary will allow the length change between the primary and secondary to be monitored with sub-micron precision. Using Michelson interferometers will provide the necessary measurements while not requiring the addition of several additional lasers since a pick-off from the primary laser beam can be used to form several Michelson interferometers.

7.6 Results

The failure analysis of the bonds, determining the proper actions to re-bond the structure, and repolishing the struts set the project back close to a year. The only stability data that was gathered from the telescope is from the Michelson interferometer that was running while the telescope was cooled down (Figure 7-15). To set up the interferometer, a non-polarizing beam splitter was mounted on the primary and a mirror was mounted on the secondary (see Figure 7-14). A mirror was placed on the primary a few inches from the beam splitter. Since the distance between the primary and secondary is about a factor of ten greater than the distance between the mirror on the primary and the beam splitter, the interferometer will essentially measure the change in distance between the primary and secondary.

From the data there are four noticeable characteristics in the data and each one will be discussed. The first characteristic is the fact that the time between peaks slowly increases over time. This is expected and is due to the temperature of the telescope reaching its equilibrium value. Initially the telescope cools down rapidly, causing the peaks to be closer together. As time increases, the telescope temperature reaches its equilibrium temperature slowly, causing the peaks to spread out in time. Analysis of the telescope temperature data shows that as the slope of the temperature decreases, the peaks spread out more. Towards the end of the data, the peaks begin to get closer again, which is due to the telescope heating up.

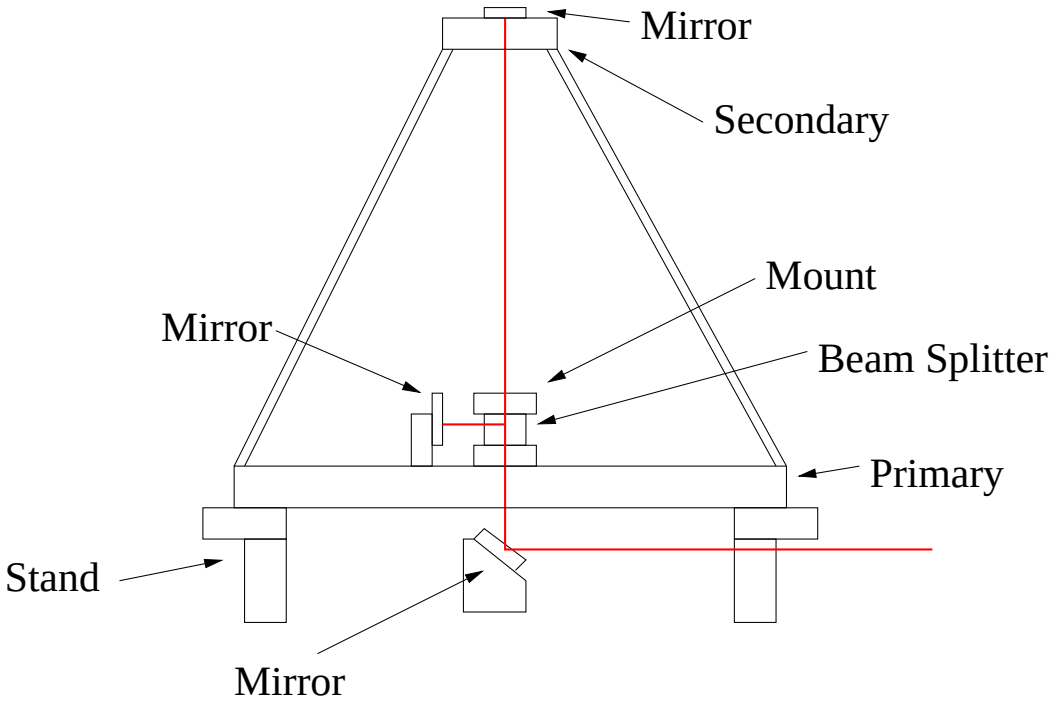

Figure 7-14. Representation of how the Michelson interferometer was setup to measure the distance change between the primary and secondary..

The second trend in the interferometer data is that the peak-to-peak values slowly decrease over time. This is due to the misalignment of the interferometer as the rods that hold the aluminum baseplate shrink. Realignment of the interferometer was done as the telescope was cooling down and this can be seen from the offset of the peaks increasing in addition to the peak-to-peak values increasing.

Another characteristic of the data are the spikes that can be seen. The spikes where the voltages drops to zero can be accounted for from occasionally blocking the laser when realignment of the interferometer was done. These are almost always seen before a change in amplitude of the voltage can be seen. The other spikes were seen when the liquid nitrogen reservoir was refilled. The exact cause of this is unknown, but it is most likely due to a settling or shifting of the thermal shields that slightly misaligned the interferometer.

The last characteristic of the data is the high frequency noise of the data as shown in Figure 7-16. This is believed to be due to a spurious interferometer that was induced

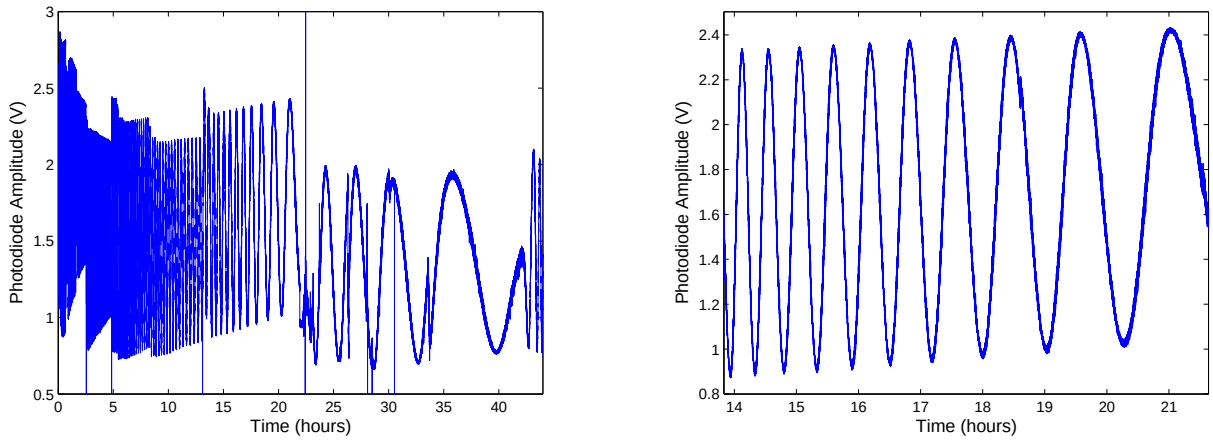

Figure 7-15. Photodiode output of the Michelson interferometer as the telescope was cooled down (left) and a detailed view of the same output over a shorter period of time (right).

from using an ND filter before the detection photodiode to avoid saturation. Subsequent interferometers on the final telescope design will use substantially less power, and so this problem should not be present. Noise associated from the drift in the laser was ruled out due to the periodic nature of the signal, and the fact that the laser drifts by less than 50 MHz/day and is significantly less than the FSR of the long arm of the interferometer.

By counting the number of fringe peaks and using the equation $\Delta d = n\lambda/2$, where Δd is the change in distance, n is the number of fringe peaks, and λ is the wavelength of the laser, the total distance the telescope shrunk can be found. From the interferometer data, it was calculated that the telescope shrunk by $\sim$60 μm. The distance the telescope shrunk can also be found using the telescope temperature and the CTE as a function of temperature provided by CoorsTek. The telescope initially started at 20°C and cooled down such that the final temperature of the secondary was -60°C and the primary was -70°C. Taking the average of these values, the assumed final temperature of the telescope is -65°C. The plot of the CTE versus temperature is shown in Figure 7-17 and is roughly linear between 200 and 300 K. Fitting a straight line between this temperature range results in a CTE given by $CTE_{ppm} = 0.011 \times T - 1.11$, where T is the temperature of the

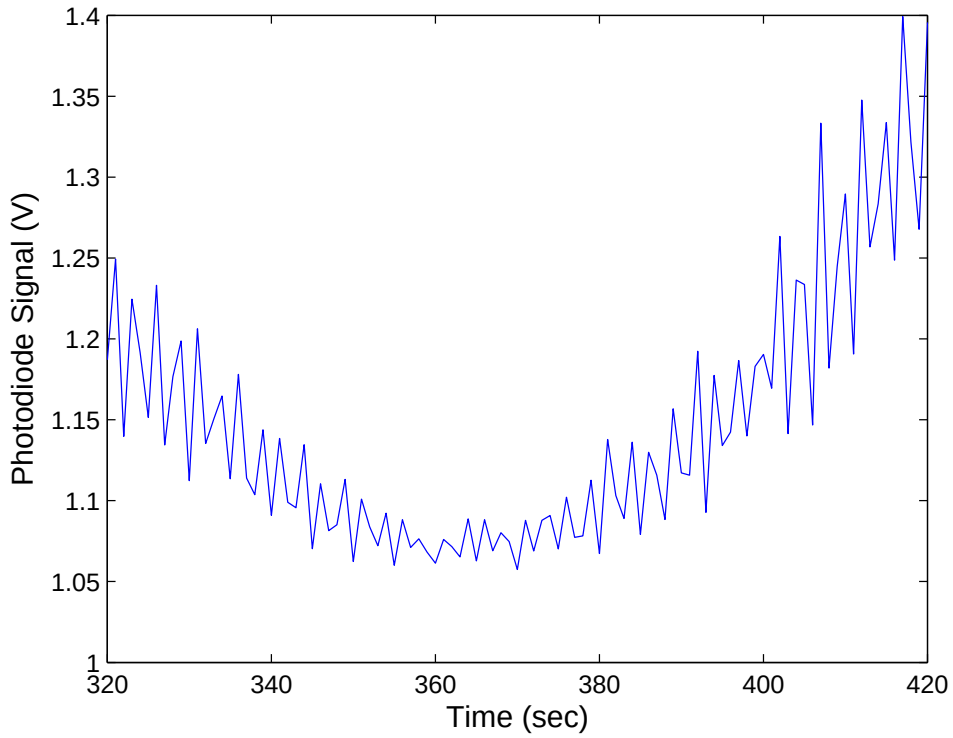

Figure 7-16. Detailed view of the oscillations in the Michelson interferometer data.

telescope in Kelvin. Using the average of the CTE at 20°C and -65°C, and multiplying by the change in temperature (85°C) and length between the primary and secondary (0.6 m), results in a length change of ∼85 μm.

Although the amount the structure shrank using the Michelson interferometer should be less than the value found using the CTE values since the interferometer arm on the primary will shrink as the telescope cools down, the discrepancy between the two should not be as large as it is. The cause of the discrepancy is not known and further testing will need to be done on the aluminum mock-up before being used on the SiC telescope.

Currently, work is underway to rebuild the telescope spacer. The alignment jig was redesigned and used to bond an aluminum mock-up using both hydroxide bonding and sister-block bonding. The mock-up was cooled to -80°C, warmed back to room temperature, and no degradation of the bonds could be found. Thus, the combination of using hydroxide bonding and epoxying the sister blocks should provide more than enough

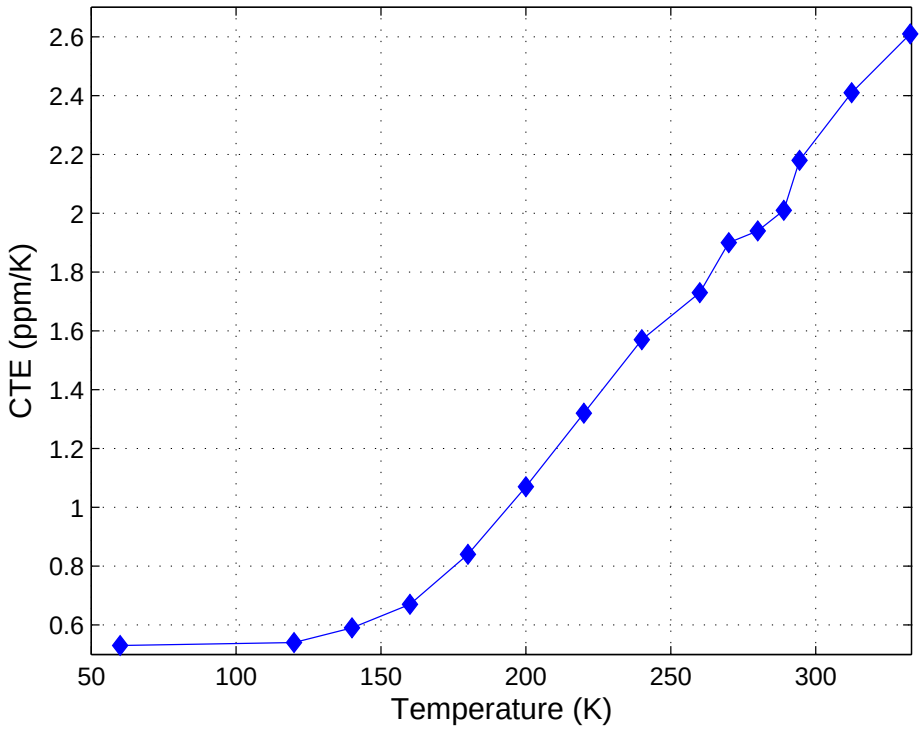

Figure 7-17. CTE as a function of temperature for CoorsTek UltraSiC SiC. Data obtained from David Bath at CoorTek.

strength to the structure. It remains to be seen how the epoxy will behave during the relative stability measurements.

CHAPTER 8
LISA BACK-LINK FIBER PHASE STABILITY

The LISA mission consists of three spacecraft each separated by five million kilometers. Each of these spacecraft contain two optical benches that contain lasers which point to the adjacent spacecraft. Each optical bench contains a proof mass that the spacecraft orientates itself around to provide a drag-free environment. Due to the geodesics of the proof masses, the lengths between the spacecraft will change by as much as 1% over the course of a year. To track the breathing of the spacecraft, the angle between the optical benches on a spacecraft will have to change by as much as 1°.

If the LISA constellation is thought of as a Michelson interferometer, then one spacecraft acts as a beamsplitter, while the other two spacecraft act like mirrors. Because two separate lasers are used at the beamsplitter spacecraft, they will need to be interfered in order to make the appropriate phase measurements. This then becomes a problem since the angle between optical benches will change over time.

The proposed solution is to use an optical fiber to transfer the beam from one bench to the other, and vice-versa. The fiber will contain both counter-propagating beams and will induce additional phase noise as it travels through the fiber but can be subtracted out through the use of appropriate metrology. If the sensitivity of LISA is not to be spoiled from induced fiber noise, then the differential phase noise of the counter-propagating beams must be less than 10^{-6} cycles/$\sqrt{\text{Hz}}$.

The current project plan is to use a single-mode polarization-maintaining fiber approximately 0.5 to 1.0 m to accommodate the counter-propagating beams. Experiments at both the Jet Propulsion Laboratory (JPL) and the Albert Einstein Institute (AEI) in Hannover have failed to confirm that a bi-directional fiber meets the LISA requirement and both appear to be limited by systematic noise [93], [94].

In order to test the differential phase noise induced in counter-propagating beams through an optical fiber, a Sagnac interferometer was constructed and an optical fiber was

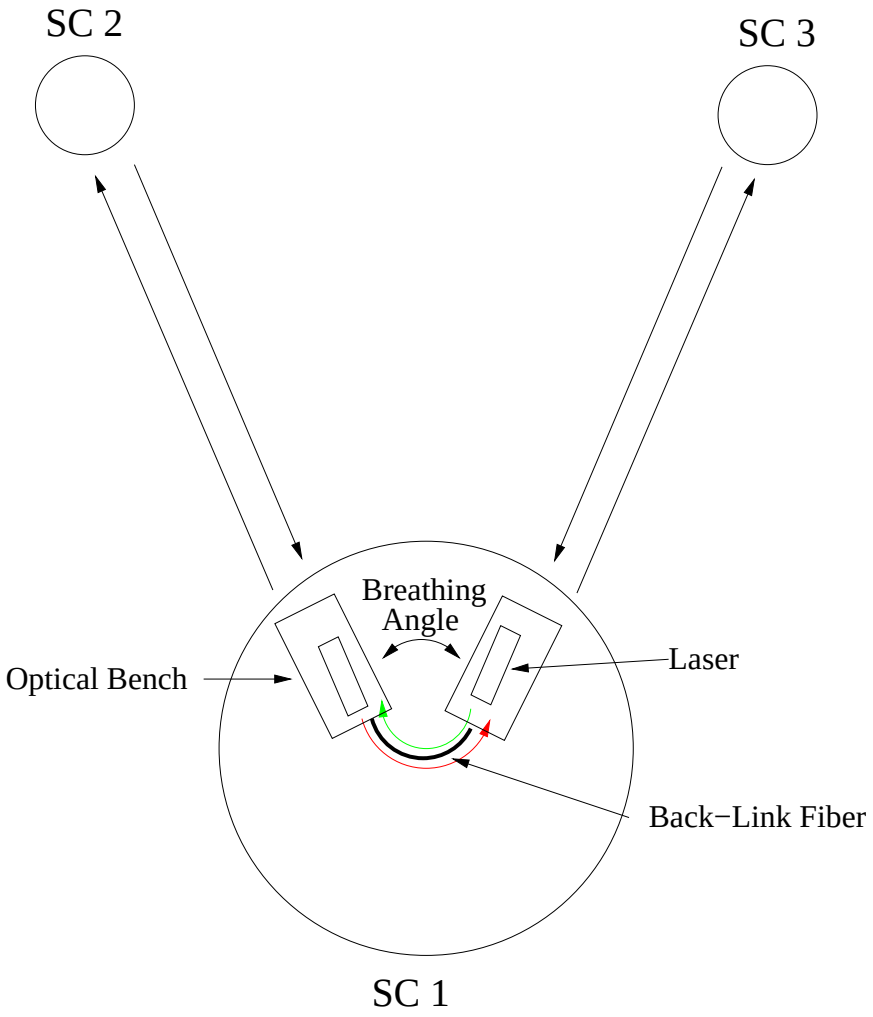

Figure 8-1. Representation of the three LISA spacecraft, the optical benches, and the back-link optical fiber.

placed in its path. The Sagnac configuration takes advantage of the fact that all noise will be common except that of the noise induced from the fiber since the optical paths are the same, but with opposite directions. This chapter contains an introduction to the Sagnac effect and interferometer, the experimental setup used to test the differential noise in an optical fiber, and the results obtained from this setup.

8.1 Sagnac Effect

Detection of rotation with the use of light was first demonstrated by Sagnac in 1913 by showing that two waves acquired a phase difference by propagating in opposite directions around a loop interferometer that was rotating. The kinematic description

of the Sagnac effect is simple and is demonstrated by considering a hypothetical interferometer with a circular path in vacuum as shown in Figure 8-2

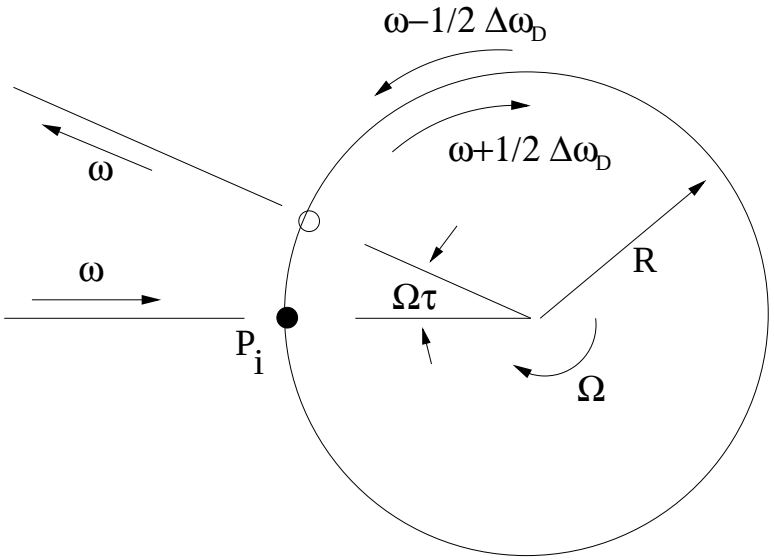

Figure 8-2. Diagram of a rotating loop interferometer to illustrate the Sagnac effect. Doppler shifted frequencies are shown with respect to the inertial space.

When the interferometer is not rotating, then the counterpropagating beams will have equal path lengths since the light travels at the same velocity in both directions. This will result in both beams returning to the same point P_i of injection after a time of $\tau = 2\pi R/c$, where R is the path radius and c is the speed of light in vacuum. When the interferometer is rotating at a rate Ω and the observer is stationary in the inertial frame, then the point P_i moves through an angle $\Omega\tau$ during the propagation time τ. Hence, the difference in propagation times to lowest order in $R\Omega/c$ is given by [95]

$$\Delta\tau = \frac{(2\pi + \Omega\tau)R}{c} - \frac{(2\pi - \Omega\tau)R}{c} = \frac{4\pi R^2\Omega}{c^2}. \tag{8–1}$$

For a continuous wave of frequency ω, the corresponding phase shift becomes

$$\Delta\phi = \omega\Delta\tau = \frac{4\pi R^2\omega}{c^2}\Omega. \tag{8–2}$$

This result will remain unchanged when the interferometer is filled with a medium of refractive index n since the Fresnel-Fizeau drag effect due to the movement of the medium will compensate for the increased optical path lengths [96].

The Sagnac phase shift may be calculated using the Doppler frequency shift, but will lead to the same result as in Eq. 8–2 since the Doppler shift will cause the wavelength from the wave propagating in one direction to be different from that of the wave traveling in the other direction. Thus, the two interpretations of the Sagnac effect are equivalent (to lowest order in RΩ/c).

A more rigorous approach to the Sagnac phase difference is to solve the electrodynamic propagation equations in the rotating medium [97], but will not be considered here. What can be derived from the electrodynamic formulism is that the phase shift depends only on the light frequency ω and on the dot product of the equivalent area vector of the mean optical path and the rotation rate vector. This results in a phase difference of

$$\Delta\phi = \frac{4\omega}{c^2}\mathbf{A}\cdot\mathbf{\Omega}. \tag{8–3}$$

Thus, the Sagnac effect is due to the difference in propagation times of the waves as they travel around the rotating loop. The waves frequency acts as a clock to measure this time difference and is independent of the velocity of the physical substrate used. Using a higher frequency light will result in a larger phase difference.

8.2 Polarization-Maintaining Optical Fibers

Even if a fiber has a circularly symmetric design, it will exhibit some degree of birefringence because there is always some amount of stress which will break the symmetry. As this happens, the polarization state of the light traveling in the fiber will change in an uncontrolled manner which is typically wavelength and temperature dependant.

To circumvent this problem, a fiber with a strong built-in birefringence will preserve the polarization state even if the fiber is bent as long as the input polarization

state is aligned with one of the birefringent axes. This type of fiber is known as a polarization-maintaining optical fiber. The propagation constants of the different polarization states are different since the strong birefringence will cause the relative phase of copropagating modes to drift away rapidly. The most common method to introduce a strong birefringence is to include two stress rods of a modified glass composition in the preform on opposite sides of the core as shown in Figure 8-3. The stress rods do not necessarily need to be cylindrical, but the modified glass composition must have a different coefficient of thermal expansion.

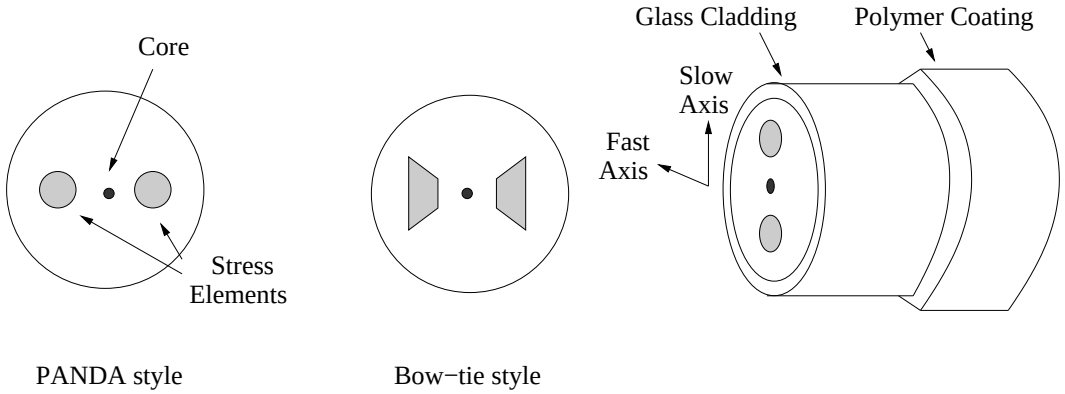

Figure 8-3. Both the PANDA and bow-tie polarization-maintaining fiber styles are shown along with the core and stress elements.

The two most common styles of polarization-maintaining fibers are the PANDA and bow-tie, although others are available. The two styles are based on the stress rods used that run parallel to the fiber's core. PANDA stress rods are cylindrical, while the bow-tie design uses trapezodial prism stress rods. For most applications other than the telecommunications industry, either style can be used, although PANDA style fibers are typically used more often since the uniformity of the fiber is much easier to maintain.

In the case of the PANDA design, the optical core of the fiber is manufactured independently of the stress rods, allowing it to be made with high chemical purity. Core compositions are either a germanium-doped or pure silica core. The stress rods are then inserted into circular holes drilled into the pristine preform allowing for a higher degree of

splicing and coupling to be done. This design also allows for lower splice loss and higher extinction ratios when compared to other designs. The PANDA construction allows for independent control over the optical core, stress rod size, location, and composition. The control of these four factors will determine the performance of the fiber, and the ability to control each one of them makes the PANDA design extremely versatile, all while maintaining the polarization state in the optical fiber.

Polarization-maintaining fibers should not be confused with single-polarization fibers, which can only guide light of a certain polarization. Polarization-maintaining fibers are used in applications where the polarization state cannot be allowed to drift as a result of temperature changes, such as for use in fiber optic gyroscopes, fiber interferometers, and certain fiber lasers [98]. These fibers usually require a much greater degree of alignment than for a standard fiber, and the polarization direction is also required for optimal performance. Propagation losses are also higher than for standard fibers, and not all types of fibers are easily obtained in polarization-preserving form.

8.3 Experimental Setup

In order to determine the amount of differential phase noise induced by a fiber optic cable with counter-propagating beams, a polarizing Sagnac interferometer was constructed and a fiber was placed in the path of the beam as shown in Figure 8-4. Both a qualitative and quantitative description of the setup are given.

8.3.1 Qualitative Description

The interferometer consists of three polarizing beam splitters (PBS1-PBS3), three half wave plates (HWP1-HWP3), one quarter waveplate (QWP), two collimating lenses to focus the light into the fiber, one fiber, one calcite wedge, one balanced photodetector (BPD), and four mirrors that are used for alignment into the fiber. The collimating lenses are free-spaces lenses and are not directly attached to the fiber. In order to get the differential phase signal, the incident beam is split before the fiber, then recombined after

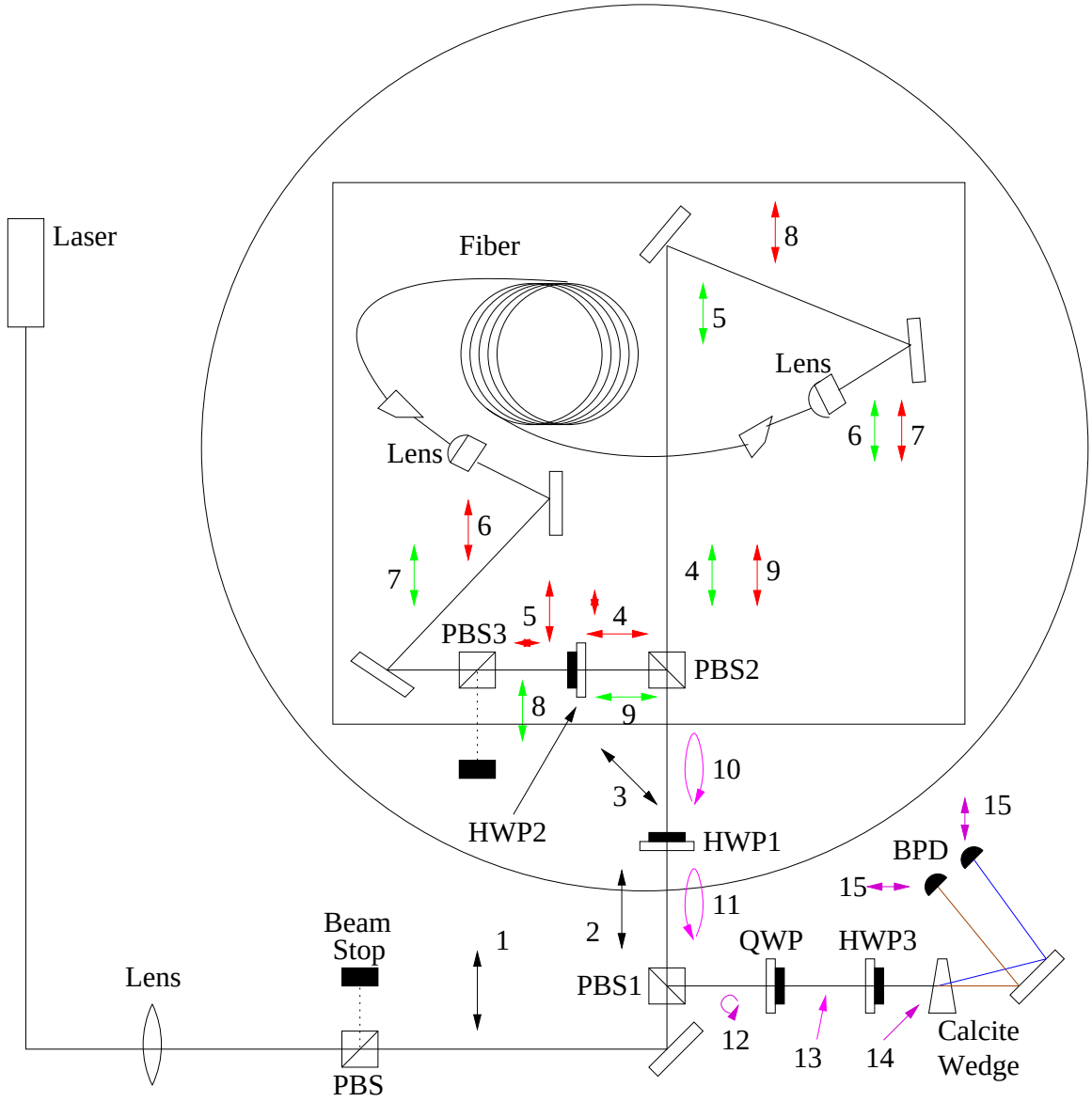

Figure 8-4. Sagnac interferometer used to measure the accumulated differential phase noise in an optical fiber. HWP1-3 are half wave plates, PBS1-3 are polarizing beam splitters, QWP is a quarter wave plate, and the balanced photodetector is represented by BPD.

the fiber in the following 15 steps (for a reference, the numbers in figure 8-4 match up with the numbers below):

1. The beam from the laser passes through a lens that produces a beam with a Rayleigh range of ∼1 m. This allows the beam to be well collimated throughout the interferometer. The beam then passes through a polarizing beam splitter (PBS) to produce a beam with almost all p-polarization.

2. The beam then passes through another polarizing beam splitter (PBS1) that acts as both an additional polarization cleaner for the incident beam and the pick-off to the detector for the outgoing beam from the interferometer.

3. The beam passes through a half wave plate (HWP1) such that there is now an equal amount of s- and p-polarization in the beam.

4. The beam is incident on a polarizing beam splitter (PBS2) that splits the beam into its polarization components. The transmitted beam (green) contains p-polarization only, while the reflected beam (red) contains primarily s-polarization, with a small amount of p-polarization due to the beam splitters.

5. The transmitted beam (green) continues towards the fiber, while the reflected beam (red) passes through a half wave plate (HWP2) orientated such that the polarizations are rotated by 90°.

6. The transmitted beam (green) passes through a collimating lens and is incident on the fiber. The reflected beam (red) passes through another polarizing beam splitter (PBS3) to isolate the spurious s-polarization that is produced from PBS2. In this manner both beams incident on the fiber have the same polarization as they go through the fiber.

7. Both beams emerge from the fiber with ∼80% efficiency.

8. The transmitted beam (green) passes through PBS3 cleanly, although ∼5% of the power is lost. The reflected beam (red) continues towards PBS2.

9. The transmitted beam (green) passes through HWP2 and is rotated by 90°, while the reflected beam (red) continues towards PBS2.

10. The beams then recombine at PBS2. If there was no differential phase noise induced from the system, then the resulting beam would emerge from the Sagnac interferometer with linear polarized light in equal amounts. If any differential phase noise is picked up from the interferometer, then the beams will recombine to produce elliptically polarized light. The minor axis of the elliptically polarized light serves as a measure of the differential phase accumulated in the interferometer.

11. The elliptically polarized light passes through HWP1 and changes the "handedness" of the beam. This means that if the beam was rotating clockwise, it would now be rotating counter-clockwise, and vice-versa.

12. Once the elliptically polarized light is incident on PBS1 the majority of the s-polarized light will be reflected, while only a fraction of the p-polarization will be reflected. The result is such that an elliptically polarized beam is reflected, but with a much lower power. If PBS1 was ideal and only the s-polarization was reflected, then the output of this port would serve as a measure of the accumulated differential phase.

13. The quarter wave plate (QWP) is orientated such that the beam is linearly polarized after the elliptically polarized beam passes through.

14. The linearly polarized light then passes through a half wave plate (HWP3) with an orientation such that the emerging beam has equal amplitudes of s- and p-polarizations.

15. The beam then passes through a calcite wedge which separates the polarizations that are then separately incident on a balanced photodetector (BPD). A calcite wedge is used to separate the polarization more cleanly than through the use of a polarizing beam splitter. The output on the BPD will read zero (or possibly a small offset) if the orientations of the waveplates are correct, and the beam is properly aligned into the fiber. Any accumulated differential phase from the interferometer will cause the s-polarization at step 12 to be larger and will propagate through the waveplates such that the amount of power on the BPD is not the same and a non-zero voltage will be measured.

The advantage of this setup is that both the reflected and transmitted beams from PBS2 see the same optical components and both experience two transmissions and one reflection through a polarizing beam splitter. These noise sources are common to each beam and will cancel on the balanced photodetector, resulting in only the differential noise induced from the optical fiber.

8.3.2 Quantitative Description

Now that a qualitative description of the Sagnac interferometer has been presented, a more rigorous approach is taken to understand how to extract the differential phase noise. The following analysis assumes an ideal case of the interferometer to determine the phase shift from the balanced photodetector.

After both beams have traveled in opposite directions around the interferometer, the resulting electric field after they recombine (step 10) is given by

$$E_{out} = E_G e^{i\phi_G}\hat{p} + E_R e^{i\phi_R}\hat{s},$$

where E_G and ϕ_G are the electric field and phase of the beam after traveling the green path in Figure 8-4, and E_R and ϕ_R are the electric field and phase of the beam after traveling the red path. If we use the following definitions

$$\bar{E} = \frac{1}{2}(E_G + E_R) \qquad \Delta E = \frac{1}{2}(E_G - E_R) \tag{8–4}$$

$$\bar{\phi} = \frac{1}{2} = (\phi_G + \phi_R) \qquad \Delta\phi = \frac{1}{2}(\phi_G - \phi_R), \tag{8–5}$$

then our electric field after recombining becomes

$$E_{out} = e^{i\bar{\phi}}[(\bar{E} + \Delta E)e^{i\Delta\phi}\hat{p} + (\bar{E} - \Delta E)e^{-i\Delta\phi}\hat{s}]. \tag{8–6}$$

The common phase shift ($e^{i\bar{\phi}}$) can be ignored since it is a factor that will be carried around and eventually canceled when finding the photodiode signals. Sorting Eq. 8–6 into a more manageable form results in

$$E_{out} = (\hat{p} + \hat{s})(\bar{E}cos\Delta\phi + i\Delta Esin\Delta\phi) + (\hat{p} - \hat{s})(i\bar{E}sin\Delta\phi + \Delta Ecos\Delta\phi). \tag{8–7}$$

As the combined electric field in step 10 passes through HWP1, the half waveplate will rotate both polarizations by 45°. This will transform the electric fields in the following manner:

$$\frac{1}{\sqrt{2}}(\hat{s} + \hat{p}) \rightarrow \hat{p} \qquad \frac{1}{\sqrt{2}}(\hat{s} - \hat{p}) \rightarrow \hat{s}, \tag{8–8}$$

which transforms the electric field at step 11 into

$$E_{11} = (\bar{E}cos\Delta\phi + i\Delta Esin\Delta\phi)\hat{p} + (i\bar{E}sin\Delta\phi + \Delta Ecos\Delta\phi)\hat{s}. \tag{8–9}$$

As the laser passes through PBS1, it will reflect all of the s-polarized light, and a fraction, r, of the p-polarized light. This results in an electric field at step 12 of

$$E_{12} = r(\bar{E}cos\Delta\phi + i\Delta Esin\Delta\phi)\hat{p} + (i\bar{E}sin\Delta\phi + \Delta Ecos\Delta\phi)\hat{s}. \tag{8–10}$$

Aligning QWP such that its fast axis is aligned with $\hat{p}$ and its slow axis with $\hat{s}$ is the ideal case since this will only produce an addition of a 90° phase shift to the s-polarized light. This results in an electric field at step 13 of

$$E_{13} = r(\bar{E}cos\Delta\phi + i\Delta Esin\Delta\phi)\hat{p} - (i\bar{E}sin\Delta\phi - \Delta Ecos\Delta\phi)\hat{s}. \tag{8–11}$$

In the ideal case, HWP3 would be aligned such that it rotates both polarizations by 45°. If there were no differential phase shifts accumulated in the interferometer, then there would be no s-polarized light, and HWP3 would rotate the p-polarization such that an equal amount of light fell on both photodiodes on the balanced photodetector. Rotating Eq. 8–11 by 45° results in

$$E_{14} = r(\bar{E}cos\Delta\phi + i\Delta Esin\Delta\phi)(\hat{p} + \hat{s}) - (i\bar{E}sin\Delta\phi - \Delta Ecos\Delta\phi)(\hat{s} - \hat{p}). \tag{8–12}$$

Rearranging Eq. 8–12 into its s- and p-polarizations results in

$$\begin{aligned} E_{14} = &[(r\bar{E}cos\Delta\phi + \bar{E}sin\Delta\phi) + i(r\Delta Esin\Delta\phi - \Delta Ecos\Delta\phi)]\hat{p} \\ &+[(r\bar{E}cos\Delta\phi - \bar{E}sin\Delta\phi) + i(r\Delta Esin\Delta\phi + \Delta Ecos\Delta\phi)]\hat{s}. \end{aligned}$$

Using a calcite crystal instead of a polarizing beam splitter will split the polarizations more efficiently, so the polarization dependance on the reflection and transmission coefficients can be ignored and the polarizations are assumed to be completely separate from each other. This results in only one polarization being incident on one photodiode of the balanced photodetector, and the other polarization being incident on the other photodiode.

Thus, at step 15 the powers in the s- and p-polarization are given by

$$P_p = \bar{E}^2(rcos\Delta\phi + sin\Delta\phi)^2 + \Delta\bar{E}^2(rsin\Delta\phi - cos\Delta\phi)^2 \tag{8–13a}$$

$$P_s = \bar{E}^2(rcos\Delta\phi - sin\Delta\phi)^2 + \Delta\bar{E}^2(rsin\Delta\phi + cos\Delta\phi)^2. \tag{8–13b}$$

To first order in $\Delta\phi$ and second order in ΔE, cos$\Delta\phi \approx 1$ and sin$\Delta\phi \approx \Delta\phi$, and the power levels are given by

$$P_p = \bar{E}^2(r^2 - 2r\Delta\phi) + \Delta E^2 \tag{8–14a}$$

$$P_s = \bar{E}^2(r^2 + 2r\Delta\phi) + \Delta E^2 \tag{8–14b}$$

and the difference in the photodiode signals is given by

$$P_s - P_p = -4r\bar{E}^2\Delta\phi. \tag{8–15}$$

Eq. 8–15 is the resulting balanced photodetector signal under ideal conditions for the interferometer. The p-polarization leakage from PBS1 acts as a local oscillator and if no differential phase is introduced, then the resulting signal from the balanced photodetector will be zero.

8.3.3 Voltage to Phase Calibration

Although a relation to find the differential phase was found in Eq. 8–15 assuming ideal operations, an experimental verification was done in order to determine the exact relation between the output voltage of the balanced photodiode and the differential change in phase. To do this, a 10 m fiber-EOM (model PM1060HF from Jenoptik) was put in series with the fiber already in the interferometer and a voltage was applied to the EOM to produce a tone at 10 MHz. This tone was then detected after HWP3 by a high bandwidth photodetector made by the EOTech company since the balanced photodetector does not have a bandwidth high enough to detect a 10 MHz signal. Rotating HWP3 will cause the amplitude of the tone to change. From this signal, the overall calibration

factor was determined. The conversion factor can then be applied to the time series of the balanced photodetector signal to get the correct differential phase induced.

To determine the calibration factor, a 10 MHz, 3 V peak-to-peak signal was applied to the EOM. The output on the EOTech photodetector was measured with a spectrum analyzer and found to have a peak height of 70 mV. Using the impedance of the spectrum analyzer (50 Ω) and the efficiency of the photodetector (0.75 A/W), the RMS power incident on the photodetector was found to be

$$\frac{0.070V}{50\Omega} \times \frac{1}{0.75A/W} = 1.87mW.$$

To convert the RMS power to the actual power, the RMS power is multiplied by $\sqrt{2}$ to get an incident power of 2.64 mW.

The phase induced from applying the voltage to the EOM was found by multiplying a conversion factor by the applied voltage. The conversion factor was taken from experiments done at the AEI in Hannover and was found to be 7.2 rad/V for the particular EOM used [99]. Using this factor and the applied voltage, results in a total phase change of 22 rad, or ∼3.5 cycles. Using the incident power, the amount of phase change from the EOM, and the responsivity of the balanced photodetector (1.28 V/mW), the overall conversion factor can be found using

$$cal = \frac{\eta \mathrm{P}_{actual}}{3.5\mathrm{cycles}},$$

where η is the responsivity of the balanced photodetector and P_{actual} = 2.64 mW as calculated above. Substituting these numbers, the calibration factor is found to be ∼1 V/cycle. Although this was found to be the calibration signal, there was substantial variability in the peak height of the tone as was measured by the spectrum analyzer. The peak height varied due to the high frequency noise of the experimental setup and an accurate value was difficult to determine. As a result, the peak height of 70 mV was chosen because it was on the lower end on the peak height variability. If a larger peak

height was used, then the calibration factor would become larger, and the differential phase noise would appear to be lower than it actually is.

8.4 Stability Results

In order to determine the sensitivity of the phase detector (in this case, this means the combination of PBS1, HWP1, HWP3, QWP, and the calcite wedge), a mirror was placed after HWP1 and the beam was aligned such that the reflected beam overlapped the incoming beam as much as possible. Placing the mirror before the interferometer acts as if the interferometer were ideal, and so the noise levels of the output fringe of the interferometer can be found. It was found using this configuration that the amount of p- to s-polarization after the calcite wedge was 7:1. HWP3 was rotated such that the powers were then equal on the balanced photodetector. The output of the balanced photodetector was sent into an amplifier where it was amplified by a factor of 20 and low pass filtered at 1 Hz. The gain on the output of the photodetector was needed so the measurement would be above the noise floor of the data acquisition card, while the low pass filter was used to filter some of the noise at higher frequencies. The setup was covered in cardboard to provide some thermal stability. The results are shown in Figure 8-5 and appears to be very flat.

Once the noise floor of the interferometer was known, a fiber was placed in the optical path, and the differential phase noise was measured. Two different optical fibers were tested and both produced similar results. The first fiber is 10 m in length with FC/APC polished ends and was bought from the Nufern company. The second fiber was bought from the Schäfter and Kirchhoff company and is 10 m long with FC/APC polished ends. The Nufern fiber has a significantly thicker outer cladding than the other fiber, but this didn't appear to effect the measurements. The ends of the fiber were polished at an angle to help avoid back-scattering of the incident light. Both fibers are single-mode polarization-maintaining fibers and have a numerical aperture (NA) of 0.12. Light was focused into the fibers through the use of free-space collimating lenses with an NA of 0.15.

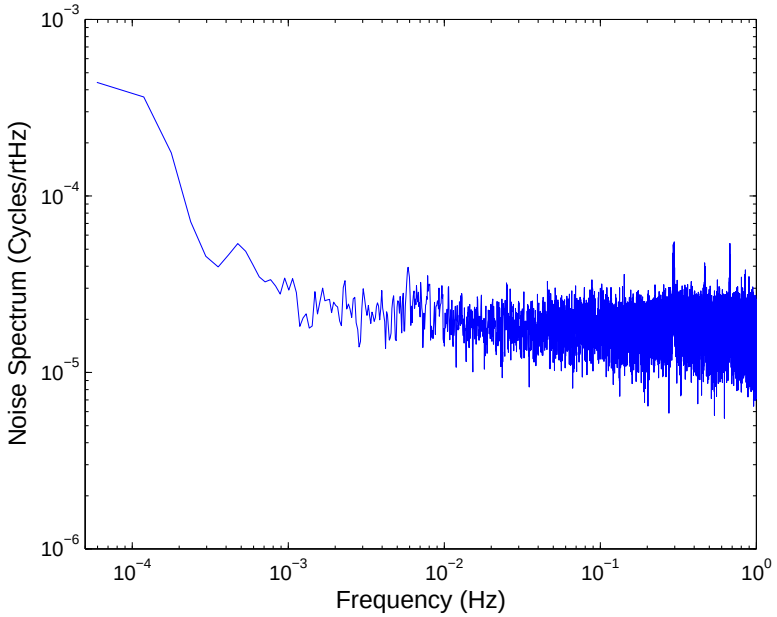

Figure 8-5. Noise spectrum of the detector components of the interferometer. This was found by placing a mirror in front of PBS1 and aligning the back reflected light.

With proper alignment, most of the time 70-80% of the light would go through the fiber each way using the collimating lenses. All optics pertaining to the interferometer were placed on a Super Invar breadboard bought from Newport (represented by the square in Figure 8-4). Typical input powers into the interferometer were between 10 to 30 mW and produced less than a few milliWatts of power on the detector photodiodes.

The interferometer was placed on a vacuum tank flange (represented by the circle in Figure 8-4). The tank lid could then be lowered on top of the flange through the use of a pulley. Several ports were available for light to go in and out of the tank. The initial alignment of the interferometer was done with the lid off and the top was then lowered after the alignment was done. This sometimes caused a small change in alignment. When the tank was on and not under vacuum, one of the ports was left open so the light didn't pass through a glass plate. Aluminum foil was placed over the port to help restrict air currents and provide a small amount of temperature stability inside the tank. A small hole was punched in the aluminum foil to allow the beam to pass through. A noticeable effect

could be seen in the noise spectrums when comparing runs with the tank top on and with it off. When the tank top was on, the noise levels were typically a factor of two to five lower than when the tank was off.

The rest of the optics outside the vacuum tank were shielded using cardboard. The noise levels didn't noticeably change because of it. The reason for the lower noise levels with the tank lid on is unknown, but it is assumed that the temperature fluctuations are less when the tank lid is on.

To try and improve the stability, the port on the tank that had been covered with aluminum foil was replaced with a glass flange and the tank was pumped down using a roughing pump. Unfortunately, as the pressure dropped, the alignment into the fiber became worse and eventually no light was going through the fiber. The misalignment as the pressure drops most likely occurs due to stresses that are induced in the optical components that change the beam trajectory. Attempts to realign the beam into the fiber through mirrors outside of the tank were unsuccessful.

After several tests with the fiber in the interferometer and the tank placed on top, it was found that a parasitic interferometer was causing the photodiode signal to be significantly more noise [100]. The solution was to modulate the laser frequency by applying a triangle wave with amplitude of 3 V peak-to-peak and frequency of 5 kHz. The noise dropped by almost an order of magnitude as shown in Figure 8-6. Modulating at this frequency changed the laser frequency by 75 GHz/s. By modulating the laser frequency at this rate, the fields reaching the detector have a frequency different from the main input beam [101]. In this manner, the noise from the parasitic interferometer is now well outside of the measurement band.

After this problem had been solved, it was then noticed that over the course of a few days, the amount of light going through the fiber dropped significantly. Often the fiber would be aligned such that 80% of the light would be transmitted and a few days later this would drop to 50% or lower. Typically the light transmitted from PBS2 was

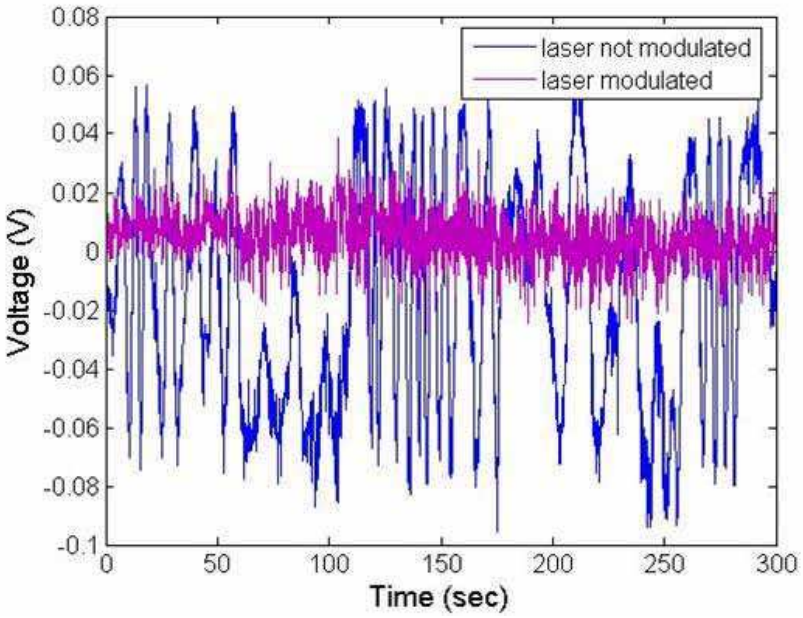

Figure 8-6. Plot of the time series before and after modulating the frequency of the laser. It is clear that modulating the laser frequency produces significantly less noise.

affected more than the reflected light. To determine the cause of this, glass plates were put in at each end of the fiber and were aligned such that the angle the surface of the glass plate made with the output of the fiber was close to the Brewster angle. The powers of both glass plate reflections were measured using a photodiode. In addition, another glass plate was placed after HWP1 in the same manner to determine if the input power was changing as well. The results of all three measurements taken at the same time are shown in Figure 8-7. It is easy to see that the input power is staying almost constant while the output powers from the fiber are changing over time. The exact cause of this was never determined, but it is speculated that it could be from pointing issues into the fibers.

While the powers measurements were being taken, the output of the balanced photodetector was monitored as well as shown in Figure 8-8. The exact relationship between the changing fiber output powers and the change in voltage of the balanced photodiode is difficult to determine. As the power through the fiber changed, it was also determined that the mode of the fiber after HWP3 changed as well. When the

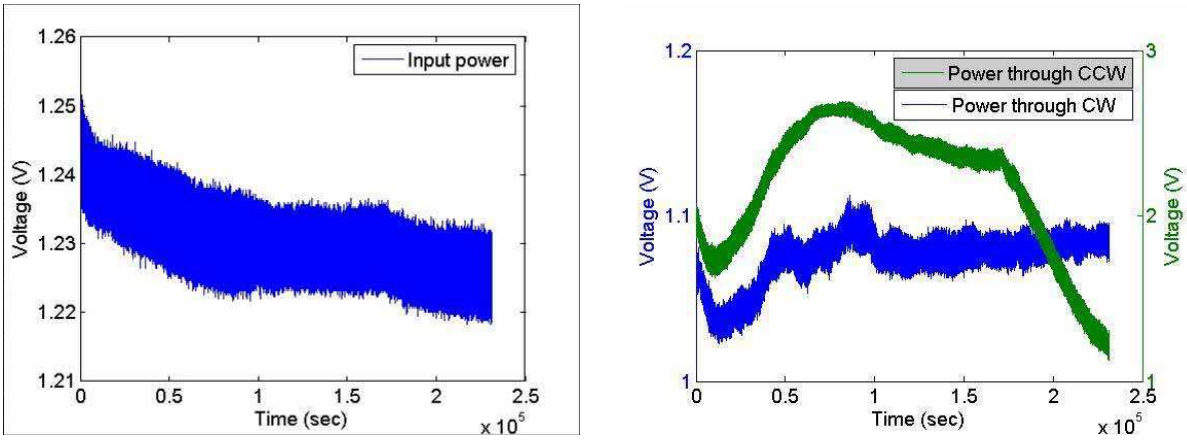

Figure 8-7. Time series of the input power to the interferometer (left) and the time series of the powers during the same time in both the clockwise and counterclockwise beams (right).

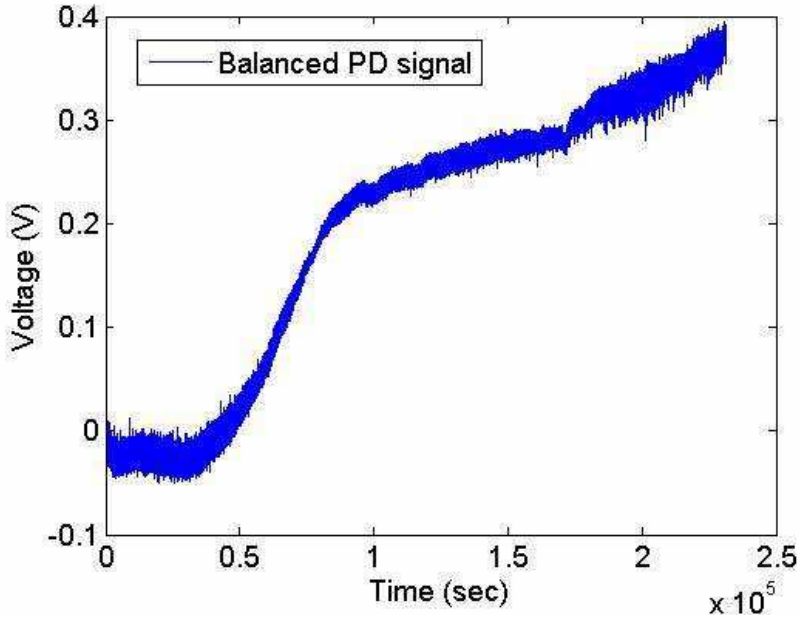

Figure 8-8. Time series of the balanced photodetector at the same time the powers of the counterpropagating beams are measured.

interferometer was properly aligned, the resulting beam shape after HWP3 appeared to be that of a TEM_{00} mode. After 8-12 hours, the mode would become oddly shaped and was most representative of a TEM_{01} or TEM_{02} mode. Realignment of the interferometer would cause the beam to revert back to its original shape. The exact cause of both the power loss through the beam and the change in made is difficult to determine from the data taken, but it may be that they are linked somehow.

The best results for the differential phase noise are presented in Figure 8-9. At higher frequencies, the noise is on the 10^{-5} level, but at lower frequencies, the noise is about two orders of magnitude higher. If the differential phase noise scales with the length of the fiber, then the levels would be 10 to 20 times lower since the LISA back-link fiber will only be 0.5 to 1.0 m in length. This would almost meet the LISA requirement at high frequencies, but a significant amount of work will need to be done in order to determine the cause of the low frequency noise.

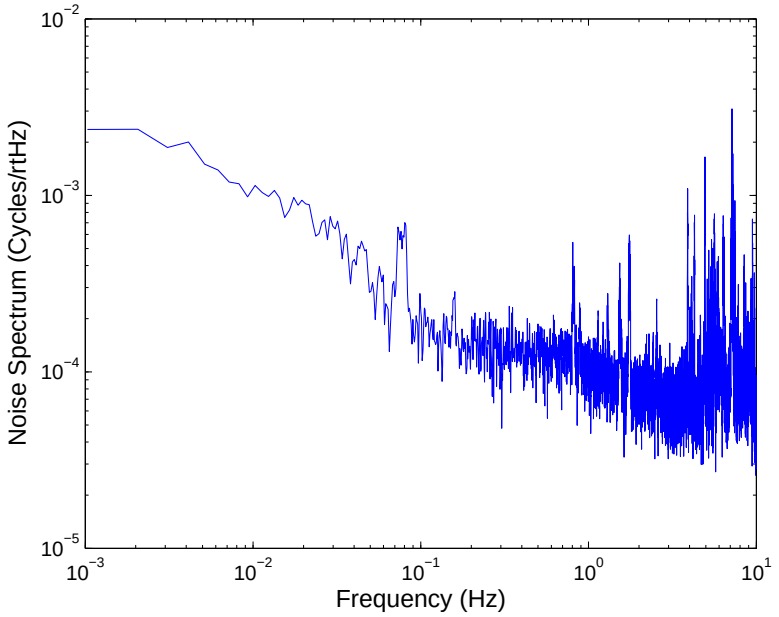

Figure 8-9. Noise spectrum of the optical fiber with counter-propagating beams.

Although the LISA requirement was not met using the Sagnac interferometer, a significant amount of information was learned about the stability of the optical fiber and

noise sources that are associated with it. The stability results are within a factor of three to five of what other groups at the AEI in Hannover [102] and JPL were able to achieve using a more LISA-like experiment. In both these experiments, the noise appears to be limited by the back-scatter of the beam into the fiber. Information about pointing and back-scatter from the fiber will be used to design another experiment that will hopefully be sensitive enough to reach the necessary requirements.

CHAPTER 9
CONCLUSION

9.1 Hydroxide Bonding

There are a variety of techniques available to joint two pieces together. The bond thickness, bonding material, and operating temperature are all factors that need to be considered when choosing the bonding technique. Hydroxide bonding is a new bonding technique that has already shown promising results. Although the this technique had been previously studied in some detail, results in this dissertation expand further on the process.

It was found that the reason the glass was breaking in the first tests were due to the wire used in the lever-arm apparatus, and not from the water in the solution weakening the glass. From this, a better way to test the materials was found and the MCST was developed. Using this device, existing glass to glass results were expanded on by varying the amount of solution used, varying the concentration of the solution, and testing bonds made with rough surfaces. It was found that there is no significant dependance in shear strength of the bond based on the amount of solution used, whether a 1:4 or 1:6 concentration is used, or if a rough surface is used instead of a polished surface. Typical shear breaking strengths were 2 to 5 MPa.

It was also found that hydroxide bonding could be used on Super Invar, which is due to its ease of oxidizing. Super Invar to BK7 bonds proved to be successful, and varying the amount of solution used showed no significant dependance on the shear breaking strength. The average breaking strength was found to be $\sim$5 MPa.

Although bonding SiC to SiC had already been done, the bonding process required the materials to be heated to over 1000°C and the bonds were not reliably made with significant strength. A more reliable and simpler way to bond SiC was found, and produced typical breaking strengths of 3 to 5 MPa. The surface profile of the materials, the amount of solution used, and the dilution factor of the sodium silicate solution were

all varied and showed no dependance on the shear strength of the bonds. In addition, the bonding mechanism was found for the SiC to SiC bonds using a sodium silicate solution. The SiO on the SiC acts to bond the SiO_2 in the solution and produces a bond with significant strength.

The versatility of the hydroxide bonding process demonstrates that it is a promising bonding technique that can be used for many space-based missions. Although promising results have been reported, further investigations are needed to determine how to achieve the optimum bond strength in a repeatable manner, and under what conditions the bond will survive. By further understanding this bonding technique, the limits to which it can be used will be found.

9.2 Material Stability

Zerodur, SiC, Super Invar, PZT, and CFRP are all materials that have either been used on space-based missions, or are promising materials to be used for future missions. While some of the materials presented in this work have been studied already, all but Zerodur have yet to be studied at the $\mathrm{fm}/\sqrt{\mathrm{Hz}}$ level.

Zerodur with both optically contacted and hydroxide bonded mirrors showed almost identical noise levels and were well below the LISA pre-stabilization requirement. Although the hydroxide bonds may produce a higher noise spectrum, it was not detectable with our system.

Both SiC and CFRP were found to meet the LISA telescope requirement. While this would appear to indicate that both materials could be used for the LISA telescope support structure, CFRP needs to be studied in greater detail before a definitive conclusion can be reached. This is due to the fact that the CFRP cavity outgassed and the overall shape is not similar to what would appear on the LISA mission. Although it was seen that the CFRP cavity initially outgassed, both the overall length contraction and outgassing constituents need to be studied further. It would also be useful to study a cavity that has a shape to what would be expected on the LISA mission, and not a cavity that was made

for maximum stability. While the outer cylinder on the CFRP cavity helps to provide the inner cylinder from twisting and contracting unevenly, its large radius is not indicative of what would be used on the LISA mission. From the results presented, it appears that SiC would be a more viable material for use as a telescope support structure than CFRP.

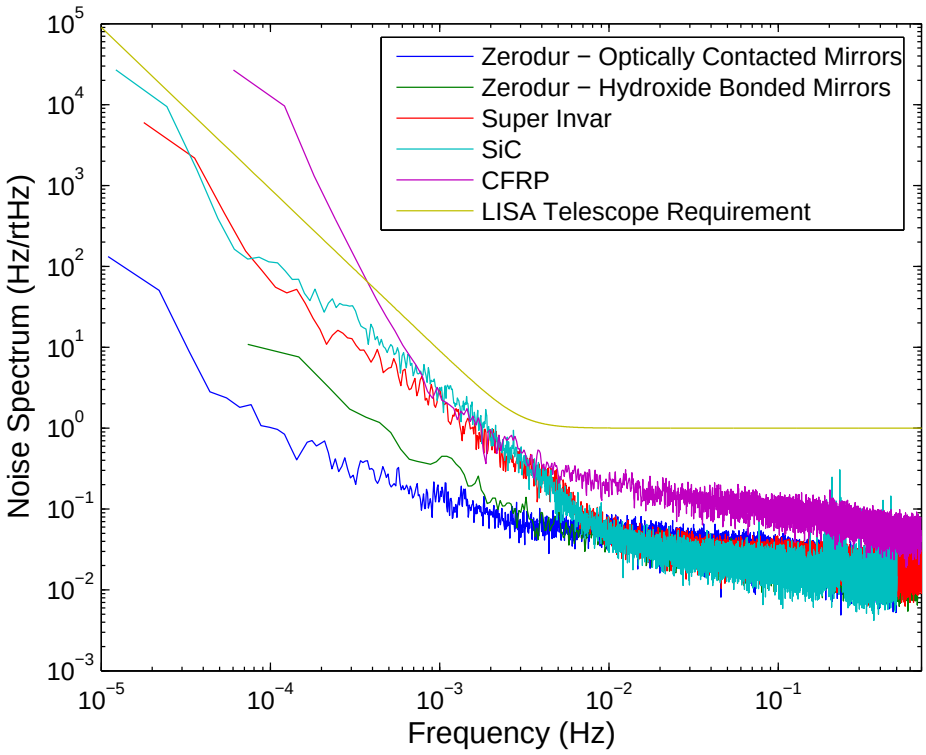

Figure 9-1. Comparison of the noise spectrums of the Zerodur cavities with both optically contacted and hydroxide bonded mirrors, SiC, CFRP, and Super Invar along with the LISA telescope requirement.

Although Super Invar was shown to meet the LISA telescope requirement, it will not be used on the LISA mission due to it magnetic properties. Despite this, its ease of machinability, high strength, high stability, and low CTE make it a material that may be suited for other missions that require ultra stable materials. In addition to finding the stability of Super Invar, it was also shown that using a sodium silicate solution to bond the mirrors appeared to produce no additional noise. This is significant since the bonds produced using the potassium hydroxide solution when bonding the mirrors for the Zerodur cavity are about a factor of four thinner than those when sodium silicate solution

are used. Thus, the hydroxide bonding technique is more than suitable for use on the LISA mission and could be used to form complex optical structures from other materials such as SiC, and not just Zerodur.

Despite the PZT cavity producing noise levels slightly above the LISA pre-stabilization requirement, it was shown that through the use of an additional feedback control that is fed to the PZT, the noise spectrum of the cavity can be pushed orders of magnitude below the pre-stabilization requirement. It was also shown that a voltage of up to ∼200 V could be applied to the PZT without a noticeable increase in the noise spectrum. This is over an order of magnitude larger than what would be needed for arm-locking. The combination of its low noise levels with an applied voltage, its ability to be used for arm-locking, and the fact that it survived vibrational conditions similar to what would be expected during launch make the PZT cavity viable for use on the LISA mission.

Even though the PZT cavity is viable for the LISA mission, by using the same PZT material and thickness and increasing the length of the Zerodur spacer, the noise of the cavity should decrease. It should also be noted that the expected temperature stability on the LISA optical bench is approximately an order of magnitude better than the temperature stability of the tank the PZT cavity was tested in. Although a beatnote drift is noticeable when a voltage is applied to the PZT, a slowly changing applied voltage should not produce any significant drifts.

From the presented results, all materials except the PZT and CFRP cavity reached a common noise floor above ∼0.01 Hz (see Figure 9-1), which is well below the LISA pre-stabilization requirement. This would imply a common noise limit of the measurement system has been reached and further improvements will be needed in order to push the noise floor down. At frequencies below ∼1 mHz, the noise is limited by temperature fluctuations in the lab that propagate through the thermal shields. Although the thermal shields provide significant attenuation at high frequencies, at low enough frequencies the thermal shields have almost no attenuation as can be seen in the beatnote frequency

oscillations. For materials with large CTE's, the beatnote oscillations will be larger, which produces a higher noise spectrum at low frequencies. To determine the amount of compactification or outgassing that occurs in materials such as SiC or CFRP over year-long time scales, active temperature stabilization will be needed since the beatnote fluctuations are most likely larger than the expected beatnote fluctuations due to the compactification process. Although further improvements are needed to fully determine the noise spectrum of these materials, promising results have been achieved already.

9.3 Cesium Locking

Both the modulation transfer spectroscopy and frequency modulation spectroscopy experimental setups were tested, and the modulation transfer technique produced a lower noise spectrum. In addition, the noise spectrum using the modulation transfer technique were about an order of magnitude lower than using a free-running laser at low frequencies. Several systematic noise sources in this setup were investigated and ruled out as the cause of the drift in the beatnote. While the exact cause is unknown, it is suspected that the beatnote drift is due to an expansion or contraction in the cavity from temperature changes in the lab, or from laser intensity fluctuations that change the thickness of the mirror coating which appear as a length change. Although promising initial results were achieved, cesium stabilization thus far has not proven to be a viable use for long term measurements due to the cesium cells consistently breaking after several months of operation, and the high frequency noise associated from heating the cesium cell to over 220°C. Significant improvements in the cesium cell design and an implementation of a fabry-perot cavity would allow the operating point of the cesium cell to be lowered and the absorption increased, which would provide lower noise.

9.4 Telescope

A design for an on-axis telescope support structure using SiC was developed and made. The design, known as the "quad-pod" for its four struts that separate the primary and secondary, was built using an alignment jig that held the struts in place while they

could be hydroxide bonded to both the primary and secondary. The first prototype was successfully built and transported to the University of Florida, where one of the struts mysteriously came undone. Despite this, the structure was cooled to approximately -65°C using a specially designed vacuum chamber. After warming up and a visual inspection, it appeared the telescope was still in tact, but applying a small force to the secondary caused the entire structure to collapse. An inspection of the bonds on the primary and secondary showed that the telescope had twisted in the alignment jig during the bonding process. While this may or may not have caused the strut to become un-bonded, a redesign of the alignment jig was done to account for this. It was also decided that using SiC "sister blocks" epoxied to the strut and either primary or secondary would provide additional strength to the overall structure. In this manner, hydroxide bonding will be used to provide the initial alignment, while the sister blocks will provide additional strength. Bonding of the next prototype is currently underway along with setting up the optics needed to test both the relative and absolute stability of the structure. At least one optical cavity will be made in the center of the structure to determine the relative stability, and an iodine stabilized laser is in the process of being set up in order to determine the absolute length change of the telescope. These future experiments will be used to determine the viability of the telescope design for the LISA mission.

9.5 Back-Link Fiber

A Sagnac interferometer was constructed in order to determine the differential phase induced in an optical fiber with counter-propagating beams. It was found that a spurious interferometer was in induced in the setup and by modulating the laser frequency, the noise could be reduced by almost an order of magnitude. It was also found that over time the power coming out of the fiber decreased, despite the input power being constant. This is most likely due to pointing issues and could be remedied through active stabilization of the interferometer mirrors using PZT mirror mounts. A calibration tone was injected into the system using a fiber EOM to determine the relationship between the output

voltage on the balanced photodetector and the differential phase noise. From this, the differential phase could be measured. At higher frequencies, it was found that the noise was a little over an order of magnitude higher than the 10^{-6} cycles/$\sqrt{\text{Hz}}$ requirement. This result is within a factor of three to five of what other groups at the JPL and the AEI in Hannover were able to achieve using a significantly more complex experimental design. Additionally, if the noise scales with the length of the fiber, then within some of the LISA band, the fiber meets the requirements. It is expected that the results using the Sagnac interferometer would improve if placed inside a vacuum chamber, but this was not able to be done because once the pressure in the tank began to decrease, the alignment through the fiber became misaligned so bad that no output signal could be detected. Using PZT mirror mounts would prove useful in this case since active alignment could be done as the pressure drops inside the tank. The information learned from the noise sources will be used to design another experiment that will hopefully show that the differential phase using counter-propagating beams in a fiber can be kept below 10^{-6} cycles/$\sqrt{\text{Hz}}$.

APPENDIX A
THERMAL SHIELD DESIGN

Temperature fluctuation inside the vacuum tank will cause the cavity to expand and contract based on its CTE. The purpose of the thermal shields will be to act as a passive low pass filter to attenuate the temperature fluctuations in the lab. A typical temperature noise spectrum for the outer wall of Tank 2 is shown in Figure A-1. Using the equations

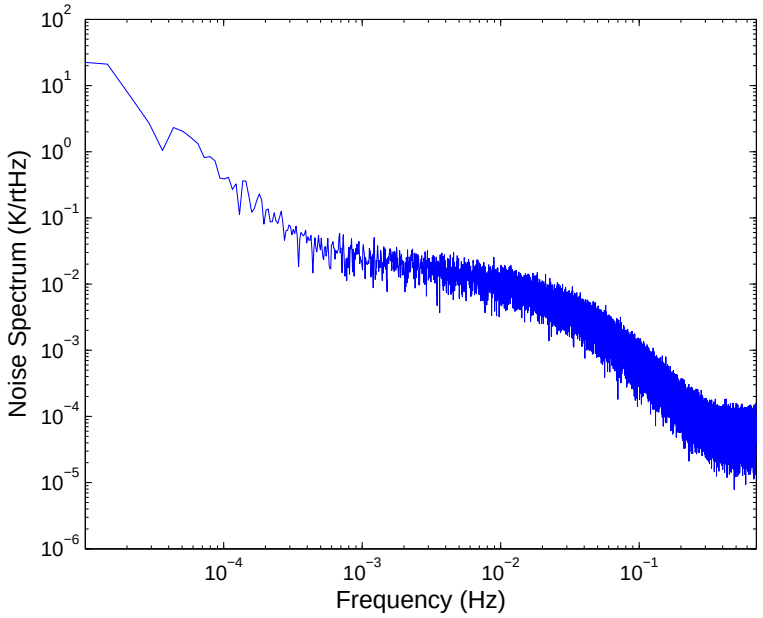

Figure A-1. Noise spectrum of the outside tank temperature.

$$\begin{aligned} \frac{\delta\nu}{\nu} &= \frac{\delta L}{L} \\ \delta L &= \alpha L \delta T_{cav} \end{aligned} \tag{A–1}$$

where $\delta\nu$ is the LSD of the frequency, ν is the frequency of the laser, δL is the LSD of the length of the cavity, L is the length of the cavity, α is the CTE of the cavity, and δT_{cav} is the LSD of the temperature of the cavity, the corresponding frequency fluctuations can be found via

$$\delta\nu = \nu\alpha\delta T_{cav}. \tag{A–2}$$

To keep the frequency noise of the cavity due to thermal fluctuations low, either the CTE of the cavity needs to be extremely low, the temperature stability in the tank needs to be low, or a combination of both should be used. Although using feedback controls and a heater or cooler could be used to actively control the temperature of the cavity, a focus on passive thermal shielding will be presented here. Based on Figure A-1, several orders of magnitude of temperature suppression will be needed in order for the frequency fluctuations to be below 1000 Hz/$\sqrt{\text{Hz}}$. The adopted set up to provide the thermal insulations is shown in Figure A-2.

The thermal shields consist of 5 cylindrical layers of an aluminized PET whose base is a sheet of aluminum. Each successively smaller cylinder is thermally insulated from the next using Macor spacers. In the center of the thermal shields is a long stand that elevates the cavity to a height such that the laser can pass through the cavity. The aluminized

Table A-1. Diameters and heights of the thermal shield cylindrical shells.

	Shell 1	Shell 2	Shell 3	Shell 4	Shell 5
diameter (m)	1.08	1.00	0.93	0.85	0.77
height (m)	0.91	0.86	0.81	0.76	0.71

PET has a low emissivity and acts to reflect the radiation from its surrounding. The large heat capacity of the aluminum allows the thermal shield to absorb large amounts of energy while changing its temperature very little. Although the aluminized PET has a higher heat capacity, its thickness is only 0.12 mm thick and has a negligible mass when compared to the mass of the aluminum. The low thermal conductivity of the Macor spacers impedes the heat flow from one cylinder to the next. A summary of properties for all three materials is listed is Table A-2. To determine the attenuation the thermal

Table A-2. Material properties of Macor, aluminized PET, and aluminum.

Material	Thermal Conductivity (W/mK)	Emissivity	Density (kg/m^3)	Heat Capacity (J/kg C)
Aluminized PET	–	0.03	1380	1190
Aluminum	250	∼0.15	2700	902
Macor	1.46	–	2520	790

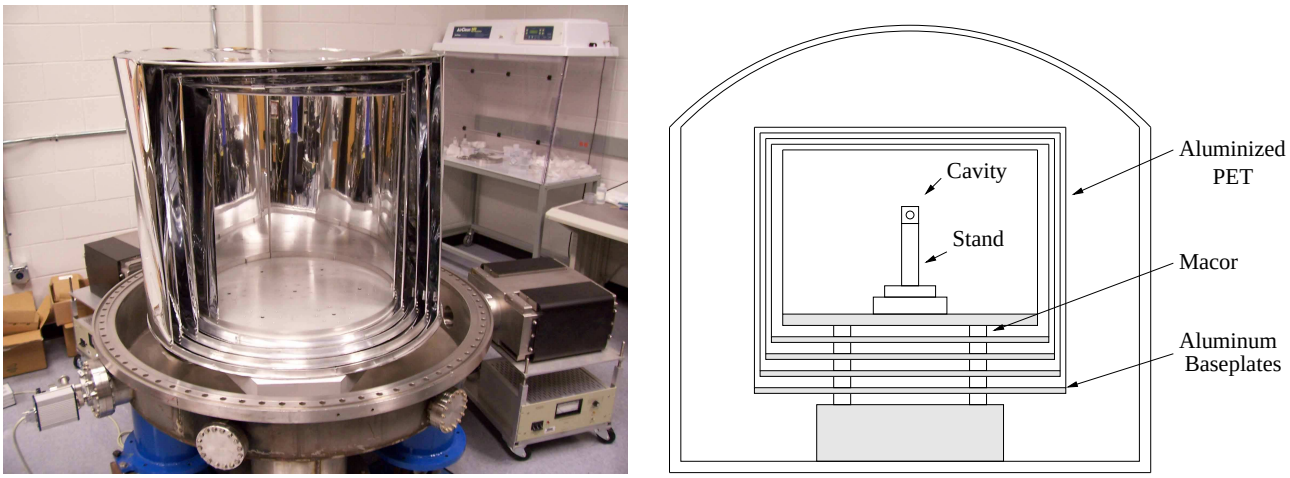

Figure A-2. Picture of the built thermal shields (left) and a model representation of them (right). Note the model is not drawn to any scale.

shields will provide, a thermal lumped model will be used. Only conduction and radiative heat transfer will be considered since the convective process will be negligible due to the high vacuum within the tank. A simplified lumped thermal model of the thermal shields is shown in Figure A-3. The thermal resistance for both conduction and radiation can be

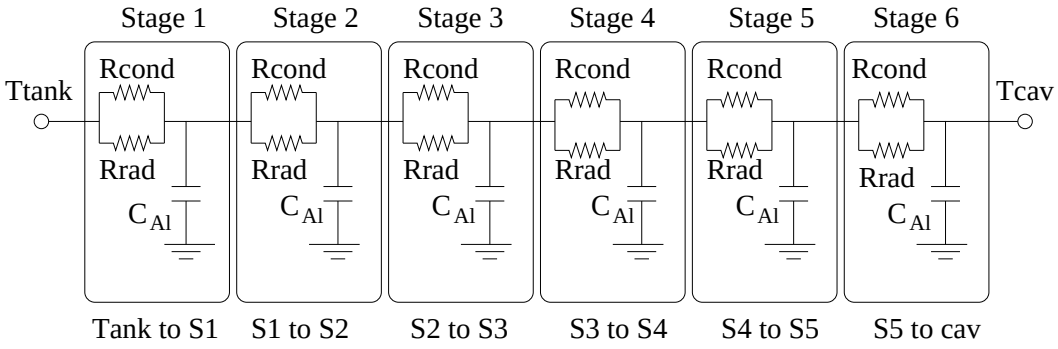

Figure A-3. Lumped thermal model of the thermal shields.

found using

$$R_{cond} = \frac{l}{\kappa A_{cond}} \tag{A–3}$$

$$R_{rad} = \frac{\beta}{4\sigma A_{rad} T^3} \tag{A–4}$$

where R_{cond} is the conductive thermal resistance, l is the length of the element between the two bodies at different temperature, κ is the thermal conductivity of the element, A_{cond} is the cross section of the element, R_{rad} is the radiative resistance, σ is Boltzmann's constant (5.67×10^{-8} W m^{-2}K^{-4}), A_{rad} is the area of the body which is heated due to radiation, T is the initial or mean temperature of the bodies, and β is a factor used when determining the radiative resistance of cylindrical shells defined by

$$\beta = \frac{1}{\epsilon_1} - \frac{1-\epsilon_2}{\epsilon_2}\frac{r_1}{r_2}. \tag{A–5}$$

The total thermal resistance and capacitance of each stage is given by

$$\begin{aligned} R &= \frac{R_{rad}R_{cond}}{R_{rad}+R_{cond}} \\ C &= c\rho V, \end{aligned} \tag{A–6}$$

where c is the heat capacitance, ρ is the density, and V is the volume of the aluminum base plates. The time constant of the low pass filter, τ, for each cylindrical shell is

$$\tau = RC. \tag{A–7}$$

The first order cutoff frequency for the filter is then

$$f_{cutoff} = \frac{1}{2\pi RC}. \tag{A–8}$$

These values for each stage of the thermal shields are given in Table A-3. The expected

Table A-3. Resistance, capacitance, time constant, and cutoff frequency for each stage of the thermal shields.

Stage	R_{rad} (KW^{-1})	R_{cond} (KW^{-1})	R (KW^{-1})	C J kg^{-1}	τ (s)	f_c (Hz)
1	68.6	0.08	0.08	40325	3085	5×10^{-5}
2	33.3	0.075	0.075	1626	122	1.30×10^{-3}
3	33.3	0.075	0.075	1626	122	1.30×10^{-3}
4	33.3	0.075	0.075	1626	122	1.30×10^{-3}
5	33.3	0.075	0.075	1626	122	1.30×10^{-3}
6	1.91	0.40	0.33	3262	1083	1.47×10^{-4}

global low pass filter can be found using the values in Table A-3 from

$$H(f) = \prod_{n=1}^{6} \frac{1}{2\pi\tau_i i f + 1} \tag{A–9}$$

where τ_i are the values of τ at stage i. Plotting |H(f)| as a function of frequency will result in the amount of suppression the thermal shields will provide at that frequency. This is shown in Figure A-4. The attenuation is not shown below 10^{-5} in order to gain an

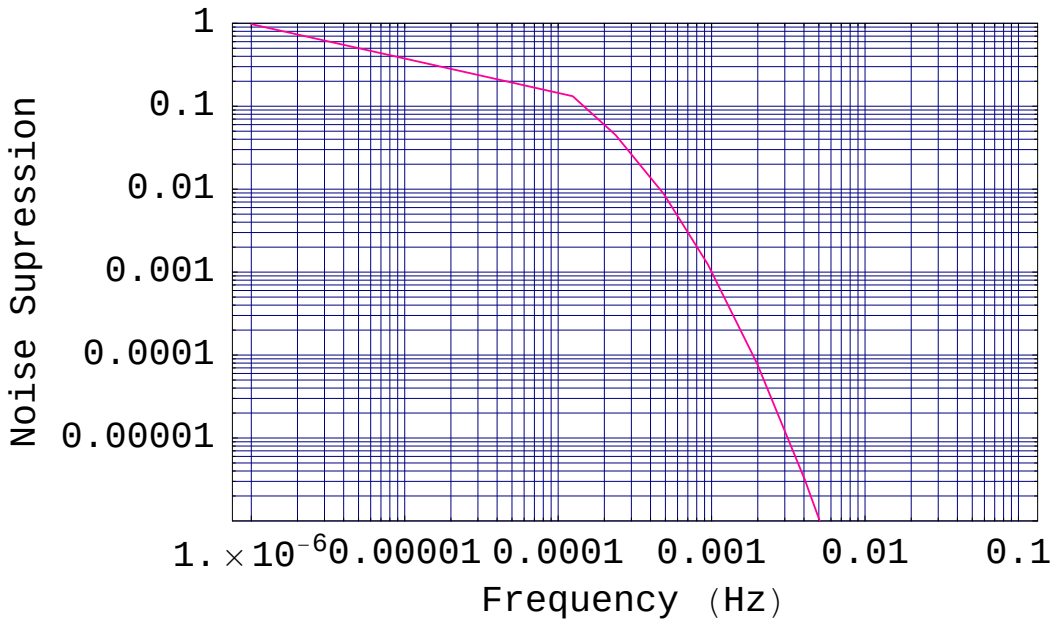

Figure A-4. Transfer function of the PET thermal shields.

understanding of the transfer function at low frequencies.

To compare this effectiveness of this model, the transfer function of the thermal shields can be used with the tank temperature data shown in Figure A-1 to determine what the expected beatnote fluctuations should be due to the temperature fluctuations of the tank. Unfortunately, the expected frequency fluctuations do not match up well with the measured beatnote fluctuations and are approximately an order of magnitude larger than what is actually measured at low frequencies. This is most likely due to the limitations of using a lumped thermal model and simplifications of the tank design that were used. In the lumped thermal mode, it was assumed that there is only a large

aluminum block that sits on the tank bottom that supports the thermal shields. In fact, there are three large posts that support the aluminum block which would provide a significant amount of thermal noise suppression at low frequency due to their large mass. A COMSOL model would provide a more accurate description of the transfer function and would provide more accurate estimates of beatnote fluctuations.

APPENDIX B
CLEANING COMPONENTS FOR BONDING

When cleaning optical components for bonding, great care must be taken to ensure the surfaces are as clean as possible. Using a clean room is optimal as this allows a smaller chance of particles to get on the surfaces. Although a clean room is preferred, optical and hydroxide bonding have been done using areas that have been cleaned thoroughly. A general guideline is presented below to clean the optical surfaces before bonding.

1. Inspect surfaces to be bonded. If there are any large particulates on the surface, wash off with methanol and clean room wipe.
2. Fold a microfiber cloth in half and place at the bottom of the sonic bath. Place pieces to be bonded on top of the cloth so that the surfaces to be bonded are facing up.
3. Fill sonic bath with deionized (DI) water.
4. Run sonic bath for 15-30 minutes. The dirtier the optical components, the longer the sonic bath should run.
5. After the sonic bath has stopped running, drain the DI water.
6. Wipe the components to be bonded using a clean room wipe wetted with methanol. If possible, use compressed nitrogen to blow off any excess water, methanol, or dirt still on the components. If any streaks or particulates can be seen on the surfaces to be bonded, repeat this step until they have been removed.

If a sonic bath is not available, an alternate cleaning method can be used to clean the surfaces to be bonded. This method is described below.

1. Wet a microfiber cloth with DI water.
2. Dab the damp part of the cloth into some powdered cerium oxide.
3. Rub on the surface to be bonded in a circular motion. Do this for approximately 5 minutes. The dirtier the surfaces, the longer this step should be done. You may need to dab the cloth into the cerium oxide again (or many times) during this time to ensure ample amount of cerium oxide is on the surface.
4. Rinse off excess cerium oxide using methanol.

5. Wet another part of the microfiber cloth with DI water again and dab with sodium carbonate. You may need to dab the cloth into the sodium carbonate many times during this step. Make sure to use plenty of sodium carbonate to ensure any cerium oxide residue is cleaned off.

6. Rub in a circular motion for approximately 5 minutes.

7. Rinse components thoroughly using methanol. If a film can be seen on the surface, then an optical wipe wetted with methanol can be used to removed the residue.

Another possible method to clean the bonding surfaces is to initially clean the surfaces using cerium oxide and then place the pieces in a sonic bath as described above.

Although using the cerium oxide will help to clean and polish the surfaces, a "pitting" effect has been noticed when this is done. To determine the effects of using cerium oxide, a WYKO profilometer was used to determine the surface profile on several spots of a SiC tile. A typical surface profile before using cerium oxide is shown in Figure B-1. The SiC tile was then polished and cleaned as described above and the surface profile was determined using the WYKO once again. The resulting surface profile is shown in Figure B-2. Although the rms roughness of the tile seems to have become smoother, there are noticeable spots where the surface has deep pits. The cause of this effect is unknown.

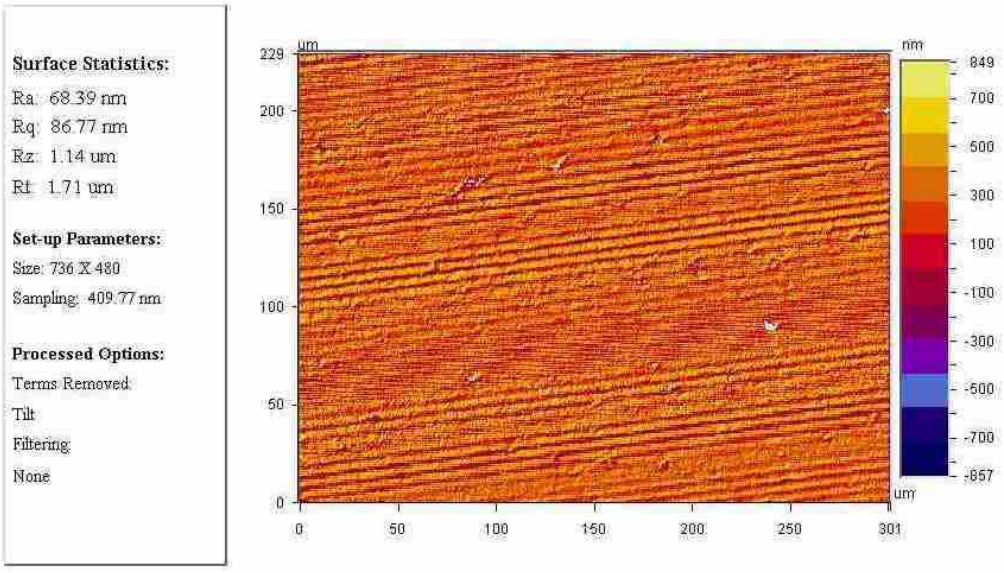

Figure B-1. Typical surface profile of a SiC surface before cleaning with cerium oxide.

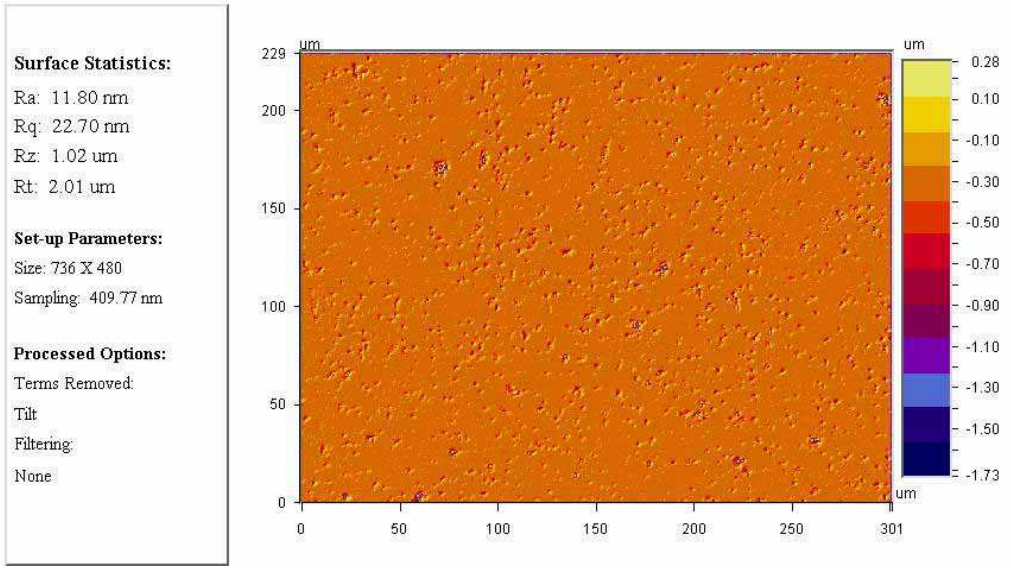

Figure B-2. Typical surface profile of a SiC surface after cleaning with cerium oxide.

APPENDIX C
CALCULATION OF THE LINEAR SPECTRAL DENSITY

The linear spectral densities (LSD) computed for the spectrums in Chapters 5-8 were done using a Matlab script. The script computes the power spectral density (PSD) using Welch's method of overlapping segmented averages of modified periodograms and is based on techniques described in "Spectrum and spectral density estimation by the Discrete Fourier Transform", G. Heinzel, et. al. [103].

A time series with a known sampling frequency (f_s) is loaded into Matlab. The time series is then divided into sections of N data points as defined by the user. It should be noted that the bin spacing will be equal to the lowest frequency and is equal to f_s/N. A linear regression is fit to the time segments and subtracted out. This residual is then multiplied by a Hanning window (not to be confused with a Hamming window) and a discrete Fourier transform is performed on the windowed residual. The power spectral density for the ith segment is then calculated and an average is taken over all segments to get the power spectral density for the entire set. The linear spectral density is then computed by taking the square root of the power spectral density.

The time series measurements of the frequency counter can be converted to a length spectrum using

$$\frac{\delta\nu}{\nu} = \frac{\delta l}{l},$$

where $\delta\nu$ is the linear spectral density of the measured beatnote, ν is the laser frequency, δl is the linear spectral density of the length of the cavity, and l is the length of the cavity.

REFERENCES

[1] B. Tapley, S. Bettadpur, M. Watkins, and Ch. Reigber. "The Gravity Recovery and Climate Experiment: Mission Overview and Early Results". *American Geophysical Union*, (2004).

[2] J. Davis, P. Elosequi, J. Mitrovica, and M. Tamisiea. "Climate-driven deformation of the solid Earth from GRACE and GPS". *Geophys. Res. Let.*, 31(L24605).

[3] G. Ramilliena, F. Frapparta, A. Cazenavea, and A Göuntner. "Time variations of land water storage from an inversion of 2 years of GRACE geoids". *Earth and Planetary Science Letters*, 235:283–301, (2005).

[4] M. Dehne, F. Guzmán Cervantes, B. Sheard, G. Heinzel, and K. Danzmann. "Laser interferometer for spaceborne mapping of the Earth's gravity field". *Journal of Physics: Conference Series*, 154, (2009).

[5] J. Taylor and J. Weisberg. "Further experimental tests of relatavistic gravity using the binary pulsar PSR 1913 + 16". *Astrophys. J.*, 345:434–450, (1989).

[6] M. Valtonen *et al.* "A massive binary black-hole system in OJ 287 and a test of general relativity". *Nature letters*, 452:851–853, (2008).

[7] NASA. "LISA – Laser Interferometer Space Antenna". for more information, go to http://www.lisa.nasa.gov, accessed 5 May 2010, Copyright 2010.

[8] M. Ando *et al.* "DECIGO Pathfinder". *Journal of Physics: Conference Series*, 120, (2008).

[9] LISA Study Team. "Laser Interferometer Space Antenna for the detection and observation of gravitational waves". Pre-phase A report, July 1998.

[10] S. Hughes. "LISA sources and science". arXiv:0711.0188v1 [gr-qc], 1 Nov 2007.

[11] B. Allen. "relativistic gravitation and gravitational radiation". In edited by J. A. Marck and J. P. Lasota, editors, *Proceeding of the Les Houches School of Physics*, page 373. Cambridge University Press, 1997.

[12] A. Kosowsky, A. Mack, and T. Kahniashvili. *Phys. Rev. D*, 55:7368, 1997.

[13] C. Hogan. "Gravitational Wave Sources from New Physics". In edited by S. M. Merkowitz and J. C. Livas, editors, *Laser Interferometer Space Antenna*, page 397. AIP Conference Proceedings 823, Mellville, New York, 2006.

[14] M. Benacquista and Holley-Bockelmann. *Astrophys. J.*, 645:589, 2006.

[15] A. Stroeer and A. Vecchio. "the LISA verification binaries". *Class. Quant. Grav.*, 23:S809–S818, 2006.

[16] M. Haehnelt. page 45. AIP Conference Proceedings 456, 1998.

[17] C. Hopman. "Astrophysics of extreme mass ratio inspiral sources". In edited by S. M. Merkowitz and J. C. Livas, editors, *Laser Interferometer Space Antenna*, page 397. AIP Conference Proceedings 823, Mellville, New York, 2006.

[18] Laser Interferometer Space Antenna (LISA) Requirements Flowdown Guide, February 2007.

[19] DRS ITAT. "LISA DRS Acceleration Noise Budget". LISA Project internal report, 2005.

[20] A. Cavalleri, G. Ciani, R. Dolesi, A. Heptonstall, M. Hueller, D. Nicolodi, S. Rowan, D. Tombolato, S. Vitale, P. Wass, and W. Weber. "A new torsion pendulum for testing the limits of free-fall for LISA test masses". *Class. Quant. Grav.*, 26, (2009).

[21] S. Anza. "the LTP experiment on the lisa pathfinder mission". *Class. Quant. Grav.*, 22:S125–S138, 2005.

[22] J. Armstrong, F. Estabrook, and M. Tinto. "Time delay interferometry". *Class. Quant. Grav.*, 20:S283–S289, (2003).

[23] M. Sallusti, P. Gath, D. Weise, M. Berger, and H Schulte. "LISA system design highlights". *Class. Quant. Grav.*, 26, (2009).

[24] S. Turyshev, M. Shao, and K. Nordtvedt Jr. "Science, Technology, and Mission Design for the Laser Astrometric Test of Relativity". *Astrophysics and Space Science Library*, 349:473–543.

[25] S. Turyshev, M. Shao, and K. Nordtvedt Jr. "Experimental Design for the LATOR Mission". *arXiv:gr-qc/0410044v1*, 8 Oct 2004.

[26] J. Yu. "Laser Astrometric Test of relativity (LATOR) mission". In Edited by M. Shao, editor, *JPL Technical Memorandum*, volume 2200. SPIE, 1994.

[27] TIE-31: Mechanical and thermal properties of optical glass. July 2004, Version 2.

[28] TIE-37: Thermal expansion of ZERODUR, August 2006.

[29] J. Baer and W. Lotz. "Figure testing of 300 mm ZERODUR mirrors at cryogenic temperatures". In *Cryogenic Optical Systems and Instruments IX, SPIE Proc.*, volume 4822, (2002).

[30] D. de Chambure, R. Laine, K. van Katwijk, and P. Kletzkine. "XMM's X-Ray Telescopes". XMM project bulletin 100, December 1999.

[31] W. Sokolowski, S. Jacobs, M. Lartc, I. O'Donnell, and C. Hsieh. "Dimensional Stability of High Purity Invar 36". *Mechanical Systems Engineering and Research Division*, Jet Propulsions Laboratory.

[32] S. Jacobs, S. Johnston, and D. Schwab. "Dimensional instability of Invars". *Applied Optics*, letter to the editor, (1984).

[33] M. van Veggel. *The Basic Angle Monitoring system: picometer stability with Silicon Carbide optics*. PhD thesis, Technische Universiteit Eindhoven, 2007.

[34] REACTION BONDED SILICON CARBIDE: SFF, PROCESS REFINEMENT AND APPLICATIONS. Department of Mechanical Engineering, The University of Texas at Austin, Austin, TX 78712.

[35] POCO Grahpite. "SUPERSiC material properties". see http://www.poco.com/MaterialsandServices/SUPERSiCSiliconCarbideMaterialSystem/tabid/66/tabid/124/Default.aspx for details, accessed 5 May 2010, Copyright 2010.

[36] Saint Gobain. "Hexoloy SA Silicon Carbide Technical Data". see http://www.hexoloy.com/data-sheets for details, accessed 5 May 2010, Copyright 2003.

[37] CoorsTek. "Technical Ceramics". see http://www.coorstek.com/materials/ceramics.asp for details, accessed 5 May 2010, Copyright 2009.

[38] S. Suyama, T. Kameda, and Y. Itoh. "Development of high-strength reaction-sintered silicon carbide". *Diamond and Related Materials*, 12:1201–1204, (2003).

[39] O Kubaschewski and C Alcock. *Metallurgical Thermochemistry*. Pergamon Press, New York, 5th edition edition, 1979.

[40] S. Black. Getting to Know "Black Aluminum". Technical report, 2008.

[41] Electroceramics. Technical report, Morgan electroceramics.

[42] C. Poizat and A. Benjeddou. "On analytical and finite element modelling of piezoelectric extension and shear bimorphs". *Computers and Structures*, 84:1426–1437, (2006).

[43] Piezo Technologies. "K-180 Lead Zirconate Titanate Piezoelectric Ceramic with High Shear Coupling Coefficient, Low Permittivity, and High Temperature Stability". for more information, go to http://www.piezotechnologies.com/k180.htm,accessed 5 May 2010, Copyright 2010.

[44] V. Greco, F. Marchesini, and G. Molesini. "Optical contact and van der Waals interactions: the role of the surface topography in determining the bonding strength of thick glass plates". *Journal of Optics A: Pure and Aplied Optics*, 3:85–88, (2000).

[45] J.-J. Ferme. "Optical Contacting". In D. Rimmer G. Roland, R. Geyl and L. Wang, editors, *SPIE Proc.*, volume 5252 of *Optical Fabrication, Testing, and Metrology*, (2004).

[46] J. van Elp, P. Giesen, and J. van der Velde. "Anodic bonding using the low expansion glass ceramic Zerodur". *American Vacuum Society*, (2005).

[47] M. Powers. "Hermetic Glass-to-Aluminum Seals for RF Packaging Applications: A University-Industry Design Project Collaboration". In editors: John Stephens and K. Scott Weil, editors, *Brazing and Soldering*, Proceedings of the 3rd International Brazing and Soldering Conference, (2006).

[48] A. Belohlav. Understanding Brazing Fundamentals. Technical report, The American Welder, 2000.

[49] D. Bath, D. Spain, E. Ness, S. Williams, and M. Bougoin. "Evaluation of segmented and brazed mirror assemblies". Technical report, collaboration between CoorsTek and Boostek companies. technical note.

[50] S. Gibb. Two Part Epoxy Adhesives. Technical report, 2006. A Technical Memo Prepared for Opti 521 Introduction to Opto-Mechanical Engineering.

[51] J. Daly. "Structural Adhesives for Optical Bonding". *SPIE short course notes*, (2001).

[52] Master Bond Inc. "Master Bond Polymer System EP21TCHT-1 Product Description". For more information see http://www.masterbond.com/tds/ep21tcht-1.html, accessed 5 May, 2010 Copyright 2009.

[53] E. Elliffe, J. Bogenstahl, A. Deshpande, J. Hough, C. Killow, S. Reid, D. Robertson, S. Rowan, H. Ward, and G. Cagnoli. "Hydroxide-Catalysis Bonding for Stable Optical Systems for Space". *Class. Quant. Grav.*, 22:S257–S267, (2005).

[54] D. Gwo. "Ultraprecision Bonding for Cryogenic Fused-Silica Optics". In *SPIE Proc.*, volume 136 of *3435*, (1998).

[55] A. van Veggel, D. van den Endeb, J. Bogenstahl, S. Rowanc, W. Cunninghamc, G. Gubbels, and H. Nijmeijer. "Hydroxide catalysis bonding of silicon carbide". *Journal of the European Ceramic Society*, 28:303–310, (2008).

[56] G. Somerjai. *"Chemistry in Two Dimensions: Surfaces"*. Cornell University Press, Ithaca, N.Y., 1981.

[57] A. Preston and G. Mueller. "Bonding SiC to SiC using a sodium silicate solution". *In preparation*, (2010).

[58] B. Lauke K. Schneider and W. Beckert. "Compression Shear Test (CST) – A Convenient Apparatus for the Estimation of Apparent Shear Strength of Composite Materials". *Applied Composite Materials*, 8:43–62, (2001).

[59] A. Preston, B. Balaban, and G. Mueller. "Hydroxide-Bonding Strength Measurements for Space-Based Missions". *Int. J. Appl. Ceram. Technol.*, 5(4):365–372, (2008).

[60] A. van Veggel, D. van den Ende, J. Bogenstahl, S. Rowan, W. Cunningham, G. Gubbels, and H. Nijmeijer. "Hydroxide Catalysis Bonding of Silicon Carbide". *Journal of the European Ceramic Society*, 28:303–310, (2007).

[61] S. Rowan, J. Hough, and E. Elliffe. "Silicon Carbide Bonding". Please contact Mr. D. Whiteford for further information: D.Whiteford@admin.gla.ac.uk.

[62] A. Preston, B. Balaban, G. Boothe, and G. Mueller. "Stable Materials and Bonding Techniques for Space-Based Optical Systems". In *NASA Science and Technology Conference*, page Session C1 P3, (2007).

[63] J. Berthold III. *Dimensional Stability of Low Expansivity Materials Time Dependent Changes in Optical Interfaces and Phase Shifts on Reflection from Multilayer Dielectrics*. PhD thesis, University of Arizona, 1976.

[64] G. Wallis and D. Pomerantz. "Field Assisted Glass-Metal Sealing". *Journal of Applied Physics*, 40:3946–3949, (1969).

[65] J. Berthold III, S. Jacobs, and M. Norton. "Dimensional Stability of Fused Silica, Invar, and Several Ultra-Low Thermal Expansion Materials". *Metrologia*, 13:9–16, (1977).

[66] D. Gwo. "Hydroxide-Catalyzed Bonding". United States Patent No. U.S. 6 548 176 B1, 2003.

[67] Personal communications with Suvrath Mahadeven at the University of Florida department of Astronomy.

[68] A. Preston. "Stable Materials for LISA". Talk presented at the Frontiers in Optics conference, October 2009.

[69] B. Young, F. Cruz, W. Itano, and J. Bergquist. "Visible Lasers with Subhertz Linewidths". *Physical Review Letters*, 82(3799), (1999).

[70] H. Kogelnik and T. Li. "Laser Beams and Resonators". *Applied Optics*, 5(10), (1966).

[71] A. Seigman. *Lasers*. Stanford Science Books, 1986.

[72] R. Cruz. *DEVELOPMENT OF THE UF LISA BENCHTOP SIMULATOR FOR TIME DELAY INTERFEROMETRY*. PhD thesis, University of Florida, 2006.

[73] Personal communications with the Space and Gravity Research group at the University of Birmingham.

[74] J. Livas, J. Thorpe, K. Numata, S. Mitryk, G. Mueller, and V. Wand. "Frequency-tunable pre-stabilized lasers for LISA via sideband locking". *Class. Quant. Grav.*, 26, (2009).

[75] E. Black. "An introduction to PoundDreverHall laser frequency stabilization". *American Journal of Physics*, 69(1):79–87, (2001).

[76] D. Shaddock *et al.* "LISA frequency control white paper". Technical report, LISA project technical note LISA-JPL-TN-823, 2009.

[77] S. Webster, M. Oxborrow, and P. Gill. "Vibration insensitive optical cavity". *Phys. Rev. A*, 75:011801(R), (2007).

[78] A. Preston, R. Cruz, J. Thorpe, G. Mueller, G. Boothe, R. Delgadillo, and S. Guntaka. "Dimensional Stability of Hexoloy SA Silicon Carbide and Zerodur Materials for the LISA Mission.

[79] A. Preston, R. Cruz, I. Thorpe, G. Mueller, and R. Delgadillo. "Dimensional Stability of Hexoloy SA Silicon Carbide and Zerodur Glass Using Hydroxide-Catalysis Bonding for Optical Systems in Space". In Joseph Antebi Edited by Eli Atad-Ettedgui and Dietrich Lemke, editors, *Proceedings of the SPIE: Optomechanical Technologies for Astronomy*, volume 6273, (2006).

[80] L. Conti, M. De Rosa, and F. Marin. "High-spectral-purity laser system for the AURIGA detector optical readout". *Journal of the Optical Society of America B*, 20(3):462–468, (2003).

[81] A. Preston and G. Mueller. "PZT-actuated tunable cavity for use in the LISA mission". *In preparation*, (2010).

[82] A. Stumner. "1-kV Piezo Amplifier Keeps Cost, Noise Low". published on http://electronicdesign.com/article/components/1-kv-piezo-amplifier-keeps-cost-noise-low3789.aspx, August 2001. accessed 25 April, 2010.

[83] S. Lin. "Study on the equivalent circuit and coupled vibration for the longitudinally polarized piezoelectric ceramic hollow cylinder". *Journal of Sound and Vibration*, 275:859–875, (2004).

[84] B. Cheng and M. Reese. "Stress relaxation and estimation of activation volume in a commercial hard pzt piezoelectric ceramic". *Bull. Mater. Sci.*, 24(2):165–167, April (2001).

[85] New Focus Corporation. "FM Spectroscopy With Tunable Diode Lasers, Application note 7". see http://www.newfocus.com/products/documents/literature/apnote7.pdf for more details, accessed 5 May 2010, Copyright 2001.

[86] O. Orlov and V. Ustyugov. "Molecular cesium frequency reference for frequency stabilization of a 1.06 μm nd:yag laser". *Sov. Tech. Phys. Lett.*, 12:120–121, 1986.

[87] P. Fritschel and R. Weiss. "Frequency match of the nd:yag laser at 1.064 μm with a line in co_2". *Appl. Opt.*, 31:1910–1912, 1992.

[88] R. Benedict, D. Drummond, and L. Schlie. "Absorption spectra of the Cs_2 molecule". *J. Chem. Phys.*, 66:4600–4607, 1977.

[89] A. Mak, O. Muravitsky, O. Orlov, and V. Ustyugov. "New laser for interferometry with long-term frequency stabilization at 1.06 μm onto molecular cesium standard". In Edited by Z. Jaroszewicz and M Pluta, editors, *in Interferometry '89*, volume 1121, pages 478–484. SPIE, 1989.

[90] E. Inbar, V. Mahal, and A. Arie. "Frequency stabilization of nd:yag lasers to $^{133}Cs_s$ sub-doppler lines near 1064 nm". *J. Opt. Soc. Am. B*, 13(7):4600–4607, July 1996.

[91] R. Schilling, P. Bender, J. Livas, T. Pedersen, A. Martino, P. McNamara, O. Jennrich, A. Preston, and G. Mueller. Notes taken from the LISA telescope subgroup teleconferences. internal document, February 2006.

[92] D. Robertson and J. Hough. Interferometry for LISA. *Class. Quantum Grav.*, 13:A271–A277, 1996.

[93] et. al. R Fleddermann. "Measurement of the non-reciprocal phase noise of a polarization maintaining single-mode optical fiber". *Journal of Physics: Conference Series*, 154, (2009).

[94] K. McKenzie. "Fiber noise measurements and photoreciever development". *Presented at the 7th International LISA Symposium*, (2009).

[95] R. Bergh, H. Lefevre, and H. Shaw. "An Overview of Fiber-Optic Gyroscopes". *Journal of Lightwave Technology*, LT-2(2), (1984).

[96] E. Post. "Sagnac effect". *Rev. Mod. Phys.*, 39:475–494, (1967).

[97] H. Lefevre and H. Arditty. "Theoretical basis of Sagnac effect in fiber gyroscopes". *Fiber-Optic Rotation Sensors and Related Technologies*, 32(8), (1982).

[98] J. Noda and et. al. "Polarization-maintaining fibers and their applications". *J. Lightwave Technol.*, 4(8):1071, (1986).

[99] S. Barke. "Phase Characterization of EOM Sidebands well within the Mission Requirements of the Laser Interferometer Space Antenna". Technical Report Presentation given at the 7th annual LISA symposium, AEI in Hannover, 2009.

[100] A. Preston. "Back-link Fiber Stability". Talk presented at the 7th Inernational LISA Symposium, 2008.

[101] P. Beyersdorf, R. Byer, and M. Fejer. "Results from the Stanford 10 m Sagnac interferometer". *Claasical and Quantum Gravity*, 19(7):1585–1589, (2002).

[102] R. Fleddermann *et al.* "Measurement of the non-reciprocal phase noise of a polarization maintaining single-mode optical fiber". In *Journal of Physics: Conference Series*, volume 154, (2009).

[103] G. Heinzel, A. Rudiger, and R. Schilling. "Spectrum and spectral density estimation by the Discrete Fourier Transform (DFT), including a comprehensive list of window functions and some new flat-top windows". Technical report, Max Plank Institute for Graviational Physics, Hannover Germany, February 15 2002.

BIOGRAPHICAL SKETCH

Alix Preston was born in Bartlesville, Oklahoma, but moved to Fort Collins, Colorado when he was five. He spent his childhood and adolescence fascinated with math and science. He took several Advanced Placement courses in High School and graduated as class Valedictorian. Alix attended the Colorado School of Mines in Golden, Colorado and graduated in the top 20% of his class with a Bachelor of Science in engineering physics in addition to taking several graduate level courses in both math and physics. In the Fall of 2004 Alix began his studies at the University of Florida and soon began working with Dr. Guido Mueller on determining the dimensional stability of materials and bonding techniques for the Laser Interferometer Space Antenna (LISA). This work carried into researching several other aspects of LISA, and is the bulk of his dissertation.